PSL
UNIVERSITÉ PARIS

THÈSE DE DOCTORAT
DE L'UNIVERSITÉ PSL

Préparée à Observatoire de Paris-PSL,
LIRA, UMR 8254 CNRS

Stellar Streams for Galactic and Cosmic Archaeology: when gravity meets complexity

Soutenue par
Salvatore Ferrone
Le 13 October 2025

École doctorale nº127
Astronomie et Astrophysique d'Ile de France

Spécialité
Astronomie et Astrophysique

Préparée au
LIRA, Observatoire de Paris

Composition du jury :

Françoise Combes Collège de France, Observatoire de Paris-PSL	*Présidente du jury*
Jorge Peñarrubia University of Edinburgh	*Rapporteur*
Anna Lisa Varri University of Edinburgh	*Rapportrice*
Chrstian Boily Université de Strasbourg	*Examinateur*
Eugene Vasiliev University of Surrey	*Examinateur*
Raffaella Schneider Università di Roma "La Sapienza"	*Examinatrice*
Paola Di Matteo LIRA, Observatoire de Paris-PSL	*Co-directrice*
Marco Montuori Istituto dei Sistemi Complessi, CNR	*Co-directeur*

Observatoire de Paris | PSL

SAPIENZA
UNIVERSITÀ DI ROMA

Stellar Streams for Galactic and Cosmic Archaeology

when gravity meets complexity

Sapienza Università di Roma
PhD program in Astronomy, Astrophysics and Space Science (XXXVIII cycle)

Salvatore Ferrone
ID number: 1935299

Advisors
Prof. Paola Di Matteo
Dr. Marco Montuori

Coordinator
Prof. Francesco Piacentini

Academic Year: 2024/2025

Acknowledgements

I would like to thank the following people for their help and support:

My advisors, Paola Di Matteo and Marco Montuori, for instructing me, working with me, and giving me a problem to solve.

The entire thesis jury, in particular, my referees, Anna Lisa Varri and Jorge Peñarrubia, for taking the time to read this document in its entirety, and provide earnest feedback. Beyond this, I sincerely thank them for extending their stay in Paris to give seminars to my colleagues and me.

My deepest thanks go to my family–my backbone–including my older brother Frank, my sister-in-law Garcelle, my nephew Roman, and my cousin Lauren. I thank my younger brother, Carmen, and soon-to-be sister-in-law, Elizabeth, for crossing the Atlantic Ocean to attend the defense. Above all, I thank my father, who, by leading through example, taught me resilience, hard work, fairness, virtue, kindness, open-mindedness, and how to retain a light-hearted spirit when confronted with any problem.

I am grateful to my friends, particularly Benjamin Kilian, for embarking on the adventure of continuing our physics studies in Europe, and Joseph Peters, for being a frequent visitor, and both of them for attending my defense. I must truly thank Ben again for this shared journey we embarked on and for being a continuous source of inspiration for my life. I also thank Michael Lathwood, whose passion for physics first inspired me to pursue the field, and Jimmy Tang, who strengthened that passion during my time at Ithaca College.

I extend my thanks to the entire Ithaca College physics department: Professors Price, Bohdi Rogers, Jerome Fung, Luke Keller, Bruce Thompson, the Sullivans, the Countrymen, and Dan Briotta. I offer special gratitude to Professor Beth Ellen Clark, my undergraduate advisor, for launching my career by giving me the opportunity to work on OSIRIS-REx. Beth expanded my life from upstate New York to the rest of the world. I truly thank her.

I am grateful to Jon Robert Brucato, Antonella Barucci, Giovanni Poggiali, Marco Delbò, and Chrysa Avdellidou for welcoming me into the Italian and French astronomical communities.

I also thank Professor Francesco Piacentini for helping coordinate my joint PhD project, and Professor Benoît Mosser for opening the Paris Observatory to international students and warmly welcoming us.

I thank the PSL Welcome Desk, especially Michelle Gray and Baptiste Biancardini, for assisting me with housing, visas, and residency permits—two guardian angels who supported me during crucial moments.

All of my officemates in Rome: Sara Santoni, Silvia Micheli, Agnese Falla, Chiara De Leo, Anna-Chiara Ferri, and Elisa Fazzari——thank you for making me solve puzzles in *La Settimana Enigmistica* and for coming to Paris for my defense. I am especially grateful to Anna-Chiara and Elisa for sheltering me when I needed a place to stay. A special thanks also to Vipul Pradassam, whose company and conversations about the CMB made my stay in Rome truly enjoyable.

A loud, resounding, heartfelt, and could-never-be-sufficient-enough thanks to Antoine Fort and his family. Thank you for welcoming me into your family home for Christmas, for all your support and generosity, for shelter, and for so much more. I offer the same gratitude to Enzo Sarti, who sheltered me for two weeks during the early days of my PhD as I searched for housing, and whose linguistic prowess and love for the world inspire me.

I am also deeply grateful to Houda Haidar, whose resilience serves as a true source of inspiration to me and whose company I always value. I truly cherish the times we navigated our master's degrees together as two foreigners starting out in France.

To my colleagues and friends: Giulia Pagini, Andrea Saccardi, Valeria Cerqui, Sofia Bisero, Jessie Palmerio, Laia Casamiquela, Niklas Moszczynski, Alice Mori, Olivier Vanel, Dylan Chosson, and Eliot Stein—thank you for making daily life in the lab enjoyable.

I extend special appreciation to Owain Snaith, Clément Hottier, Nicolas LeClerc, and Alessandra Mastrobuono-Battisti, whose mentorship and discussions helped me unlock new computational powers. Likewise, Paolo Bianchini, who possesses infectious joy, a vast command of globular clusters and computational methods, and has ascended to the rank of a true polyglot, is an absolute role model.

I would like to thank those whose contagious passion for their work continually inspired me. Mathías Liempi, for his tireless work ethic, his initiative in organizing seminars, his constant openness to discuss any aspect of science, and physical strength; Julia Claire Reitzer, for introducing me to worlds as diverse as feudal Japan, textiles, and design, and for embodying an insatiable curiosity and the courage to step boldly into new disciplines; Pierre Boldrini, whose enthusiasm after every conversation leaves me ready to tackle projects with renewed intensity; and Wassim Tenachi and Rodrigo Ibata, whose depth of knowledge, kindness, intellectual curiosity, light-heartedness, and remarkable ability to bridge domains continue to inspire me to grow in the same spirit.

My sincere thanks go to those who helped me adapt linguistically and culturally to life in Italy and France: Riccardo La Placa, Juliette Hoffemann, Francesca De Nardis, and Jessica Martin. As well as fellow foreigners David Paiypa, Antigone Papanikolaos, Angela Spidal, and Eugenia Urquiza, whose shared experiences and company made the transition a joyful shared adventure.

I thank all of my friends from Utica who make every homecoming a special occasion: Andrea Cvijanovic, Ashley Fredsell, Dzeneta Pajetovic, Senad Libic, Dominic Facciolo, Chaz San Flippo, Joe LaPaglia, Belmin Avdic, Stone Hickey, Noah Jones, Robert and Nicholas Julian, Phat Huynh, Dzenan Racic, Almir Tricic, Ishmail Kucevic, Ruvem Karpovich, and Trey Liggins.

To my housemates from Ithaca College: thank you. Connor, for being a true comrade, having a shared chapter in France, for still coming to Europe so often, your spirit of adventure, open-mindedness, vast knowledge, personal responsibility, kindness, and for always welcoming me when I return home. Niman Doowa, six years apart on opposite sides of the Earth, was nothing to overcome; thank you for introducing me to Thailand, the perfect adventure after this thesis. And to Frank and Eugene Iovine, two master musicians who gave me shelter on Long Island for two weeks in September 2020, when I was unable to board my flight to France after arriving with a rapid COVID test instead of a PCR test.

The list could almost continue indefinitely, but to name some more necessary mentions, to those still actively in my life or who have at one time significantly impacted my journey, either professionally or personally: Manny Zatley, Felix Cabrera, Cheyenne Dorasagno, Rebecca Simon, Kevin Pomer, Julien Hsing, Charlotte Roos, Nathan Jue, Adam Rabayda, Thy Doan Mai Le, Alex Tong, Robert Melikyan, Stravrini Tsangari, Hannah Kaplan, Xiaoduan Zou, Sanford Selznick, Rose Tirrito, and lastly, despite it all, Herminia de Oliveira Amorim.

Résumé

La mission astrométrique *Gaia* a permis l'étude à grande échelle des étoiles et des sous-structures galactiques. Environ 160 amas globulaires (AG) de la Voie lactée, chacun contenant de centaines de milliers à plusieurs millions d'étoiles, peuvent désormais être caractérisés par des distances, des mouvements propres, des vitesses radiales, des masses et des tailles précises. Parallèlement, le nombre de courants stellaires connus est passé d'environ 60 au début de cette thèse à plus de 120 aujourd'hui. Comme les courants tracent les orbites de leurs progéniteurs, ils constituent d'excellents sondages du potentiel gravitationnel de la Voie lactée et des perturbations induites par la matière noire. Grâce à ces données, nous avons étudié le système des courants stellaires et des amas globulaires galactiques. J'ai développé le code open-source tstrippy, qui modélise la perte d'étoiles d'amas par effet de marée via le problème restreint à trois corps. Dans ce cadre, nous prédisons la distribution des débris de marée de tous les AG galactiques et réalisons des simulations du courant de Palomar 5, en montrant la formation de « gaps » dus aux passages proches d'autres amas globulaires. Nous présentons les premières prédictions globales des débris de marée de tous les AG de la Voie lactée. Ces simulations sont accessibles publiquement et utilisées par la communauté. Dans l'étude suivante, nous quantifions la fréquence et l'ampleur des rencontres d'amas globulaires perturbant Palomar 5, montrant que ces interactions doivent être prises en compte pour éviter les faux positifs dans les recherches de sous-halos de matière noire. Nous démontrons également que la présence, dans la même région d'un courant, de populations d'étoiles perdues à différents moments, peut réduire la persistance des gaps, diminuant la sensibilité des courants aux perturbations externes. Ce travail établit la distribution attendue des courants stellaires des AG galactiques et quantifie l'importance des perturbations induites par les AG sur Palomar 5. C'est une première étape pour distinguer l'origine des perturbations des courants, étudier la dynamique interne et l'évolution des amas globulaires, et contraindre le potentiel gravitationnel de la Voie lactée dans sa partie visible et noire.

Mots clés : Voie Lactée ; Amas globulaires ; courants stellaires ; Matière noire ; Dynamique galactique ; Forces de marée

Abstract

The *Gaia* astrometric mission has enabled large-scale studies of stars and Galactic substructures. About 160 Milky Way globular clusters (GCs), each with hundreds of thousands to millions of stars, can now be characterized via accurate distances, proper motions, radial velocities, masses, and sizes. Meanwhile, known stellar streams have grown from about 60 at the start of this thesis to over 120 today. Because streams trace progenitor orbits, they provide excellent probes of the Milky Way's gravitational potential and dark matter perturbations. Enabled by this data, we studied the Galactic stellar stream and globular cluster system. I developed the open-source code `tstrippy`, which models tidal stripping of cluster stars via the restricted three-body problem. Using this framework, we predicted the distribution of tidal debris from all Galactic GCs and ran targeted simulations of Palomar 5's stream, finding that "gaps" can be generated by GC flybys. We present the first global predictions of tidal debris from all Milky Way GCs. These simulations are publicly available and used by the community. In a follow-up study, we quantified the frequency and range of GC encounters perturbing Palomar 5, showing such interactions must be considered to avoid false positives in dark matter subhalo searches. We also showed that the presence, in a given region of the stellar stream, of populations of stars lost at different times can reduce gap persistence, lowering stream sensitivity to external perturbations. This work establishes the expected distribution of tidal streams from Galactic GCs and quantifies the rate at which GCs perturb Palomar 5. It provides a foundation for disentangling the origins of stream perturbations, studying the internal dynamics and evolution of globular clusters, and constraining the Milky Way's gravitational potential in both visible and dark matter.

Keywords: Milky Way; Globular Clusters; Stellar Streams; Dark Matter; Galactic Dynamics; Tidal Forces

Contents

List of Figures

List of Tables

Chapter 1

Introduction

This thesis investigates stellar streams originating from globular clusters (GCs) in the Milky Way. Stellar streams are long, thin structures composed of stars that have escaped their host stellar system, forming coherent tails that can span large regions of the sky (Fig. 1.1). Globular clusters were first systematically cataloged by Charles Messier in the late 1700s – not for their scientific interest at the time, but to help comet hunters avoid mistaking these nebula-like objects for new comets (Messier, 1781). Many of the most prominent globular clusters, along with diffuse nebulae and external galaxies, are included in the Messier catalog (Fig. 1.2). Physically, globular clusters are dense, gravitationally bound systems containing hundreds of thousands to millions of stars, and are an important source of stellar streams.

In Chapter 4, I present our study in which we simulated the expected distribution of stellar streams originating from the entire Milky Way globular cluster system. This study was the first of its kind. Stellar streams have high hopes for being inferential tools for fine details of the gravitational field of the Milky Way, notably for constraining the presence of *dark matter subhalos*. These halos may perturb the stellar streams leaving "gaps" in their wake. Since structure of stellar streams are sensitive to local and global gravitational field, all phenomena that can influence the streams must be well calibrated to ensure proper inference of the distribution of dark matter within the Milky Way. In Chapter 5, we explored how the collective gravitational influence of all globular clusters can perturb streams to produce such gaps.

The structure of the thesis is as follows. The remainder of the introduction provides background on stellar streams, globular clusters, and their astrophysical context, as well as an overview of the current state of the field. Chapter 2 outlines the physical framework used to model stream formation and interpret their morphology. Chapter 3 describes the numerical methods employed in the simulations, including convergence tests and estimates of computational cost. Chapters 4 and 5 present two published studies (S. Ferrone, Delbo, et al., 2023; S. Ferrone, Montuori, et al., 2025), with the final chapter discussing these

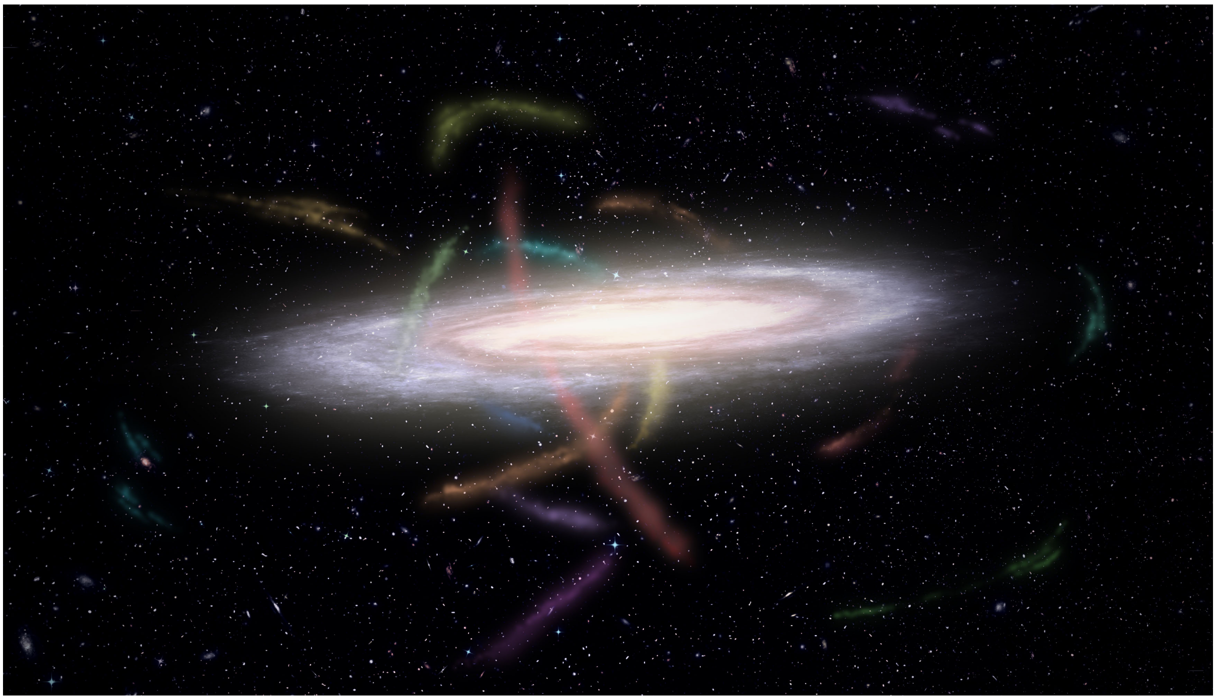

Figure 1.1 – An artist's rendition of a galaxy surrounded by stellar streams. Credit: James Josephides and S^5 Collaboration (T. S. Li, Koposov, Zucker, et al., 2019).

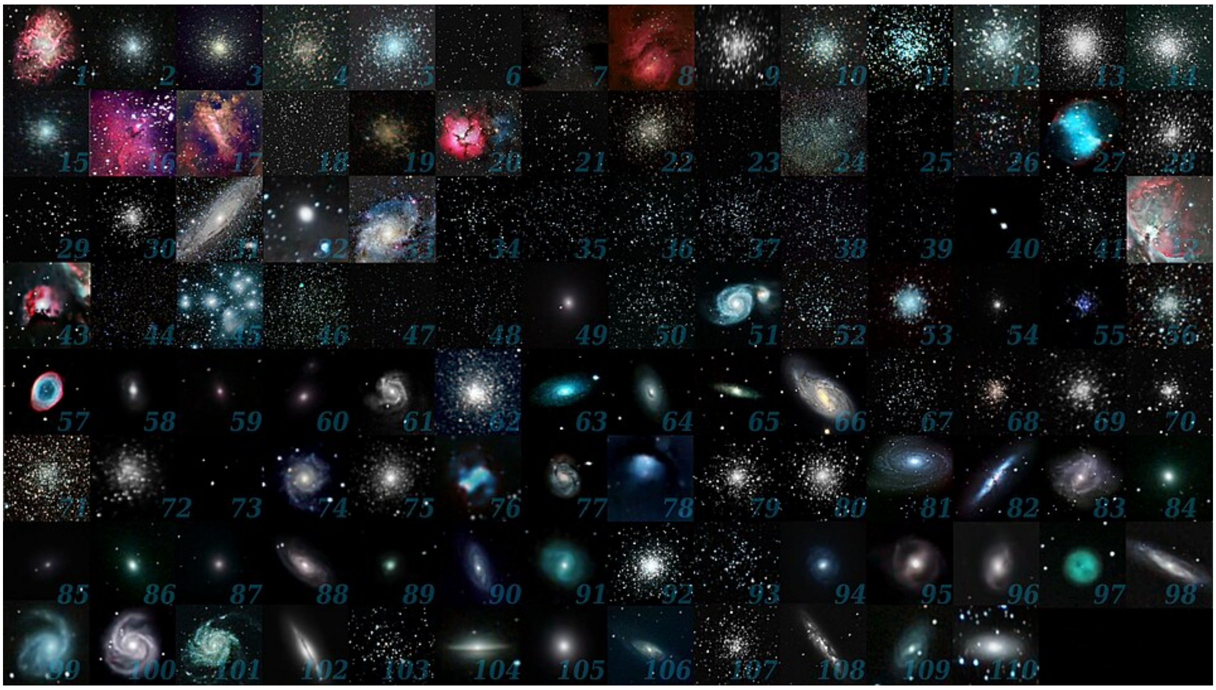

Figure 1.2 – The Messier catalog containing "nebulae-like" objects: planetary nebulae, diffuse nebulae, supernovae remnants, open clusters, globular clusters, and foreign galaxies. By Michael A. Phillips, an amateur astronomer. [1]

results in the broader context of the literature and highlighting future directions. The appendices presents additional studies I have contributed to during this thesis, concerning either the study of stellar streams or the population of asteroids in the solar system – another field of research that I have explored over the years.

1 General context

Before explaining why Milky Way globular clusters and stellar streams are scientifically interesting, it is important to first set the scene. This thesis fits neatly within the field of galactic astronomy, which, at its core, studies the current state of our galaxy and the processes that shaped its formation within the broader context of the Universe.

If we start this narrative from the beginning and place stellar streams and globular clusters in the timeline of cosmic history, their importance becomes clear. The story begins best at the very start. The Lambda Cold Dark Matter (ΛCDM) cosmological model is currently the leading theory of the Universe, successfully unifying a variety of observational evidence from the Cosmic Microwave Background Radiation and the large-scale distribution of galaxies to the accelerating expansion of the Universe, etc. (Carroll, 2001; Perivolaropoulos & Skara, 2022).

Shortly after the Big Bang, conditions allowed protons, neutrons, and electrons to form and interact. For a few minutes, these particles collided and fused into heavier elements in a process known as Big Bang Nucleosynthesis (Steigman, 2007). When this phase ended, the Universe's composition was mostly hydrogen, deuterium (^{2}H), helium-4 (^{4}He), and trace amounts of helium-3 (^{3}He) and lithium-7 (^{7}Li). By mass, hydrogen made up roughly 75%, and helium about 25% of the primordial Universe (Peebles, 1966; Cyburt et al., 2016).

ΛCDM posits the existence of dark matter and that it has about five times more mass than ordinary matter (Planck Collaboration et al., 2020). Dark matter plays a critical role in galaxy formation. In the early Universe, dark matter was distributed nearly uniformly. Over dense regions caused it to collapse into a cosmic web of filaments and nodes. These massive nodes created deep gravitational wells that attracted ordinary matter (Press & Schechter, 1974). The infilling gas subsequently cooled and formed stars. The resulting complex of stars, gas, and dark matter constitutes a galaxy (Plionis et al., 2008; Mo et al., 2010).

Galaxies contain stars that are born, fuse hydrogen and helium into heavier elements, and eventually die, at times as supernovae, enriching the interstellar medium with these heavier elements (Maiolino & Mannucci, 2019). The stellar formation process is a strong function of cosmic time as the chemical evolution of the Universe becomes more metal rich. For example, the first generation of stars, known as Population III (Pop III) stars [2] are thought to have formed in a very different environment, one devoid of metals (Abel et al., 2002; Glover, 2005; Bromm, 2013).

The chemical composition of the gas is crucial since it influences the initial mass function (IMF) of stars. Stars formed from pristine, metal-free gas tend to have a top-heavy IMF, favoring the formation of massive stars (Schneider, Ferrara, et al., 2002; Schneider, Salvaterra, et al., 2006). In contrast, even small amounts of metals introduced into the gas can dramatically shift the IMF toward favoring the formation of lighter stars (Chon et al., 2021).

Globular clusters are, to first approximation, single-stellar populations: their constituent stars formed from the same molecular cloud over a timescale shorter than the internal dynamical time (S. J. Aarseth et al., 1988; Fellhauer et al., 2009; Krumholz, 2014). Owing to their uniform chemical composition, stellar evolution within a cluster proceeds along the color-magnitude diagram as a function solely of initial mass (Kippenhahn et al., 2013). This property enables precise age determinations from photometric observations, a method that historically provided the first robust lower limits on the age of the Universe (Hoyle, 1959; Sandage, 1970; R. G. Gratton, 1985; Murray & Lin, 1992). With their low metallicities and advanced ages, globular clusters are dominated by Population II stars, indicating that they formed in environments enriched exclusively by the earliest generations of stars (Corazza et al., 2022). They thus constitute valuable fossil records of the initial phases of star formation and chemical evolution in the Universe.

Globular clusters are among the most ubiquitous stellar systems in the Universe (Brodie & Strader, 2006; Krumholz et al., 2019). They are found in virtually all galaxy types, from dwarfs to giant ellipticals, and their total number correlates with global properties of their host galaxies such as mass and luminosity (e.g., W. E. Harris, G. L. H. Harris, et al., 2013; Forbes, Read, et al., 2018). In the local Universe, we can directly observe the formation of massive bound stellar systems – so-called young massive star clusters – which may represent present-day analogs of the GC formation process (e.g., Portegies Zwart et al., 2010; Adamo et al., 2020), though whether all such systems will evolve into globular clusters remains an open question.

Globular clusters serve as unique astrophysical laboratories, offering insights into stellar dynamics, stellar evolution, and galaxy assembly. Their evolution involves stellar structure and evolution, gravitational dynamics, and relativistic effects in dense environments. For instance, close stellar encounters and binary interactions – such as mass transfer or mergers – are common in such environments and significantly shape cluster

---

2. Baade (1944) first categorized stars into two groups based on their photometric properties: Population I, stars similar to the Sun, and Population II, metal-poor stars such as those found in globular clusters. Population III stars were later theorized to be the first, primordial stars formed from material produced by Big Bang nucleosynthesis (Blaauw, 1965; Bond, 1981; Bromm & Larson, 2004). The nomenclature therefore labels stellar populations in reverse chronological order.

evolution (Davies et al., 2004; L. Wang, Spurzem, S. Aarseth, Giersz, et al., 2016; Arca Sedda et al., 2024). Additionally, globular clusters are suspected to be a pathway for forming intermediate-mass black holes (IMBHs) (Breen & D. C. Heggie, 2013; Giersz et al., 2015). The origin of IMBHs remains uncertain, as their masses are too large to be explained by isolated stellar evolution, yet too small to fall into the supermassive category (Greene et al., 2020).

Moreover, while traditionally considered as single stellar populations that are homogeneous in age and chemical composition, decades of spectroscopic and photometric evidence have revealed the presence of multiple stellar populations in most GCs (D'Ercole et al., 2008; Conroy & Spergel, 2011; R. G. Gratton et al., 2012; Bastian & Lardo, 2018). The origin of these multiple populations remains debated, with proposed explanations ranging from self-enrichment to accretion of external material, but no consensus has yet emerged.

A striking property of many GC systems is the bimodality in their metallicity distribution, with one population of metal-poor GCs and another of metal-rich GCs (e.g., Brodie & Strader, 2006; W. E. Harris, G. L. Harris, et al., 2015). This bimodality is now widely interpreted as evidence for multiple formation channels: metal-rich GCs likely formed in situ within the main progenitor galaxy during intense star-formation episodes, whereas metal-poor GCs were predominantly accreted from lower-mass satellites. The persistence of this bimodality across a wide range of galaxies suggests that hierarchical accretion has been a fundamental process shaping GC systems, and thus galaxies themselves.

Indeed, from the perspective of galaxy formation, the hierarchical model of structure growth posits that galaxies assemble through repeated mergers and accretion of smaller systems (Somerville & Davé, 2015). In this framework, GCs can form in situ within the main progenitor or be accreted from satellite galaxies (e.g., Forbes & Remus, 2018; Kruijssen, Pfeffer, et al., 2020; Malhan, Yuan, et al., 2021; Malhan, 2022; Pagnini, Di Matteo, Khoperskov, et al., 2023; Belokurov & Kravtsov, 2024; Pagnini, Di Matteo, Haywood, et al., 2025). Consequently, the spatial distribution, kinematics, chemical abundances, and metallicity substructure of a galaxy's GC system retain valuable information about its merger history and assembly pathways. This makes GCs not only tracers of early star formation, but also fossil records of the build-up of their host galaxies.

In essence, globular clusters are involved in many astrophysical processes such as the hierarchical formation of galaxies, formation of intermediate black holes, and being products of barely enriched gas in the early states of the Universe (Kimm et al., 2016; Kruijssen, 2025). Fully understanding their formation and evolution ties neatly into a variety of astrophysical problems.

Globular clusters are of considerable astrophysical interest – not only for studies of stellar formation and evolution, rich internal dynamics, black hole formation, and their role in the build-up of galaxies – but also because they are prolific progenitors of *stellar streams*. As we will show in the next chapter, tidal forces excite stars within the clusters to eventually escape with small speeds that keep the ejected material along more or less the same trajectory, creating the stellar streams.

These streams are particularly valuable astrophysical tools. Their discovery and theoretical explanation date back to the 1990s (see the introductions to Chapters 4 and 5, after which both observational and theoretical work accelerated rapidly. For example, R. A. Ibata, Lewis, M. J. Irwin, et al. (2002) proposed that stellar streams could be sensitive probes of the dark matter subhalo population (see Chapter 5 for a more detailed discussion).

Because stellar streams trace extended, coherent arcs across the sky, they serve as natural guides for mapping the Galactic gravitational field. Koposov, H.-W. Rix, et al. (2010) used the GD-1 stream to constrain the Milky Way potential, while Varghese et al. (2011) performed numerical experiments demonstrating that streams can constrain their host potential even with incomplete phase-space information (e.g., sky positions alone, positions plus radial velocities, or positions plus distances). Bovy et al. (2016) also applied this approach to the Palomar 5 and GD-1 streams, and Law & Majewski (2010) investigated the shape of the Galactic dark matter halo using the Sagittarius stream.

These pioneering studies demonstrated the potential of stellar streams as astrophysical probes, but they represented only the beginning. With the advent of the *Gaia* mission (Perryman, K. S. de Boer, et al., 2001), the volume and precision of available data have transformed what is possible.

2 The state of the art

The current era of Galactic astronomy is undoubtedly defined by the Gaia space mission (Gaia Collaboration, Prusti, et al., 2016; Gaia Collaboration, Brown, Vallenari, Prusti, de Bruijne, Mignard, et al., 2016; Gaia Collaboration, Brown, Vallenari, Prusti, de Bruijne, Babusiaux, Bailer-Jones, et al., 2018; Gaia Collaboration, Brown, Vallenari, Prusti, de Bruijne, Babusiaux, Biermann, et al., 2021b; Gaia Collaboration, Vallenari, et al., 2023). The European Space Agency's space-based observatory conducted continuous observations of the sky to perform precise astrometric measurements. Operating since 2014, Gaia improves its data volume and quality each year through repeated parallax measurements. As of Data Release 3, the mission has provided distances and proper motions for nearly two billion stars in the Galaxy, along with more than thirty-three million of radial velocity measurements (Gaia Collaboration, Vallenari, et al., 2023). This yields five-dimensional phase-space information (positions and on-sky velocities) for about 1-2% of the Galactic stellar population. Although the radial velocities are limited to relatively bright stars, the resulting dataset is still unprecedented in scope.

When additional measurements are required, Gaia data are often complemented with observations from other facilities. For example, Gaia struggles to determine parallaxes in the crowded interiors of globular clusters, where high stellar densities pose challenges for its instruments (Pancino et al., 2017). To address this, Baumgardt & Vasiliev (2021) combined Gaia EDR3 astrometry with *Hubble Space Telescope* observations, enabling precise distance measurements for 162 globular clusters.

Several ground-based spectroscopic surveys aid in extending Gaia's radial velocity measurements to fainter magnitudes and in providing detailed chemical abundances. Examples include the Apache Point Observatory Galactic Evolution Experiment (APOGEE; (Majewski, Schiavon, et al., 2017)), the Gaia-ESO Survey (Gilmore, Randich, et al., 2022), GALAH (Zucker et al., 2012) and upcoming wide-field facilities such as 4MOST (de Jong et al., 2019) and WEAVE (Dalton et al., 2014).

These large data sets have led to a rapidly increasing number of stellar stream discoveries. With the advent of the `streamfinder` algorithm (Malhan & R. A. Ibata, 2018; Malhan, R. A. Ibata, Goldman, et al., 2018), many streams could be detected simultaneously. This was possible because `streamfinder` agnostically applies a friend-finding algorithm to identify coherent stellar groups in the data. It was initially applied to a small number of streams to reassess their properties and discuss their characteristics in light of the improved quality and quantity of the data (R. A. Ibata, Bellazzini, et al., 2019; R. Ibata, G. Thomas, et al., 2020).Encouraged by these initial successes, the method was scaled up to the full Gaia dataset, allowing for a systematic search across a much larger region of the sky. R. Ibata, Malhan, N. Martin, et al. (2021) subsequently applied `streamfinder` to Gaia DR2 and EDR3, resulting in a major increase in the number of known stellar streams. This analysis improved the data quality for many previously known streams and led to several new detections, a selection of which is reproduced in Fig. 1.3. They reported nine new streams, bringing the total number of known Galactic stellar streams to about sixty.

The work of R. Ibata, Malhan, N. Martin, et al. (2021) was a primary motivation for this study. They showed that, of the roughly sixty stellar streams known at the time, only twenty were associated with globular clusters. As summarized in Piatti & Carballo-Bello (2020), no clear correlations have been found between a cluster's orbital or structural parameters and the presence (or absence) of tidal tails. This motivated our simulation of the expected mass-loss distribution for the entire Milky Way globular cluster population, presented in Chapter 4.

The improved quality and completeness of stellar stream catalogs in the Gaia era have rapidly expanded the scope of scientific applications. With these data, many studies have already begun to address a wide range of questions, including:

1. reconstructing the accretion history of the Milky Way;
2. measuring the local and global gravitational potential;

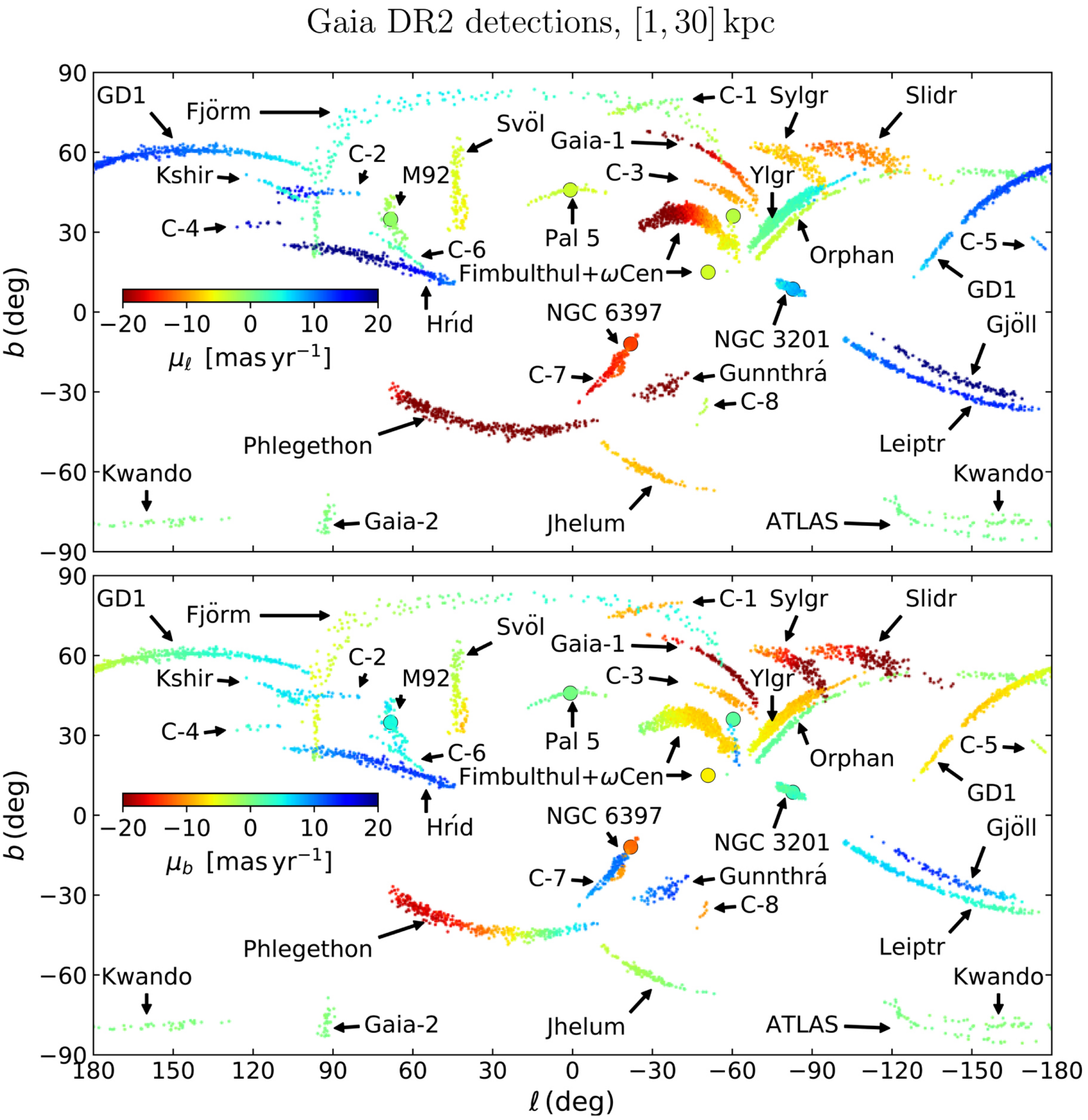

Figure 1.3 – Milky Way stellar streams discovered with `streamfinder` in Gaia DR2. Both plots are shown in Galactic coordinates. The top panel is color-coded by proper motion in longitude, while the bottom is color-coded by proper motion in latitude. This is Fig. 1 from R. Ibata, Malhan, N. Martin, et al. (2021).

3. probing the influence of time-dependent dynamical processes such as the bar, giant molecular clouds, and dark matter subhalos.

A recent review by Bonaca & Price-Whelan (2025) provides a comprehensive overview of some of these efforts. Usefully, they classify stream morphology as the result of three main factors: (1) the internal dynamics of the progenitor system, which determine the rate and energy of escaping stars; (2) the smooth, time-independent gravitational field, which sets the orbital path and tidal forces; and (3) time-dependent perturbations, including those from baryonic and dark matter substructure. We refer the reader to that review for a detailed discussion, and return to some of these aspects in Chapters 4 and 5.

Stellar streams are also providing new insights into globular cluster formation. Several proposed scenarios exist, one of which suggests that clusters formed within their own dark matter subhalos (Kruijssen, 2025). While kinematic studies have explored the consequences of this hypothesis (Vitral & Boldrini, 2022), current evidence disfavors it. For example, Kimm et al. (2016) showed that clusters forming in deep dark matter potential wells would display metallicity spreads larger than those observed, and Malhan, Valluri, Freese & R. A. Ibata (2022) used Gaia data to demonstrate that the velocity dispersions of several Milky Way streams are inconsistent with predictions for clusters embedded in massive, cuspy halos.

Streams can also help distinguish between globular cluster and dwarf galaxy progenitors (Bonaca, Naidu, et al., 2021). For instance, Yuan, Chang, et al. (2020) discovered a metal poor "Low Mass Stream" which they were able to associate dynamically with two globular clusters and argued that one of the clusters was actually the nuclear star cluster of the now defunct dwarf galaxy that has been completely merged into the Milky Way. Malhan, Yuan, et al. (2021) further characterized the stream and remarked that it has a broad metallicity distribution and a high velocity dispersion—properties more consistent with a disrupted dwarf galaxy than with a globular cluster.

N. F. Martin et al. (2022) presented the metallicity of over 25 streams that were detected with `streamfinder` using the PRISTINE survey (Starkenburg et al., 2017). N. F. Martin et al. (2022) found that many streams are indeed metal poor. Despite the fact that globular clusters are already metal-poor objects compared to typical field stars within the galactic disk (Brodie & Strader, 2006), some streams are even more metal poor than all the known globular clusters (Wan et al., 2020; N. F. Martin et al., 2022; Yuan, Matsuno, et al., 2025).

Next, regarding the gravitational potential of the Milky Way, streams are being used to probe the granularity of the Milky Way's gravitational field. A striking example is the GD-1 stream: Bonaca, Hogg, et al. (2019) identified a gap in its density profile and modeled it as the result of a perturbation by a massive object. Follow-up work by Bonaca, Conroy, et al. (2020) localized a potential dark matter subhalo whose orbit is consistent with having originated from the Sagittarius dwarf galaxy. Such cases illustrate how streams can simultaneously constrain the Milky Way's assembly history and the distribution of dark matter substructure.

The information content of streams in constraining the Galactic potential has been quantified by Bonaca & Hogg (2018), who showed that a single stream cannot simultaneously constrain all relevant parameters due to strong degeneracies. However, they also demonstrated that fitting multiple streams jointly can break these degeneracies – an approach realized by R. Ibata, Malhan, Tenachi, et al. (2024), who used Gaia DR3 to discover even more streams using `streamfinder` and then employed roughly 20 to create a best fit model of the Milky Way's gravitational field.

In summary, stellar stream science is rapidly evolving. The expanding stream catalog – enabled by Gaia and complementary surveys – is unlocking new opportunities to probe globular cluster formation, the accretion history of the Milky Way, the nature of the Galactic gravitational potential, and the properties of dark matter itself. As the number and quality of identified streams continue to grow, so too will their impact on Galactic archaeology.

Chapter 2

Theory

In this chapter, I summarize the theoretical background necessary to understand how we model the disruption of globular clusters to form stellar streams. My goals are threefold:

1. To describe the modeling process in detail;
2. To describe the physical mechanisms that govern this process;
3. To acknowledge other physical ingredients that are relevant to globular cluster evolution but were deliberately omitted in our modeling, and to discuss the consequences of these omissions.

I aimed to write the chapter, if handed to myself in 2022, would have jumped-start this research. Conceptually, the chapter is divided into three sections that mirror these motivations:

- **Explicit physics**: These are the fundamental equations that underpin our models;
- **Implicit physics**: Often, while the governing equations can be written exactly, they are too terse to provide intuition. This section interprets simplified versions of the equations to explain qualitatively what is happening in the simulations;
- **Ignored physics**: Here I highlight physical effects excluded from our models, many of which appear in the broader literature. I discuss why we excluded them and how that limits our results.

1 The Explicit Physics

Globular clusters are dense stellar systems containing hundreds of thousands to millions of stars. Each star orbits within the gravitational potential of the cluster, while the cluster itself orbits the center of mass of the host galaxy. This galaxy, in turn, is composed of billions of stars, along with gas and dark matter, all contributing to its gravitational potential. A natural modeling approach is to treat the stars as point masses and to represent the gas and dark matter as continuous density distributions. This strategy would allow the construction of the Galactic gravitational field, potentially through a combination of hydrodynamical simulations for the gas and N-body simulations for the stars. However, the feasibility of such an approach must be carefully considered.

The scaling of computation time is often analyzed using Big-O notation. For direct N-body simulations, the computational cost scales as $\mathcal{O}(N^2)$, since the gravitational force on each particle must be computed from every other particle. For the Milky Way, with approximately 10^{11} stars, we need to compute 5×10^{21} pairwise distances per time step.

Let us consider the practicality of performing such a computation. *Frontier* is one of the most powerful modern supercomputers and operates at approximately one exaflop, or 10^{18} FLOPS (Floating Point Operations Per Second) (Atchley et al., 2023). Assuming – conservatively – that each pairwise computation requires a single FLOP, a full N-body computation of the Galaxy at one time step would still require several hours. While this may seem manageable, a single time step is insufficient for modeling the long-term evolution of the system, which could require millions of steps or more. Dedicating an entire exascale machine to such a task is therefore a considerable demand.

Moreover, the cost of power is non-negligible. At an estimated rate of $\sim$ 0.10 USD/kWh (Table, 2024), and with Frontier consuming roughly 21 MW, a single 6-hour computation would cost approximately 12,600 USD. Running the system for a full day would amount to about 50,000 USD, or 42,000 EUR (European Central Bank, 2025). This is nearly twice the annual salary of a PhD student in France (Ministere de l'Enseignement superieur et de la Recherche, 2025).

Throughout this thesis, I have access to the Paris observatory's super computer [1], which currently has about 85 nodes. However, as a humorous aside, consider attempting this computation on a personal research laptop, such as a MacBook Air with an M2 processor. Its estimated speed of $\sim$0.1 TFLOPS (i.e., 10^{11} FLOPS) (Hübner et al., 2025) is approximately 10 million times slower than Frontier. A single time step would thus take over 1,500 years.

Clearly, we require a more tractable modeling approach for studying the evolution of globular clusters and the formation of stellar streams. Fortunately, it is well justified to approximate all the stars in the galaxy as a smooth background density field rather than as a collection of point masses. This argument, presented in Section 1.2 of Binney & Tremaine (2008), shows that the inaccuracy of such a model becomes significant only on timescales far exceeding the age of the Universe. This is known as two-body relaxation. This process compares two hypothetical orbits for the same star. One within a smooth medium, and a second within a medium composed of point masses. The two-body relaxation time is how long it takes for these two trajectories to deviate significantly. We

---

[1] https://dio.obspm.fr/

revisit this in Section 3.1.1.

In globular clusters, where stars are densely packed into a relatively small volume, stellar encounters become significant over the system's lifetime. According to Chapter 5.1 of Bovy (2025a), the relaxation timescale within globular clusters is typically ~ 1 Gyr. To contextualize this, we must consider the orbital period of a typical star within a cluster, and the age of a cluster. First, the characteristic time for a star to traverse the system is roughly 1 Myr (which can be estimated as the size of a system divided by its internal velocity dispersion Baumgardt & Hilker, 2018). Secondly, globular clusters are old systems, with ages ranging from several billion to over ten billion years (VandenBerg et al., 2013). These timescales establish the following hierarchy for globular clusters:

$$t_{\text{cross}} << t_{\text{relax}} < t_{\text{age}}$$

This has two major consequences. First, because the crossing time is much shorter than the relaxation time, the cluster can be considered in dynamical equilibrium at any given moment. The stars thus follow orbits determined by a smooth potential. Second, since the age of the cluster exceeds the relaxation time, cumulative stellar encounters (i.e., "collisions") significantly influence the system's long-term evolution.

Despite the importance of collisional effects for the long-term evolution of globular clusters, explicitly modeling them via direct N-body simulations remains prohibitively expensive for our purposes. We return to this point in more detail in Section 3. In this thesis, we therefore adopt the collisionless approximation for both the Galactic background and the globular cluster. While this is well-justified for the Galaxy, treating the cluster as collisionless is a simplification that limits the generality of our results. Nonetheless, our goal is to accurately model the stellar streams, and the internal dynamics of the globular clusters are beyond the scope of this work.

To make the problem computationally tractable, we model the stars as test particles – massless bodies that feel the gravitational potential but do not contribute to it. The Galaxy and the globular cluster are each represented as smooth, time-independent density distributions. In this approximation, the stars do not interact with one another or with the cluster, and their trajectories are determined solely by the external potentials. This setup is a version of the *restricted three-body problem*, in which the Galaxy acts as the primary body (fixed at the origin), the globular cluster as the secondary (modeled by its center of mass), and the star as the tertiary object. This is shown in Fig. 2.1. This formulation dramatically simplifies the dynamics: the full N-body problem is approximated by N independent realizations of the restricted three-body problem. This reduction allows us to efficiently simulate the formation and evolution of tidal features without incurring the computational cost of tracking all mutual interactions among stars. This approximation has been shown to work very well for certain stellar streams and this thesis is not the first

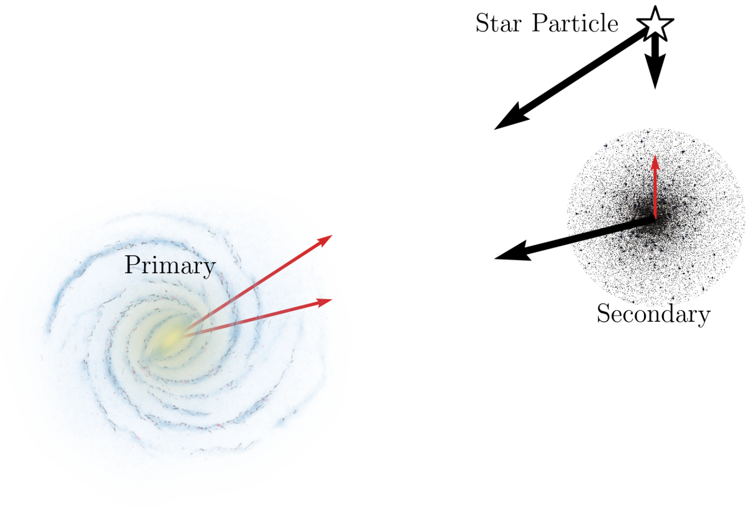

Figure 2.1 – Schematic illustration of the restricted three-body setup. The system is reduced to three interacting components: the Galaxy (primary), the globular cluster (secondary), and a single star (tertiary). Red vectors indicate forces that are neglected, while the black vectors are those that we model.

time such methods have been employed. For instance, consider the work of Mastrobuono-Battisti, Di Matteo, et al. (2012), who modeled the evolution of the Palomar 5's stellar stream with both an N-body code as well as the restricted three body problem. The differences between the two models for reproducing many characteristics of the stream are minimal.

In the remainder of this section, I present the theoretical framework underlying the simulations. At their core, the simulations involve solving N sets of six coupled ordinary differential equations – one set for each star particle. Section 1.1 introduces the equations of motion. Section 1.2 describes the gravitational field used to compute the forces acting on the particles. Finally, Section 1.3 details the procedure used to generate initial conditions that faithfully represent a globular cluster.

1.1 Equations of Motion

In galactic dynamics, we can well describe the motion of stars through Poisson's equation, which extends Newton's law of gravity from point masses to smooth density distributions:

$$\nabla^2\Phi = 4\pi G\rho, \tag{2.1}$$

where ρ is the mass density and Φ is the gravitational potential. We use Newtonian mechanics throughout this work because $\Phi << c^2$ in all relevant regimes, meaning General Relativity is not required (see Appendix C of Bovy, 2025a). Poisson's equation assumes

Newton's postulate that gravitational forces act instantaneously and that masses attract each other along the line connecting them.[2]

Instead of writing down the gravitational forces through Newton's second law, I will write down Hamilton's equations derived from the variational principle of Lagrangian mechanics. The full interacting system includes the kinetic energy of the globular cluster and the star particle, as well as three gravitational potential energy terms: the cluster-galaxy interaction, the particle-galaxy interaction, and the particle-cluster interaction:

$$\mathcal{L} = \frac{1}{2}M_{\text{gc}}\dot{\mathbf{R}}_{\text{gc}}^2 + \frac{1}{2}m\dot{\mathbf{r}}^2 - M_{\text{gc}}\Phi_{\text{gal}}(\mathbf{R}_{\text{gc}}) - m\Phi_{\text{gal}}(\mathbf{r}) - m\Phi_{\text{gc}}(\mathbf{r} - \mathbf{R}_{\text{gc}}). \tag{2.2}$$

M_{gc} is the mass of the globular cluster, m is the mass of a star, $\mathbf{R}_{\text{gc}}$ is the galacto-centric position of the globular cluster, r is the galacto-centric position of the star, Φ_{gal} is the potential generated by the galaxy and Φ_{gc} is the potential generated by the globular cluster. We decouple the equations of motion of the globular cluster and the star. The justification for this approximation is evident when we normalize the Lagrangian by the cluster mass. This yields:

$$\frac{\mathcal{L}}{M_{\text{gc}}} = \frac{1}{2}\dot{\mathbf{R}}_{\text{gc}}^2 - \Phi_{\text{gal}}(\mathbf{R}_{\text{gc}}) + \underbrace{\frac{m}{M_{\text{gc}}}\left[\frac{1}{2}\dot{\mathbf{r}}^2 - \Phi_{\text{gal}}(\mathbf{r}) - \Phi_{\text{gc}}(\mathbf{r} - \mathbf{R}_{\text{gc}})\right]}_{\text{negligible correction to GC's motion}} \tag{2.3}$$

In the limit where $m << M_{\text{gc}}$, the terms in brackets become negligible, and the star's motion has no influence on the cluster. The Lagrangian for the cluster's orbit thus becomes:

$$\frac{\mathcal{L}_{\text{gc}}}{M_{\text{gc}}} = \frac{1}{2}\dot{\mathbf{R}}_{\text{gc}}^2 - \Phi_{\text{gal}}(\mathbf{R}_{\text{gc}}) \tag{2.4}$$

Switching to the star's perspective, we normalize the Lagrangian by the particle mass m, obtaining:

$$\frac{\mathcal{L}_{\text{star}}}{m} = \frac{1}{2}\dot{\mathbf{r}}^2 - \Phi_{\text{gal}}(\mathbf{r}) - \Phi_{\text{gc}}(\mathbf{r} - \mathbf{R}_{\text{gc}}(t)) \tag{2.5}$$

Here, the cluster's influence on the particle is retained through its time-dependent position $\mathbf{R}_{\text{gc}}(t)$. This influence becomes important when the gravitational forces from the cluster and the galaxy on the particle are comparable. For a quick estimate, we can treat both the galaxy and the cluster as point masses. The two forces become comparable when the particle is sufficiently close to the cluster, which occurs when: $|\mathbf{r} - \mathbf{R}_{\text{GC}}| < \sqrt{\frac{M_{\text{gc}}}{M_{\text{gal}}}}|\mathbf{r}|$. In other words, the cluster's gravitational field dominates over the galaxy's on sufficiently

---

[2] Galaxies span millions of light-years, so how can Newton's assumption of instantaneous gravity be valid, given that gravitational waves travel at the speed of light? As shown by Carlip (2000), this is well understood in General Relativity: the gravitational field encodes not only the position but also the motion of massive bodies. This ensures that the resulting spacetime curvature produces a force equivalent to attraction toward the body's instantaneous position, rather than where it was when the gravitational influence was emitted.

small scales around the cluster – as expected. For a quick sanity check: a typical globular cluster may have a mass of $10^5\,M_\odot$, while the Milky Way may be around $10^{12}\,M_\odot$ (Hunt & Vasiliev, 2025). If the cluster is a few kiloparsecs from the galactic center, then the cluster's influence dominates within a region of order a few parsecs – which checks out. A better limit is the tidal radius and is presented in the next section.

Next, working in the Hamiltonian formalism often provides deeper insight into the physics of the system. Additionally, Hamiltonian mechanics reduces the equations of motion to a set of $2N$ first-order differential equations, rather than N second-order ones, which is more convenient for computational integration.

The Hamiltonian can then be obtained via a Legendre transform: $\mathcal{H} = \sum p_i \dot{q}_i - \mathcal{L}$, where q is a generic position coordinate, p is its conjugate momentum, while i indicates the coordinate of interest. If we use the *specific* Lagrangian – normalized by the mass of the body of interest – then, in Cartesian coordinates, the conjugate momenta reduce to the velocities: $p_i = \frac{\partial \mathcal{L}}{\partial \dot{q}} \to p_i = v_i$. Another useful result comes from Noether's theorem: if a coordinate does not explicitly appear in the Lagrangian, its conjugate momentum is conserved. Most of the galactic potentials considered in our simulation are axis-symmetric meaning they have cylindrical symmetry, except for case of a rotating stellar bar. Since the Lagrangian does not depend on the azimuthal angle θ in the x-y plane for the cluster's motion, the z-component of angular momentum is conserved: $p_\theta = L_z = \frac{\partial \mathcal{L}}{\partial \dot{\theta}} = R^2\dot{\theta} =$ constant.

If we consider a star within an isolated globular cluster with spherical symmetry, its total angular momentum vector is conserved. However, if we consider the Eq. 2.5, then no quantities are conserved. There are no symmetries, and due to the explicit time dependence, energy is not conserved either. On the other hand, if a star-particle is sufficiently far from the globular cluster, such that its motion is governed solely by the galactic potential, then conservation of L_z is recovered in the case of an axisymmetric Galactic potential.

Hamilton's equations thus provide the time evolution of the momenta and the positions. In Cartesian coordinates, the equations of motion for the cluster are:

$$\begin{aligned}
\dot{p}_{x,\mathrm{gc}} &= -\frac{\partial \Phi_{\mathrm{gal}}\left(\mathbf{R}_{\mathrm{gc}}\right)}{\partial x} \\
\dot{p}_{y,\mathrm{gc}} &= -\frac{\partial \Phi_{\mathrm{gal}}\left(\mathbf{R}_{\mathrm{gc}}\right)}{\partial y} \\
\dot{p}_{z,\mathrm{gc}} &= -\frac{\partial \Phi_{\mathrm{gal}}\left(\mathbf{R}_{\mathrm{gc}}\right)}{\partial z} \\
\dot{x}_{\mathrm{gc}} &= p_{\mathrm{gc},x} \\
\dot{y}_{\mathrm{gc}} &= p_{\mathrm{gc},y} \\
\dot{z}_{\mathrm{gc}} &= p_{\mathrm{gc},z}.
\end{aligned} \tag{2.6}$$

For the star particle, the equations of motion become:

$$\begin{aligned}
\dot{p}_x &= -\frac{\partial \Phi_{\mathrm{gal}}\left(\mathbf{r}\right)}{\partial x} - \frac{\partial \Phi_{\mathrm{gc}}\left(\mathbf{r}-\mathbf{R}_{\mathrm{gc}}(t)\right)}{\partial x}\\
\dot{p}_y &= -\frac{\partial \Phi_{\mathrm{gal}}\left(\mathbf{r}\right)}{\partial y} - \frac{\partial \Phi_{\mathrm{gc}}\left(\mathbf{r}-\mathbf{R}_{\mathrm{gc}}(t)\right)}{\partial y}\\
\dot{p}_z &= -\frac{\partial \Phi_{\mathrm{gal}}\left(\mathbf{r}\right)}{\partial z} - \frac{\partial \Phi_{\mathrm{gc}}\left(\mathbf{r}-\mathbf{R}_{\mathrm{gc}}(t)\right)}{\partial z}\\
\dot{x} &= p_x\\
\dot{y} &= p_y\\
\dot{z} &= p_z,
\end{aligned} \tag{2.7}$$

Note that equation 2.7 describes the motion of a single particle. In general, if we use 100,000 particles, the motion of each is described with this same equation, but has different initial conditions.

Equation 2.6 describes the motion of a globular cluster within the Galactic potential, while Equation 2.7 models the evolution of stars within the cluster and the formation of a stellar stream, assuming a fixed orbital path for the cluster. However, globular clusters do not evolve in isolation. To explore interactions, such as those between clusters and nearby streams, we must extend the equations of motion accordingly. This is the central focus of Chapter 5, which investigates how globular clusters can perturb neighboring stellar streams.

To capture such interactions, we first modify Equation 2.6 to include mutual gravitational forces between all clusters, effectively computing N-body interactions among them. While full N-body dynamics are typically avoided due to computational cost, this extension is tractable here, as the system includes only about 160 clusters. The resulting modified equations are:

$$\begin{aligned}
\dot{p}_{x,i} &= -\frac{\partial \Phi_{\mathrm{gal}}}{\partial x} - \sum_{j\neq i}^{N}\left[\frac{\partial \Phi_{\mathrm{gc}}\left(\mathbf{R}_i-\mathbf{R}_j|M_j,b_j\right)}{\partial x}\right],\\
\dot{p}_{y,i} &= -\frac{\partial \Phi_{\mathrm{gal}}}{\partial y} - \sum_{j\neq i}^{N}\left[\frac{\partial \Phi_{\mathrm{gc}}\left(\mathbf{R}_i-\mathbf{R}_j|M_j,b_j\right)}{\partial y}\right],\\
\dot{p}_{z,i} &= -\frac{\partial \Phi_{\mathrm{gal}}}{\partial z} - \sum_{j\neq i}^{N}\left[\frac{\partial \Phi_{\mathrm{gc}}\left(\mathbf{R}_i-\mathbf{R}_j|M_j,b_j\right)}{\partial z}\right],
\end{aligned} \tag{2.8}$$

where i is the index of a target cluster and j iterates over the others. Note that in Φ_{gc}, I explicitly write M_j, b_j to indicate the mass and scale length of the j^{th} cluster. Each cluster has its own scale-length, which were computed from the half-mass radii reported in Baumgardt & Hilker (2018). Since each cluster is modeled with a distinct scale radius, Newton's third law is not strictly satisfied: $\dot{\mathbf{p}}_{ij} \neq -\dot{\mathbf{p}}_{ji}$ [3]. This violation is not dynamically significant in practice. Since each cluster is modeled as a Plummer sphere, the force profile converges to that of a point mass at distances much greater than the scale radius. As a result, the approximation remains valid for most inter-cluster separations.

Lastly, in terms of the stream generation for Chapter 5, equation 2.7 are also modified to include the force from all the clusters, instead of just the host cluster. This becomes:

$$\begin{aligned}
\dot{p}_x &= -\frac{\partial \Phi_{\mathrm{gal}}\left(\mathbf{r}\right)}{\partial x} - \sum_i^N \frac{\partial \Phi_{\mathrm{gc}}\left(\mathbf{r} - \mathbf{R}_i(t)\right)}{\partial x} \\
\dot{p}_y &= -\frac{\partial \Phi_{\mathrm{gal}}\left(\mathbf{r}\right)}{\partial y} - \sum_i^N \frac{\partial \Phi_{\mathrm{gc}}\left(\mathbf{r} - \mathbf{R}_i(t)\right)}{\partial y} \\
\dot{p}_z &= -\frac{\partial \Phi_{\mathrm{gal}}\left(\mathbf{r}\right)}{\partial z} - \sum_i^N \frac{\partial \Phi_{\mathrm{gc}}\left(\mathbf{r} - \mathbf{R}_i(t)\right)}{\partial z}
\end{aligned} \tag{2.9}$$

The first two sets of equations are used to model the streams associated with each of the Galactic globular clusters, in a system where each cluster is subject only to the gravitational pull of the Galaxy. The second set of equations takes into account the fact that each cluster, and each particle in its stream, is generally also influenced by the gravitational pull of all the other Galactic globular clusters. The next two subsections introduce the various forms that Φ can take, followed by the generation of the initial conditions.

1.2 The Gravitational Field

Determining the gravitational field of the Milky Way remains an open and complex problem. From our location within the Galaxy, it is difficult to obtain a global perspective. Since the advent of extragalactic astronomy and early classification efforts such as those by Hubble (1926), we have begun to ask what the total structure of our own Galaxy is. Before providing a robust estimate for the global mass distribution, some simpler questions were addressed. For example, Oort (1927) studied the motion of stars in the local solar neighborhood and showed that the Galaxy not only has net rotation, but also differential rotation – as opposed to solid-body rotation.

The field has come a long way since then, and today we possess a number of viable models for the Galactic gravitational field. Much of our understanding owes to the fact

---

[3] We define the force exerted by cluster j on cluster i as $\mathbf{p}_{ij} = \frac{-GM_iM_j}{\left(b_j^2+r_{ij}^2\right)^{3/2}}\mathbf{r}_{ij}$, where $\mathbf{r}_{ij} = \mathbf{r}_i - \mathbf{r}_j$ and b_j is the Plummer scale radius of cluster j. When $b_i \neq b_j$, the forces are not equal and opposite, thus violating Newton's third law. However, in the limit $r_{ij} \gg b_i, b_j$, this asymmetry vanishes, and the interaction reduces to that of point masses.

that Poisson's equation is linear:

$$\nabla^2 \left(a_0\Phi_0 + a_1\Phi_1\right) = a_0\nabla^2\Phi_0 + a_1\nabla^2\Phi_1 = 4\pi G \left(a_0\rho_0 + a_1\rho_1\right), \tag{2.10}$$

which allows us to treat the Galaxy as a superposition of separate components, each described by its own potential-density pair. This decomposition enables the construction of composite models from a collection of structural elements that are also commonly observed in external galaxies. The Galaxy Zoo project (Lintott et al., 2008), for instance, has shown that many galaxies share similar morphologies, justifying this modular approach. The Milky Way is no exception. Typical components of disc like galaxies are:

- A stellar disk,
- A gaseous disk,
- A dark matter halo,
- A stellar halo,
- A bulge,
- A galactic bar,
- Spiral arms.

In addition, smaller-scale structures such as globular clusters, giant molecular clouds, and open clusters can locally perturb the field. Even external sources, such as the Large and Small Magellanic Clouds, play a role by inducing measurable tidal effects on the Galaxy (see, for example Vasiliev, Belokurov, et al., 2021; Arora et al., 2022).

Despite this framework, modeling remains difficult because the structural components are not isolated. As emphasized by Bland-Hawthorn & Gerhard (2016), the components co-evolve within a shared potential, meaning that even those formed separately eventually become dynamically mixed. This interdependence implies that the potential cannot be cleanly partitioned into independent contributions, and even with a complete dataset, degeneracies would persist. Their review illustrates this point by listing 37 parameter groups required to characterize the Galaxy – including the local standard of rest, Galactic reference frame, and the geometric and density properties of various components – underscoring the system's complexity.

The challenge is compounded by limitations in the available data. The Gaia mission has delivered the most comprehensive survey of the Galaxy to date (Gaia Collaboration, Vallenari, et al., 2023), providing photometric and astrometric data for over two billion stars and radial velocities for tens of millions (Gaia Collaboration, Katz, et al., 2018). However, this still represents only a small fraction of the total stellar population. The stellar mass of the Milky Way is estimated to be approximately $6 \times 10^{10}\mathrm{M}_\odot$ (Licquia & Newman, 2015), corresponding to roughly one hundred billion stars (see also McMillan,

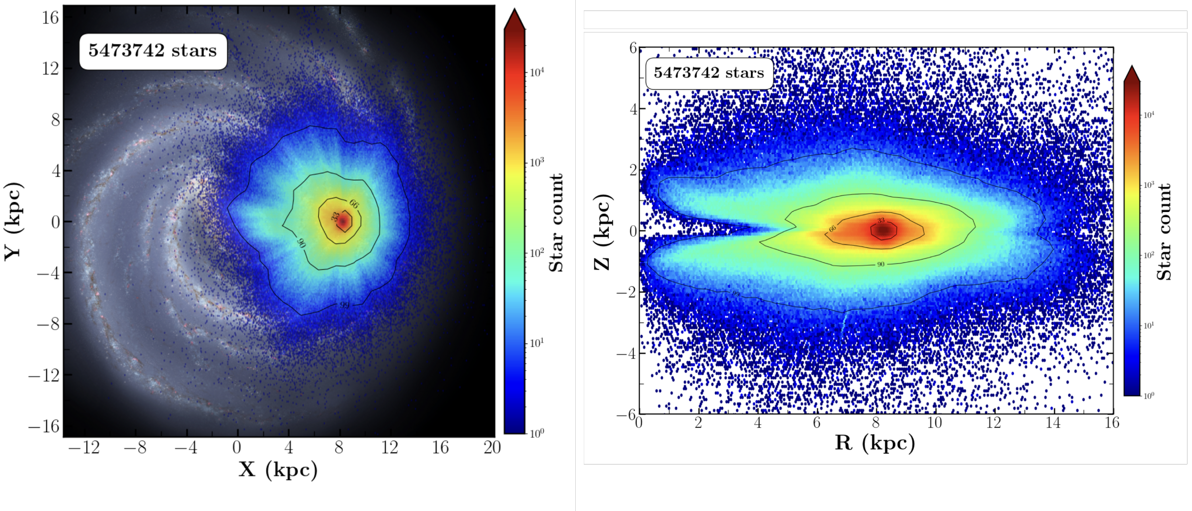

Figure 2.2 – The spatial distribution of stars with spectroscopic measurements in Gaia DR3. Figure 5 from Gaia Collaboration, Recio-Blanco, et al. (2023).

2017). Thus, Gaia provides 5D phase-space information for only about 1-2% of all stars, and full 6D information for just a fraction of a percent.

Moreover, the data suffer from unavoidable selection effects. As illustrated in Fig. 2.2, which shows the spatial distribution of stars with spectroscopic observations from Gaia DR3, the bulk of high-quality measurements are clustered near the Sun. This is a natural consequence of the inverse-square law for luminosity, and it implies that any model of the Galactic potential must account for these biases (Khoperskov, van de Ven, et al., 2025). In summary, while we now possess sophisticated models and rich datasets, constructing a comprehensive and precise model of the Milky Way's gravitational field is still inherently difficult – constrained both by observational incompleteness and the physical complexity of a system in which all components are tightly coupled. Given these challenges, the construction of a Galactic model depends on the scientific question being asked.

Consider `TRILEGAL` (Girardi et al., 2005). This model aims to answer the question: if I observe the sky from a given location with a given instrument, what do I expect to see? The focus of these models are stellar populations. Dynamics—such as orbits or gravitational forces—are secondary and not included in the construction. The primary goal is to reproduce observed star counts and understand the underlying stellar populations. Such models are designed to simulate the sky as it would appear to missions like Hipparcos (Perryman, Lindegren, et al., 1997), 2MASS (Skrutskie et al., 2006), and SDSS (York et al., 2000).

Some models attempt to address both stellar populations and dynamics. For example, the Besançon model aims to construct a dynamically self-consistent model of the Milky Way that reproduces observables such as the rotation curve, as well as the spatial and chemical distributions of stars. The model originated with A. Robin & Creze (1986) and

Bienayme et al. (1987), and was eventually improved with Hipparcos data (A. C. Robin, Reylé, et al., 2003). The authors decomposed the galaxy into a thin disk, a thick disk, a stellar halo, and a bulge, with each component assigned its own star formation rate and initial mass function. The model has been continuously refined; for instance, A. C. Robin, Bienaymé, et al. (2022) incorporated Gaia DR3 kinematics to further constrain it. As noted by Klüter et al. (2025), who recently introduced the open-source Python package `SYNTHPOP` for simulating on-sky photometry, the success of TRILEGAL and the Besançon model lies in their openness: they are publicly available and have web interfaces for widespread use. These tools are particularly valuable for creating mock surveys of the sky.

A different approach is taken by Binney & Vasiliev (2024), building on Binney & Vasiliev (2023), who constructed a dynamical model of the Milky Way in which the distribution function depends on orbital actions—quantities that are conserved along orbits in a steady-state potential. In axisymmetric potentials, the actions are J_r, J_ϕ, and J_z, and represent how much motion an orbit has in the radial, azimuthal, and vertical directions, respectively. The moments of the distribution function yield observable quantities such as stellar surface densities, volume densities, and velocity dispersions. In addition to dynamical consistency, the model includes the chemical properties of stars, specifically metallicity ([Fe/H]) and α-element abundances. The model is constrained using Gaia DR3 data (Gaia Collaboration, Vallenari, et al., 2023), particularly stars with full phase-space information, as well as APOGEE DR17 (Majewski, Schiavon, et al., 2017). Their model involves over 40 parameters to describe the distributions of stars and metallicities throughout the Milky Way.

Then, there are many models of the Milky Way that are primarily dynamically motivated, with stellar populations treated as secondary (see, for example, Allen & Santillan, 1991; Bovy, 2015; McMillan, 2017; Pouliasis et al., 2017; R. Ibata, Malhan, Tenachi, et al., 2024). Despite the variety, their construction generally follows the same template: the authors must select a dataset, tracer populations, and the parametric form of the Milky Way potential. Often, fitting all model parameters is infeasible, whether due to lack of data, high computational cost, or non-converging likelihoods. Thus, the authors will assume fixed values for some parameters.

All of the above models assume axisymmetry, which is already a limitation. This makes it difficult to model the dynamics in the inner Galaxy (within a few kpc). Both McMillan (2017) and Binney & Vasiliev (2024) fix the parameters describing the gas in the Galactic disk and only fit those related to the stellar and dark matter distributions. McMillan (2017) specifically constructed their model to support orbit calculations for stars in anticipation of Gaia data releases. They aimed to improve upon their earlier model (McMillan, 2011), motivated by (1) a tripling of the maser population used to trace disk kinematics, and (2) the realization that omitting a gaseous disk in their earlier work had led to underestimating the forces in the solar vicinity.

Many of the models described above rely on fitting data using kinematic information, comparing the model's predictions for velocity dispersion to observations of large samples of stars. This is because direct astrometric measurements of stellar accelerations are still in their infancy. Measuring changes in angular position through parallax is so challenging that stars were long referred to as *fixed stars* (Kant & Jaki, 1981). Precise, year-over-year positional measurements are required to observe motion on the celestial sphere, precisely what Gaia does.

That said, accelerations have been measured in some cases. Brandt (2018) and Brandt (2021) created a cross-catalog between Hipparcos and Gaia DR2 (Gaia Collaboration, Brown, Vallenari, Prusti, de Bruijne, Babusiaux, Bailer-Jones, et al., 2018) and later EDR3. This provided a baseline of over 25 years, long enough to detect accelerations for some stars. However, the Hipparcos catalog only contains around 100,000 stars, and the typical acceleration of a field star in the Galaxy is extremely small. Consequently, the cross-matched catalog is currently being used to study stars with unusually high accelerations. These stars are typically in binary systems or have massive planets (Waisberg et al., 2023; Giovinazzi et al., 2025), and their detectable accelerations are not due to the Galactic gravitational field.

As stated in the motivation for undertaking this thesis, stellar streams are particularly useful for recovering information about the Galactic gravitational field. The stars within a stream are on similar orbits (but shifted in phase), and their orientation and curvature encodes detailed information about the Galactic gravitational field. R. Ibata, Malhan, Tenachi, et al. (2024) is the first study to use an ensemble of stellar streams to directly fit a gravitational potential model of the Milky Way (see also Law, Majewski & Johnston, 2010; Bovy et al., 2016, who also used streams to infer Galactic potential parameters). Even in that case, R. Ibata, Malhan, Tenachi, et al. (2024) needed to fix some of the model parameters. For example, they adopted the same bulge model as McMillan (2017).

In this thesis, we use the models of Pouliasis et al. (2017), which build upon the work of Allen & Santillan (1991). These models were developed within our research group and were available at the start of the project. They were designed to fit observational data similar to those used in Bovy (2015), including the Galactic rotation curve and local stellar kinematics. Pouliasis et al. (2017) were motivated to create a new Galactic model that included a thick disk (Gilmore & N. Reid, 1983) since Haywood, Di Matteo, Lehnert, Katz, et al. (2013) and Snaith et al. (2015) demonstrated that the thick disk has comparable mass to the thin disk. Pouliasis et al. (2017) thus provide two Milky Way potential models: one with a bulge and one without. Below, we describe the second version, which is used in both Chapter 4 and Chapter 5.

An excellent quality of the models presented Pouliasis et al. (2017) is that they are fully analytic. The first model comprises two disks, a bulge, and a halo, while the second model omits the bulge. The disk are modeled with the Miyamoto-Nagai potential (Miyamoto & Nagai, 1975):

$$\Phi(R, z \mid M, a, b) = -\frac{GM}{\sqrt{R^2 + \left(a + \sqrt{z^2 + b^2}\right)^2}}, \tag{2.11}$$

where M is the total mass of the disk, a is the radial scale length, and b is the vertical scale height. This form smoothly interpolates between a flattened disk and a spherical distribution, depending on the values of a and b. Bovy (2015) also used this form for their disk model.

However, it is worth noting that galactic disks can have more complicated functional forms. For instance, Freeman (1970) noticed that stellar densities in disks generally decay exponentially:

$$\rho(R, z) = \rho_0 \exp\left(-\frac{R}{R_d} - \frac{|z|}{z_d}\right), \tag{2.12}$$

where ρ is the mass density, R is the cylindrical radius, z the vertical height, and the model has three parameters: a characteristic density ρ_0, scale radius R_d, and scale height z_d. Pohlen & Trujillo (2006) continued this analysis and showed that a single exponential often cannot capture the true decay, and in many galaxies there is a transition radius where the profile can significantly change. A drawback of this model in equation 2.12 is that it cannot be integrated analytically to obtain the potential, since the R and z coordinates are not separable. Often, basis function expansions are needed to approximate the potential and compute forces. McMillan (2017) and R. Ibata, Malhan, Tenachi, et al. (2024) both adopted this model for their Galactic disks.

Regarding the halo, Pouliasis et al. (2017) use a single halo model to represent both the stellar and dark matter contributions, since the stellar mass contribution is negligible; A. C. Robin, Bienaymé, et al. (2022) estimate the stellar halo mass to be 3.17×10^8 M$_\odot$. The halo model is inherited from Allen & Santillan (1991), originally proposed in Allen & Martos (1986). It is designed so that beyond a certain scale radius, the enclosed mass grows linearly with distance, leading to the desirable feature of a flat rotation curve:

$$M_{\text{enc}}(r|M_0, \gamma, r_0, r_c) = M_0 \begin{cases} \frac{(r/r_0)^\gamma}{1+(r/r_0)^{\gamma-1}} & r < r_c, \\ \frac{(r_c/r_0)^\gamma}{1+(r_c/r_0)^{\gamma-1}} & r > r_c, \end{cases} \tag{2.13}$$

where M_0 is a mass scaling parameter (not the total mass), r_0 is the characteristic radius, γ is the power-law index, and r_c is a cutoff radius beyond which the mass is held constant. Thus, for $r > r_c$, Eq. 2.13 yields the total mass.

In the outer regime $(r/r_0) >> 1$, the enclosed mass scales as $M(r) \propto r$, producing a flat rotation curve. In the inner regime $(r/r_0) << 1$, the mass grows as a power law, $M(r) \propto r^{\gamma-1}$, which provides flexibility in shaping the central density slope. Since the unmodified profile leads to an nonphysical divergence in total mass, a truncation at r_c is imposed.

Given spherical symmetry, we may use the relation $\nabla\Phi = \frac{GM_{\mathrm{enc}}(r)}{r^2}$. Requiring that the potential vanish at infinity, the corresponding gravitational potential can be obtained by integrating:

$$\Phi(r|M_0, \gamma, r_0, r_c) = \begin{cases} \frac{GM_0}{r_0(\gamma-1)} \ln\left|\frac{1+(r/r_0)^{\gamma-1}}{1+(r_c/r_0)^{\gamma-1}}\right| - \frac{GM_t}{r_c}, & r < r_c \\ -\frac{GM_t}{r} & r > r_c. \end{cases} \tag{2.14}$$

where M_t denotes the total mass, $M_{\mathrm{enc}}(r_c)$. In general, a good halo model should reproduce the observed flat rotation curve at large radii. Another class of models that achieves this are the double power-law profiles:

$$\rho(r \mid \alpha, \beta, r_s) = \rho_0 \left(\frac{r}{r_s}\right)^{-\alpha} \left(1 + \frac{r}{r_s}\right)^{\alpha-\beta}, \tag{2.15}$$

where r_s is a scale radius, α controls the inner slope, and β the outer slope. Common choices include the NFW profile ($\alpha = 1$, $\beta = 3$) and the Hernquist profile ($\alpha = 1$, $\beta = 4$). These families of models were implemented in the works of Bovy (2015) and McMillan (2017) to describe the dark matter halo.

The two disks and the halo constitute the second model of Pouliasis et al. (2017). I present this in Fig. 2.3, as it was employed in both studies. See their paper for more visualizations of the potential and the version that includes a bulge.

In Chapters 4 and 6 (preliminary results), we model the inner Galaxy using the triaxial bar potential of Long & Murali (1992). The model is constructed by representing the bar as a uniform-density "needle" aligned with the x-axis and convolving it with a Miyamoto-Nagai disk flattened along the z-axis. The resulting potential is:

$$\Phi(x, y, z \mid M, a, b, c) = \frac{GM}{2a} \ln\left(\frac{x - a + T_-}{x + a + T_+}\right), \tag{2.16}$$

with

$$T_\pm = \left[(a \pm x)^2 + y^2 + \left(b + \sqrt{c^2 + z^2}\right)^2\right]^{1/2}. \tag{2.17}$$

Here M is the total mass of the bar, a is the semi-major axis, and b and c are the intermediate- and short-axis scales, respectively. The axis ratio c/b controls the vertical thickness: $c/b \to \infty$ corresponds to a prolate bar, while $c/b \to 0$ yields a flat, planar bar.

While the bar can account for much of the inner Galaxy's mass distribution, some models include an additional, centrally concentrated component conventionally referred to as the *bulge*. In the mass model of Pouliasis et al. (2017), the bulge is represented by a Plummer sphere (Plummer, 1911), an analytic potential with two parameters—the total

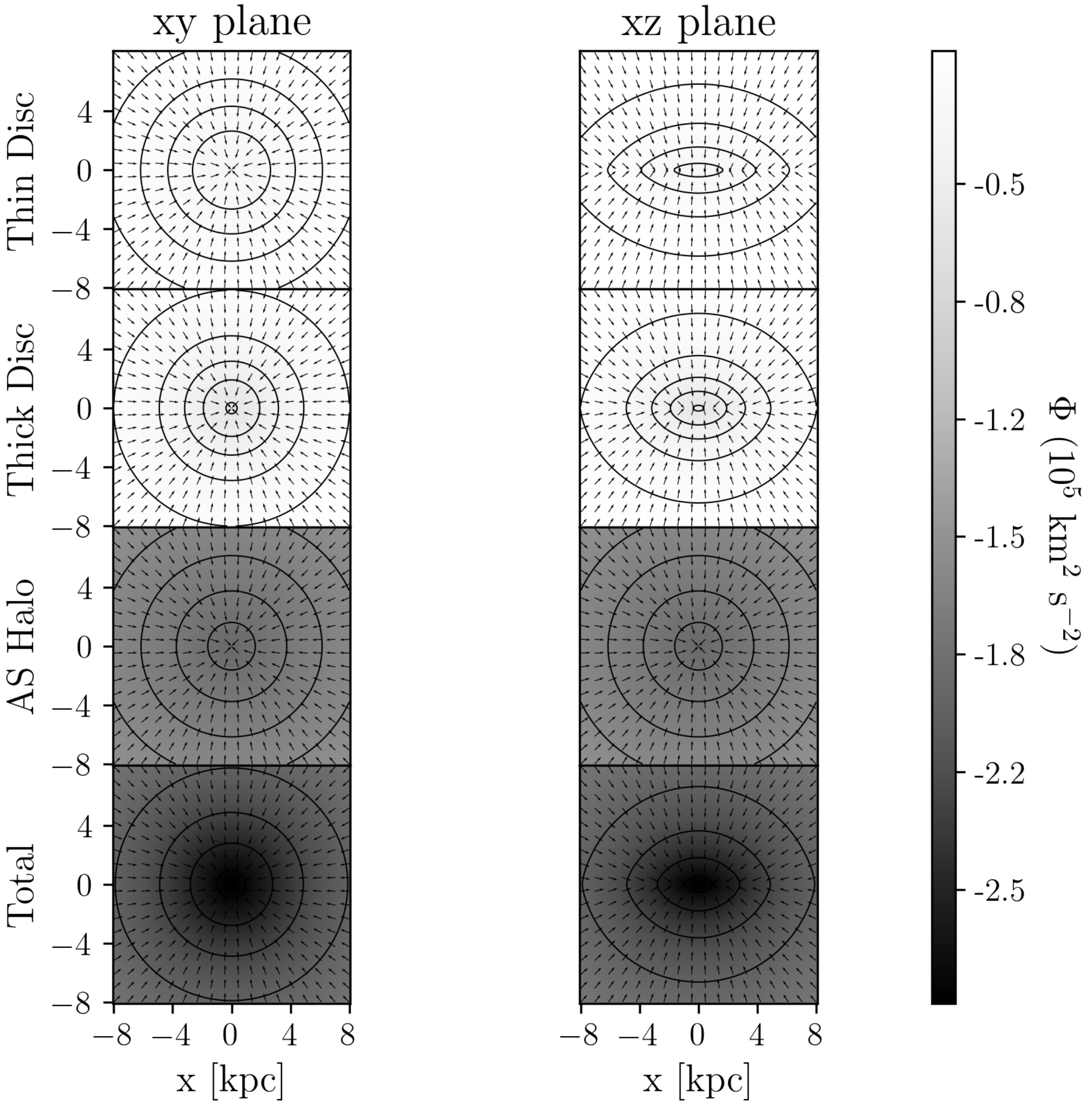

Figure 2.3 – Individual components of the second Galactic potential model from Pouliasis et al. (2017). The vector field illustrates the normalized gravitational force at each position, corresponding to $\vec{g} = -\nabla\Phi$. Equipotential contour lines are overlaid to guide the eye.

mass and a scale length—given by

$$\Phi(r \mid M, b) = -\frac{GM}{\sqrt{r^2 + b^2}}, \tag{2.18}$$

where M is the total mass and b is the scale length. In the limit $a \to 0$, the Miyamoto-Nagai potential reduces to the Plummer form. The Plummer sphere has a finite central potential, asymptotically approaches the potential of a point mass for $r >> b$, and produces a density profile that falls off as $\rho \propto r^{-5}$ at large radii. We also adopt the Plummer sphere as the analytic model for the globular clusters.

How important is the choice of potential model when modeling the orbits of globular clusters? It depends on the specific cluster. Take, for instance, Fig. 2.4. The position and spread of some clusters are virtually identical between different models—for example, NGC 288. This suggests that the observational uncertainties in the kinematic data are larger than the discrepancies introduced by the choice of potential. However, for other clusters, the model choice has a much greater impact. A notable case is Pyxis, where the inferred orbits differ significantly depending on the potential. This effect is more pronounced for clusters located farther from the Galactic center, where the models diverge more strongly. Differences in cluster orbits-or in stellar streams evolved in different potentials-can help constrain the underlying Galactic potential and eventually lead to more accurate models of the Milky Way. This was the motivation behind recent work such as R. Ibata, Malhan, Tenachi, et al. (2024). However, if the goal is to make robust predictions or extrapolate properties of the halo, it is prudent to explore a variety of Galactic models, especially when no single model is clearly preferred.

1.3 Generating a Globular Cluster

Now that the equations of motion established, and we have an accurate model for computing the gravitational force at each point in the Galaxy, what are the initial conditions? First, the initial conditions for the kinematics, mass, and size, of the globular clusters are taken observationally from Baumgardt & Hilker (2018) (this catalog was assembled across a series of works, see also Baumgardt, 2017; Baumgardt, Hilker, et al., 2019; Baumgardt, Sollima, et al., 2020; Baumgardt & Vasiliev, 2021) [4]. Specifically, their estimated total masses, half-mass radii, as well as their on-sky ICRS coordinates, that we then convert to galacto-centric coordinates (see Chapters 4 and 5). What about initial conditions for the stars within the cluster?

We have chosen the gravitational potential of each cluster to follow a Plummer sphere, as given in Eq. 2.18. The corresponding mass profile can be sampled to generate initial positions for individual particles. However, positional information alone is insufficient,

---

[4] https://people.smp.uq.edu.au/HolgerBaumgardt/globular/

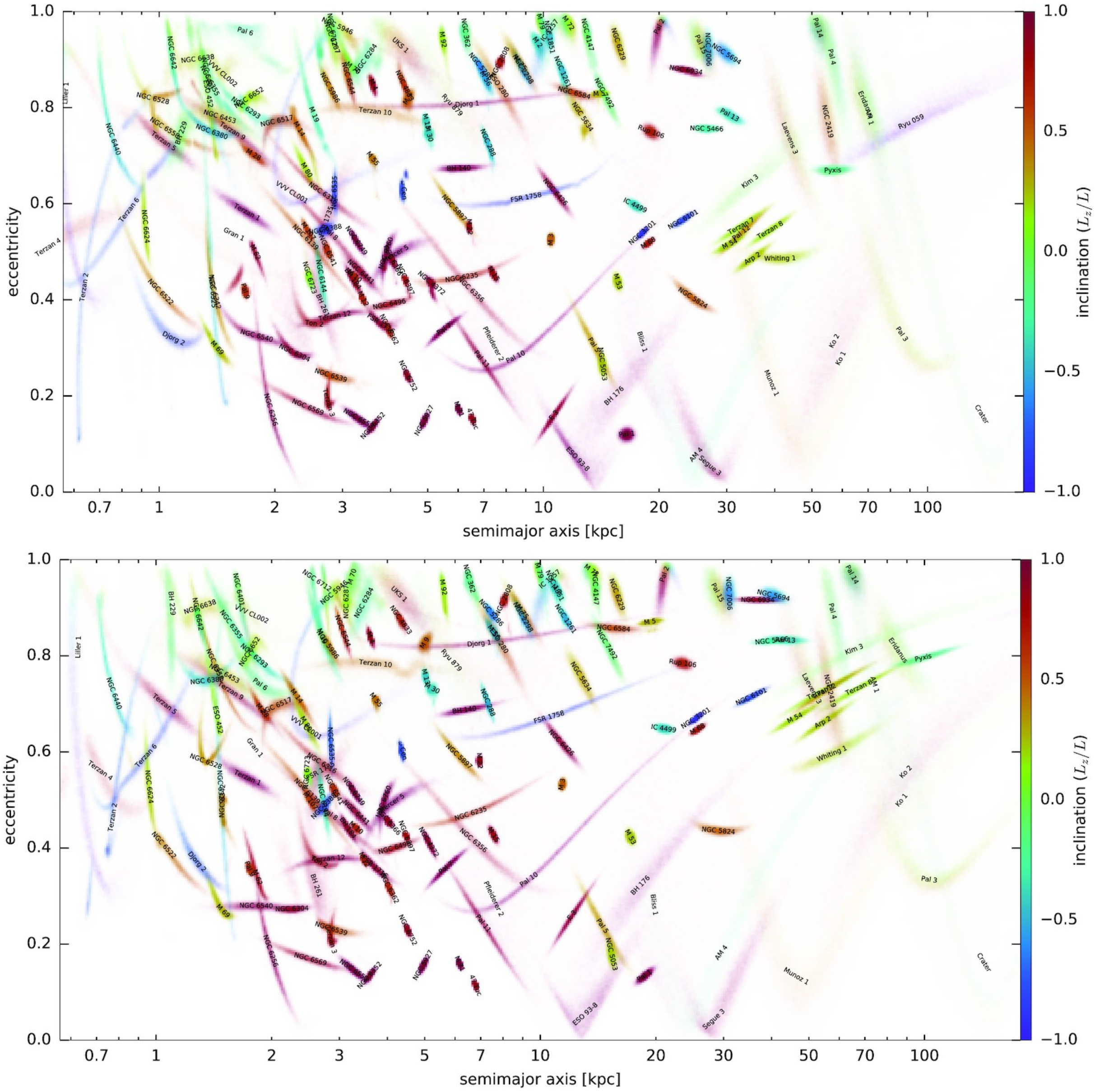

Figure 2.4 – Distribution of eccentricities, inclinations, and semi-major axes for the globular cluster population, based on Gaia EDR3 kinematics. Each point corresponds to a single realization of a globular cluster orbit, given its observational uncertainties. The top panel shows orbits computed using the potential from McMillan (2017), while the bottom panel uses the model from Bovy (2015). (Credit: Fig. 10 from Vasiliev & Baumgardt (2021))

we must also assign appropriate velocities. One crude approach, following the sampling of positions, is to assign a velocity vector drawn isotropically; that is, with a direction uniformly distributed over the sphere. Furthermore, the speed could be sampled uniformly between zero and the local escape velocity. While this method can produce plausible initial conditions, it lacks *self-consistency*, as the resulting phase-space distribution would not correspond to a stable equilibrium configuration of the chosen potential.

In galactic dynamics, a fundamental challenge is the *self-consistency problem.* This involves a loop of three steps:

1. Given a density distribution and a gravitational potential (linked via Poisson's equation), one samples the positions of stars.
2. One then assigns initial velocities and evolves the system forward in time.
3. The potential is updated based on the evolved mass distribution.

If the system is in equilibrium and self-consistent, then the mass distribution remains stable under its own gravity. That is, the same density that generated the potential continues to persist as the system evolves. For the rest of the section, I will describe in detail how one creates a self consistent system through the Collisionless Boltzmann Equation, and the simplifying assumptions employed in this thesis tackle our specific problem.

Our starting point is to characterize the system statistically, with a distribution function (DF) over phase-space. That is, what is the probability density of finding a particle at a given position and velocity? This is encoded in the function $f(\vec{x}, \vec{v}, t)$. If we treat this as a true probability density function that integrates to 1 over all phase space, we are implicitly assuming a closed system: no stars enter, leave, are born, or die.

Already, by writing $f(\vec{x}, \vec{v}, t)$, we are assuming that a particle's phase-space position is independent of any other attributes — such as mass. Let us define $\mathbf{w} = (\vec{x}, \vec{v})$ as the 6D phase-space coordinate. Then, for a system of N particles, the full distribution function lives in $6N$-dimensional space:

$$f(\mathbf{w}_1, \dots, \mathbf{w}_N)$$

This expression represents the joint probability density of finding particle 1 at $\mathbf{w}_1$, particle 2 at $\mathbf{w}_2$, and so on. In general, this object can be extremely complicated. But we can simplify it with two strong assumptions: that particles are independent and identically distributed (i.i.d.). This leads to:

$$\begin{aligned} f \quad &\xrightarrow{(1)\ N\text{-body DF}} f(\mathbf{w}_1, \dots, \mathbf{w}_N) \\ &\xrightarrow{(2)\ \text{independence}} \prod_{i=1}^{N} f^i(\mathbf{w}_i) \\ &\xrightarrow{(3)\ \text{identical distribution}} [f(\mathbf{w})]^N \end{aligned}$$

The consequence of this factorization is that the total DF no longer accounts for correlations in other variables — such as mass. Therefore, this model cannot represent mass segregation, multiple stellar populations, or any other effects that differentiate stars. Instead, we describe a single homogeneous population of stars, each drawn independently from the same distribution.

Because of this, we can focus our attention entirely on the single-particle DF $f(\mathbf{w})$, which encodes all the statistical information we need about the system.

The next key assumption is that particles are uncorrelated not just in identity, but dynamically — they do not scatter off one another. This means the system is *collisionless.* The DF then evolves under the Collisionless Boltzmann Equation:

$$\frac{Df}{Dt} = \frac{\partial f}{\partial t} + \dot{\mathbf{x}} \cdot \nabla_{\mathbf{x}} f + \dot{\mathbf{v}} \cdot \nabla_{\mathbf{v}} f = 0 \tag{2.19}$$

This is a material (Lagrangian) derivative following a phase-space trajectory. The physical interpretation is that the DF is conserved along the orbits of stars in phase space. No bunching up, no spreading out. Stars simply move under the influence of a smooth, mean gravitational potential. Next, we often impose the equilibrium condition:

$$\frac{\partial f}{\partial t} = 0$$

This implies that the DF is time-independent: the number of stars at any given phase-space location remains constant. If some leave a region, others must replace them. This assumption is only valid in isolation — for instance, in an isolated galaxy or globular cluster. It is violated during mergers or tidal disruptions. In my simulations, I model such disruptions, so this assumption is not globally valid. However, I begin with an equilibrium system and study how it departs from equilibrium numerically.

Now, let us focus on globular clusters. These are often modeled as spherically symmetric systems. However, spherical symmetry in density does not imply isotropy in velocity. A system can be spherically symmetric but have velocity anisotropy, meaning that orbits are preferentially radial or circular. This is quantified by the anisotropy parameter: $\beta = 1 - \frac{\sigma_\theta^2 + \sigma_\phi^2}{\sigma_r^2}$, where σ is the velocity dispersion with each spherical coordinate, latitude, longitude, and radius: θ, ϕ, r, respectively. In the simulations presented in this thesis, I assume isotropy, meaning that the DF depends only on the energy:

$$f(\mathbf{w}) = f(E)$$

At this point, it is useful to mention Jeans equations, which relate the moments of the DF to observable quantities. For example, by integrating the DF over all velocities, we recover the spatial mass density:

$$\rho(\mathbf{r}) = M \int f(\mathbf{x}, \mathbf{v})\, d^3\mathbf{v}$$

In fact, an inversion formula exists — known as the Abel transform — that allows one to reconstruct $f(E)$ from a known $\rho(r)$. This technique is presented in Binney & Tremaine (2008) and Bovy (2025a). At this point, one can obtain a complete analytic expression for the distribution function. For a Plummer sphere, this distribution function is $f = C(-E)^{7/2}$, where C is a constant that ensures $\int f dE = 1$.

1.3.1 Sampling the Initial Conditions

There are many techniques for sampling a distribution function. In my code, I use *inverse transform sampling*, a method that facilitates sampling from one-dimensional probability distribution functions.

Although the full distribution function depends on six variables—three positions and three velocities—it can be marginalized such that we treat each variable independently. This allows us to apply inverse transform sampling to each component separately.

Inverse transform sampling works by first constructing the cumulative distribution function (CDF) of the desired probability distribution function (PDF):

$$\mathcal{F}(x) = \int_{-\infty}^{x} f(x')\, dx'. \tag{2.20}$$

By definition, the probability that a random variable x is less than a given value x_0 is given by the value of the CDF at x_0:

$$\mathcal{P}(x < x_0) = \mathcal{F}(x_0). \tag{2.21}$$

Since CDFs are monotonically increasing and invertible, we also have:

$$\mathcal{P}(\mathcal{F}(x) < \mathcal{F}(x_0)) = \mathcal{P}(x < x_0). \tag{2.22}$$

Now, consider a uniform random variable Y distributed on the interval $[0, 1]$. Then,

$$\mathcal{P}(Y < \mathcal{F}(x_0)) = \mathcal{P}(x < x_0), \tag{2.23}$$

which implies:

$$x = \mathcal{F}^{-1}(Y). \tag{2.24}$$

Thus, we can generate samples from the target PDF $f(x)$ by applying the inverse CDF $\mathcal{F}^{-1}$ to uniformly distributed random numbers. This is practical, since uniform random

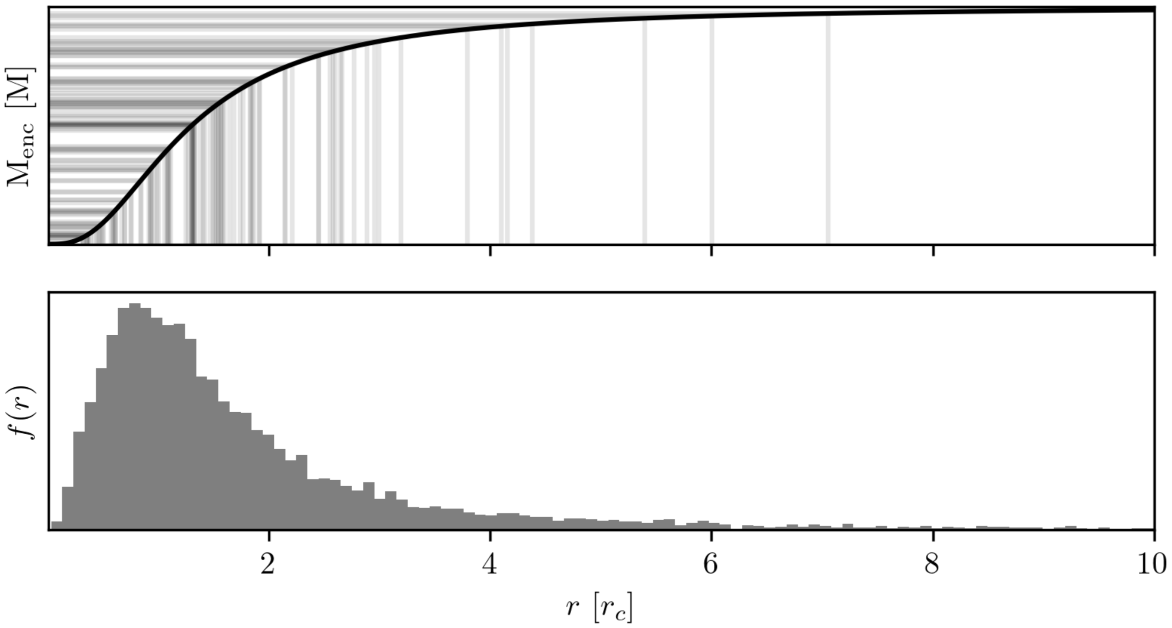

Figure 2.5 – Inverse transform sampling of the enclosed mass distribution of a Plummer sphere. One thousand uniform random numbers between [0,1] were generated and intersected with the normalized enclosed mass profile. The top panel shows the sampling of positions; only 100 samples are shown to avoid overcrowding. The bottom panel shows the resulting distribution of radial distances.

number generators—such as `numpy.random.rand`—are widely available.

The probability distribution for an isotropic Plummer sphere depends only on the energy, which itself depends on a particle's radial distance and speed: $f(r, v) \propto (-E)^{7/2}$. If we marginalize over the velocities, we obtain the one-dimensional density profile. The CDF of this marginalized distribution is the enclosed mass as a function of radius. For a Plummer sphere, it takes the form:

$$M_{\rm enc}(r) = \frac{r^3}{(1+r^2)^{3/2}}, \tag{2.25}$$

where $M_{\rm enc}$ is normalized to the total mass and r is normalized to the characteristic radius.

Figure 2.5 demonstrates inverse transform sampling applied to this CDF. Intersections between uniform random numbers and the CDF are computed; these intersections yield the sampled radial distances. The joint distribution function can be written as the product of a conditional and a marginal distribution: $f(r, v) = f(v|r)f(r)$. The number of particles at a given speed can be obtained by integrating over the angular velocity components and differentiating with respect to speed:

$$\frac{dN}{dv} = \frac{d}{dv}\int f(\mathbf{v}|r)\, v^2 \sin\theta\, d\theta\, d\phi\, dv = 4\pi v^2 f(v|r). \tag{2.26}$$

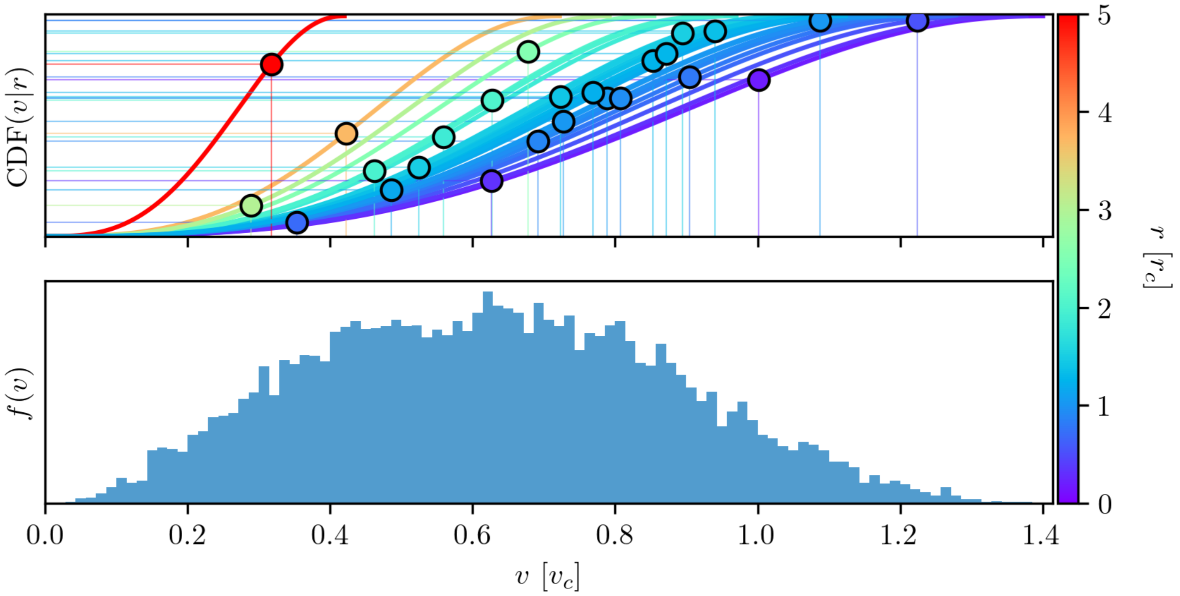

Figure 2.6 – Inverse transform sampling of the speed distribution conditioned on position for particles in a Plummer sphere ($N = 1000$). The top panel shows 25 samples (to avoid clutter), each colored by its sampled distance. For each particle, a uniform random number is mapped onto its corresponding CDF to obtain the speed. The bottom panel shows the distribution of sampled speeds. The theoretical maximum value, corresponding to the escape speed at the center, is $\sqrt{2GM/r_c}$.

To construct the CDF of this conditional distribution, we must determine the appropriate limits. The allowed speed for a particle at radius r ranges from zero to the escape speed, $v_{\text{esc}} = \sqrt{2\Phi(r)}$. The resulting CDF is:

$$\mathcal{F}(v) = C \int_0^{v<v_{\text{esc}}} 4\pi v^2 f(v|r) dv, \tag{2.27}$$

where C is a normalization constant. Although I do not present an analytical expression for C, it is straightforward to normalize numerically. In practice, I omit multiplicative constants and normalize a-posteriori using:

$$C = \frac{1}{\mathcal{F}(v_{\text{esc}})}. \tag{2.28}$$

Sampling the speeds is shown in Fig. 2.6. Since this is a conditional distribution, each particle has its own CDF based on its position—unlike Fig. 2.5, where all particles are sampled from the same marginal distribution. Note that for particles located farther from the center, fewer speeds are available before they become unbound. This process could be inverted: one could marginalize over position to obtain a global speed distribution, then condition on speed to sample positions. While valid, this approach is less intuitive. Most models are motivated by their density profiles, which are observable and conceptually accessible, making them a natural starting point for inverse transform sampling. To convert radial distances into 3D positions and speeds into velocity vectors, we must sample directions uniformly over the surface of a sphere. A common pitfall is to sample latitude and longitude uniformly, which leads to an over-density near the poles. Instead, we aim for a uniform distribution over the sphere's surface, where the differential area element is given by:

$$f(\theta, \phi) = \frac{1}{4\pi} \sin(\theta) \tag{2.29}$$

with θ the co-latitude and ϕ the longitude. Since f does not depend on ϕ, it can be sampled uniformly over its domain $[0, 2\pi)$. However, for θ, inverse transform sampling must be used. Drawing a uniform random variable $y_i \in [0, 1]$, the corresponding co-latitude is:

$$\theta_i = \cos^{-1}\left(1 - 2y_i\right). \tag{2.30}$$

By sampling radial distances, speeds, and directions uniformly over the unit sphere, we obtain full position and velocity vectors for each particle. With these, the initial conditions for a Plummer sphere are fully specified. The user needs only to provide the total mass, characteristic radius, and the desired number of star particles.

With the equations of motion defined, a model for the Galactic gravitational field established, a force model for the globular cluster in place, and initial conditions assigned to each star particle, we are now ready to simulate the tidal disruption of a globular cluster in the Galaxy.

2 The Implicit Physics

The previous section provided everything needed to simulate the dissolution of globular clusters. However, given the equations of motion, the model for the gravitational field, and the initial conditions for both the globular clusters and their constituent stars, why should we expect stars to escape? While the formalisms in the previous section supply the necessary machinery for running simulations, they do not explain *why* disruption occurs.

In this section, I aim to describe the underlying mechanisms that cause stars to escape from globular clusters and form stellar streams. Gaining intuition for this process involves simplifying the equations *even further*, in order to obtain analytical insights. I refer to this as the *implicit physics*—not because it was explicitly implemented in the simulations, but because it arises naturally from the equations that be.

To provide a brief overview: in Section 2.1, I present the circular restricted three-body problem, the simplest formalism for understanding the types of motion a massless body can undergo when influenced by two significantly more massive ones, following

Koon et al. (2000). In Section 2.2, I introduce the tidal tensor, which explains how and why the Galactic field eventually strips stars from their host clusters. This section is largely inspired by the works of Dehnen et al. (2004) and Bovy (2025a). In Section 2.3, I discuss phase mixing, which describes the evolution of escaped stars and how they come to form coherent stellar streams. This treatment is also primarily based on Bovy (see chapter 19.4 of 2025a), although I present the phenomenon in terms of orbital energy. Finally, I introduce the study of *gaps*—how perturbations can affect a stream and generate observable gaps within it. This topic is not yet formalized in textbooks and remains an active area of research. I primarily synthesize the works of Carlberg (2012) and Carlberg (2013), Erkal & Belokurov (2015), Bovy (2016), and Sanders, Bovy, et al. (2016).

2.1 The Planar Circular Restricted Three-Body Problem

This section introduces the fundamental concept of the Lagrange points and regions of influence. In general, if a star is very close to the center of mass of a globular cluster, then its dynamics are determined by the cluster and the galaxy's influence is minimal. On the other hand, if the star is far from the cluster then its motion is completely described by the galaxy's gravitational field and the cluster is completely negligible. The Lagrange points are transitions between these two regime and are the points out of which the stars escape from the cluster. The magic that makes this analysis possible is decoupling the motion of the smallest body from the larger two, and studying the system in a non-inertial reference frame with a constant angular rotation rate: $\omega = 2\pi/T$, where T is the orbital period of the primary and secondary.

To begin, even though we simplify the simulation by modeling the cluster as $\mathcal{N}$ independent three-body problems, the problem remains challenging. Indeed, if we consider all three bodies to have mass, we can write down a Hamiltonian with 18 dimensions: three positions and three momenta in $\mathcal{R}^3$ for each particle. The dimensionality of the problem can be reduced by using the conservation of total linear momentum and total angular momentum, and by expressing the dynamics in terms of relative coordinates about the system's center of mass. This reduces the total dimensionality to 9. Nevertheless, the problem remains analytically intractable due to its high dimensionality. To gain analytical insight, we simplify the system further.

Instead of writing the full Lagrangian for the three-body motion, we focus on the third particle subject to the gravitational influence of the two massive bodies, in an inertial reference frame centered at the system's center of mass. The Lagrangian then contains the kinetic energy of the third particle and two gravitational potential energy terms from the primary and secondary. However, since the positions and momenta of the primaries are not treated as dynamical variables in our system, they appear as explicit functions of time, making the Lagrangian non-autonomous. This implies that the corresponding

Hamiltonian is time-dependent and the total energy of the third particle is not conserved, as the primaries can exchange energy with it.

We introduce a further simplifying assumption: the two primaries move on circular orbits. Under this assumption, we transform to a reference frame rotating with the primaries, placing them along the $x-$axis. In this rotating frame, the Lagrangian becomes autonomous; it no longer depends explicitly on time and requires no external information to determine the particle's subsequent motion.

Two effects make this possible. First, by moving to the rotating frame, we introduce non-inertial forces: the Coriolis force and the centrifugal force. The centrifugal force is conservative, associated with a scalar potential. The Coriolis force depends on the particle's velocity as $2\omega \times v$, but because it is always perpendicular to the velocity, it does no work and thus does not change the particle's kinetic energy. After performing the coordinate transformation, the canonical momenta—now position-dependent—can be derived. The resulting Hamiltonian is:

$$\mathcal{H} = \frac{1}{2}\left((p_x + \omega y)^2 + (p_y - \omega x)^2\right) + \Phi_{\text{eff}}(x, y), \tag{2.31}$$

where

$$\Phi_{\text{eff}}(x, y) = -\frac{1}{2}\omega^2(x^2 + y^2) - \frac{Gm_1}{|r_1|} - \frac{Gm_2}{|r_2|}. \tag{2.32}$$

The potential can be normalized by noting that the orbital angular velocity from the two-body problem satisfies $\omega^2 = \frac{GM}{a^3}$, where a is the separation between the primaries and $M = m_1+m_2$ is the total mass of the system. With this normalization, the system depends on a single dimensionless parameter μ, the relative mass ratio defined as $\mu = \frac{m_2}{m_1+m_2}$.

At this point, the system can be studied qualitatively. Unfortunately, no general closed-form solution exists for the circular restricted three-body problem that describes the subsequent motion as a function of time. However, by studying the effective potential Φ_{eff}, we gain valuable insights.

Our Hamiltonian depends on the four variables (x, y, p_x, p_y) and has one integral of motion.[5] A well-known quantity in this context is the Jacobi integral (or Jacobi constant), often written as $C_j = -2\mathcal{H}$. Defining this constant is somewhat arbitrary, since the non-inertial mechanical energy $\mathcal{H}$ is itself conserved, and any scalar multiple of it is also conserved. The utility of the Jacobi constant is mostly conventional: it is often defined to be positive and multiplied by 2, which simplifies the expression for forbidden regions and zero-velocity curves. By using $p_x = \dot{x} - \omega y$ and $p_y = \dot{y} + \omega x$, one can write:

$$\dot{x}^2 + \dot{y}^2 = -\left(2\Phi_{\text{eff}}(x, y) + C_j\right),$$

---

[5] The term "integral of motion" is often used interchangeably with "constant of motion," but strictly speaking, the latter is preferable, as it refers to a quantity that remains constant throughout the orbital evolution—not to an integral in the mathematical sense of the word (i.e., the area under a curve).

instead of the equivalent:

$$\dot{x}^2 + \dot{y}^2 = -2\Phi_{\text{eff}}(x, y) + 2\mathcal{H}.$$

Since we have four variables and one constraint, the motion is restricted to a three-dimensional hypersurface (or manifold) embedded in the four-dimensional phase space.

At this stage, we find the points where $\nabla\Phi_{\text{eff}} = 0$, which correspond to the Lagrange points—locations where all effective forces balance. Of particular importance are the first two Lagrange points L_1 and L_2, which lie along the line connecting the primary and secondary. The effective potential at L_1 is lower than at L_2.

Given a certain energy level, setting the kinetic energy to zero defines boundaries between regions where the particle can and cannot move. Regions where the kinetic energy would have to be negative (which is physically impossible) are forbidden, since that would require imaginary velocities.

The points L_1 and L_2 are especially important for our study of a globular cluster with stars initially bound to it. Stars can escape through these Lagrange points: lower-energy particles tend to escape through L_1, while higher-energy particles can also escape through L_2. Figure 2.7 illustrates these forbidden and allowed regions clearly. The distance from the secondary to the first and second Lagrange points is approximately equal, defining a region around the secondary known as the Hill sphere. Within this zone, the gravitational influence of the secondary dominates over that of the primary. The Hill radius is commonly approximated as $r_h \approx r\sqrt[3]{m_2/m_1}$, where r is the separation between the primaries. Interestingly, the expression for the Hill radius arises from a fifth-order polynomial expansion of the effective potential—a detail that might seem minor, but is actually quite delightful. In most areas of physics, approximations typically emerge from Taylor expansions, basis function decomposition's, or limits where the governing equations simplify.

At conferences, we have been asked whether we have ever observed *recapture*—that is, a star becoming bound to globular cluster. Capture is a fascinating phenomenon, particularly in the case of dark matter sub-halos that could in theory capture field stars that were not formed within them (Peñarrubia et al., 2024). If the system were as simple as the circular restricted three-body problem, recapture could occur for star particles with energies in the range $E_1 < E < E_2$ or $E_2 < E < E_3$. In such cases, depending on initial conditions, a particle might orbit the secondary, escape, and later return. However, in our simulations, the galaxy and globular clusters are not treated as point masses, and the clusters follow eccentric, inclined, and non-closed orbits. This means the topology of the forbidden region evolves over time. For a particle with a given energy E, it may be unbound at one moment but later find itself within the Hill sphere again, as the potential landscape changes dynamically. Indeed, we have observed such behavior in our simulations.

The Lagrange points, forbidden regions, and Jacobi energy are powerful concepts

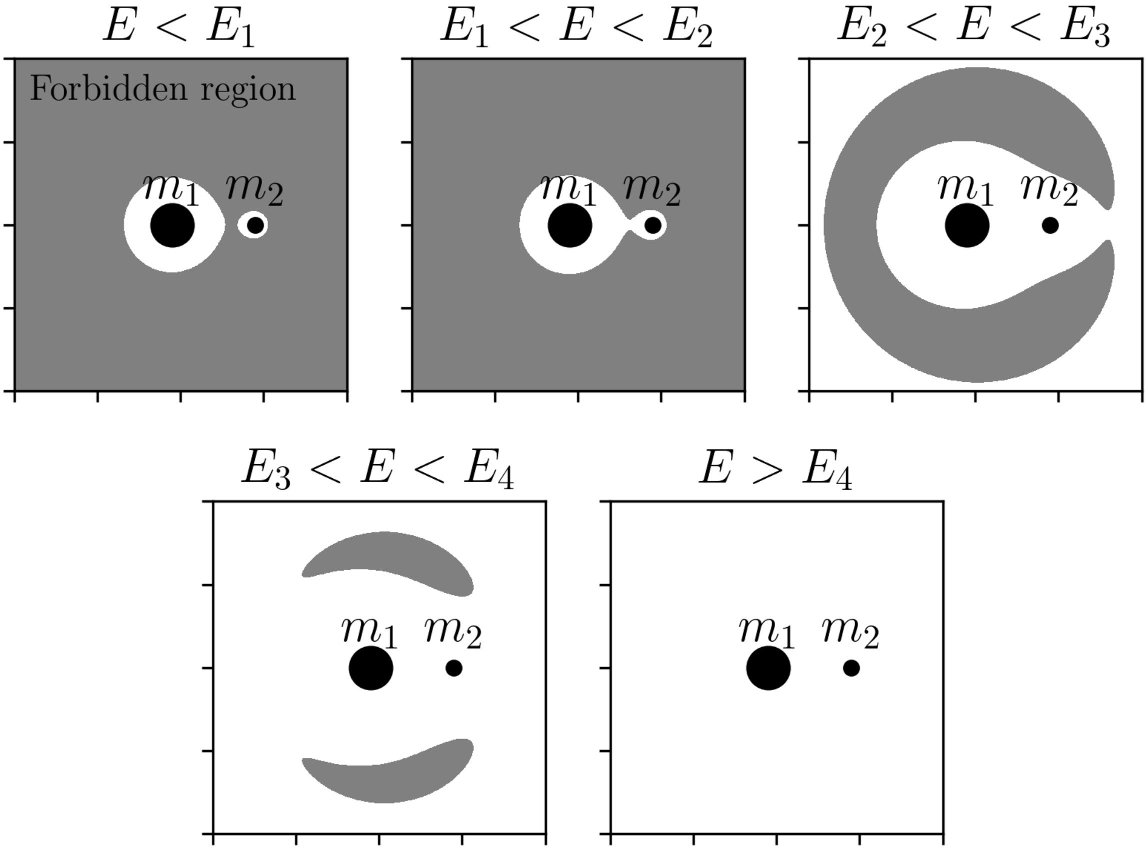

Figure 2.7 – A reproduction of Fig. 2.4.2 from Koon et al. (2000). Each plot is shown in the non-inertial reference frame rotating with the orbital frequency of the primary and secondary about their common center of mass. In this example, the mass ratio is $m_1 = 10m_2$. The gray regions represent areas inaccessible to the test particle for a given energy. In the first case, where $E < E_1$, the particle remains confined to orbit either around the primary or the secondary, depending on its initial position. As the particle's energy increases, more of the xy-plane becomes accessible. The narrow passage between m_1 and m_2 corresponds to the L_1 Lagrange point, while the choke point allowing escape to the exterior when $E > E_2$ is the L_2 point.

which, while they do not rigorously apply in our more complex setup, still offer valuable qualitative insights. In our regime, it is more fruitful to think in terms of tidal forces as the underlying mechanism that gradually transfers energy and angular momentum, nudging stars across Lagrange boundaries and ultimately enabling escape. It is to this process—tidal stripping—that we now turn.

2.2 Tidal Forces

For star-particles within a globular cluster that is itself orbiting within a galaxy, there are no exact integrals of motion. The system lacks symmetries in its Lagrangian, and the potential varies with time, so even the orbital energy is not conserved. In such a time-dependent and asymmetric context, it is more insightful to frame the problem in terms of forces rather than conserved quantities. In particular, tidal forces arise when the gravitational field of the galaxy (the primary) is treated as an external perturbation to the field of the globular cluster (the secondary). In this section, I aim to build an intuitive and formal understanding of tidal forces, framing them as tensor quantities. We begin with the simplest case—the familiar Sun-Earth system—before extending the discussion to the Galactic context. I also provide a broader overview of how tidal forces vary depending on the cluster's orbit within the galaxy.

To start, tidal forces arise due to spatial variations in the gravitational field with respect to a reference point, which is almost always the secondary body. There are two equivalent options to quantify this. The first is to consider a Taylor expansion of the gravitational potential of the primary, Φ_g, evaluated at the star's position $\vec{x}_s$, relative to the secondary's position $\vec{x}_c$:

$$\Phi_g\left(\vec{x}_s\right) \approx \Phi_g\left(\vec{x}_c\right) + \left[\nabla\Phi_g(\vec{x}_c)\cdot\Delta\vec{x}\right] + \left[\Delta\vec{x}\cdot\mathcal{D}^2\left(\Phi_g\right)\cdot\Delta\vec{x}\right], \tag{2.33}$$

where $\Delta\vec{x} = \vec{x}_s - \vec{x}_c$, and $\mathcal{D}^2\Phi_g$ is the Hessian matrix of second derivatives of the potential: $\partial^2\Phi/\partial x_i\partial x_j$.

The second expression can be derived by linearizing the gravitational force in a non-inertial frame co-moving with the secondary. Let us write Newton's second law for the star-particle and the secondary in an inertial frame:

$$\begin{aligned} \vec{F}_s &= \nabla\Phi_c\left(\Delta\vec{x}\right) + \nabla\Phi_g\left(\vec{x}_s\right), && (2.34)\\ \vec{F}_c &= \nabla\Phi_g\left(\vec{x}_c\right), && (2.35)\end{aligned}$$

where $\vec{F}_s$ is the force on the secondary and $\vec{F}_c$ is the force on the secondary. Then the relative acceleration of the star in the non-inertial frame is:

$$\begin{aligned}
\vec{f}_s &= \vec{F}_s - \vec{F}_c + \vec{F}_{\text{fictitious}} && (2.36)\\
&= \nabla\Phi_c\left(\Delta\vec{x}\right) + \nabla\Phi_g\left(\vec{x}_s\right) - \nabla\Phi_g\left(\vec{x}_c\right) + \vec{F}_{\text{fictitious}} && (2.37)\\
&\approx \nabla\Phi_c\left(\Delta\vec{x}\right) + \text{Jac}\left(\nabla\Phi_g(\vec{x}_c)\right)\cdot\Delta\vec{x} + \vec{F}_{\text{fictitious}}, && (2.38)
\end{aligned}$$

where the last line uses a first-order Taylor expansion of the gravitational force field, valid under the assumption that $|\Delta\vec{x}| << |\vec{x}_c|$.

The Jacobian of the gravitational field is equal to the Hessian of the potential, owing to the symmetry of second derivatives and the fact that $\vec{g} = -\nabla\Phi_g$. This matrix, known as the *tidal tensor* $\mathcal{T}$, describes the linearized spatial variation of the gravitational field:

$$\mathcal{T} = -\mathcal{D}^2\Phi_g = \text{Jac}(\nabla\Phi_g) = \begin{pmatrix} \partial_x g_x & \partial_y g_x & \partial_z g_x \\ \partial_x g_y & \partial_y g_y & \partial_z g_y \\ \partial_x g_z & \partial_y g_z & \partial_z g_z \end{pmatrix}. \tag{2.39}$$

While the Hessian and Jacobian are formally equivalent, the Jacobian viewpoint offers a more geometric interpretation: it acts as a linear transformation on nearby displacements, mapping them to differences in acceleration. Diagonalizing the tidal tensor reveals the principal axes of tidal deformation. A positive eigenvalue corresponds to stretching along the associated eigenvector; a negative eigenvalue indicates compression. The magnitude gives the rate of stretching or compression.

Finally, we note that although many relevant potentials exhibit spherical or cylindrical symmetry, Cartesian coordinates are preferred here. In curvilinear systems, computing the Jacobian or Hessian requires accounting for Christoffel symbols, which complicates the interpretation and computation.

2.2.1 The Moon

Nothing clarifies the concept of tides like the most familiar example: the Moon. Tidal forces are invoked to explain a wide range of phenomena in the Earth-Moon system. The most relatable effect is, of course, the periodic variation in sea level on Earth. While accurately modeling these changes requires fluid dynamics—beyond the scope of this thesis—NASA provides several accessible explanations and visualizations at https://science.nasa.gov/moon/tides/, including daily high and low tides, as well as spring and neap tides.

Another key example is the tidal deformation of the Moon, which ultimately led to its tidal locking—explaining why we always see the same side of the Moon from Earth.

A particularly insightful illustration is the angular offset between the Earth's tidal bulge and the Moon's position, caused by the Earth's rotation. This offset results in a torque that transfers angular momentum from the Earth's rotation to the Moon's orbit. As a consequence, Earth's rotation gradually slows while the Moon slowly recedes from Earth.

All of the above phenomena require using the tidal tensor for a Keplerian potential:

$$\mathcal{T} = -\frac{GM}{r^3}\begin{pmatrix} 1-\frac{3x^2}{r^2} & -\frac{3xy}{r^2} & -\frac{3xz}{r^2} \\ -\frac{3yx}{r^2} & 1-\frac{3y^2}{r^2} & -\frac{3yz}{r^2} \\ -\frac{3zx}{r^2} & -\frac{3zy}{r^2} & 1-\frac{3z^2}{r^2} \end{pmatrix}, \tag{2.40}$$

which has eigenvalues $2\frac{GM}{r^3}$, $-\frac{GM}{r^3}$, and $-\frac{GM}{r^3}$, with corresponding eigenvectors:

$$\vec{v}_0 = \frac{1}{r}\begin{bmatrix} x \\ y \\ z \end{bmatrix}, \quad \vec{v}_1 = \frac{1}{\sqrt{x^2+y^2}}\begin{bmatrix} -y \\ x \\ 0 \end{bmatrix}, \quad \vec{v}_2 = \frac{1}{r\sqrt{x^2+y^2}}\begin{bmatrix} -xz \\ -yz \\ x^2+y^2 \end{bmatrix}. \tag{2.41}$$

Notably, the first eigenvalue is positive and corresponds to stretching along the position vector $\vec{r}$. The other two eigenvalues are equal and negative, representing compression in the plane perpendicular to $\vec{r}$. Any orthonormal pair of vectors spanning this plane forms valid eigenvectors, so the choice is not unique. In this work, we illustrate this by choosing $\vec{v}_1$ perpendicular to both $\vec{r}$ and the z-axis, i.e., effectively projecting along $[0, 0, 1]$, and taking the cross product to define $\vec{v}_2$. This choice leads to a singularity when $\vec{r}$ is aligned with the z-axis; in that case, any other reference axis can be chosen to define the perpendicular plane.

From this, several tidal effects become evident. For instance, the Earth's oceans stretch along the Earth-Moon axis due to the Moon's tidal forces. While the Sun also exerts tidal forces on Earth, their magnitude is weaker due to the r^{-3} scaling with distance. When the Moon is either full or new, the Sun and Moon's tidal forces act constructively, leading to spring tides. At first and third quarters, they interfere destructively, causing neap tides. Additionally, Earth's tidal influence distorts the Moon from spherical symmetry into an ellipsoid. The Moon's most stable orientation is one where its longest axis aligns with the Earth-Moon line—resulting in tidal locking.

A more quantitative treatment of these phenomena would require modeling the Moon's internal structure and Earth's ocean dynamics—well beyond the gravity-only scope of this thesis. However, we can still explore one instructive effect: how solar tidal forces *perturb* the Moon's orbit away from the idealized two-body Earth-Moon configuration. Figure 2.8 shows a toy model comparing two scenarios. In both, I used initial conditions based on JPL NASA ephemerides (Folkner et al., 2014) and integrated two sets of equations of motion. Neglecting solar tides causes the predicted Moon orbit to drift ahead of the more accurate trajectory. With about three to four years, the two body predicted solution would off by half a moon phase.

In the first scenario, the Moon's motion is governed by the two-body Earth-Moon problem with a rotating reference frame correction:

$$\ddot{\vec{r}} = -\frac{GM_\oplus}{r^3}\vec{r} - \omega_\oplus \times \left(\omega_\oplus \times \vec{r}_\oplus\right), \tag{2.42}$$

while in the second, we include the effect of solar tidal forces:

$$\ddot{\vec{r}} = -\frac{GM_\oplus}{r^3}\vec{r} - \omega_\oplus \times \left(\omega_\oplus \times \vec{r}_\oplus\right) - \frac{GM_\odot}{r_\oplus^3}\begin{pmatrix} 1 - \frac{3x^2}{r_\oplus^2} & -\frac{3xy}{r_\oplus^2} & -\frac{3xz}{r_\oplus^2} \\ -\frac{3yx}{r_\oplus^2} & 1 - \frac{3y^2}{r_\oplus^2} & -\frac{3yz}{r_\oplus^2} \\ -\frac{3zx}{r_\oplus^2} & -\frac{3zy}{r_\oplus^2} & 1 - \frac{3z^2}{r_\oplus^2} \end{pmatrix} \cdot \vec{r}, \tag{2.43}$$

where $r_\oplus$ is the Earth's position relative to the Sun, $\vec{r}$ is the Moon's position relative to Earth, $M_\odot$ is the mass of the Sun, and $M_\oplus$ is the mass of the Earth. The coordinates x, y, z refer to the components of Earth's heliocentric position.

2.2.2 Tides from the disk

In the Milky Way, the disk, bulge, and halo each contribute differently to the tidal forces experienced by a globular cluster. The Miyamoto-Nagai disk produces strong, rapidly varying tidal fields near the Galactic plane, leading to phenomena such as disk shocking when clusters cross the disk. The Allen-Santillan halo, on the other hand, provides a more slowly varying, generally weaker tidal field at large Galactocentric radii.

The strength and orientation of the tidal field at a cluster's location determine both the rate at which stars are stripped and the geometry of the resulting stellar streams. For example, clusters on eccentric or inclined orbits experience time-dependent tidal forces, with strong compressive shocks during disk crossings and enhanced stretching near pericenter. The eigenvalues and eigenvectors of the tidal tensor at each point along the orbit reveal the principal axes of stretching and compression, which in turn set the directions along which stars are most likely to escape.

By computing the tidal tensor for the Miyamoto-Nagai disk and Allen-Santillan halo potentials, as shown below, we can visualize and quantify these effects. The following figures illustrate how the tidal field evolves for representative orbits, highlighting the interplay between the cluster's trajectory and the Galactic mass distribution. This analysis underpins our understanding of stream formation and the morphological diversity of observed tidal tails.

We can construct the tidal tensor for the Miyamoto-Nagai potential. First, it is convenient to non-dimensionalize the potential. Below, we normalize the potential by the total mass and gravitational constant, $\Phi' = \Phi/(GM)$, and each distance by the characteristic length of the disk, $x' = x/a$, $b' = b/a$. For clarity, we omit the prime

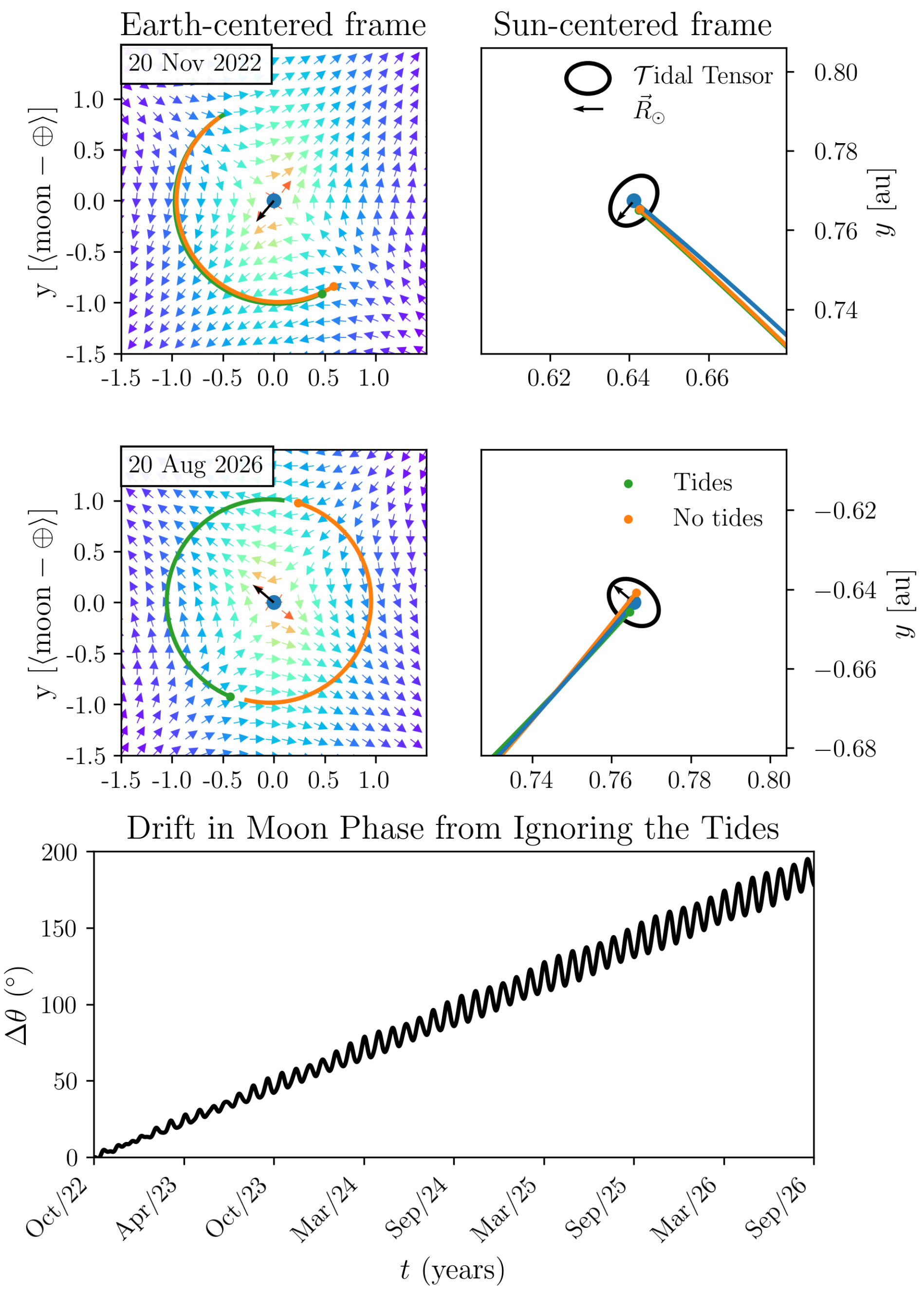

Figure 2.8 – An illustrative experiment demonstrating the effect of the Sun's tidal field. The left panels show the tidal field, and the right panels show two snapshots of the Moon's orbital trajectory. The green curve include the Sun's tidal effects, while the orange curve corresponds neglects them. The black ellipse represents the tidal ellipsoid, whose major axis aligns with the Sun's position vector relative to the Earth. The bottom panel shows the accumulated phase difference between the two solutions.

notation in what follows. The dimensionless potential then becomes:

$$\Phi = \frac{1}{D}, \tag{2.44}$$

$$D = \sqrt{x^2 + y^2 + \beta^2(z)}, \tag{2.45}$$

$$\beta(z) = 1 + \sqrt{z^2 + b^2}. \tag{2.46}$$

The dimensionless tidal tensor is then:

$$\mathcal{T} = -\frac{1}{D^3}\begin{pmatrix} 1 - \frac{3x^2}{D^2} & -\frac{3xy}{D^2} & -\frac{3x\beta\beta'}{D^2} \\ \dots & 1 - \frac{3y^2}{D^2} & -\frac{3y\beta\beta'}{D^2} \\ \dots & \dots & \beta'^2 + \beta\beta'' - \frac{3(\beta\beta')^2}{D^2} \end{pmatrix}, \tag{2.47}$$

where $\beta' = \frac{d\beta}{dz}$ and $\beta'' = \frac{d^2\beta}{dz^2}$. We immediately notice that, due to the cylindrical symmetry, the eigenvectors are not as simple as in the spherical case. As long as

$$\beta'^2 + \beta\beta'' - \frac{3\left(\beta\beta'\right)^2}{D^2} \neq 1 - \frac{3z^2}{D^2},$$

(1) the stretching axis is no longer parallel to the position vector, and (2) the compression axes do not necessarily lie in the same plane—they may instead be fixed in orientation and differ in magnitude. The exact orientation of all three eigenvectors depends on the cluster's position in the galaxy. Note that if $z = 0$, we recover the case where the stretching eigenvector is parallel to the position vector, although the compression axes remain unequal in magnitude and fixed in orientation. If instead $b = 0$, then we recover spherical symmetry, and the compression eigenvalues become equal. I have prepared Figs. 2.9-2.13 to illustrate the diversity of tidal forces experienced by clusters on various orbits within a Miyamoto-Nagai disk potential. I generate initial conditions with prescribed pseudo-eccentricities and inclinations. Each initial condition is set at apocenter, specified by a radial distance and an inclination from the disk plane. The initial velocity vector is oriented perpendicular to both the z-axis and the position vector. The circular speed at the initial position is computed as $v_{\mathrm{circ}} = \sqrt{|\mathbf{r}| \cdot |\nabla\Phi(\mathbf{r})|}$. The pseudo-eccentricity is applied via $v_0 = v_{\mathrm{circ}}\sqrt{\frac{1-e}{1+e}}$.

Fig. 2.9 shows a cluster on an inclined, non-eccentric orbit. In contrast, Fig. 2.10 presents a planar but eccentric orbit. The former experiences repeated disk shocks, while the latter undergoes enhanced tidal forces primarily near pericenter passages.

Fig. 2.11 presents an orbit in which the radial and vertical oscillation periods are nearly resonant, producing two disk shocks per pericenter passage. Fig. 2.12 shows a cluster on an orbit with a large apocenter, resulting in very weak tidal forces overall. Finally, Fig. 2.13 demonstrates a case with a very thick disk potential. In this case, disk shocks occur over longer timescales and are less abrupt.

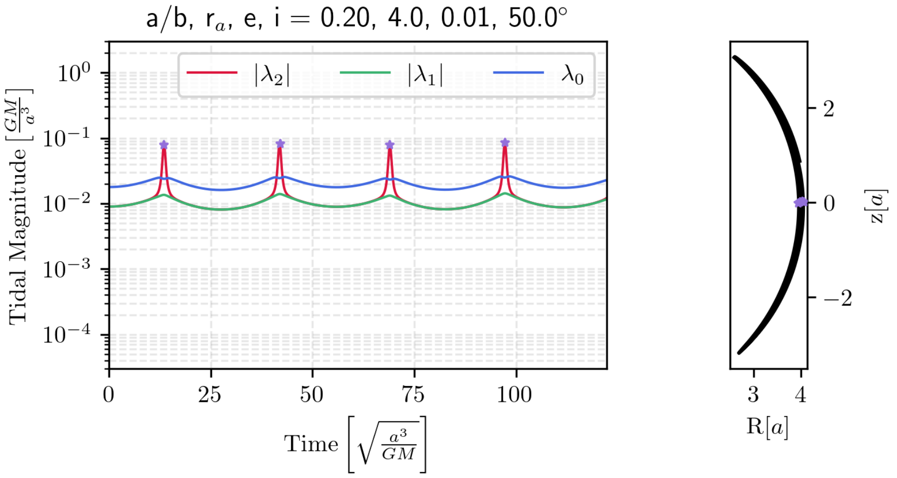

Figure 2.9 – Tidal forces on an inclined yet non-eccentric orbit. Disk shocks are present, yet there is no tidal stretching from pericenter passages. **Left**: The three eigenvalues of the tidal tensor matrix are plotted against time. Both the forces and time are normalized to the characteristic values of the Miyamoto-Nagai model, where a is the radial scale length and M is the total mass of the system. The red and green curves correspond to the two compressive axes, while the blue curve shows the magnitude of the stretching axis. The parameters listed at the top describe the orbit: the ratio of cylindrical to vertical scale lengths, the apocenter distance, the eccentricity, and the initial orbital inclination. **Right**: The orbit is shown in the meridional plane. The purple stars indicate disk crossing events and correspond to the peaks in the magnitude of the eigenvalues.

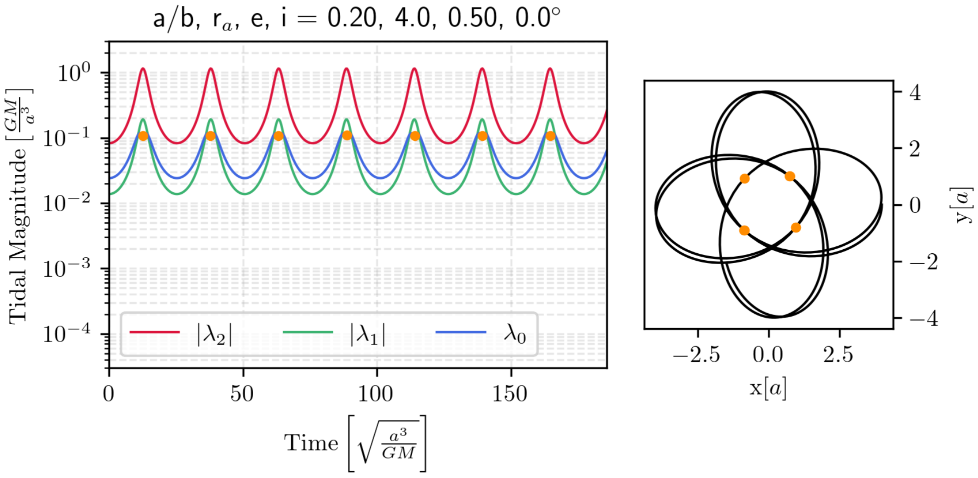

Figure 2.10 – Same as Fig. 2.9. Evolution of the tidal eigenvectors for an eccentric, non-inclined orbit, resulting in a compressed meridional plane. Orange dots mark the pericenter passages. Since the cluster remains confined to the plane, no disk shocks occur.

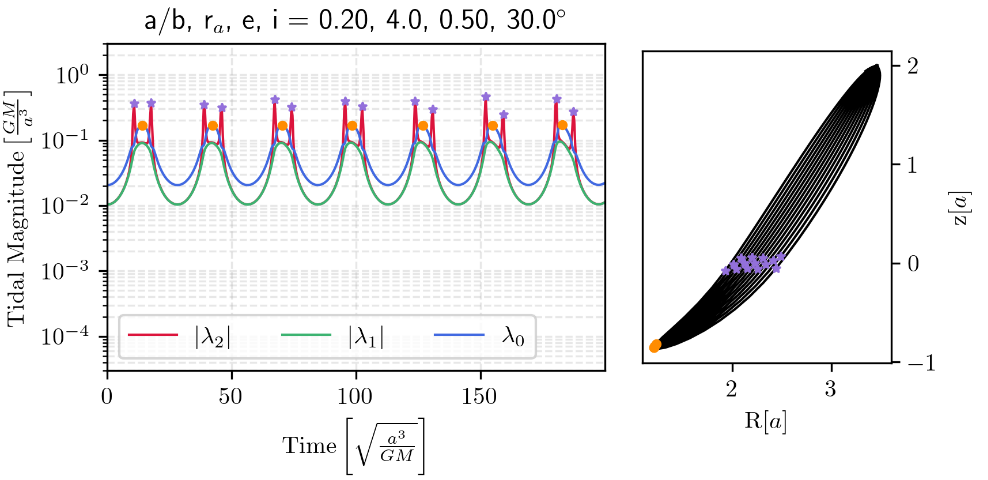

Figure 2.11 – An inclined, eccentric orbit in which the frequencies in both the R, p_R and z, p_z planes are nearly resonant. The axis are the same as: Fig. 2.11. The cluster crosses the disk just before and just after each pericenter passage. This is the same orbit as the video presented in this section that is available in the online version.

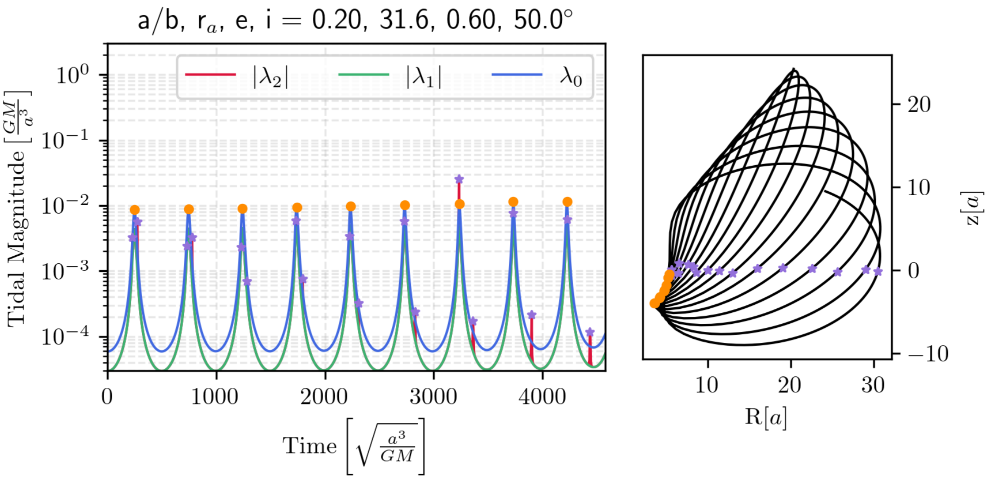

Figure 2.12 – As the cluster evolves through phase space, disk crossings that occur farther out happen at steeper angles and in lower-density regions, reducing the strength of the resulting disk shocks. In contrast, crossings near pericenter remain strong. Because this orbit has higher energy than the previous cases, the overall magnitude of the tidal forces is lower.

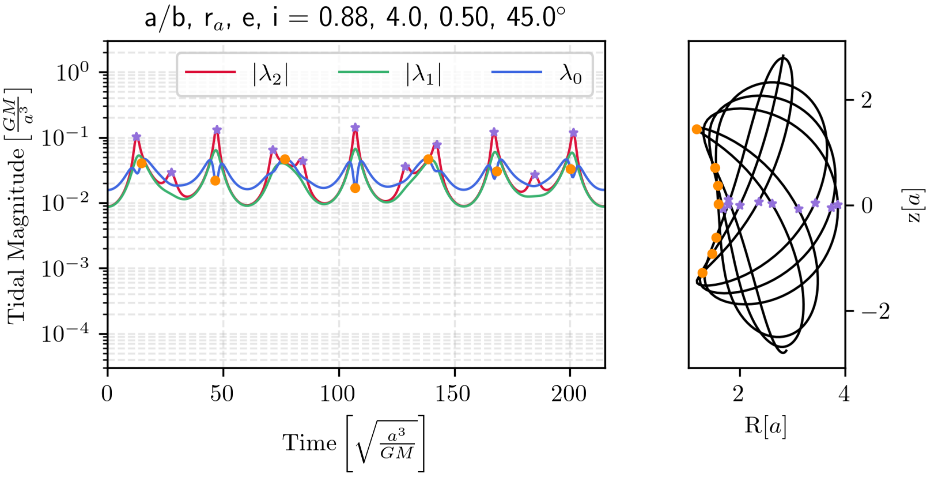

Figure 2.13 – Eccentric and inclined orbit in a weak disk. The ratio of the cylindrical scale length to characteristic height (a/b) is close to 1. The disk crossings still produce significant tidal compression, but the resulting shocks are broader.

2.2.3 Tides from the dark matter halo

Given spherical symmetry, we expect the tidal tensor of the halo to be similar to that of a Keplerian tidal tensor. Perhaps the magnitude of the tidal forces will not scale as simply with $\propto r^{-3}$, since the mass is not concentrated in a single point. However, we can still expect the stretching axis to be parallel with the position vector.

To explore this, first we rewrite equation 2.13, the mass distribution of the Allen-Santillan halo (Allen & Martos, 1986; Allen & Santillan, 1991), in a non-dimensional form:

$$M'_{\mathrm{enc}}(s) = \frac{s^\gamma}{1+s^{\gamma-1}}, \tag{2.48}$$

where γ is the exponential slope parameter, s is the radial distance scaled to the characteristic radius r_0 and M' is the enclosed mass normalized to the mass parameter: M_{enc}/M_0. From Poisson's equation in spherical symmetry: the force is: $\nabla\Phi = -M_{\mathrm{enc}}/r^2$. The dimensionless tidal tensor can be written as:

$$\mathcal{T}' = -\frac{M'_{\mathrm{enc}}(s)}{s^3}\begin{pmatrix} 1-\frac{x^2}{s^2}f(s) & -\frac{xy}{s^2}f(s) & -\frac{xz}{s^2}f(s) \\ -\frac{yx}{s^2}f(s) & 1-\frac{y^2}{s^2}f(s) & -\frac{yz}{s^2}f(s) \\ -\frac{zx}{s^2}f(s) & -\frac{zy}{s^2}f(s) & 1-\frac{z^2}{s^2}f(s) \end{pmatrix} \tag{2.49}$$

where

$$f(s) = 2 - \frac{\gamma-1}{1+s^{\gamma-1}}. \tag{2.50}$$

While exploring this tidal tensor, I came across an interesting area of the parameter space, that I would like to show here.

Taking the Allen-Santillan tidal tensor in Eq. 2.50, we can see that for $\gamma > 3$ and $s < 1$, then $f(s) < 0$. Physically, this would be a sphere whose density increases with distance. This is not natural, as, in general, gravity sends the more massive objects towards the center. However, it is interesting to indulge in this situation to learn some insight about the flexibility of tidal fields. The consequence of $f(s) < 0$ is that all terms in the tidal tensor are negative, which means that the force is compressive everywhere. Consequently, no stars escape from the cluster.

In Fig. 2.14, I present a small experiment demonstrating the consequence of such a tidal force on a globular cluster, which is that no tidal stream forms. Briefly, I created a Plummer sphere of 10^6 $\mathrm{M}_\odot$ and half mass radius 20 pc and evolved it in a Allen-Santillan halo potential of mass parameter 10^{12} $\mathrm{M}_\odot$ a characteristic radius of 30 kpc. Each cluster was placed at the same initial conditions, a distance of 1/4 the scale radius from the center of the potential. The initial velocity was made perpendicular to the position vector with a speed of $(1-e)v_\mathrm{c}$. This is a pseudo-eccentricity, which was added to have a non-circular orbit to demonstrate how the trajectories change in the two cases. The top panel uses a γ of 2.02, which is the same value in the model where the halo was originally presented, and the value I employ in this thesis. Next, the bottom panel uses γ of 4.5, which corresponds to a density profile where $\rho(r) \propto r^{1.5}$.

To get a feel for the strength of the tidal stretching and compression, I apply the tidal deformation to a circle and show the resulting ellipse, as shown by the black lines in the right panels of Fig. 2.14 and Fig. 2.15. I computed the coordinates of the ellipse by adding

$$\vec{Ell} = \vec{C} + \frac{1}{2} t_\mathrm{char}^2 \mathcal{T} \cdot \left(\vec{C} - \vec{r_o} \right). \tag{2.51}$$

This way, force can be mapped to position space, and the strengths of the tidal forces can be seen visually. The characteristic time, t_char, is a free parameter that scales the deformation. I choose to set it to $\frac{1}{10} 2\pi r_\mathrm{halo}/v_\mathrm{c}$.

In the case of Fig. 2.15, the tidal field returns to the typical situation where one axis is compressive and the other stretches. Notice how the deformations are similar in magnitude, while in the case of $\gamma = 2.02$ for the top panel of Fig. 2.14, the compression is stronger than the expansion. Both of these are different than the Keplerian tidal deformation where the stronger deformation is stretching and whose axis is parallel to the position vector.

2.3 The Distribution of Escaped Stars

Tidal forces cause stars to escape from the Lagrange points of the globular cluster. As we have seen, these forces can be compressive—pushing stars toward the cluster—or stretching—pulling them away, and specifically toward the Lagrange points. The stretch-

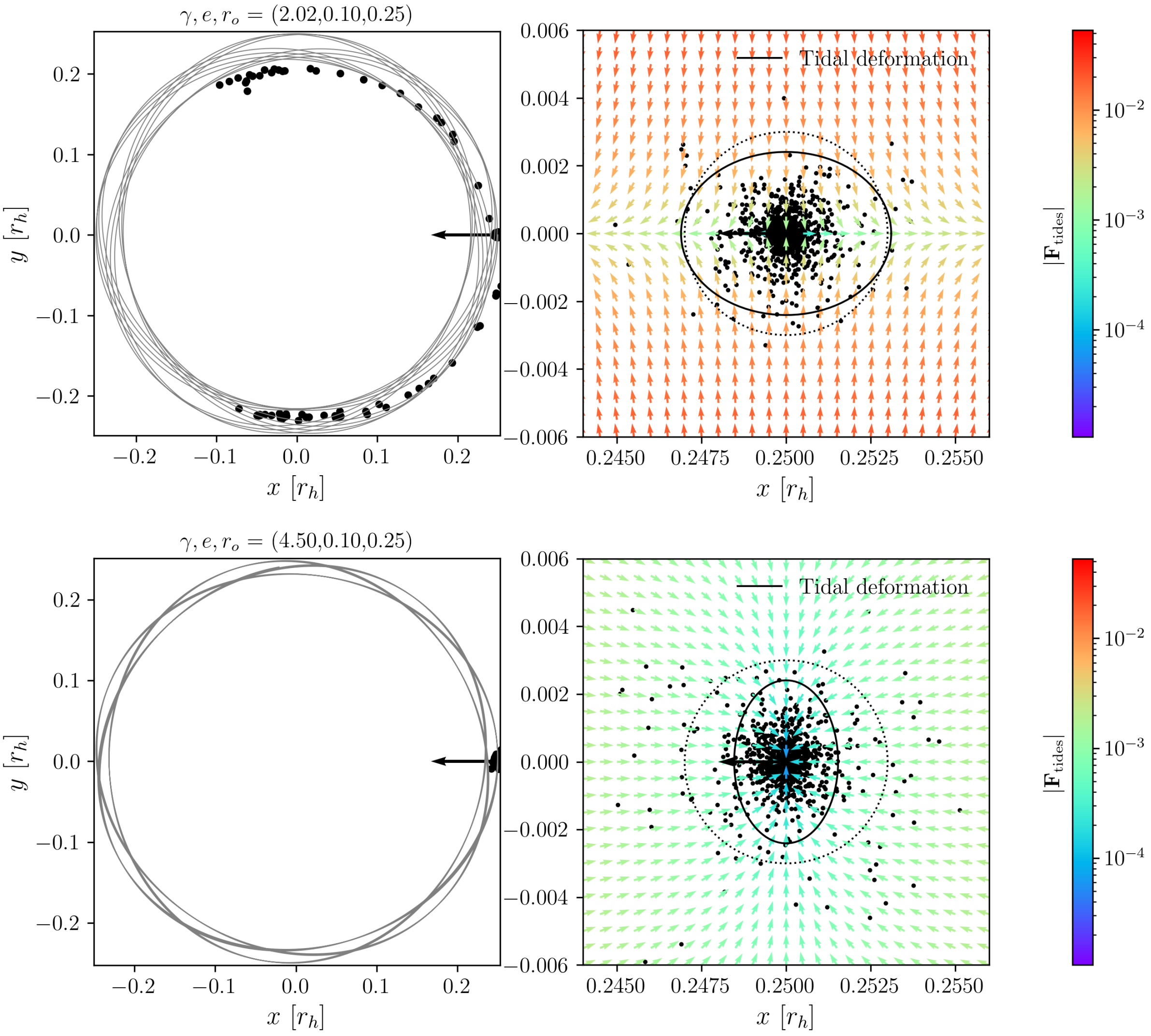

Figure 2.14 – The plots show two low-resolution streams (N = 1000) created by dissolving a Plummer sphere in the Allen-Santillan halo potential. The units are scaled to the halo's characteristic radius. Gamma is the mass exponent and is the sole variable between the two simulations. The panels on the left show the orbit in gray and the stars in black. The black arrow points towards the center of the potential. The panels on the right show the tidal field, which is the tidal tensor evaluated at each position in space. The gray dotted circle is plotted with an arbitrary radius and is deformed by the tidal field into a black ellipse.

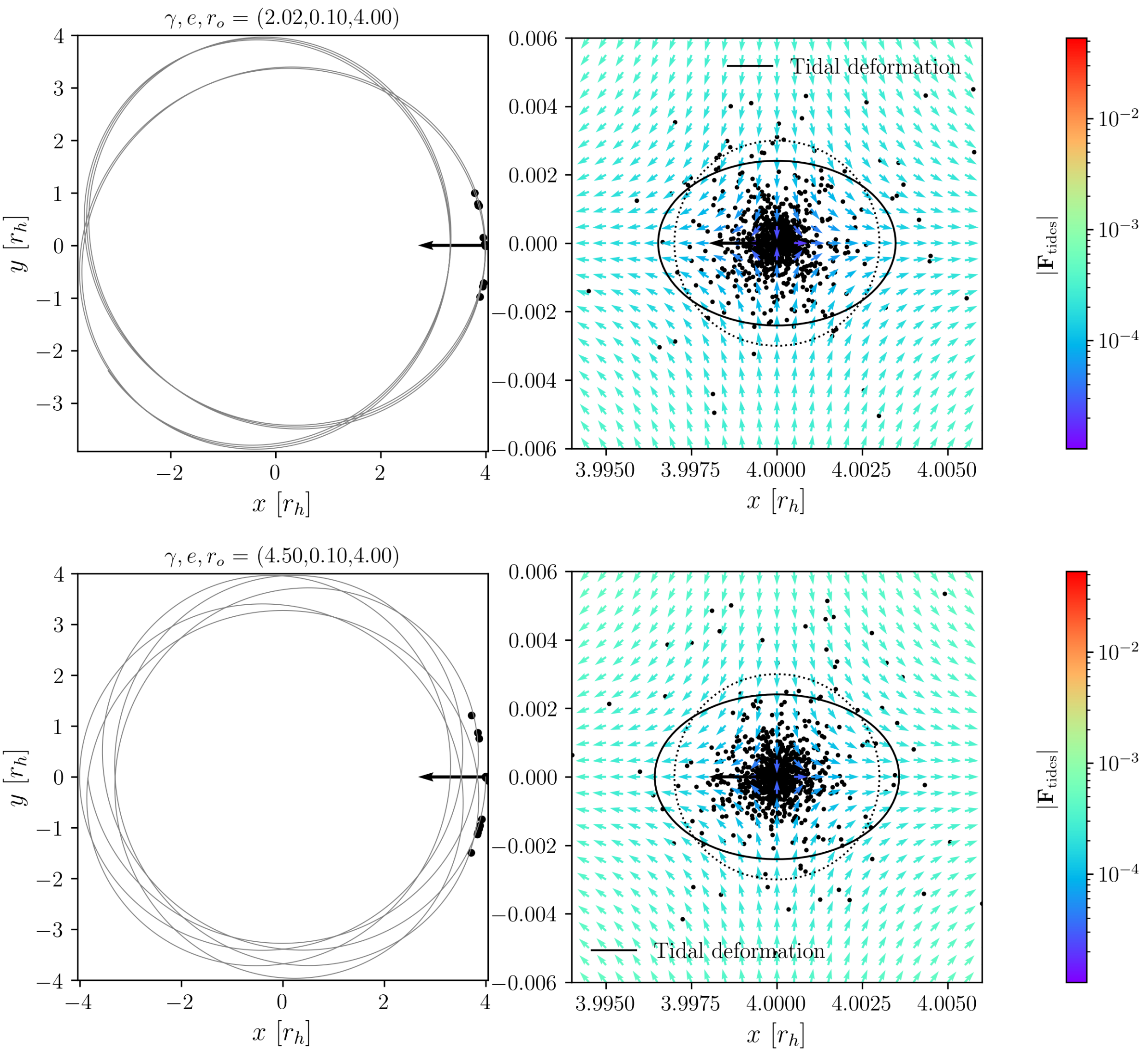

Figure 2.15 – The same experiment as Fig. 2.14, but the cluster was placed at a larger distance of 4 r_{halo}, since we are beyond the characteristic radius, the tidal fields are the same, despite the different exponents γ.

ing component is significantly amplified during pericenter passages, causing many stars to escape in bursts.

This process does not fling stars into intergalactic space. Rather, the Galactic tidal field is typically weak compared to the cluster's own gravitational pull, and escaping stars gain just enough energy to leave the cluster. As a result, they are still on very similar orbits to the clusters once they escape.

But once stars escape, why do they form coherent stellar streams? And do they do anything else? To answer this, I must first introduce the concept of *phase mixing*. This naturally leads us to discuss the range of possible orbits a globular cluster can follow, given observational uncertainties. I'll cover this fully before returning to the topic of stellar streams, which will be much easier to understand once this groundwork is in place.

Phase mixing is a direct consequence of Liouville theorem, which follows from the collisionless Boltzmann equation. Liouville's theorem states that the infinitesimal volume element in phase space, $d\mathbf{p}\,d\mathbf{q}$, is preserved under Hamiltonian evolution. In other words, the phase-space density $f(\mathbf{q},\mathbf{p},t)$ remains constant along a particle's trajectory.

To visualize this, instead of considering a single infinitesimal element, imagine a small cloud of initial conditions centered around $(\mathbf{q}_0,\mathbf{p}_0)$, with spread σ_q and σ_p. While the total 6D volume of this cloud, $\sigma_q^3\sigma_p^3$, remains constant, differences in momentum cause the particles to move through phase space at different rates. Particles with higher momenta advance more quickly, while those with lower momenta lag behind. This leads to the cloud stretching and dispersing, even as its total volume is conserved. Since solutions to Hamilton's equations are unique, this dispersion reflects how nearby trajectories gradually diverge and spread over the available phase space—a process we call phase mixing.

We can estimate the timescale for this spreading by considering how long it takes for orbits with slightly different energies to drift apart in phase. For example, in a Keplerian potential, the orbital period is given by

$$T^2 = \frac{4\pi^2 a^3}{GM}, \tag{2.52}$$

which depends on the semi-major axis, and thus on energy. In general, orbits in non-Keplerian potentials are not closed; particles precess and eventually fill out invariant tori in phase space. A characteristic timescale for this process can be estimated by dimensional analysis as

$$T_{\text{char}} = C\frac{GM}{E^{3/2}}, \tag{2.53}$$

where C is a constant and E is the specific orbital energy.

Consider now two nearby particles with energies $E-\Delta E$ and $E+\Delta E$. Their orbital frequencies differ by:

$$\Delta f = \frac{1}{T(E-\Delta E)} - \frac{1}{T(E+\Delta E)}. \tag{2.54}$$

The time required for the faster particle to lap the slower one in phase is the *phase mixing time*, which is the inverse of the difference $2\pi/\Delta f$ and is given by:

$$T_{\mathrm{mix}} = \frac{2\pi}{\Delta f} = \frac{2\pi T_1 T_2}{T_2 - T_1}. \tag{2.55}$$

For small energy differences $\Delta E << E$, we can expand the period in a Taylor series to first order. This leads to:

$$T_{\mathrm{mix}} \approx T_{\mathrm{char}} \cdot 2\pi \left(\frac{E}{3\Delta E} \right), \tag{2.56}$$

Thus, the phase mixing time grows inversely with the relative energy spread in the population.

2.3.1 Orbital drift

The first manifestation of phase mixing is the growth of uncertainty in orbital solutions for globular clusters over time. This originates from the initial spread in orbital energies caused by observational uncertainties. In Fig.2.16, I present an example based on Palomar 5, for which I compute 50 orbital solutions in our potential model. These initial conditions are sampled according to the uncertainties reported in the Baumgardt catalog. The figure shows that while the orbital solutions remain broadly similar, the lower-energy orbits progress through phase space more rapidly. In the bottom panel, the rightmost side includes overplotted dots indicating the final (t, z) coordinates of each solution, illustrating that they span nearly the full range of z values allowed by the initial conditions. In essence, once the integration time exceeds the phase-mixing timescale, any individual solution becomes speculative: the system could plausibly occupy any location in phase space permitted by the initial conditions. By inspecting Eq.2.56, we note that if the phase-mixing time is normalized by the characteristic orbital time, the resulting dimensionless mixing time is inversely proportional to the uncertainty in orbital energy. This relationship is general and holds for all orbits, regardless of their periods. However, it is still illustrative to examine this behavior in the context of the globular cluster catalog. In Fig.2.17, I present the phase-mixing times for all Galactic globular clusters, based on current uncertainties from the Gaia DR3 catalog. The top panel shows the distribution for all 165 clusters. The bottom panels highlight the mixing behavior in cylindrical radius for a selection of statistically representative clusters: Gran 1, which has the shortest mixing time; Gran 5, the median case; NGC 6752, whose mixing time is closest to the mean; and NGC 2419, which has the longest mixing time.

It is important to emphasize that these estimates are highly model-dependent. In some cases, the models predict phase-mixing timescales exceeding the age of the Universe. Unsurprisingly, the phase-mixing time correlates with the orbital period, which itself is related to the cluster's distance from the Galactic center. At large Galactocentric

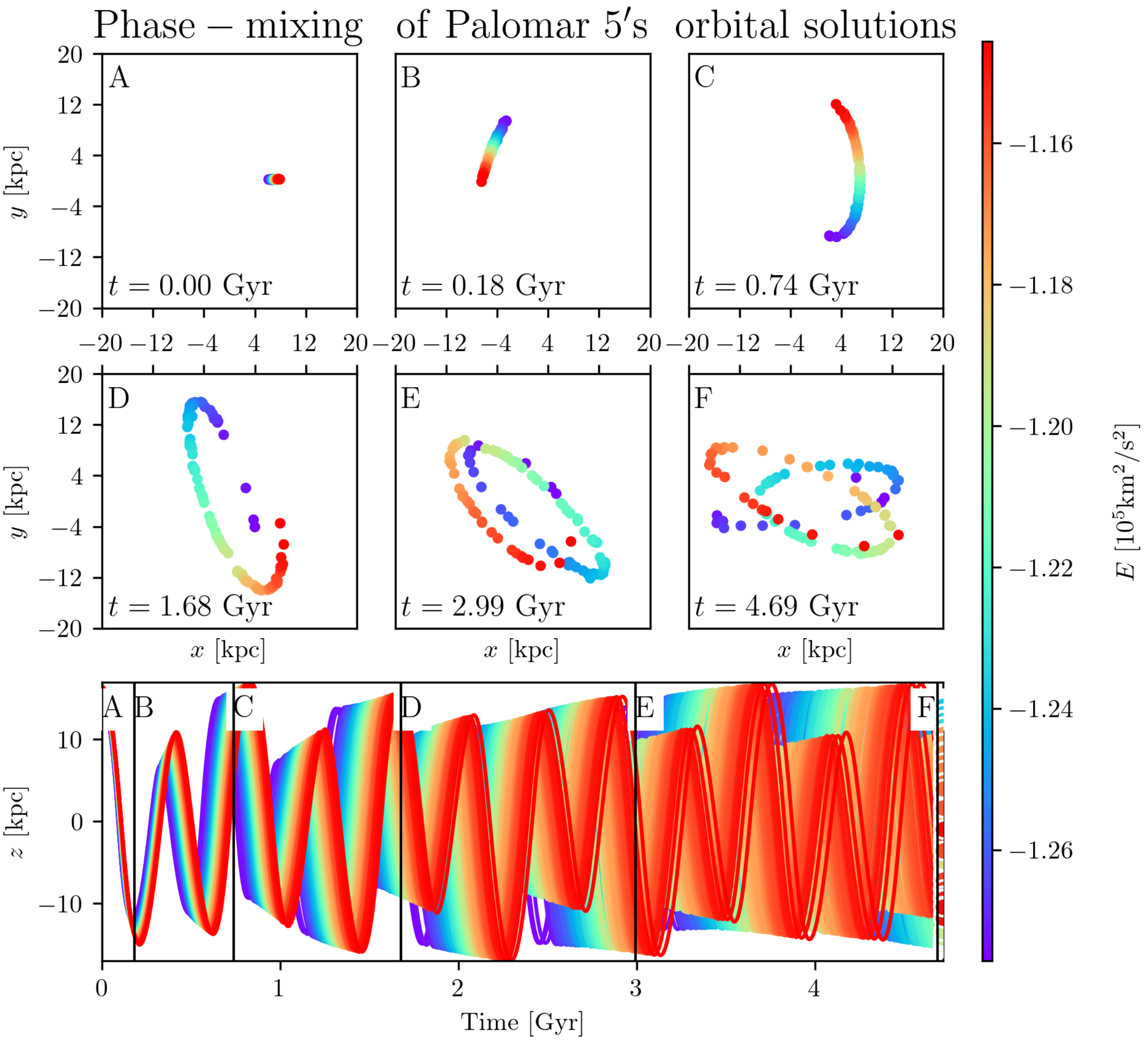

Figure 2.16 – Phase mixing of Palomar 5's orbital solutions in the bulge-less model potential of Pouliasis et al. (2017). We sample 50 different initial conditions based on the observational uncertainties in distance, radial velocity, and proper motions. Each orbital solution is color-coded by its initial total orbital energy E. The top six panels show snapshots of the positions in the xy-plane of the orbital solutions at different times. The bottom panel shows the evolution of the z coordinate as a function of time. Black vertical bars mark the timestamps corresponding to the snapshots in the top panels, which are labeled with matching alphabetical identifiers.

distances, the gravitational potential of the Milky Way becomes increasingly uncertain, as observational constraints on the Galactic mass distribution are weaker—See Fig. 2.4 (Vasiliev & Baumgardt, 2021). Therefore, these extreme mixing times should not be interpreted as implying that we can predict the phase-space location of certain clusters with high confidence over cosmological timescales. It is also informative to examine how uncertainties in orbital energy relate to uncertainties in the individual observables. In Fig. 2.18, I illustrate this with a simple calculation. The measurements of the globular clusters, along with their associated uncertainties, are reported in the ICRS. I sample the observables assuming Gaussian errors and transform the coordinates to the Galactocentric reference frame. In short, the phase-mixing time for a given set of orbital solutions and the uncertainty in the initial conditions can be interpreted as: "how long until I have no idea where this cluster is?" Beyond this timescale, the cluster's position has an equal probability of being anywhere in phase-space permitted by its integrals of motion. This concept will be important in Chapter 5, where we assess whether different possible orbits for the globular clusters could have brought them into contact with the Palomar 5 stream.

2.3.2 Mixing of globular cluster tidal debris

A cloud of points that starts tightly packed in phase space and gradually disperses provides a useful analogy for the evolution of tidally escaped stars from globular clusters into stellar streams. At first glance, Fig. 2.16 may appear to show the time evolution of a single stream, but it actually depicts different orbital solutions. The visual similarity highlights that both phenomena are governed by phase mixing.

However, there is a key distinction. The divergence of orbital solutions is a direct consequence of Liouville's theorem: the particles are non-interacting and evolve independently in a fixed potential. In contrast, stars in globular clusters are bound by their mutual gravity, which slows down phase mixing. As a result, the cluster dissolves over a longer timescale than the idealized mixing time in Eq. 2.56. Still, phase mixing governs the long-term behavior of the unbound stars.

Crucially, we do not need to model the entire cluster to study tidal debris as a phase-mixed population. For clusters with short mixing times relative to the simulation length, the escaped stars can explore the accessible phase space, even if the debris remains non-uniform and overdense near the cluster. This insight is central to the results presented in Chapter 4.

This idea is evident in Pearson, Bonaca, et al. (2024), who predict that many more stellar streams remain to be discovered in the Milky Way. They note that while about 170 globular clusters are known today, many others likely existed in the past but have since dissolved. Their tidal debris may now form stellar streams, many of which remain undetected. Indeed, most of the ∼90 known streams are unassociated with any surviving

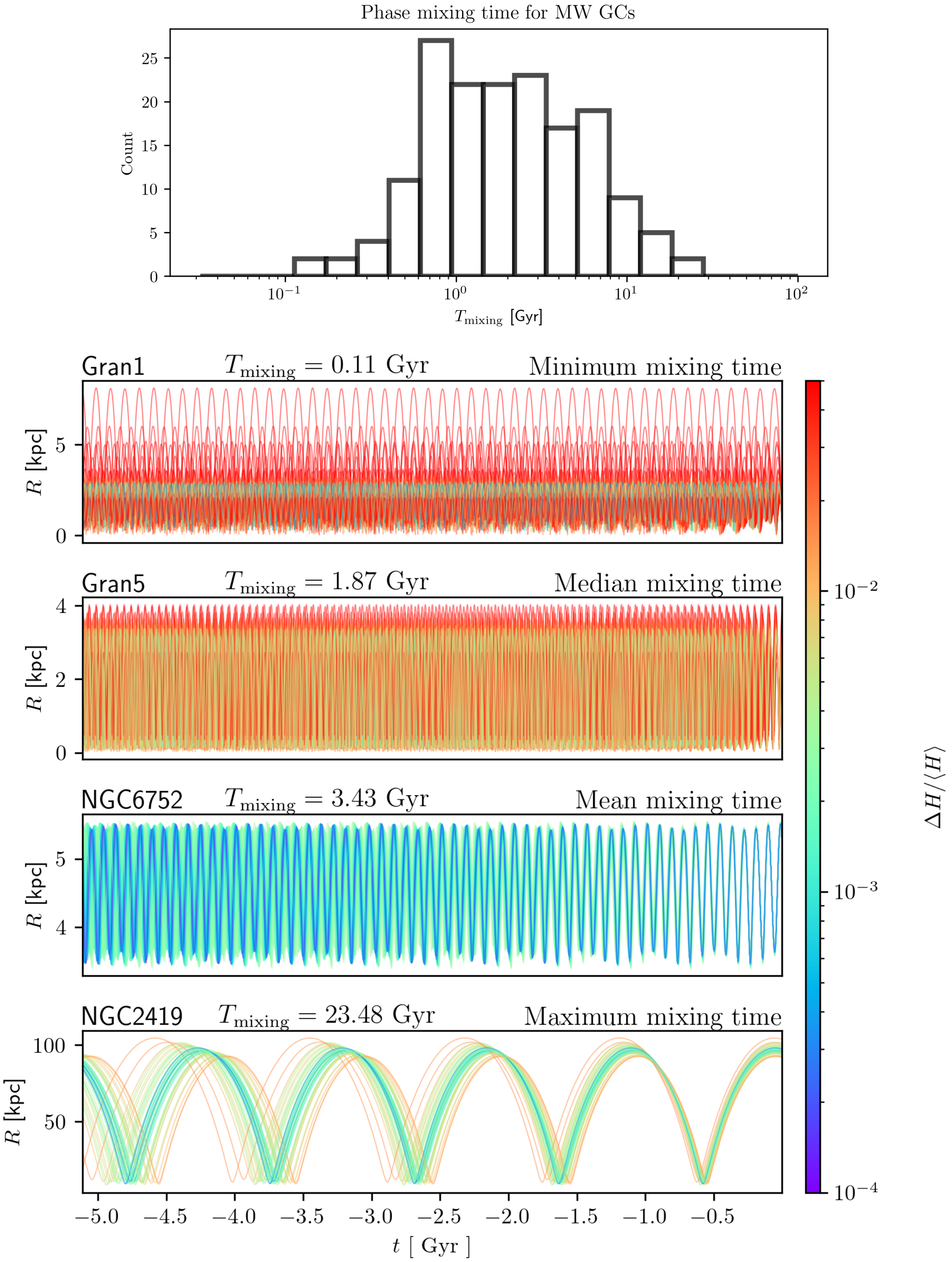

Figure 2.17 – The top panel shows the distribution of phase-mixing times for globular clusters, computed using Eq. 2.56. The following four rows illustrate the phase-mixing behavior for four selected clusters over the time range considered in this experiment. Orbital solutions are color-coded by their normalized deviation from the mean orbital energy.

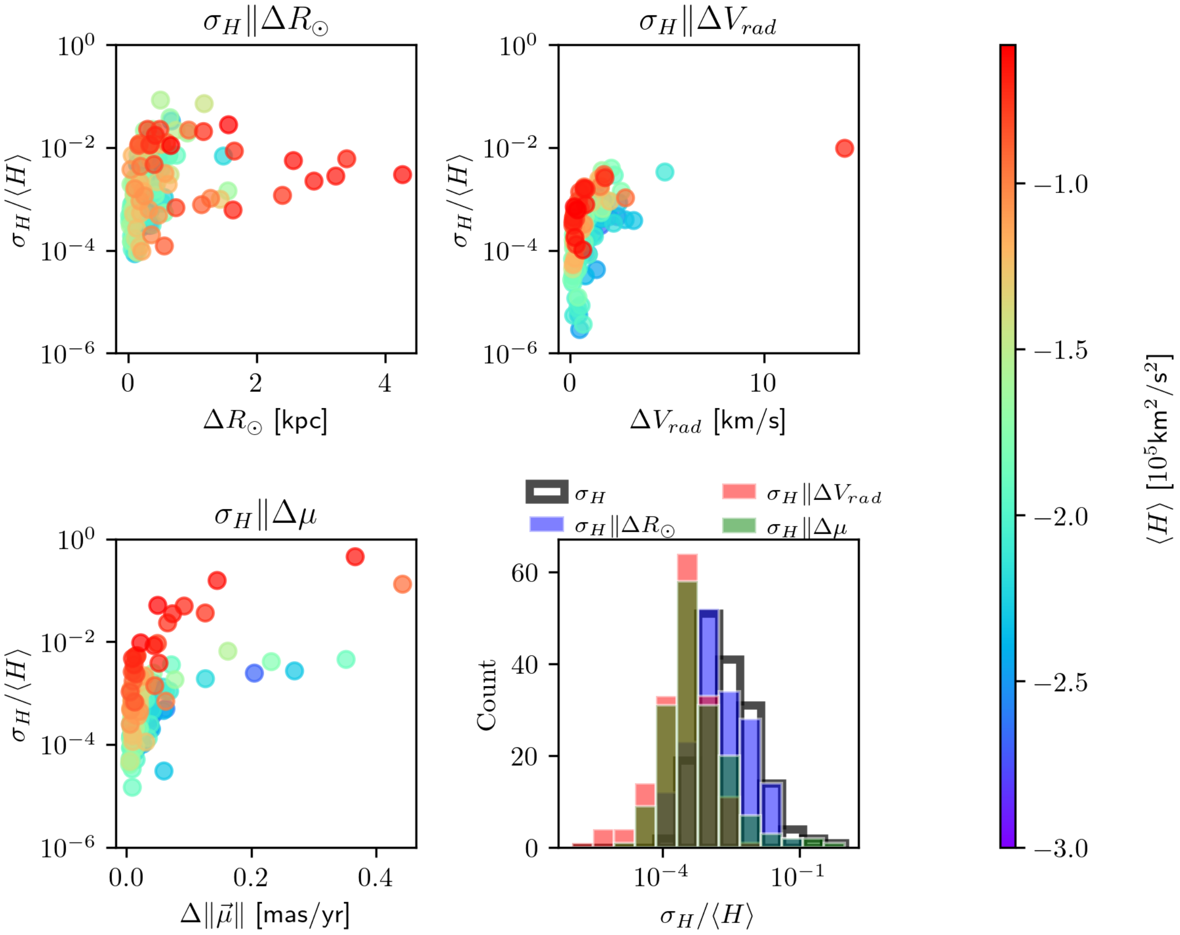

Figure 2.18 – An analysis on the spread in orbital energies of the globular cluster population for each of its reported uncertainties. Each panel finds the STD in the Hamiltonian given the uncertainties in the specific variable. So the top left allows the distances to vary but holds the proper motions and radial velocities constant. It is plotted against the distance. The clusters are color-coated by their mean energies.

globular cluster (Malhan, R. A. Ibata, Sharma, et al., 2022), and only about 20 have confirmed associations (R. Ibata, Malhan, Tenachi, et al., 2024).

To estimate the full population of globular cluster streams, Pearson, Bonaca, et al. (2024) used the IllustrisTNG simulations (Nelson et al., 2019), injecting globular clusters both formed in situ and accreted via dwarf galaxies following the prescriptions of Y. Chen & Gnedin (2022) and Y. Chen & Gnedin (2023). They then modeled the dissolution of these clusters and studied the resulting tidal debris. A panorama of their predicted streams is shown in Fig. 2.19.

To assess stream detectability, Pearson, Bonaca, et al. (2024) introduced a "streaminess" criterion based on two metrics. One is the angular distance between a stream's center of mass and the Galactic center in Galactic coordinates:

$$\Delta_0 = \sqrt{\mathrm{medn}(b)^2 + \mathrm{medn}(l)^2}.$$

A small Δ_0 indicates the debris is symmetrically distributed about the Galaxy, and thus fully phase-mixed.

Remarkably, even such fully mixed debris can still be detected as co-moving groups (Malhan & R. A. Ibata, 2018; Malhan, R. A. Ibata, Goldman, et al., 2018). Although these stars appear spatially diffuse, they continue to follow similar orbits, merely offset in phase. A striking example is the *Fimbulthul* stream, which has been linked to ω Centauri (NGC 5139), the most massive globular cluster and a suspected remnant of an accreted dwarf galaxy (Majewski, Patterson, et al., 2000; C. I. Johnson & Pilachowski, 2010). Our simulations in Chapter 4 predict that ω Centaur's debris should be fully phase-mixed and fail the "streaminess" criterion. Yet, *Fimbulthul* aligns precisely with the cluster's predicted orbit and matches N-body expectations (R. Ibata, Malhan, N. Martin, et al., 2021).

This highlights an important point: even when tidal debris is diffuse and mixed, the underlying orbital coherence can still enable its detection as a stellar stream.

2.4 Massive objects colliding with stellar streams

Previously, we described how stars escape from globular clusters, and how the escaped stars can redistribute themselves within the Galaxy under the influence of its smooth gravitational field. However, other processes can affect the stream. Notably, massive objects in the Galactic field can pass nearby and perturb the orbits of some of these stars.

For such an interaction, we may compute the change in a star-particle's momentum between before and after the encounter. We can simplify the scenario by assuming that the star-particle is initially at rest, and that the perturber (the subhalo) passes by with a minimum distance of approach b—the *impact parameter*.

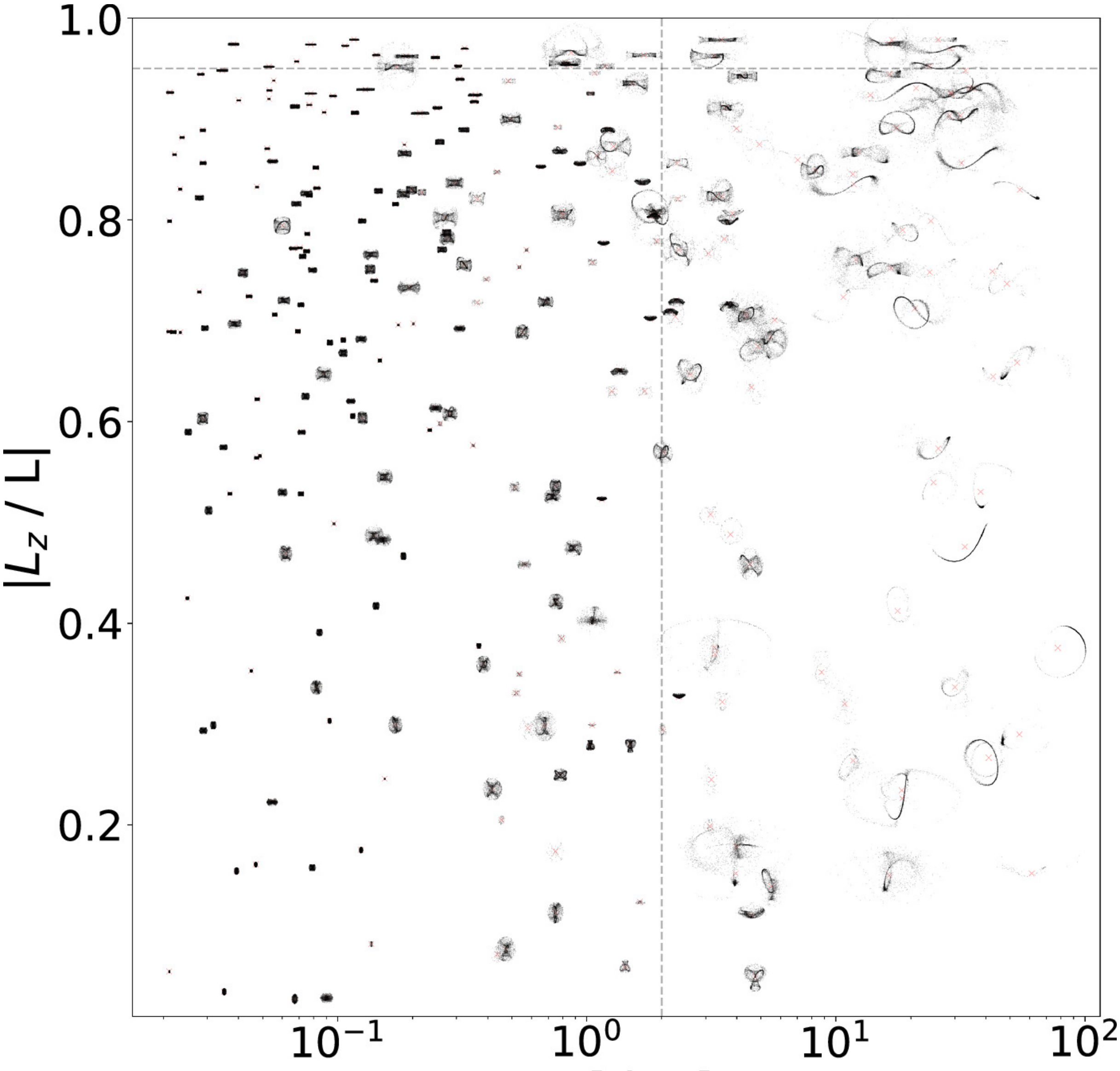

Figure 2.19 – A catalog of predicted debris from a fully disrupted population of globular clusters in a Milky Way analog. The y-axis shows the normalized z-component of angular momentum (0 = polar, 1 = planar). The x-axis shows the distance of the stream's center of mass from the Galactic center. Each stream is plotted in Galactic coordinates and to scale. The bottom-right quadrant satisfies their "streaminess" criterion. Credit: Fig. 7 of Pearson, Bonaca, et al. (2024).

Since both objects exert gravitational forces on each other, the star-particle will gain energy and begin to move, while the perturber will be slightly deflected and slow down. However, to simplify the calculation, we assume the perturber is unperturbed by the star-particle—i.e., it moves on a straight-line trajectory with constant speed v.

In this *impulse*-approximation, we compute the star-particle's change in momentum change by integrating the gravitational force over time of the interaction. Gravity is always attractive: the perturber pulls the star-particles particle to the left before the closest approach and to the right afterward. If the trajectory is symmetric and unperturbed, the components of the force parallel to the motion cancel out. Thus, the net momentum transfer is perpendicular to the motion of the perturber.

Assume the perturber moves along the x-axis with impact parameter b, and the star-particles lies at the origin. Then the net force acts in the $+y$ direction. The gravitational force scales as $1/d^2$, so for distances $d >> b$, the force becomes negligible. We can then approximate the force as roughly constant over a short time interval during the closest approach.

We estimate the duration of the interaction as the time it takes the perturber to travel a distance $2b$ (from $x = -b$ to $x = +b$), giving $\Delta t = 2b/v$. Assuming a constant perpendicular force $F_\perp \approx GMm/b^2$, the change in momentum is:

$$\begin{aligned} m\,\delta v_y &= \int F_\perp\,dt && (2.57)\\ &\approx F_\perp \cdot \Delta t && (2.58)\\ &= \frac{GMm}{b^2}\cdot\frac{2b}{v} && (2.59) \end{aligned}$$

Dividing both sides by m, the change in velocity is:

$$\delta v_y = \frac{2GM}{bv} \tag{2.60}$$

It is interesting to note that this result is inversely proportional to the velocity of the perturber. This behavior contrasts with contact collisions, where a higher speed typically results in a greater momentum transfer. In gravitational encounters, a faster flyby leads to a shorter interaction time and thus less momentum exchange.

2.4.1 Gap formation and evolution

Gaps in stellar streams are underdensities that appear after encounters with dark matter subhalos or – as we will show in Chapter 5 – globular clusters. These can be understood as resulting from collisions. However, modeling the interaction as one point mass hitting another is too simplistic. What happens when an extended object, like a subhalo, interacts with a continuous stellar stream? Before delving into the technical details, it is worth clarifying a misconception—one that I myself held when first approaching this problem. Encounters between stellar streams and perturbers are not violent collisions in which stars are physically ejected or stripped from the stream. Rather, the perturber imparts a small, localized change in velocity to nearby stars, subtly altering their orbital periods. Over time, these tiny shifts accumulate, causing stars to drift apart and gradually sculpting a visible underdensity: the gap.

To address this, we turn to the work of Erkal & Belokurov (2015), who studied a simplified model: a stream with uniform density on a circular orbit. This idealized setup allows for an analytical treatment of the gap's formation and evolution. A gap can be characterized by two main quantities: its angular width, $\Delta\theta$, and the density contrast, $\rho_{\text{peak}}/\rho_0$, between the overdensities at the gap's edges and the central underdensity.

To understand how these evolve, the authors derived a parameterization of the change in velocity $\Delta\vec{v}$ for stars along the stream after a perturbation. This vector function depends on the position y along the stream relative to the impact point and on several parameters describing the perturber and the impact geometry:

$$\Delta\vec{v} = f(y \,|\, M, r_s, b, w_{\parallel}, w_{\perp}, \alpha),$$

where M is the impactor's mass, r_s its scale radius, b the impact parameter, $w_{\parallel}$ and $w_{\perp}$ the components of its velocity parallel and perpendicular to the stream, and α the angle between the impactor's trajectory and the (x, z)-axes.

To set up the problem, a coordinate system is defined where the stream lies along the y-axis, and the impact occurs at $y = 0$. Because the stream has spatial extent, the impactor's motion must be decomposed into parallel and perpendicular components with respect to the stream. Unlike the simpler point-mass approximation, here $\Delta\vec{v}$ generally has nonzero components in all directions. In particular, Δv_y alters the speed along the stream, while Δv_x and Δv_z displace stars out of the stream's plane. Δv_x or Δv_z can be zero if the trajectory of the impactor is parallel to the x axis or z axis, respectively.

The expression for Δv_y is:

$$\Delta v_y \left(y \,|\, M, r_s, b, w_{\parallel}, w_{\perp}\right) = -\frac{2GMw_{\perp}^2 y}{w\left[\left(b^2 + r_s^2\right) w^2 + w_{\perp}^2 y^2\right]},$$

which is an odd function of y, as expected for a gravitationally attractive force: stars ahead of the impact point ($y > 0$) are slowed down, while those behind ($y < 0$) are sped up.

Several assumptions underlie this formulation. First, the stream is approximated as a straight line, which requires the size of the impacted region to be much smaller than the orbital circumference. Second, the velocities of both the stream and the perturber are assumed constant, implying that the duration of the impact is much shorter than the

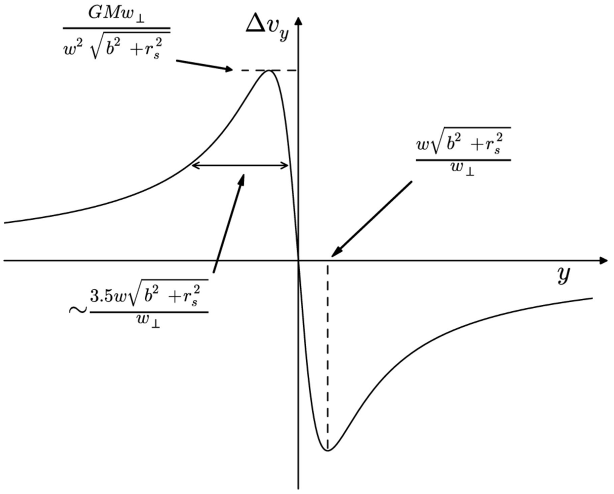

Figure 2.20 – The change in velocity, Δv_y, of stars along the stream after an impact. The stream lies along the y-axis, with the point of impact at the origin. Key features are labeled: the maximum value of Δv_y, its location, and the full width at half maximum. Taken from Fig. 3 of Erkal & Belokurov (2015).

system's orbital period. These assumptions also imply that the impactor must pass close to the stream and be compact relative to the stream's orbital radius.

The authors then developed the time evolution of the stream's density following the impact. To study these, the authors employed three complementary approaches:

1. A numerical solution of a transcendental equation governing $\Delta\theta(t)$;
2. A fully analytic solution for a low-order analytical approximation valid when the gap opening $\Delta\theta$ is still small;
3. An N-body simulation of the full system.

Together, these revealed three distinct phases of gap evolution:

1. **Compression phase** – Shortly after the impact, stars on opposite sides swap places, briefly compressing the stream until the right and left sides overtake one another.
2. **Linear growth phase** – The gap grows roughly linearly in time, as stars move apart under their velocity differences.
3. **Caustic phase** – Eventually, stars bunch up at different locations at the edges of the gap, creating sharp overdensity features ("caustics"). Additionally, the gap's growth is slowed to a sublinear rate, scaling roughly as $\propto \sqrt{t}$.

The authors make an important realization. Even in a scenario where the Galactic potential and the stream's orbit are perfectly known, there are still seven parameters that describe the shape of the gap's density profile: $M, r_s, b, w_\perp, w_\parallel, \alpha, t_{\text{impact}}$. The authors state that the gap's profile provides two additional pieces of information and, with a constraint on the perturber's density, we would still be left with four degrees of freedom. The problem is thus underdetermined and it is thus impossible to uniquely determine the properties of the perturber. A large statistical sample of gaps would be required to constrain a population of dark matter subhalos. With the ever increasing data quality, perhaps this could be possible someday.

While powerful, the authors describe how the limiting assumptions impact the interpretations of their? work. First, the framework is limited to circular orbits which poses a significant constraint especially for globular clusters which often have inclined and eccentric trajectories. Indeed, as they discussed in their work, streams do not have uniform densities. Stars that populate the streams come from tidally disrupting stellar systems. As they leave the cluster and enter the stream, they come with a range of energies and angular momenta that in essence eliminate any caustic features.

Sanders, Bovy, et al. (2016) expanded on this foundation and provided a truly exhaustive and comprehensive exploration of stream-subhalo interactions. Their primary methodological innovation was the development of a framework for modeling the impact of dark matter subhalos on cold, thin streams in angle-frequency space. This space significantly simplifies stream dynamics, allowing for the rapid generation of general stream models and proving ideal for incorporating velocity perturbations from subhalos. They developed methods to compute velocity, angle, and frequency kicks for general subhalos and impact geometries, then translated these into angle and frequency perturbations. This framework allowed for an extensive range of experiments:

- **Various perturber models**: Sanders, Bovy, et al. (2016) compared velocity kicks produced by various astrophysically relevant subhalo profiles, including Plummer, Hernquist, truncated Navarro-Frenk-White (NFW), and non-truncated NFW profiles. They found that while there are differences in kick amplitudes depending on the profile, the absolute differences between these methods were generally small, especially for lower-mass impacts, suggesting the simpler "curved approximation" (which accounts for stream curvature but assumes fixed relative velocity during flyby) is often sufficient.
- **Different Orbits for the Progenitor**: key advancement was the focus on streams formed from progenitors on eccentric orbits. This directly addressed a limitation of Erkal & Belokurov (2015), which primarily restricted its analysis to streams on circular orbits. The angle-frequency space formalism is particularly well-suited for modeling these more complex, realistic eccentric stream dynamics.
- **Different Impact Points**: The study thoroughly investigated how the stream changes depending on where along the stream the impact occurs. They simulated impacts both close to the progenitor (where particles are more mixed in energy) and further downstream (where particles are better ordered by energy), finding that the growth rate of the gap depends on the impact location.

Drawing from these comprehensive investigations, Sanders, Bovy, et al. (2016) reached several essential conclusions and insights into the physics of gaps:

- **Dominance of Frequency Kicks**: They found that angle perturbations from a flyby are generally only significant on short timescales (less than a radial period). At later times, the frequency perturbations become much more important, controlling the future structure of the gap. These frequency perturbations are simply related to the velocity perturbations (specifically, the change in energy, $v \cdot \delta v_g$) in scale-free potentials.
- **Gap Growth and Density Plateau**: While Erkal & Belokurov (2015) predicted gap growth slowing to a $t^{1/2}$ rate in the caustic phase and the central density decreasing as t^{-1}, Sanders, Bovy, et al. (2016) observed that the minimum gap density eventually plateaus in time. This plateau value decreases with increasing subhalo mass and is attributed to the stream's non-zero velocity dispersion, allowing upstream material to fill in the gap, and the non-uniform unperturbed stream density.
- **Impact Location Affects Growth Rate**: They discovered that gaps formed far downstream grow more rapidly than those closer to the progenitor. This is because stream members far from the progenitor are more "ordered" by energy, leading to an already growing underlying stream structure that enhances gap formation.

For many of the experiments, the authors cross validate the semi-analytic formalism against N-Body simulations and present truly robust results. Below, I want to show how one can understand a 1D stream.

To first order, a stellar stream can be modeled as a *collisionless*, non-accelerating ensemble of stars, i.e., a one-dimensional *streaming* solution to the collisionless Boltzmann equation. In this case, the equation simplifies to:

$$\frac{\partial f}{\partial t} + v\frac{\partial f}{\partial x} = 0, \tag{2.61}$$

where $f(x, v, t)$ is the phase-space distribution function. We assume the initial condition $f(x, v, t = 0) = 0$, and a boundary condition of a constant source at $x = 0$:

$$f(0, v, t) = g(v \mid v_0, \sigma_v) = \mathcal{N}(v \mid v_0, \sigma_v), \tag{2.62}$$

i.e., a Gaussian ejection velocity distribution centered at v_0 with dispersion σ_v. The total flux amplitude is arbitrary here.

Using the method of characteristics, we find that f is constant along lines of the form $x - vt = \text{const}$. This means we are solving a PDE in the (x, t) plane for fixed values of v. The initial condition implies that $f = 0$ in regions not yet reached by any particles —

that is, wherever $x/t > v$. Thus, the solution is:

$$f(x,v,t) = \begin{cases} \mathcal{N}(v \mid v_0, \sigma_v) & \text{if } v > \frac{x}{t}, \\ 0 & \text{otherwise.} \end{cases} \tag{2.63}$$

We can now compute the moments of this distribution. The density at each position is given by:

$$\rho(x,t) = \int_{x/t}^{\infty} f(x,v,t)\, dv = \frac{1}{2}\,\mathrm{erfc}\left(\frac{x/t - v_0}{\sqrt{2}\sigma_v}\right), \tag{2.64}$$

i.e., the integral of a truncated Gaussian. Similarly, the *mean velocity* and *velocity dispersion* at fixed (x,t) are computed from the conditional distribution $f(v|x,t) = f(x,v,t)/\rho(x,t)$, via:

$$\begin{aligned} \langle v \rangle(x,t) &= \frac{1}{\rho(x,t)} \int_{x/t}^{\infty} v f(x,v,t)\, dv, \\ \langle v^2 \rangle(x,t) &= \frac{1}{\rho(x,t)} \int_{x/t}^{\infty} v^2 f(x,v,t)\, dv, \\ \sigma_v^2(x,t) &= \langle v^2 \rangle(x,t) - \langle v \rangle(x,t)^2. \end{aligned} \tag{2.65}$$

Each of these integrals can be expressed analytically in terms of the error function and exponential functions, since they are the moments of a truncated Gaussian.

In Fig. 2.21, I show a plot of the *density*, *mean velocity*, and *velocity dispersion* as a function of position at a given time. The figure illustrates how the leading edge of the stream (larger x) contains only the fastest particles and thus has a lower density and higher average velocity. Conversely, the trailing regions have a broader mix of velocities and higher local dispersion.

Understanding the velocity dispersion within the stream is crucial for assessing the formation and persistence of gaps. In Chapter 5, we return to this point in the appendix, where—thanks to a reviewer's suggestion—we analyzed our results by exploring different internal velocity dispersions in the streams, achieved by varying the progenitor's mass. In that chapter, the velocity dispersion is not as simple as in the present case, since particles are released periodically at a rate that scales with the strength of the tidal forces. At each pericenter passage, a large number of particles are ejected, creating conditions even less favorable for gap formation, particularly in regions close to the cluster. We present this analysis in more detail in the Appendix of Chapter 5.

This section outlined the physics implicit in the equations of motion that underlie our results. Next, we explore some phenomena that were intentionally omitted and discuss how their omission limits the applicability of our findings.

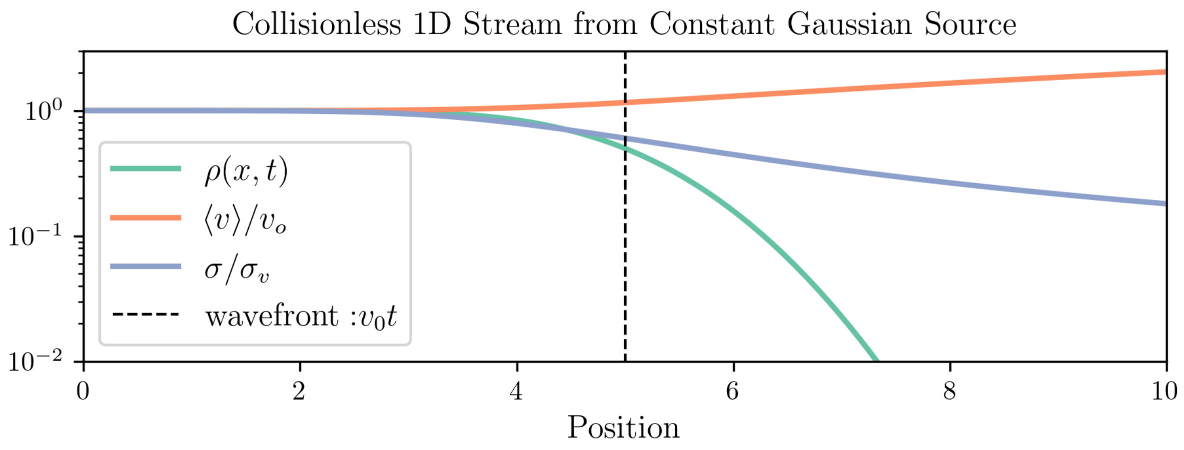

Figure 2.21 – A snapshot at a fixed time of selected moments of the distribution function describing one-dimensional collisionless streaming, used here as an approximation for a stellar stream, as given by Eq. 2.63. Particles are continuously injected at the origin with velocities drawn from a Gaussian distribution with mean v_0 and dispersion σ_v. Shown are the particle density, local mean velocity, and local velocity dispersion, all normalized.

3 The Ignored Physics

This section could, in principle, be extremely large, since much of physics is irrelevant to our specific problem—neither Schrödinger's equation nor Maxwell's equations are of concern here. But that is not the point. In the previous two sections, I presented our methods and argued for their appropriateness in studying stellar streams originating from Galactic globular clusters. Here, I want to step back and sketch the landscape of what we have chosen to ignore, and highlight other techniques used in the literature. Chief among these is treating the globular cluster as a collisional system.

I had originally considered discussing additional physical processes, such as a time-varying Milky Way potential or particle-spray methods for modeling globular cluster disruption. However, these are more properly regarded as alternative approaches rather than corrections to our framework. Thus, I limit the discussion here to internal cluster dynamics, and cite two exemplary works that demonstrate how our simulated tidal tails can differ—not only from other models, but potentially from reality itself. For discussion of a time-evolving Galactic potential and particle-spray techniques, see the concluding section on future prospects.

3.1 Globular Cluster Internal Dynamics

In this thesis, globular clusters are treated primarily as the sources of stellar streams, because our interest lies more in the streams themselves than in the internal structure of the clusters. To that end, we simplified the internal dynamics by assuming a smooth, mean-field potential, fully aware that this is a limiting assumption. We made a deliberate trade: computational efficiency at the cost of dynamical fidelity.

But how severe is this limitation? By neglecting the collisional nature of globular clusters and adopting a test-particle framework, we constrain our ability to model the rate at which stars escape, the manner of their ejection, and the identity of the stars that escape. Below, I present a basic demonstration of two-body relaxation, followed by a summary of key studies that explore the consequences of including internal cluster dynamics more fully.

3.1.1 Two-body Relaxation Time: a derivation and example

While it is appropriate to treat the orbits of stars in galaxy as collisionless, this approximation breaks down in the context of globular clusters. Here, I present a brief numerical experiment to illustrate the concept of two-body relaxation, which quantifies the breakdown of the mean-field approximation.

Two-body relaxation asks: how long does it take for the discrete, granular nature of the stellar medium to cause a star's trajectory to deviate significantly from the one it would follow in a perfectly smooth (mean-field) potential? This timescale is defined by the condition: $\delta v/v_0 \sim 1$, meaning that the change in the velocity due to the medium roughly the original speed.

In this context, we simplify the star's motion, neglecting the complexity of orbital paths in a galaxy. Instead, we consider uniform motion through a medium composed of discrete masses. If the medium consists of many small-mass particles, the potential is smoother and better approximates the mean field. If there are fewer particles with larger mass, each interaction can cause a significant deflection.

For a single interaction in the impulse approximation, the change in velocity is:

$$\delta \mathbf{v} = \frac{Gm}{bv} \begin{bmatrix} 0 \\ \cos\theta \\ \sin\theta \end{bmatrix}, \tag{2.66}$$

where b is the impact parameter, m the perturber's mass, v the relative velocity, and θ the angle in the transverse plane. These impulses deflect the star sideways but not along the direction of motion — a key assumption in the impulse approximation.

Now consider not just one fly-by, but a sequence of them. A real galaxy has a radially decreasing density, so a star never sees a symmetric distribution unless it is exactly at the center — but we are interested in fluctuations from the mean field, not the mean field itself. That is, if $\Phi_{\mathrm{MW}} = \Phi_{\mathrm{mean}}(\vec{r}) + \Phi_{\mathrm{stochastic}}(\vec{r})$, we are isolating the stochastic part.

To simplify further, we idealize the galaxy as a cylinder of radius and length R, with uniform number density $n = N_p/(\pi R^3)$. As the star moves through this medium, we

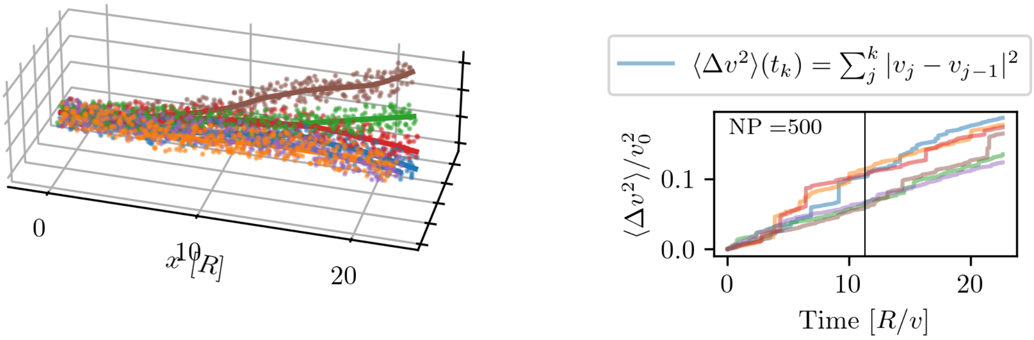

Figure 2.22 – Demonstration of two-body relaxation. A star travels through a medium with uniform number density ($n = 500/\pi R^3$). Six independent trajectories are shown, each sampling a different realization of the same underlying number density. Particles are generated on-the-fly as the star moves. The right panel shows the cumulative squared change in velocity. The vertical line indicates the theoretical two-body relaxation time

apply Eq. 2.66 to compute cumulative velocity kicks. This is demonstrated numerically in Fig. 2.22. To perform this experiment, I normalize units such that $G = M = R = t_{\text{cross}} = 1$, giving $v_0 = 1$ and $m = M/N_p$. For Fig. 2.22 [6], $N_p = 500$, so the number density is $500/\pi$.

At each timestep dt, a cylindrical volume $\pi R^2 v dt$ is populated with a Poisson-sampled number of particles, where the expected number is $\langle N_{p,\text{disc}} \rangle = n\pi R^2 v dt$. Each particle contributes a velocity kick via Eq. 2.66, which is summed over time to compute the net velocity and trajectory.

I would like to present some key steps in the theoretical derivation. In this idealized model, we expect:

$$\langle \delta \mathbf{v} \rangle = \mathbf{0}, \tag{2.67}$$

since the medium is isotropic and random, so kicks cancel on average. However, the mean squared change is non-zero:

$$\left\langle \delta v^2 \right\rangle \neq 0. \tag{2.68}$$

$\langle \delta v^2 \rangle$ can be found by reasoning on the number of expected interactions from each shell of a cylinder, where the volume infinitesimal is: $r d\theta dr (v dt)$. We find that this *diffusion*

---

[6] The two-body relaxation experiment is purely illustrative. Despite multiple attempts, I was unable to make the numerical results consistent with the theoretical prediction. Not only is the relaxation process significantly slower than expected, but the discrepancy also worsens with increasing particle number. I rewrote the script several times but was unable to identify the issue. Nonetheless, the main takeaway remains valid: gravitational two-body encounters induce a random walk in velocity space.

grows linearly with time, and its rate of change gives the two-body relaxation timescale:

$$\tau_{2-\text{body}} = \frac{v_0^2}{\frac{d\langle \delta v^2 \rangle}{dt}}. \tag{2.69}$$

Another key in this derivation is the Coulomb integral, which involves a logarithmic divergence:

$$\int \frac{1}{R}\, dR.$$

We must regularize this with appropriate limits. The upper limit is the system size (no perturbers beyond this). The lower limit corresponds to where the impulse approximation breaks down — I choose the distance at which a star becomes gravitationally bound to the perturber, though this is generous and the impulse approximation breaks down at larger distances.

The resulting expression for the two-body relaxation time is (Binney & Tremaine, 2008):

$$\tau = t_{\text{cross}} \frac{N}{8 \ln(N/2)}. \tag{2.70}$$

Let's apply this to globular clusters using their catalog values. Take the median crossing time per star as

$$t_{\text{cross}} = \sqrt{\frac{r_{1/2}^3}{GM}},$$

assuming an average stellar mass of 0.41 $M_\odot$ (Baumgardt, 1998). With this, only a handful of clusters have relaxation times greater than the 5 Gyr integration time used in our simulations. In ascending order, these include: *NGC6356, NGC5897, NGC6715, Pal4, AM1, Arp2, NGC5053, Crater, NGC5024, Pal5, NGC6101, IC4499, Pyxis, Pal3, Ter8, Pal15, Pal14, FSR1758, SagittariusII, NGC5139, NGC2419.* Across the catalog, the average relaxation time is 2.8 Gyr, the median is 1.5 Gyr, the maximum is 40 Gyr, and the minimum is 0.07 Gyr.

3.1.2 Beyond Two-Body Relaxation

Our modeling of globular cluster dissolution via the restricted three-body problem neglects internal dynamics such as two-body relaxation, binary interactions, and stellar evolution. While this simplification allows us to isolate the effects of tidal stripping, it limits the generality of our predictions. In particular, internal processes can influence both the rate and nature of stellar escape, affecting the morphology, kinematics, and observability of stellar streams.

A range of internal mechanisms can eject stars from a cluster independently of tidal forces (D. Heggie & Hut, 2003), and have been studied for decades (Lightman & Shapiro, 1978; Chernoff & Weinberg, 1990; Meylan & D. C. Heggie, 1997). For instance, binary stars are common in globular clusters, and given the high stellar densities, interactions with a third body can occur. At the end of such encounters, one of the stars may be ejected with sufficient energy to escape the cluster. This process was studied in detail by Grondin, Webb, Leigh, et al. (2023) and Grondin, Webb, J. M. M. Lane, et al. (2024), who simulated the Milky Way globular cluster system using three-body ejections rather than tidal stripping as the escape mechanism. Their results—one of which is shown in Fig. 2.23—produce a much more diffuse distribution of escaping stars than our models. In some cases, the ejection energy is sufficient to overcome the effective potential barrier entirely (see Fig. 2.7), allowing stars to escape in any direction. Some may even reach velocities above the Galactic escape speed, potentially contributing to the population of hypervelocity stars observed by Gaia (Y.-B. Li et al., 2021). Incorporating a stellar mass function introduces additional dynamical effects. One of the earliest empirical mass functions was proposed by Salpeter (1955), and a widely used modern version is the piecewise form by Kroupa (2001), which accounts for the tapering at the low-mass end. A well-known consequence of having a range of masses is *dynamical friction* (Chandrasekhar, 1943a; Chandrasekhar, 1943b; Chandrasekhar, 1943c), whereby massive stars lose orbital energy through interactions with lighter stars and sink toward the cluster center. This process leads to *mass segregation*, the tendency for massive stars to concentrate near the core. The statistical trend underlying this is toward energy equipartition, where the average kinetic energy per star is constant. Since $E \propto m\langle v^2\rangle$, this implies $\langle v^2\rangle \propto 1/m$. In real clusters, however, the relaxation time can be long, and complete equipartition may never be achieved (Bianchini, van de Ven, et al., 2016; Ziliotto et al., 2025). Moreover, tides preferentially remove stars on weakly bound (i.e., high-energy) orbits, which tend to be lower-mass stars—so tidal stripping acts as a mass filter.

Beyond assigning mass to the stars, we can consider them as actual stars, i.e., luminous, gaseous bodies in hydrostatic equilibrium. Relaxing the point-mass assumption leads to a much richer picture. Stars differ in mass, age, and composition, all of which affect their luminosities and thus their detectability. Kruijssen & Lamers (2008) showed that low-mass stars and remnants like white dwarfs are preferentially ejected from globular clusters, altering the cluster's global luminosity profile. Extending this, Balbinot & Gieles (2018) explored how internal dynamics shape the escape of stars with different luminosities and found a seemingly paradoxical result: more massive clusters can produce *less detectable* streams. The reasoning is twofold: more massive clusters retain more low-mass stars, which are intrinsically fainter, and these same stars are more likely to be stripped. As a result, even though the streams may be more massive, they are harder to detect (see Fig. 2.24). Stellar evolution affects not only the stars' luminosities but also the dynamics of the cluster. Balbinot & Gieles (2018) included stellar evolution in their simulations and showed how mass loss from evolving stars alters the cluster's potential. The most significant phase occurs in the first ∼1 Gyr, when massive stars explode as

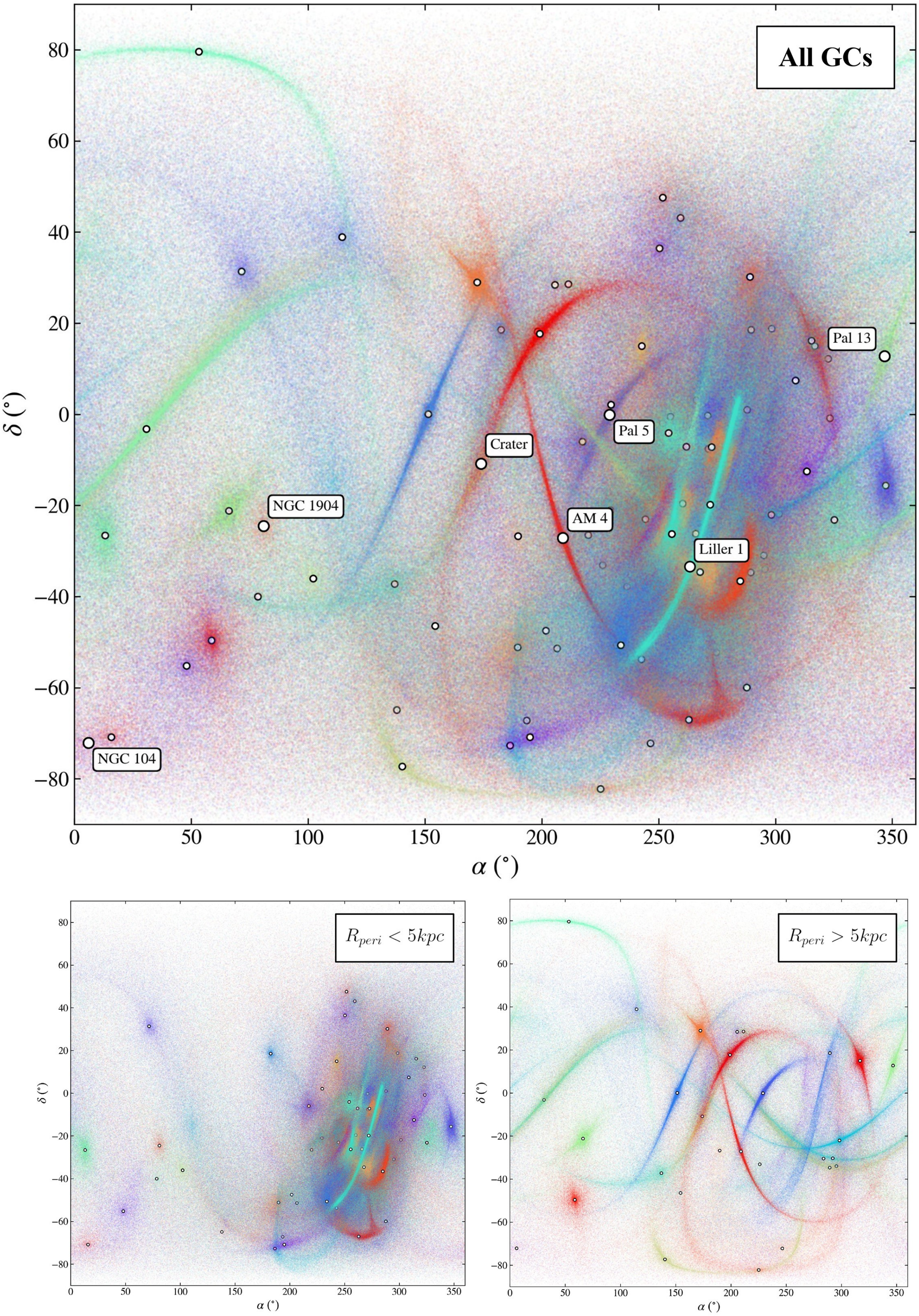

Figure 2.23 – Expected distribution of stars from the Milky Way globular clusters that are ejected from globular cluster cores via 3-body interactions. Reproduced from Grondin, Webb, J. M. M. Lane, et al. (2024).

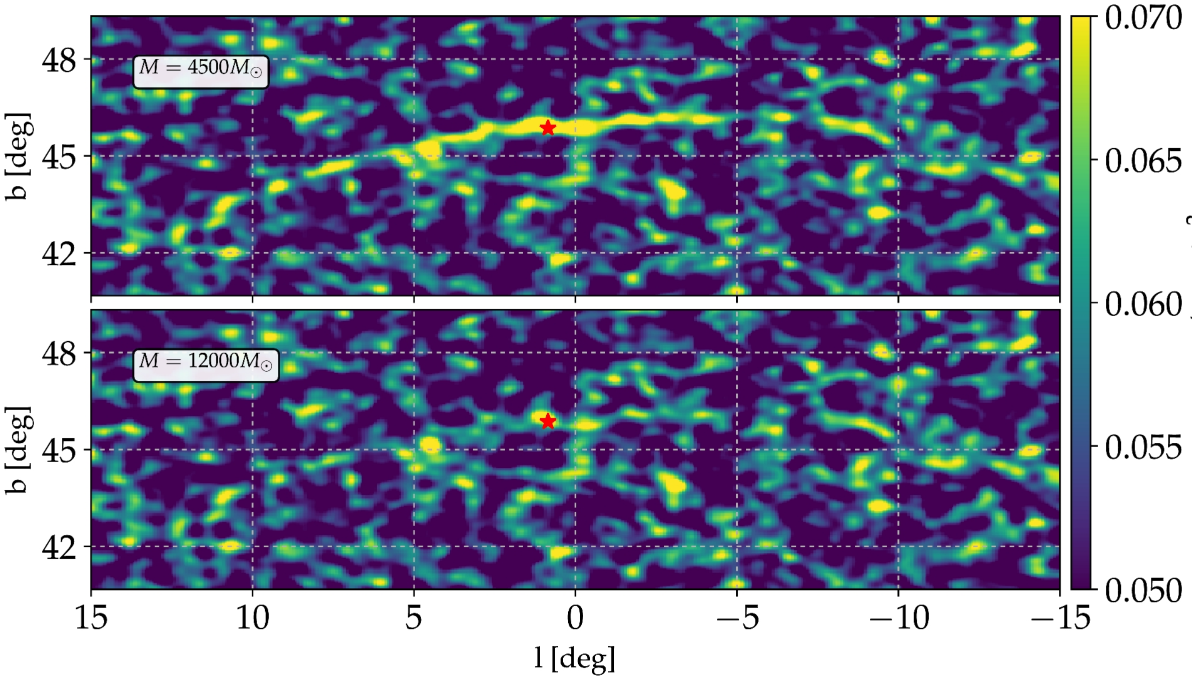

Figure 2.24 – Effects of mass-segregation on stream observability. Two different simulations of Palomar 5, one in which it's mass is artificially increased, which in turn preferentially ejects low-mass dim stars. Reproduced from (Balbinot & Gieles, 2018).

supernovae, ejecting substantial mass and weakening the cluster's potential well. Lamers et al. (2010) decomposed cluster mass loss into three stages, the first of which—driven by stellar evolution—dominates the early lifetime. If an exploding star is part of a binary, its companion may also be ejected. The extent of this effect depends strongly on both the initial mass function and metallicity of the cluster.[7]

---

[7] I once wondered whether the kinetic energy deposited by a supernova's ejecta might dynamically affect nearby stars. A quick back-of-the-envelope estimate suggests it is negligible. The mass simply puffs out of the cluster.

Chapter 3

Numerical methods

As is oftentimes the case when aiming to model realistic physical systems, the equations of motion presented here do not admit closed-form analytical solutions. As such, we must rely on numerical methods and computer simulations to solve them. Specifically, we solve N independent sets of Hamilton's equations, each consisting of six first-order, coupled differential equations.

Numerical integration presents several challenges. First, there is the practical question: how do we actually solve these equations? How can we be confident that our numerical solutions faithfully approximate the true dynamics, especially when the true solution is unknown? How do we handle performance, data volume, or the trade-offs between speed and accuracy?

To do this, I chose to write my own code, `tstrippy`, despite other codes on the market already existing (Pelupessy et al., 2013; Bovy, 2015; L. Wang, Spurzem, S. Aarseth, Nitadori, et al., 2015; Price-Whelan, 2017; Vasiliev, 2018). My motivation was part practical: I wanted to avoid installation difficulties, steep learning curves, and uncertainty over whether existing tools could implement my specific setup. But above all else, I wanted to try my hand at it.

This chapter documents how we solve the equations of motion numerically, how we validate the accuracy of the solutions, and how the code is organized under the hood.

1 Astronomical units and scaling

When writing any code, the choice of units is important. Astronomical units are rarely the same as SI units. Their creation were often times observationally and historically motivated, resulting in a system that uses multiple units for the same physical quantity, which can be confusing at first.

For instance, sky positions are typically reported in spherical coordinates. Right as-

Table 3.1 – Units for various astronomical quantities in Galactic and SI systems.

	Distance	RA	DEC	$\mathrm{v}_{\mathrm{LOS}}$	μ_α	μ_δ
Galactic:	[kpc]	[deg] [HHMMSS]	[deg]	km/s	[mas/yr]	[mas/yr]
S.I.	[m]	[rad]	[rad]	m/s	[rad/s]	[rad/s]

cension (analogous to longitude) is often expressed in either degrees or hours, while declination (similar to latitude) is given in degrees. Distances are reported in parsecs when derived from parallax measurements. Line-of-sight velocities, obtained via spectroscopic Doppler shifts, are reported in kilometers per second. Proper motions describe angular displacements over time on the sky and are usually reported in milliarcseconds per year. Already, we encounter several different units for angles (degrees, hours, arcseconds), time (years, seconds), and distance (km, kpc), none of which align with SI's standard units of radians, seconds, or meters, as summarized in Table 3.1. This raises practical concerns—for example, what would be the unit of acceleration? km/s^2? parsec/year/second? To systematically manage units, we turn to dimensional analysis, notably the Buckingham Pi theorem (Buckingham, 1914). In classical mechanics, physical quantities are typically expressed in terms of three fundamental dimensions: length, time, and mass. Any quantity can then be represented as a product of powers of these base units:

$$[\text{Quantity}] = l^a t^b m^c = \begin{bmatrix} a \\ b \\ c \end{bmatrix} \tag{3.1}$$

For example, velocity has dimensions $[1, -1, 0]$, momentum is $[1, -1, 1]$, and acceleration is $[1, -2, 0]$.

It is not strictly necessary to adopt length-time-mass as the fundamental basis, as long as the three chosen base units are linearly independent. In stellar dynamics, it is often more natural to use distance, velocity, and mass as the base units. In this thesis, we adopt:

- Distance: 1 kpc
- Velocity: 1 km/s
- Mass: 1 solar mass $\mathrm{M}_\odot$

In this system, time has derived units of:

$$[t] = \frac{\text{distance}}{\text{velocity}} = \frac{\text{kpc}}{\text{km/s}}. \tag{3.2}$$

While not immediately intuitive, this unit of time is convenient because:

$$1\text{Gyr} \approx 1 \text{ s} \cdot \frac{\text{kpc}}{\text{km}}. \tag{3.3}$$

The gravitational constant has dimensions:

$$[G] = \frac{v^2 \cdot l}{m}, \tag{3.4}$$

which evaluates numerically to:

$$G = 4.301 \times 10^{-6} \,(\text{km/s})^2 \cdot \text{kpc} \cdot \text{M}_\odot^{-1}. \tag{3.5}$$

Once the base units are defined, derived quantities such as acceleration follow directly. Whether considering acceleration as $v^2\, l^{-1}$ or $l{\cdot}t^{-2}$, they are equivalent and yield: $(\text{kpc/s})^2 \cdot \text{kpc}^{-1}$.

It is worth mentioning that N-body codes often select distance, velocity, and the gravitational constant as the base units, setting $G = 1$. While this choice simplifies force computations, it introduces less intuitive units for mass. For instance, by choosing 1 kpc for distance and 1 km/s for velocity, and setting $G = 1$, the derived mass unit becomes:

$$[\text{mass}] = \frac{l \cdot v^2}{G} = 232509 \text{ M}_\odot. \tag{3.6}$$

This approach was used in our first paper (see Chapter 4). The famous galactic dynamical python code, `Galpy`, makes a different choice and introduced *natural units* (Bovy, 2015). More specifically, Bovy (2015) uses a normalization in which R, the cylindrical scale length of the galaxy, and v_circ, the circular velocity at this radius, are both set to 1. This choice is motivated by a galaxy's rotation curve and is embodied in:

$$\frac{v_\text{circ}^2}{R_0} = \nabla\Phi\left(R_0, z = 0\right). \tag{3.7}$$

Note that the gravitational constant is also set to 1. Whatever the form of the potential, the scale lengths must be normalized to R, and the mass parameter is subsequently determined through Eq. 3.7. The total potential is a linear combination of individual components, with the user selecting the contribution of each component to the force at the characteristic radius. For example, $\Phi = \sum_i a_i \Phi_i$, where a_i are weights such that $\nabla\Phi_i(R_0, z = 0) = a_i$ in normalized units. In this system of units, emphasis is placed on the rotation curve and how much each component contributes to it at the reference radius of the galaxy. Note that $v_\text{circ}(R_0)$ is not necessarily the maximum rotational velocity.

In short, each code presents its own preferred units and normalization. `Tstrippy`, by contrast, expects the user to pass masses in solar masses, velocities in kilometers per second, and distances in kiloparsecs. However, physical constants are not hard-coded, so the user may pass any numerical values to the code as long as they are based on a self-consistent unit system. Nonetheless, the code comes equipped with parameters for the `pouliasis2017pii` potential (Pouliasis et al., 2017) and for the catalog of globular clusters (Baumgardt & Hilker, 2018) in units of kpc, km/s, and $M_\odot$.

A valid general strategy when developing numerical codes is to implement a module that converts user-defined units to the internal units. This functionality also exists in `Galpy` and a similar system is implemented in `Agama` (Vasiliev, 2018). I chose not to add such a layer to `Tstrippy` since `Astropy` provides an excellent unit-handling module that allows users to convert between units easily (Astropy Collaboration, Robitaille, et al., 2013), and I recommend its use in the documentation.

2 Solving the equations of motion

Long before the advent of computers, Euler (1707-1783) proposed a simple method for numerically solving differential equations. In this method, a solution is approximated by

$$y_{i+1} = y_i + \Delta t \frac{dy}{dt} \left(y_i, t_i\right), \tag{3.8}$$

where i is a timestep index. This means that at each point (t_i, y_i), the function is extrapolated forward using a linear approximation.

The accuracy of this method can be understood using a Taylor series expansion of the exact solution $y(t_i + \Delta t)$ about t_i:

$$y(t_i + \Delta t) = y(t_i) + \Delta t y'(t_i) + \frac{1}{2!}\Delta t^2 y''(t_i) + \ldots \tag{3.9}$$

Euler's method captures only the first two terms. The difference between the exact solution and the Euler estimate is dominated by the second-order term. Thus, the *local truncation error* (error per step) is

$$\mathrm{Err}_{\mathrm{step}} \approx \frac{1}{2}\Delta t^2 y''(t_i) = \mathcal{O}(\Delta t^2).$$

The *global error* (accumulated over many steps) is approximately the number of steps times the average error per step:

$$\mathrm{Err} \approx N_{\mathrm{step}} \cdot \langle \mathrm{Err}_{\mathrm{step}} \rangle \approx \frac{T}{\Delta t} \cdot \Delta t^2 \langle y'' \rangle = \mathcal{O}(\Delta t).$$

This means that halving the timestep roughly halves the global error.

It is important to note that using a Taylor series to estimate the error is not mathematically rigorous and not always generalizable. The actual error behavior depends strongly on the properties of the function being integrated. For instance:

- If y is linear in t, then y' is constant and Euler's method gives the exact result.
- If $y(t) = t^a$, the local errors accumulate and grow monotonically.
- If y has curvature that changes sign, local errors can partially cancel out over the course of the integration.

For a more systematic treatment of integration methods and their error properties, Chapter 16 of *Numerical Recipes in C* provides an excellent introduction (Press, Teukolsky, et al., 1992).

Regardless of the method used, sanity checks are essential to validate the result. These include:

- Trying different integration schemes.
- Performing convergence tests to ensure the solution stabilizes as $\Delta t \to 0$.
- Leveraging any known properties of the solution to verify correctness.

For example, we can exploit the properties of Hamiltonian systems to design integrators. In this thesis, we implemented the Leapfrog integrator and the Forest-Ruth scheme (Bovy, 2025a; Forest & Ruth, 1990). These schemes are derived from the structure of Hamiltonian mechanics and are known as *symplectic integrators*. Before continuing, I would like to quote (Bovy, 2025a):

> *Hamiltonian integrators are often called symplectic. This name comes from the fact that these integrators are Hamiltonian maps, whose mathematical structure is that of a vector flow on a symplectic manifold. Many fine dynamicists have made great contributions to the field without delving deeply into the meaning of the previous sentence and we do not discuss this further.*

However, my curiosity about linguistics pushed me to delve further: What does *symplectic* mean? Weyl (1946) coined the term because *complex* was already taken. The prefix Latin *com-* refers to *together*, and *plexus* comes from Greek meaning “woven” or “braided”. Symplectic translates exactly the same way: *sym-* is a Greek prefix for “together.” The idea remains the same: in Hamiltonian dynamics, the evolution of position and momentum are interdependent. This becomes clearer in matrix form:

$$\begin{bmatrix} \dot{\mathbf{q}} \\ \dot{\mathbf{p}} \end{bmatrix} = \begin{bmatrix} 0 & I_n \\ -I_n & 0 \end{bmatrix} \begin{bmatrix} \frac{\partial \mathcal{H}}{\partial \mathbf{q}} \\ \frac{\partial \mathcal{H}}{\partial \mathbf{p}} \end{bmatrix} \tag{3.10}$$

Here, the skew-symmetric symplectic matrix “weaves” the positions and momenta together.

Although the equations of motion do not admit analytical solutions, they possess several known properties. First, trajectories governed solely by gravity are time-reversible. This property is important for our methodology, where we integrate the equations of motion backward in time and then forward again to the present-day position. Secondly, the total orbital energy is conserved. Moreover, according to Liouville's theorem, Hamiltonian flows preserve the local phase space volume. A corollary of this is that the determinant of the Jacobian matrix of the transformation from $(q, p) \to (q', p')$ must be one, which means that the transformation only rotates or translates an infinitesimal volume but does not shrink or expand the volume. We can view the transform as:

$$\begin{aligned} q' &= q + \tfrac{\partial \mathcal{H}}{\partial p}\Delta t, && (3.11) \\ p' &= -\tfrac{\partial \mathcal{H}}{\partial q}\Delta t + p, && (3.12) \end{aligned}$$

The Jacobian matrix is given by $\left(\frac{\partial x_i'}{\partial x_j}\right)$:

$$\begin{bmatrix} 1 & \Delta t\frac{\partial^2\mathcal{H}}{\partial p^2} \\ -\Delta t\frac{\partial^2\mathcal{H}}{\partial q^2} & 1 \end{bmatrix} \tag{3.13}$$

and the subsequent determinant is:

$$\det(J) = 1 - \Delta t^2 \frac{\partial^2\mathcal{H}}{\partial q^2}\frac{\partial^2\mathcal{H}}{\partial p^2}. \tag{3.14}$$

In general, neither $\frac{\partial^2\mathcal{H}}{\partial q^2}$ or $\frac{\partial^2\mathcal{H}}{\partial p^2}$ are zero. There is a quick fix to this dilemma, namely, only stepping in q or p while holding the other constant. In turn, the transformation of a single step will have a Jacobian whose determinant is 1. The transformation order becomes: $(q, p) \to (q', p) \to (q', p')$. This is commonly referred to as a sequence of *drifts* and *kicks*. A *drift* updates the position while holding the momentum fixed, and a *kick* updates the momentum while holding the position fixed. Symplectic integrators alternate these operations in a specific sequence to preserve the Hamiltonian and phase space volume.

The scheme outlined above is essentially a first-order method and is closely related to Euler's method. More sophisticated integrators use values from multiple timesteps to construct higher-order estimates of the system's evolution. For example, some schemes temporarily evolve the position to an intermediate value q_{temp}, use this to compute a momentum p_{temp}, and then adjust both using weighted averages or predictor-corrector steps to reach the final state. These methods carefully balance forward and backward steps to optimize accuracy while preserving the symplectic structure.

One of the most commonly used symplectic integrators in galactic dynamics is the Leapfrog scheme. It works by interleaving updates of positions and momenta using time-centered averages. Specifically, the average momentum between q_i and q_{i+1} (denoted $p_{i+1/2}$) is used to advance the position, and then the average force (derived from the potential) is used to update the momentum. In Cartesian coordinates—used throughout this thesis—the Leapfrog algorithm can be written as:

$$
\begin{aligned}
x_{i+1/2} &= x_i + \tfrac{1}{2}\dot{x}_i\Delta t, && (3.15)\\
\ddot{x}_{i+1/2} &= -\nabla\Phi(x_{i+1/2}), && (3.16)\\
\dot{x}_{i+1} &= \dot{x}_i + \ddot{x}_{i+1/2}\Delta t, && (3.17)\\
x_{i+1} &= x_{i+1/2} + \tfrac{1}{2}\dot{x}_{i+1}\Delta t. && (3.18)
\end{aligned}
$$

As will be shown in the next section, the Leapfrog algorithm is sufficient. However, the question of computational efficiency and numerical accuracy is ever present. Leapfrog uses the two local points about the position and momenta to evolve them. Other schemes can use more points to have more accurate estimations for the local derivatives.

Forest & Ruth (1990) proposed one such method for symplectic integration. The method involves finding roots of high order polynomials which determine the distances about the local point for finding the best estimate of the derivative for evolving the system. The method involves solving a cubic polynomial to determine the optimal coefficients. While the derivation is mathematically involved, the final scheme is straightforward to implement. I implemented this method and tested its efficiency against the Leapfrog and present the results in the following section. There are eight coefficients in this method, which are presented in Table 3.2. The coefficients are all based on the solution to the cubic polynomial: $48w^3 + 24w^2 - 1 = 0$. For a single step, the positions and velocities are updated as follows:

Table 3.2 – Velocity (c_n) and acceleration (d_n) coefficients for the Forest-Ruth symplectic integrator.

Velocity coefficients (c_n)				Acceleration coefficients (d_n)			
c_1	c_2	c_3	c_4	d_1	d_2	d_3	d_4
$w + \frac{1}{2}$	$-w$	$-w$	$w + \frac{1}{2}$	$2w + 1$	$-4w - 1$	$2w + 1$	0

$$
\begin{aligned}
x' &= x + c_n v\Delta t && (3.19)\\
t' &= t + c_n\Delta t && (3.20)\\
\ddot{x} &= \nabla\Phi(x') && (3.21)\\
\dot{x}' &= \dot{x} + d_n\ddot{x}\Delta t, && (3.22)
\end{aligned}
$$

where n is the *mini-step*. Notice that the sum of $\sum_n^4 c_n$ and $\sum_n^4 d_n$ both equal 1, which is a full timestep Δt.

Lastly, it is important to note that the Leapfrog algorithm is symplectic and time-reversible only for Hamiltonians that are both time-independent and separable—that is, where the Hamiltonian can be written as a sum of a kinetic term depending only on momenta, $T(p)$, and whose potential depends only on position $\Phi(q)$. These conditions are satisfied for systems in an inertial frame with conservative forces. This is true when integrating the motion for the center of mass of the globular clusters. However, the Hamiltonian for the integration of the particles does depend on time. So the Leapfrog algorithm may introduce systematic integration errors due to the violation of its underlying assumptions, beyond ordinary rounding errors.

Similarly, when we integrate the orbits of either the particles or the globular clusters in the Galaxy containing a bar, we are faced with a choice: we can either work in a time-dependent inertial frame, where the potential rotates and the Hamiltonian explicitly depends on time, or we can transform to a rotating frame, in which case the kinetic energy becomes position-dependent due to Coriolis and centrifugal forces, which breaks the necessary criterion of separability: $\mathcal{H}(q,p) = T(p) + \Phi(q)$. In both cases, the standard assumptions of the Leapfrog algorithm are violated.

Nonetheless, we will continue to use Leapfrog as it remains a robust and efficient integrator for a wide range of astrophysical systems. Its good long-term energy conservation makes it a reasonable approximation even when the ideal assumptions are not strictly met. However, this highlights the need for careful validation: we must verify that the integration errors remain within acceptable bounds, especially in systems with non-separable or time-dependent dynamics. This validation is the subject of the next section.

3 Numerical Error and Computation Time

To ensure the quality of the integration, we perform two main checks. The first is to ensure that the initial orbital energy of a given particle is conserved to high precision. At each timestep, the relative error in the energy conservation is:

$$\mathrm{err}(E(t)) = \left| \frac{E(t) - E_0}{E_0} \right|, \tag{3.23}$$

where E_0 is the initial energy and E is the orbital energy at a given timestep t. For the case of a globular cluster, the total orbital energy is its own kinetic energy plus its gravitational potential energy in the Galaxy: $E = T(\mathbf{v}_{\mathrm{GC}}) + \Phi_{\mathrm{MW}}\left(\mathbf{x}_{\mathrm{GC}}\right)$, where $\mathbf{x}_{\mathrm{GC}}$ and $\mathbf{v}_{\mathrm{GC}}$ are the Cartesian galactocentric position and velocity of the globular cluster. For the case of the i-th star-particle within a globular cluster, the potential energy of the cluster is included: $E_i = T(\mathbf{v}_i) + \Phi_{\mathrm{MW}}\left(\mathbf{x}_i\right) + \Phi_{\mathrm{GC}}\left(\mathbf{x}_i - \mathbf{x}_{\mathrm{GC}}\right)$, where $\mathbf{x}_i$ is the position relative to the Galactic center. The same approach holds when a bar is included, the only difference being that the Galactic potential has a time-dependent element.

For potentials with the galactic bar, the total energy is not conserved but rather the Jacobi energy, and this is true only for the globular clusters since we treat them as point masses. For the star-particles, the energy is not conserved in the simulations, since they are subject to the force from the globular cluster. However, we track the energy particularly when we perform the second check, which is time-reversibility.

To check the time-reversibility, we integrate a cluster back in time, and then change the sign of its velocity to subsequently integrate forward in time. If the integration is correct, the cluster should remain on the same trajectory retracing its steps. We investigate this for the following scenarios and show the results below:

- The globular cluster population orbiting within a static Milky Way potential;
- Star-particles orbiting within a stationary and isolated globular cluster;
- Full stream generation, i.e., star particles orbiting within a globular cluster that orbits the Galaxy.

At this stage, I did not have time to perform a full quality check of orbits within the barred potential. However, I refer the reader to the `tstrippy` documentation, where I demonstrate the time-reversibility of cluster orbits in the barred potential. [1]

3.1 Globular Cluster Orbits in a Static Galaxy

The initial conditions for the globular cluster system (positions and velocities) were taken from Baumgardt & Hilker (2018)'s online globular cluster catalog whose data derived from Gaia Early Data Release 3 among other sources (Baumgardt & Vasiliev, 2021; Gaia Collaboration, Brown, Vallenari, Prusti, de Bruijne, Babusiaux, Biermann, et al., 2021a; Vasiliev & Baumgardt, 2021; Gaia Collaboration, Vallenari, et al., 2023).

To test the integrator, we integrated the whole globular cluster system for 5 Gyr, and then integrated it back to the initial conditions. We used four timesteps: $10^4, 10^5, 10^6, 10^7$ years which corresponds to $[500, 5000, 50000, 500000]$ integration steps, respectively. In general, the timestep should scale with the dynamical time of the orbit. In other words, the timestep should be inversely proportional to the orbital energy. The further the system is from the galactic center, a larger timestep can be used to obtain a given numerical error.

Of course, the timestep does not just simply scale with a body's orbital energy, it should scale with the maximum acceleration experienced in the system. A highly eccentric orbit requires a smaller timestep to properly integrate the motion near the pericenter, compared to a circular orbit at the same orbital energy. To not clutter the graph, Fig. 3.1 only present the whole globular cluster system twice, once integrated with the smallest timestep, 10^4 years, and once with the largest timestep: 10^7 years.

---

[1] `https://tstrippy.readthedocs.io/en/latest/reverse_integrability_bar.html`.

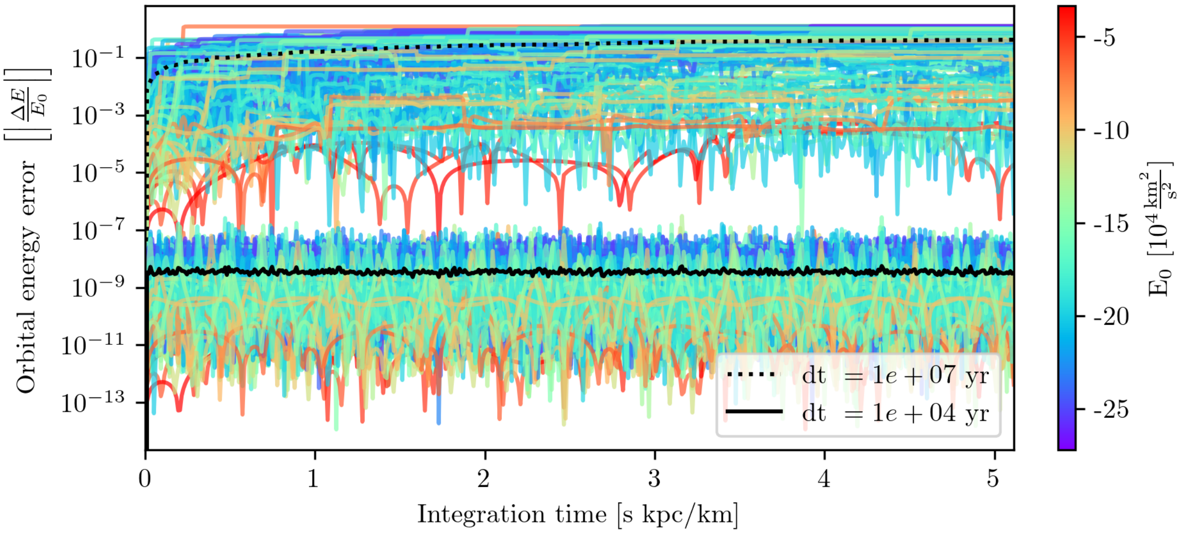

Figure 3.1 – Relative error in orbital energy for the whole globular cluster system with two different timesteps, dt = 10^7 and 10^4 years. Each cluster's is colored by its initial orbital energy. The average of the whole system for a given timestep is indicated with dotted and solid black lines, respectively.

In Fig. 3.1 we can notice that orbits with higher orbital energies (in red) have low numerical error compared to those with lower energies (in blue), which penetrate deeper in the potential well. It is clear that, for the whole system, 10^7 years is a timestep that is far too large, however, interestingly enough, for some of the farthest globular clusters, a timestep of 10 million years resolves their orbits to an error of $\langle \Delta E/E_0 \rangle \sim 10^{-5}$, which is still far less than the uncertainties due to observational uncertainties. Note that in both cases, the errors neither accumulate nor grow with time. This is a testament to the quality of the Leapfrog integration scheme, which is designed to conserve the Hamiltonian accurately.

Fig. 3.2 illustrates the *time reversibility* of the integrator, i.e., its ability to retrace its own steps. For each timestep, I compute the difference between the forward integration and the backward retrace, normalizing to the mean of the two positions. The same computation is performed for the velocities. Specifically, I take the current kinematics of each cluster and integrate them forward in time for five billion years, storing positions and velocities at each step. Starting from the final state, I then integrate backward for the same duration, again recording positions and velocities at every step. At each corresponding time stamp t_i, I calculate the vector differences in position and velocity, normalizing the positional error to the mean position of the forward and backward steps.

The timestep of 10^7 yr saturates only after 2 Gyr. The distances do not continue to grow because the orbital energy only differs by one part in ten, so at later timesteps, the cluster is still within the same region of phase-space, but the retrace is at a completely

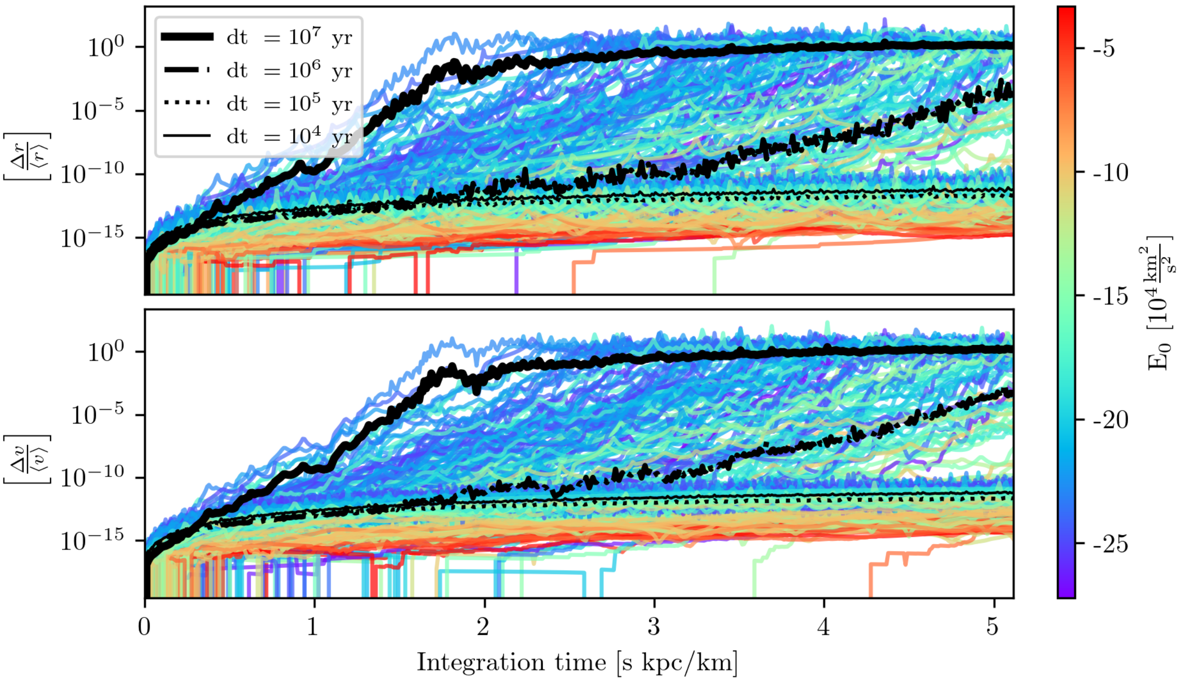

Figure 3.2 – The *time-reversibility* of the Leapfrog scheme for the 165 Galactic globular cluster's for four different timesteps indicated in the legend. The whole system is only shown for 10^4 yr and 10^7 yr to avoid clutter. The clusters are color-coded to their initial orbital energy just as Fig. 3.1

different location than the initial integration. The errors in the timestep of 10^6 yr become significant, though by the end of the integration period of 5 Gyr they are still only one part in ten thousand. The timesteps of 10^5 and 10^4 yr have excellent retraceability and on average, only differ by one part in 10^{-14}, and are thus only limited by round off error from the use of double precision floating point numbers.

Computation time is quite important. Fig. 3.3 presents the total computation time of integrating the globular cluster system, and the time of a single integration step, which is computed by normalizing the total time by the number of objects and number of steps taken: $T_{\text{total}}/N_{\text{GCs}}/N_{\text{steps}}$. In general, the relationship is linear and the integration time per step per object is roughly constant. The downward trend presented in Fig. 3.3 is in part a coincidence, as some time realizations minimize this, and in part due to the overhead computation time with initializing and finalizing the calculation contributes less and less with increasing integration time. Nonetheless, for this processor (Apple M2 processor), for a single integration step the mean time is ~ 128 nanoseconds.

The Ruth-Forest algorithm discussed in the previous section was implemented and is reported in Fig. 3.4. Here, as expected, we see that the precision greatly increases when decreasing the timestep. However, since there are four force evaluations for a single timestep, this method is naturally slower per step than Leapfrog. How do the two methods

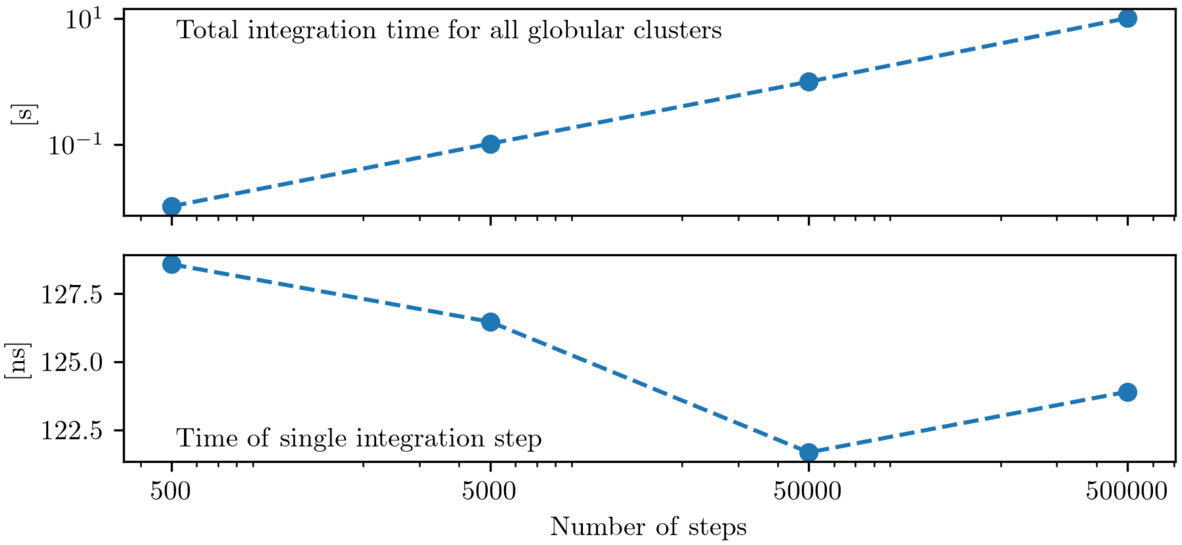

Figure 3.3 – Computation time for integrating the entire globular cluster system using the Leapfrog scheme. The top panel shows the total time while the bottom shows computation time for a single step, for a single object being integrated. This was performed on a 2022 MacBook Air with an Apple M2 processor.

compare over all? Fig. 3.5 compares the numerical error for again the total number of steps (which is inversely proportional to the timestep). It is clear that, for a given step size, the Ruth-forest outperforms the Leapfrog, but is it actually better? To answer this question, I fit the two curves with their own trend lines to find the number of steps required to have a relative error of 10^{-8}. With this requirement, The Leapfrog scheme requires 262,641 steps while the Ruth-Forest scheme requires 102,773 steps. However, given the difference in computation time per step, on average, the Forest-Ruth scheme takes $\sim$ 1.5x more time for the same degree of numerical precision than the Leapfrog. For this reason, we use the Leapfrog algorithm. In this problem, numerical uncertainties are must less of a limiting factor compared to modeling uncertainties and observational uncertainties, so a better integrator for numerical precision is not worth the pay off of longer computation times.

3.2 Star-particles in a static globular cluster

A classic challenge in astronomy and the physical sciences arises when a problem involves two or more physical processes that operate on very different time scales. This is certainly the case when studying globular clusters. Figure 3.6 illustrates the orders-of-magnitude differences in time scales both across the globular cluster population and within individual clusters.

A useful metric for characterizing a system's time scale is the *crossing time*, which is

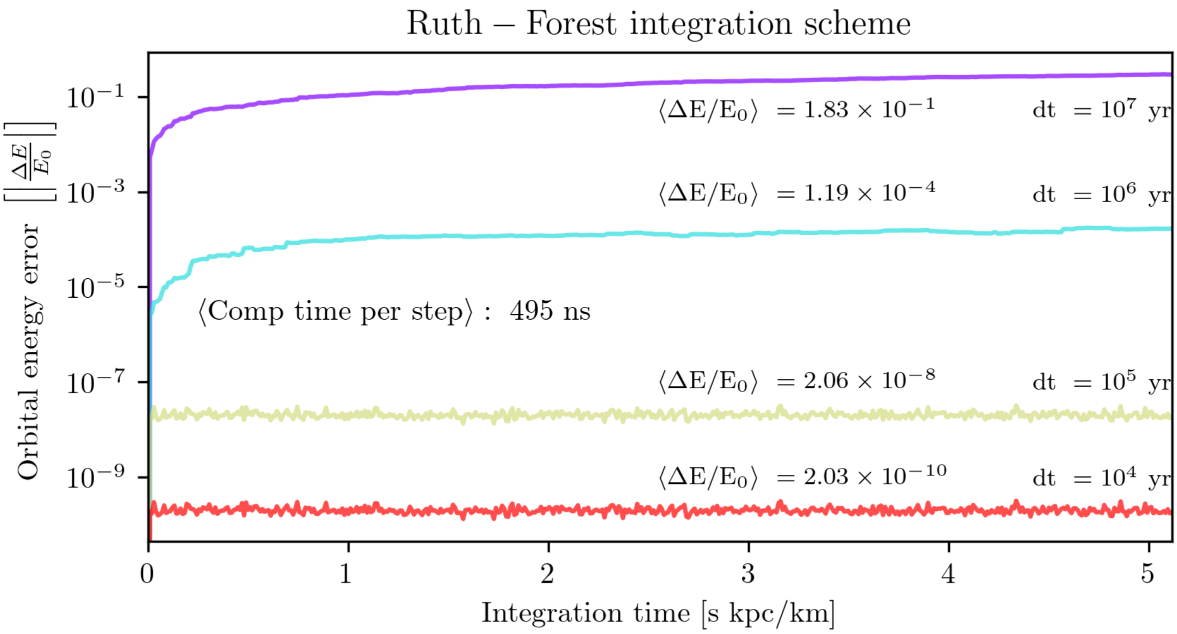

Figure 3.4 – The conservation of energy error for the Ruth-Forest integration scheme for the globular cluster system. This plot is similar to Fig. 3.1, but does not present on the whole globular cluster system, just the average error in energy for the whole system with a given timestep. The timestep and time-average numerical error for the whole system is presented next to each curve. The average computation time per integration step per single object is as well.

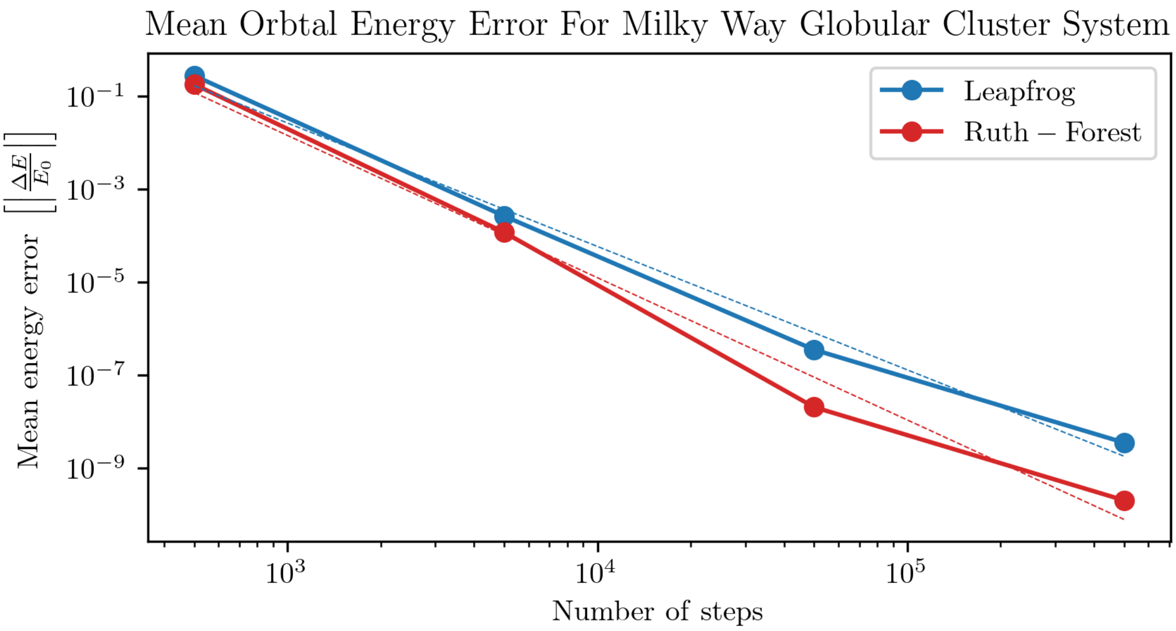

Figure 3.5 – The time averaged error in the conservation of energy for the entire globular cluster system for four different timesteps, for two different integration techniques: the Leapfrog against the Ruth-Forest. Their respective trend lines are shown.

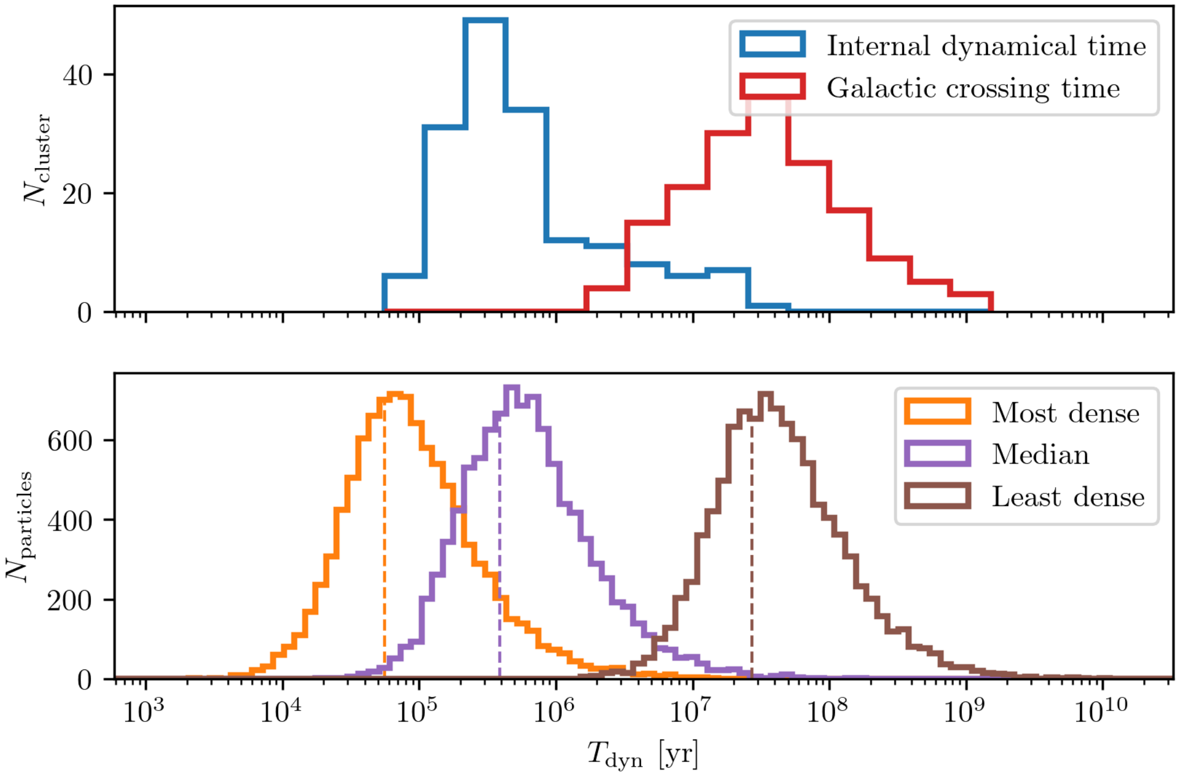

Figure 3.6 – The top panel shows orbital characteristic times of the globular cluster system, while the bottom panel shows internal characteristic times for three selected clusters. *Top*: The red distribution shows the orbital crossing time of each cluster within the Galaxy, while the blue distribution shows a characteristic internal dynamical time. *Bottom*: The distribution of crossing times for 1,000 sampled star particles within the globular clusters with the smallest, median, and largest internal dynamical times. The vertical dashed lines mark the characteristic internal dynamical times.

the time it would take a star to reach the center of the system given its current speed:

$$t_{\text{cross}} = \frac{r}{v}. \tag{3.24}$$

While this quantity is not an integral of motion and varies as a star moves, it still provides a convenient and informative estimate of the dynamical time scale. It breaks down in extreme cases, such as a purely radial orbit near pericenter or apocenter where the instantaneous velocity approaches zero, but such cases are rare and do not undermine its utility. We compute the crossing time for each globular cluster in the galaxy (red distribution in the top panel of Fig. 3.6) as well as for each individual star particle within the clusters.

For the cluster as a whole, a robust characteristic dynamical time can be defined as:

$$\tau = \sqrt{\frac{a^3}{GM}}, \tag{3.25}$$

where a is a characteristic size of the system. This is often taken to be the half-mass radius. In this work, I adopt the half-mass radius rather than the Plummer scale radius, though the two are related by $r_{1/2} \approx 1.3a$. This time scale was computed for each cluster and is shown as the blue distribution in the top panel of Fig. 3.6.

Note that the distribution of cluster dynamical times has a long tail toward longer values, overlapping with the galactic crossing times. A natural question arises: could any cluster have a longer internal dynamical time than its orbital crossing time? The answer should be *no*. If it takes longer for stars to orbit within the cluster than for the entire cluster to orbit the Galaxy, the cluster is effectively unbound or fully disrupted. I examined this question for the Galactic globular cluster population, and the results are shown in Fig. 3.7. As expected, all clusters have internal dynamical times shorter than their orbital crossing times.

Interestingly, the ratio of these two time scales serves as a useful diagnostic of cluster stability. Clusters in which stars complete hundreds or thousands of internal orbits per galactic orbit are significantly more stable than those where stars complete only a few.

To properly compute the orbits of the star particles, the timestep must be small enough to resolve the orbit accurately while the star is inside the cluster. How should we choose this timestep? There are two criteria. The first is that the timestep should be some fraction of the cluster's dynamical time:

$$\Delta t' = \alpha' \tau. \tag{3.26}$$

I use a prime to indicate that this is a trial timestep, since the second criterion must also

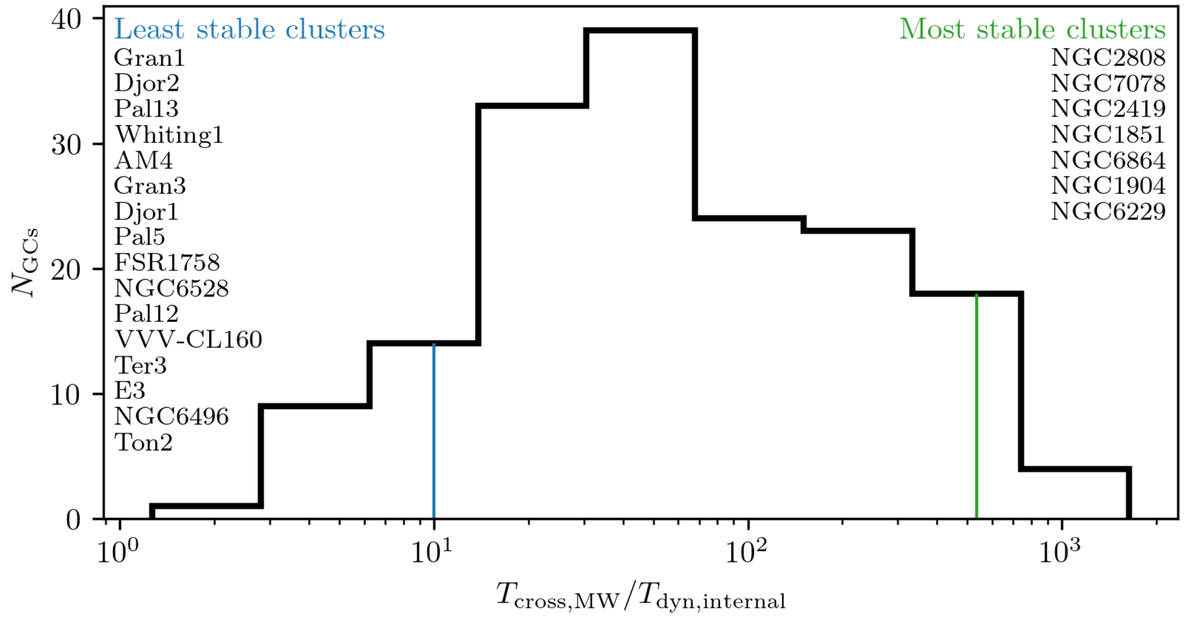

Figure 3.7 – Ratio of each globular cluster's galactic crossing time to its internal dynamical time (as shown individually in the top panel of Fig. 3.6). Clusters whose internal dynamical times approach their galactic crossing times are near disruption. In contrast, denser clusters with much shorter internal times are more stable. The vertical bars indicate selected thresholds. Both lists rank clusters by increasing stability, with Gran 1 being the least stable and NGC 6229 the most.

be satisfied: the total number of timesteps should be an integer,

$$N = \left\lceil \frac{T}{\alpha' \tau} \right\rceil,$$

where T is the total integration time. We round N up to ensure a slightly smaller timestep, which becomes $\Delta t = T/N$. This also redefines the effective timestep fraction as $\alpha = \Delta t/\tau$.

In the experiments presented in this section, I choose several fractions of each cluster's dynamical time and examine the resulting numerical errors. To efficiently explore a wide range of α, I begin with a few trial values of α' and then round the number of steps down so that N is not only an integer, but also a power of two. This leads to the following condition:

$$N = 2^{k-1} \tag{3.27}$$

where $k \in \mathbb{N}$ is an integer index. The expression for k becomes:

$$k = \left\lceil \log_2 \left(\frac{T}{\alpha' \tau_{\rm dyn}} \right) + 1 \right\rceil. \tag{3.28}$$

The goal is now to determine the appropriate value of α to ensure energy conservation and time-reversibility. In the analysis presented in the previous sections, I selected timesteps without explicitly relating them to the crossing times of globular cluster orbits. Fig. 3.1 shows that a timestep of $\Delta t = 10^4$ yr achieves a mean relative energy error of 10^{-8}. Meanwhile, Fig. 3.2 shows that a timestep of $\Delta t = 10^5$ yr already achieves convergence in time-reversibility. Comparing these values to the typical crossing time shown in Fig. 3.6, we find that they correspond to α values of approximately 2×10^{-4} and 2×10^{-3}, respectively.

In Fig. 3.8, I investigate energy conservation in a static Plummer sphere using trial values of $\alpha \in [10^{-4}, 10^{-3}, 10^{-2}, 10^{-1}, 1, 2]$. This experiment shows that values of $\alpha < 10^{-2}$ yield excellent energy conservation. In this section, we do not consider the time-reversibility as the previous section has shown the integration's robustness with regard to this metric. However, this is our main metric for the next section.

3.3 Full stream generation

The preceding sections assessed the numerical stability of integrating globular cluster orbits within the Milky Way, focusing on time-reversibility and relative energy error across two integration schemes: Leapfrog and Forest-Ruth. I also considered the computational cost associated with different temporal resolutions. Separately, I evaluated the energy conservation for star particles evolving within a stationary Plummer sphere, quantifying the relative error as a function of timestep. In that context, the cluster's potential was scaled to its scale radius, mass, and the gravitational constant. This non-

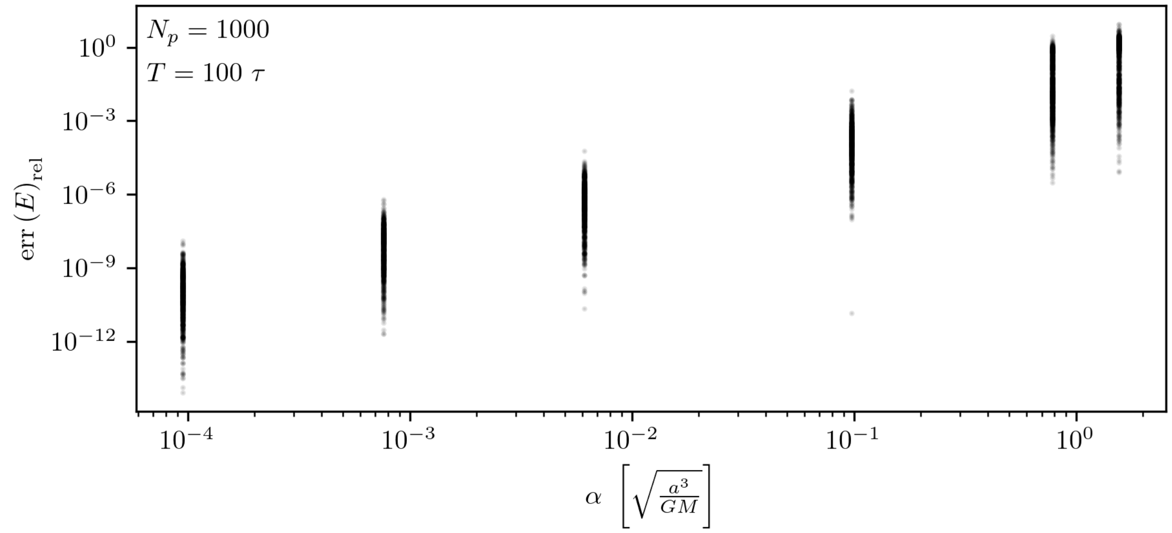

Figure 3.8 – Relative orbital energy for an isolated Plummer sphere evolved with different timesteps. Each model contains the same number of particles, N_p, and is integrated for the same duration, T, as indicated on the plot. The x-axis shows the timestep size α, defined as a fraction of the internal dynamical time $\tau = \sqrt{a^3/GM}$.

dimensionalization allowed me to select timesteps as fractions of the internal dynamical time τ of each cluster.

In this section, I combine them: I examine the quality of orbit integration for star particles evolving within a globular cluster, which in turn is orbiting in the Galactic potential.

I restrict the analysis here to the Leapfrog integrator for two main reasons. First, although the Forest-Ruth scheme achieves better energy conservation (see Fig. 3.5), this comes at a significantly higher computational cost, which outweighs its marginal gains for this application. Second, the equations of motion used to model stream generation require loading the position of the host cluster for each force computation. Because Forest-Ruth evaluates forces at non-uniform substeps, using it would require either: (1) storing and loading the cluster orbit at each substep, which would demand excessive disk space and complex code restructuring; or (2) interpolating the orbit at intermediate times, which introduces ambiguity regarding whether time-reversibility is preserved with linear or cubic interpolation. For these reasons, I opted not to explore Forest-Ruth further in the context of full stream generation.

To assess the performance of the stream-generation method, I designed a quality assurance experiment, illustrated in Fig. 3.9. I began by integrating the orbit of a globular cluster's center of mass backward in time by 1 Gyr. At that point, I initialized a Plummer sphere with 512 star particles using the cluster's half-mass radius and total mass. This system was translated to the center-of-mass phase-space coordinates and then integrated forward to the present day, forming a stream. I recorded the resulting positions and computation time. To test time-reversibility, I subsequently integrated the stream particles backward again for 1 Gyr.

A note on terminology: although the cluster orbit is initialized from present-day observations, in the context of stream generation, I refer to the past position (1 Gyr ago) as the “initial conditions”. The forward-integrated system represents the “stream”, and the backward-integrated version of the stream is referred to as the “retrace”.

Fig. 3.9 shows the results for four different timesteps. As expected, increasing the timestep degrades time-reversibility. For the largest timestep ($\alpha \approx 1$, top left), the retrace fails to recover the original configuration. The retraced structure remains a stream and does not re-coalesce into a cluster. The results improve rapidly with decreasing timestep: at $\alpha \approx 2 \times 10^{-1}$, most particles return close to their starting positions with only slight offsets. At $\alpha \approx 2 \times 10^{-2}$, nearly all particles recover their initial conditions, and by $\alpha \approx 6 \times 10^{-3}$, the retrace is nearly perfect.

Fig. 3.10 presents the integrator’s energy conservation performance during the retrace phase of Fig. 3.9, across the same timesteps.

Although the retrace fails for the largest timestep in Fig. 3.9, Fig. 3.10 shows that the relative energy error remains modest—between 10^{-4} and 10^{-2}. However, this metric requires careful interpretation. What appears as an “error” primarily reflects the intrinsic spread in orbital energies among star particles, relative to the center-of-mass energy.

We can estimate this ratio by comparing the internal potential energy scale of the cluster to its orbital energy in the Galaxy. The cluster’s characteristic potential is roughly $\Phi \sim GM/a$, with $M \sim 10^5\ M_\odot$ and $a \sim 0.005$ kpc, giving $\Phi \sim 10^2\ \mathrm{km}^2\,\mathrm{s}^{-2}$. Meanwhile, the typical orbital energy of a globular cluster is around $10^5\ \mathrm{km}^2\,\mathrm{s}^{-2}$.

This three-order-of-magnitude difference implies that the intrinsic energy spread from the Plummer sampling is about 10^{-3} of the total orbital energy, which is consistent with the the apparent energy “error” in the stream of Fig. 3.10. Thus, this differences does not arise from numerical drift, but from the physical energy distribution encoded in the initial conditions.

Fig. 3.9 & Fig. 3.10 demonstrate the case of a single cluster. How is the energy conservation for the entire catalog? Fig. 3.11 presents the relative error in the conservation of energy for retracing the orbit of each individual star particle per globular cluster for each cluster in the catalog. Each data point reports the mean error in the conservation of energy. Each cluster was integrated for 5 Gyr. The upper limits for the timesteps were sampled logarithmically between 10^0 and 10^{-2}, the exact timesteps are based on the criterion from Eq. 3.28.

The quality of the solutions is fundamental for proper results. However, computation time and cost is also very important. The main motivation in using the restricted three body problem was to save computation time. With N body, the computation time should

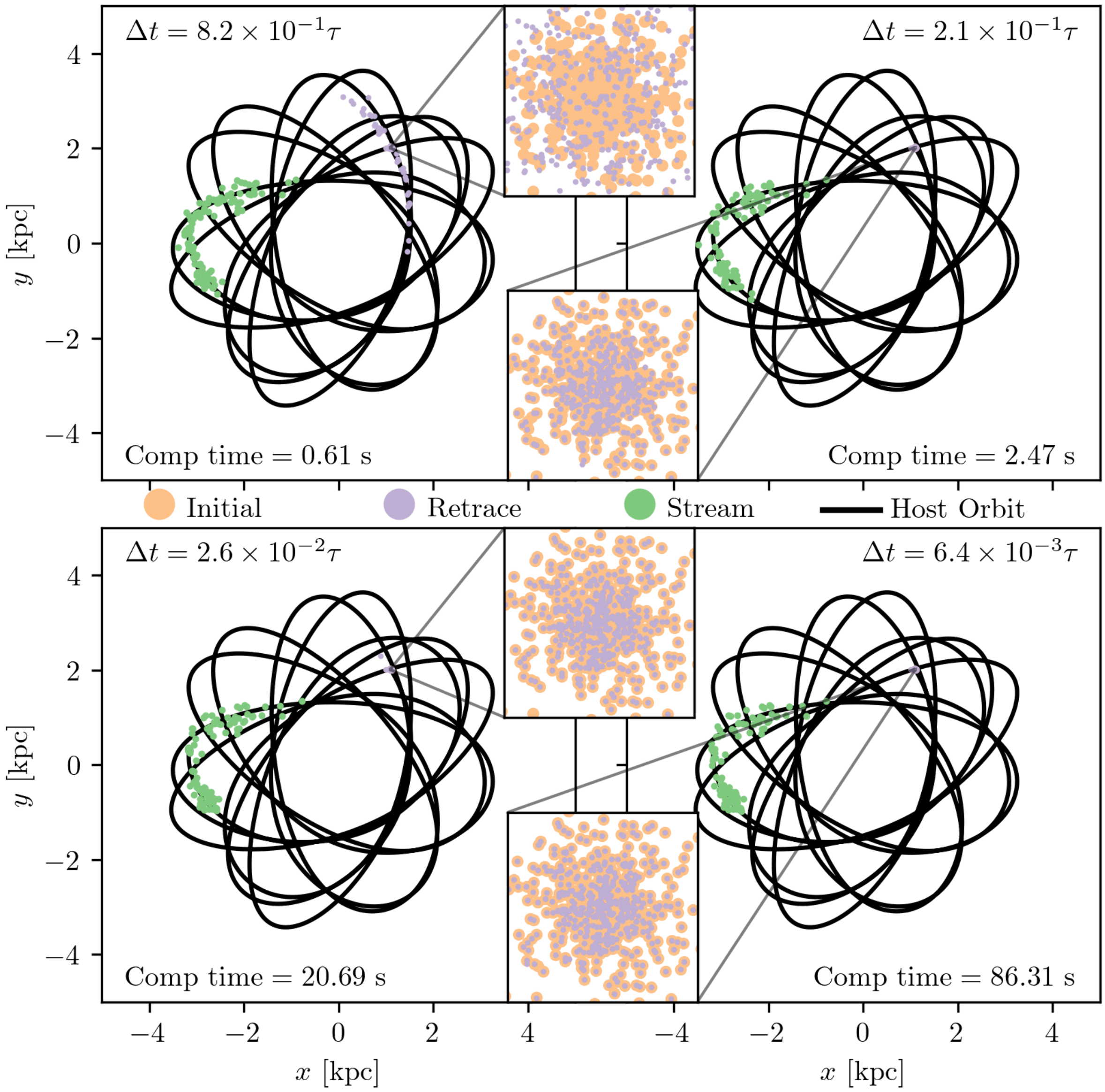

Figure 3.9 – Time-reversibility test for NGC 6171. The cluster's orbit was integrated backward by 1 Gyr, and a Plummer sphere of 512 particles was initialized at that position ("Initial"). The system was then integrated forward ("Stream") and backward again ("Retrace"). Each panel shows a different timestep, which was selected as a fraction of the internal dynamical time τ. The sub-panels zoom in on the cluster core, comparing the initial and retraced positions. Accuracy improves from top to bottom as the timestep decreases.

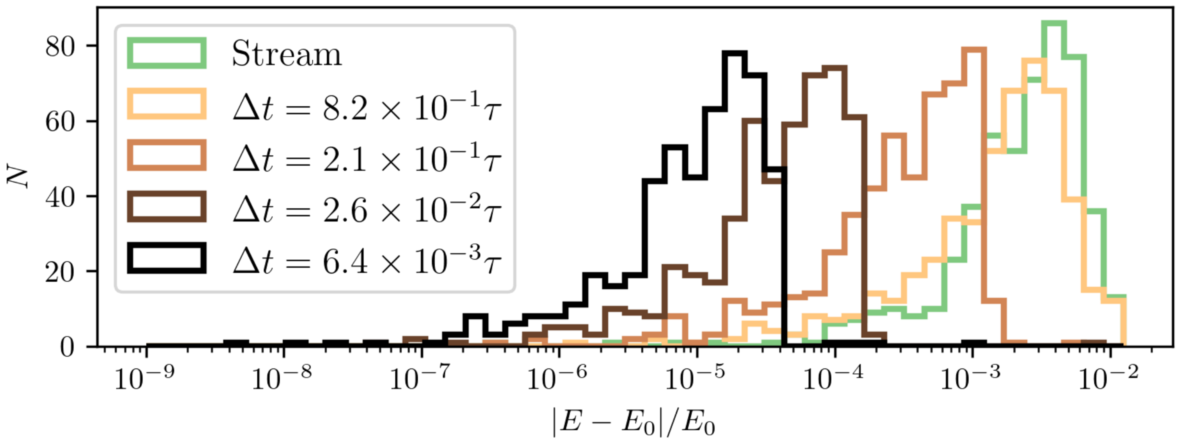

Figure 3.10 – Relative error in energy conservation during the retrace. As expected, accuracy improves with decreasing timestep. The *stream* distribution shows the final energy of each particle relative to its initial energy and *not* the quality of the integration. This reflects the spread in orbital energies imparted during initial sampling. At large timesteps, the retrace energy distribution approaches that of the stream.

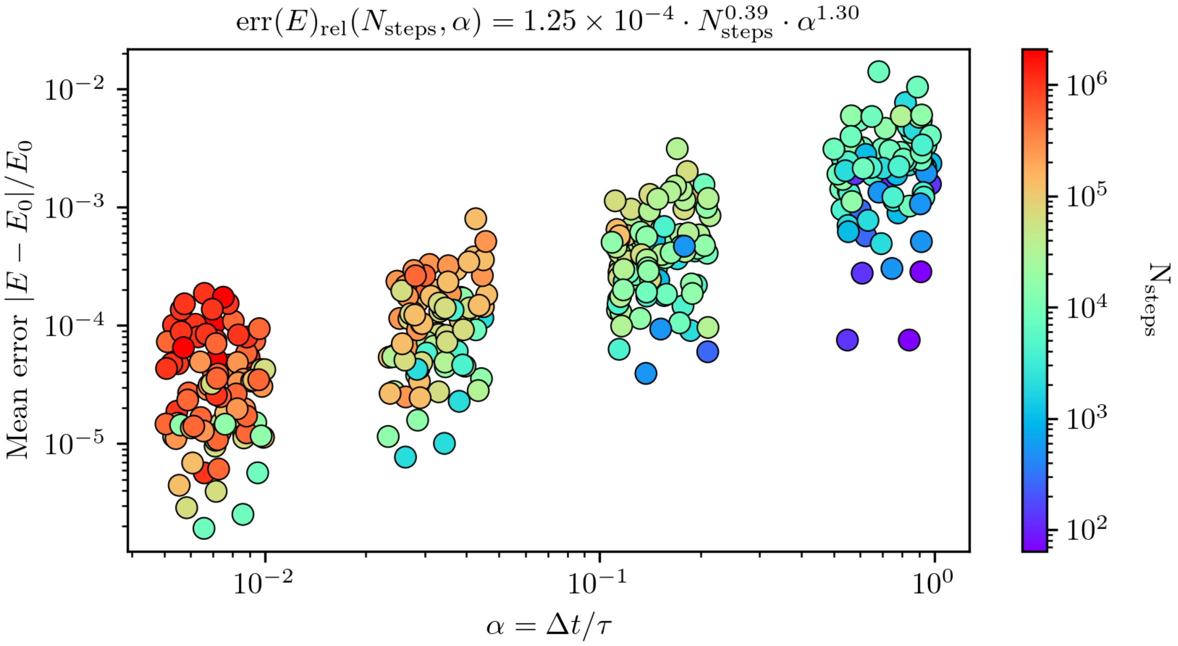

Figure 3.11 – The conservation of energy for the retrace of each globular cluster in the catalog. Each cluster was sampled with 512 particles and integrated for 5 Gyr. Four upper thresholds for each timestep were logarithmically sampled between 10^0 and 10^{-2}, and selected individually for each cluster in combination with it's internal dynamical time that evenly divided the integration time.

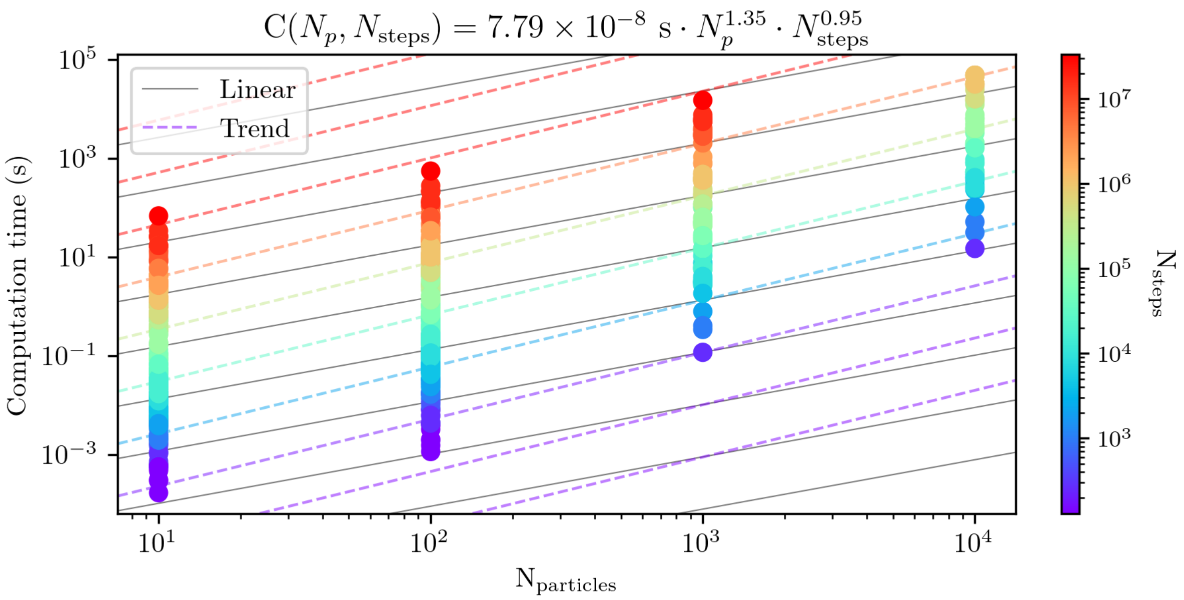

Figure 3.12 – How the computation scale time scales with the number of particles and the number of steps taken.

scale with N_p^2, while for the restricted three body problem it should scale with N_p. For both, it should scale linearly with the number of integration steps.

How does `tstrippy` perform? Fig. 3.12 presents the results from an experiment with all the globular clusters, integrating them each for 1 Gyr. I choose the timestep to be at most 1/20 of each internal dynamical time, thus since each cluster has a different dynamical time, it will require a different number of steps. For each of these tests I use 10^1, 10^2, 10^2, 10^3 particles and launched them on cluster at the Paris observatory. Then, I fit a scaling law of $C(N_p, N_s) = \langle C \rangle N_p^a N_s^b$. If the code scales linearly, then each exponent, a, b, should be 1 and $\langle C \rangle$ would be the mean computation time.

Fig 3.12 shows that the code is *less* efficient than linear scaling with number of particles, since the best fit exponent is 1.35. However, it scales *better* than linear with the number of steps. Perhaps this can be explained by the fact that there is overhead time involved for initiating and ending each simulation. As the number of steps increases the fixed overhead proportionally takes up less of the total time. Since the power law has an exponent of 0.95, the overhead is marginal. However, it is fortunate that the exponent is not greater than 1, which would mean the code would slow down with execution time. Putting Fig. 3.11 and Fig. 3.12 together, we may estimate for how long it completes to run these simulations. If we want all simulations to have error better relative error on the retraced conservation of energy than about 10^{-3}, then we must pick timesteps that are smaller than about 1/20 of the dynamical time. With this criteria selected, we can compute the number of timesteps necessary for each globular cluster, which is a function of its internal dynamical time. By doing so, I find that the fastest cluster can be computed in $\sim$ 30 minutes. The median computation time is $\sim$17 hours. The largest computation time was $\sim$ 5 days. The total CPU time for the whole catalog is $\sim$ 194 days.

3.3.1 A note on non-symplectic integration

During the writing of this thesis, I discovered a bug in my code that affected the integration scheme. Specifically, the error concerned the way I handled the host orbit during the integration of the star particles. In earlier implementations, I would integrate the orbit of the host using the same timestep that I used later to integrate the orbits of the star particles. However, this approach violated the structure of the Leapfrog integration scheme.

In Hamiltonian integration, it is essential that the drift and kick steps alternate in a consistent manner. Since I implemented a *drift-kick-drift* (DKD) scheme, the kicks occur at the midpoint of each timestep, meaning that forces should be evaluated at intermediate positions. Previously, I erroneously computed the relative position vector as

$$\Delta\vec{r}_i = \vec{r}_{p,i+1/2} - \vec{r}_{\mathrm{GC,i}},$$

instead of the correct expression:

$$\Delta\vec{r}_i = \vec{r}_{p,i+1/2} - \vec{r}_{\mathrm{GC,i+1/2}}.$$

This mistake appeared in both S. Ferrone, Di Matteo, et al. (2023) and S. Ferrone, Montuori, et al. (2025). Does this invalidate our results? To assess the impact, we can compare Figs. 3.13 and 3.10. In Fig. 3.13, the same retracing experiment was performed, but using the flawed integration: the host orbit was only provided at the same grid points as the stream. In the left panel, we see that the globular cluster does not perfectly recoalesce when integrating backward in time, but the result is not catastrophic. Physically, we do not expect this process to be perfectly time-reversible; however, such irreversibility should ideally arise from physical modeling, not from numerical artifacts.

We also observe that the distribution of the relative error in energy conservation is nearly identical between the retraced and the original stream. In any case, once the stars move beyond the Jacobi radius, their dynamics are dominated by the galactic potential. Since this potential was integrated correctly and symplectically, the orbits of stars outside the cluster remain reliable and physically meaningful.

As a result of this discovery, I updated the `tstrippy` code to warn users if the host orbit is not sampled at $2N+1$ points, where N is the number of integration steps. While the flawed implementation breaks strict symplecticity for the internal cluster dynamics, the Leapfrog integration for the globular cluster orbits was still used correctly. This ensures that the cluster center of mass returns to its present-day sky position and that

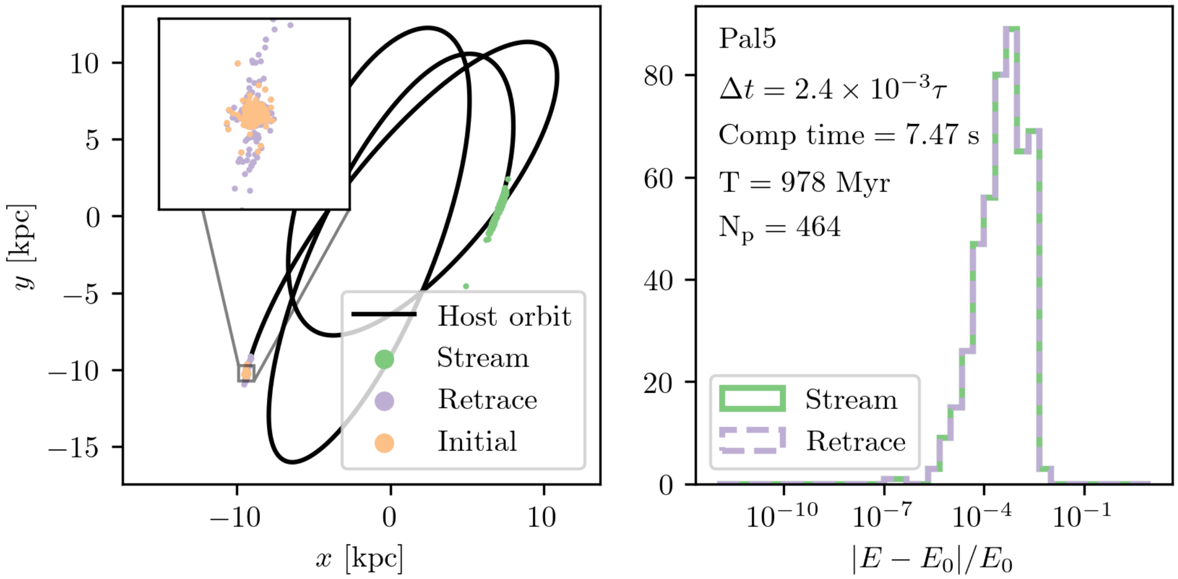

Figure 3.13 – An illustration of how an incorrect integration scheme breaks time reversibility. The center of mass of Palomar 5 was integrated backward in time by 1 s $\frac{\mathrm{kpc}}{\mathrm{km}}$. A Plummer sphere with 464 particles was sampled around this position (labeled "Initial"), then integrated forward to produce the "Stream." The right panel shows the distribution of relative energy error. The stream was then integrated backward in time by the same amount, resulting in the "Retrace" configuration. The timestep was chosen as a fraction of the internal dynamical time scale, τ.

stars outside the cluster follow accurate galactic orbits. Ultimately, the simplification of using a static Plummer sphere—whose mass and size remain fixed—is a greater limitation than this particular numerical error.

Lastly, I discovered this error while writing about the Forest-Ruth integration method. To implement this scheme correctly, I would need to know the position of the globular cluster's center of mass at four intermediate points across two timesteps, with the spacing determined by the coefficients in Table 3.2. This would require either storing additional mini-time-step data or interpolating the globular cluster's trajectory between saved snapshots. Both options would necessitate a substantial refactoring of the code or an impractical increase in memory usage per orbit. Given the results shown in Fig. 3.5, the gain in accuracy does not justify the computational cost.

4 Tstrippy

This project is built on `f2py`, which allows integration between Fortran and Python. The core motivation behind this choice is performance: Fortran, as a compiled language, provides significantly faster execution for numerically intensive tasks, while Python—especially within Jupyter notebooks—offers a convenient environment for development, experimentation, and visualization. `F2py` stands for *Fortran to Python* (Peterson, 2009), and it is included as a module within NumPy (NumPy Developers, 2025; C. R. Harris et al., 2020). The name of the project, `tstrippy`, stands for `T`idal `Strip`ping in `Py`thon.

`F2py` supports Fortran 77, 90, and 95 standards, so we chose to write the code in Fortran 90 to make use of *modules*. In Fortran, a module encapsulates data and subroutines in a manner somewhat analogous to classes in object-oriented programming. However, Fortran modules do not support inheritance, and only a single instance of a module can exist at a time—unlike classes, which can be instantiated multiple times.

`Tstrippy` package is structured around five core Fortran modules, each responsible for a distinct aspect of the simulation:

- `integrator`: This is the central module of the code. It stores particle positions and velocities, computes forces, and evolves the system forward in time. It also handles the writing of output data at specified intervals and interfaces with all other modules in the code.
- `potentials`: This module defines the analytical potentials used to compute gravitational forces. It currently supports several models, including `Plummer`, `Hernquist`, `AllenSantillian`, `MiyamotoNagai`, the bar model `LongMuraliBar` from Long & Murali (1992), and the composite model from `pouliasis2017pii` (Pouliasis et al., 2017). This module can also be called in Python, allowing users to call potential functions directly, e.g., for computing energies during post-processing.

- `hostperturber`: This module handles the host globular cluster. It stores its orbit (i.e., timestamps, positions, and velocities) and ensures its synchronization with the simulation's internal clock. It computes the gravitational influence of the host cluster on each star particle. This is an internal module only.
- `perturbers`: Similar in function to `hostperturber`, this module supports additional perturbing clusters. It allows for the inclusion of multiple perturbers and computes their collective force on each particle. If object-oriented programming were available in Fortran, both this module and `hostperturber` would naturally inherit from a shared parent class. This module only uses the positions, masses, and characteristic radii of the other perturbers. The velocities are not imported.
- `galacticbar`: This module stores parameters for the bar, including the polynomial coefficients for its angular displacement as a function of time:

  $$\theta(t) = \theta_0 + \omega t + \dot{\omega} t^2 + \ddot{\omega} t^3 + \ldots$$

  If a user wants a bar with a constant rotation speed, then they may pass two coefficients. If they want a bar that accelerates for decelerates, they may mass more coefficients for the higher order terms. The module performs transformations into the rotating bar frame, computes the forces in that frame, and then transforms the forces back to the Galactocentric reference frame.

This modular structure makes it straightforward to extend the code by adding new physics in the form of additional modules.

To make the package installable and easy to distribute, I initially followed the guide by Bovy (2025b), which describes how to create a Python package using `setuptools`—the standard build system in the Python ecosystem. However, compatibility between `setuptools` and `f2py` was broken starting with NumPy > 1.22 (released June 22, 2022[2]) and Python $> 3.9.18$ (released June 24, 2024[3]). This meant that Fortran extensions could only be compiled using deprecated versions of both. These older versions of NumPy were also not compatible with Apple's ARM-based M1 and M2 processors, rendering the code unusable on modern Mac systems.

This limitation stemmed from the deprecation and eventual removal of `numpy.distutils`, the tool that previously enabled seamless integration of Fortran code in NumPy-based packages. As of NumPy 1.23 and later, `numpy.distutils` was deprecated, and with NumPy 2.0, it was removed entirely. The NumPy developers recommended migrating to `meson` (Meson Developers, 2025) or `Cmake`.

To address these issues, I migrated the build process to `meson`, a language-agnostic build system capable of compiling Fortran, C, and Python extensions across architec-

---

[2] https://github.com/numpy/numpy/releases/tag/v1.22.0

[3] https://www.python.org/downloads/release/

tures. This eliminated compatibility problems and made the build process architecture-independent. The build system now automatically detects the system architecture and compiles accordingly.

The code is fully open source and available on GitHub.[4] To support users, I created documentation hosted on `readthedocs.io`[5], which includes working examples and basic usage guides. A minimal test suite, written using `pytest`, is also included. While not exhaustive, the tests ensure that core functionality remains intact as the code evolves. In the next section, I present a minimal example of how the user may use the code within a python script.

4.1 Minimum example

If the package is properly installed on the system, it can be imported at the top of any Python script:

```
import tstrippy
```

Next, the user must load or define the initial conditions. The code provides:

- The masses, sizes, and kinematics of the globular cluster catalog from Baumgardt & Hilker (2018);
- The galactic potential parameters for model II of Pouliasis et al. (2017); and
- A galactic reference frame.

```
GCdata      = \
    tstrippy.Parsers.baumgardtMWGCs().data
MWparams    = \
    tstrippy.Parsers.potential_parameters.pouliasis2017pii()
MWrefframe  = \
    tstrippy.Parsers.potential_parameters.MWreferenceframe()
```

The user must then select the system to integrate. For example, to integrate the orbits of observed globular clusters, one must convert the ICRS coordinates to a Galactocentric frame using `astropy` and the provided MW reference frame. Alternatively, to simulate a star cluster, one can generate a Plummer sphere:

```
xp,yp,zp,vxp,vyp,vzp=\
tstrippy.ergodic.isotropicplummer(\
    G,massHost,halfmassradius,NP)
```

Here, `NP` is the number of particles, `halfmassradius` is the system's half-mass radius, `massHost` is the total mass of the Plummer sphere, and `G` is the gravitational constant. All values must be in the same unit system.

---

[4] https://github.com/salvatore-ferrone/tstrippy

[5] https://tstrippy.readthedocs.io/en/latest/

The integrator must then be initialized. All parameters are passed via lists that are unpacked at the function call. Here is an example of initializing the integrator for a stellar stream in a potential that includes a rotating bar:

```
tstrippy.integrator.setstaticgalaxy(*staticgalaxy)
tstrippy.integrator.setinitialkinematics(\
    *initialkinematics)
tstrippy.integrator.setintegrationparameters(\
    *integrationparameters)
tstrippy.integrator.inithostperturber(*hostperturber)
tstrippy.integrator.initgalacticbar(*galacticbar)
tstrippy.integrator.setbackwardorbit()
```

- `setstaticgalaxy` specifies the static potential model and passes its parameters.
- `setinitialkinematics` provides the initial positions and velocities of the particles.
- `setintegrationparameters` defines the initial time, timestep, and number of steps.
- `inithostperturber` specifies the globular cluster's trajectory and mass as a function of time.
- `initgalacticbar` defines a rotating bar. It takes the name of the bar model, potential parameters, and spin parameters.
- `setbackwardorbit` reverses the velocity vectors and sets the internal clock to count down: $t_i = t_0 - i \cdot \Delta t$. For the usecase presented in this work, `setbackwardorbit` is used for computing the globular cluster orbits and not for the star-particles.

The user can choose between two output modes during integration:

```
tstrippy.integrator.initwriteparticleorbits(\
    nskip,myoutname,myoutdir)
tstrippy.integrator.initwritestream(\
    nskip,myoutname,myoutdir)
```

Conceptually, these represent two output paradigms:

- `initwriteparticleorbits` saves the full orbit of each particle to an individual file.
- `initwritestream` saves full snapshots of all particles at selected timesteps.

Both functions take:

- `nskip`: number of timesteps to skip between outputs;
- `myoutname`: the base file name;
- `myoutdir`: the output directory.

The output files will be named like: `../dir/temp0.bin`, `../dir/temp1.bin`, ..., up to `../dir/tempN.bin`, where $N = N_{\mathrm{step}}/N_{\mathrm{skip}}$. Note that the files are written in Fortran binary format. Although `scipy.io.FortranFile` can read them, I use a custom parser based on `numpy.frombuffer` to avoid the SciPy dependency. Once all parameters are set, the user can proceed with integration using one of two methods:

Full orbit integration (in memory)

```
xt,yt,zt,vxt,vyt,vzt=\
    tstrippy.integrator.leapfrogintime(Ntimestep,nObj)
timestamps=\
    tstrippy.integrator.timestamps.copy()
```

`leapfrogintime` stores the full orbit of each particle in memory. This is useful for a small number of particles or short integrations—e.g., rapid parameter studies in a notebook. However, for large simulations it can be prohibitively memory-intensive. For instance, integrating all globular clusters at high time resolution might require:

$$7 \times N_p \times N_{\mathrm{step}} \times 8 \text{ Byte} \approx 450 \text{ GB} \tag{3.29}$$

if $N_{\mathrm{step}} \approx 10^7$. This will likely exceed system RAM.

Final state only

```
tstrippy.integrator.leapfrogtofinalpositions()
xf  = tstrippy.integrator.xf.copy()
yf  = tstrippy.integrator.yf.copy()
zf  = tstrippy.integrator.zf.copy()
vxf = tstrippy.integrator.vxf.copy()
vyf = tstrippy.integrator.vyf.copy()
vzf = tstrippy.integrator.vzf.copy()
finaltime=tstrippy.integrator.currenttime.copy()
```

`leapfrogtofinalpositions()` performs the integration but only returns the final phase-space coordinates. These arrays must be copied before deallocating memory:

```
tstrippy.integrator.deallocate()
```

Deallocating is necessary to avoid memory leaks or crashes in Jupyter when rerunning code cells.

4.2 Reflection on developing `tstrippy`

The earliest version of this code began as a simple Fortran script that was interfaced to python via `f2py` and was built to integrate test particles in specific gravitational potential models. Since I was already familiar with Fortran and had working routines, I chose to build on that foundation, gradually transforming the script into a modular and more reusable package. Rather than switching to C++ or a Python-only solution, I continued using Fortran in combination with `f2py`.

One of the primary motivations for writing my own code was flexibility. When I attempted to implement a particle spray method in *Galpy*, I found that performance degraded significantly when using custom potentials not constructed from its internal C++ backend. For example, I wanted to use the `AllenSantillian` halo model, which is not natively supported. I followed the documentation and implemented a class for it. However, custom potentials bypass `Galpy`'s optimized C++ backend, resulting in slow computations and rendering actions uncomputable (or at least with the functions I tried). This pushed me to continue developing `tstrippy`. I had a similar experience with `Amuse`.

This choice, however, came with challenges. At one point, I tried implementing potentials derived from exponential density profiles, which do not admit closed-form solutions for the potential. I attempted to work in elliptical coordinates, motivated by the idea that the potential would depend only on the "distance" from the center along the equipotential surfaces. While I successfully implemented simple potential models in elliptical coordinates, I naively overlooked that this changes the equations of motion entirely due to the underlying geometry. I found that my orbits always diverged (except in special cases). It was only later that I realized I would need to account for the metric tensor and Christoffel symbols to properly integrate orbits in elliptical coordinates. At that point, I chose not to pursue this further, prioritizing scientific analysis and launching other simulations instead. This experience helped me appreciate why many codes and other published works prefer basis function expansions for such problems. In hindsight, this episode was a perfect example of how even unsuccessful attempts can lead to valuable insights. Below, I summarize some of the key advantages and limitations I encountered while developing a code from scratch to answer a scientific question.

4.2.1 Advantages and Limitations

Developing and maintaining this codebase brought several clear benefits:

- *Understanding.* Writing the code forced me to deeply understand the modeling techniques involved. Otherwise, the results would have been incorrect.
- *Flexibility.* I could implement exactly the models I needed and extend them as required.
- *Transparency.* Results produced by my code can be verified and reproduced by others.
- *Reusability.* Ongoing development helped me uncover and fix subtle bugs (e.g., related to non-symplectic integrators) that do not trigger obvious errors and only

appear in edge cases or after close inspection. Long-term engagement with the code is key to catching these issues.

- *Collaboration.* A fellow researcher at the Paris Observatory is now using the code. I also used it to supervise a master's student during their semester research project, something that would not have been possible without building a user-friendly tool.
- *Growth.* This project pushed me to adopt best practices: version control, documentation, modularity. Developing my own code has also made it easier to understand external libraries. For example, when I implemented the King model, I studied `Galpy`'s internals to cross-check my own method. I was delighted by how much easier it was for me to use, despite the fact that I had not touched it within a year.

However, there were also drawbacks:

- *Time cost.* Developing the code took time away from direct scientific analysis. It's possible I could have performed more simulations or performed more analyses had I not develop my code to such an extent.
- *Feature limitations.* My code still lacks capabilities present in other packages: such as basis function expansions, action-angle variable computation, or parallelization strategies using MPI or OpenMP.
- *Changing relevance.* Scientific priorities and available tools evolve rapidly. A general-purpose tool may become obsolete more quickly than a single-use script written for a specific question.
- *Compatibility and maintenance burden.* Making the code accessible to other users also introduces challenges related to cross-platform compatibility and dependency management. Software environments evolve, compilers are updated, dependencies can deprecate, and build tools change. Even with the help of modern tools like `meson` or `f2py`, ensuring continued compatibility requires regular testing and adaptation. As the codebase grows, the maintenance load increases, and sustaining it as a single developer becomes increasingly difficult, especially if the tool is made too general.

Nonetheless, the code was designed to address concrete scientific questions about Milky Way stellar streams and globular clusters. In the next two chapters, I present how this tool contributed to advancing our understanding of the Galaxy.

Chapter 4

Extra tidal debris of Milky Way Globular Clusters

reference

Ferrone, Salvatore, et al. “The e-TidalGCs project-Modeling the extra-tidal features generated by Galactic globular clusters.” Astronomy & Astrophysics 673 (2023): A44.

This chapter presents the material published in S. Ferrone, Di Matteo, et al. (2023). The aim of this work is to provide the first prediction of the expected tidal debris from all Milky Way globular clusters and to characterize their spatial distribution. For this study, we used `GCsTT`, a predecessor of `tstrippy`, which follows the same philosophy of representing stars as test particles that experience the gravitational field but do not contribute to it.

1 Introduction

Globular clusters are the oldest gravitationally bound stellar systems in the Galaxy (Meylan & D. C. Heggie, 1997). About 170 are currently known in the Milky Way (Vasiliev & Baumgardt, 2021) and the census is still incomplete, particularly in the inner regions of the bulge and disk of our Galaxy, where dust extinction and high stellar number density limit detections. It is in these regions in particular that new globular cluster candidates have been recently discovered, especially thanks to the analysis of near-infrared surveys

(Minniti, Hempel, et al., 2011; Moni Bidin et al., 2011; Minniti, Palma, Dékány, et al., 2017; Minniti, Geisler, et al., 2017; Minniti, Schlafly, et al., 2018; Gran, Zoccali, Contreras Ramos, et al., 2019; Garro, Minniti, M. Gómez, Alonso-García, Barbá, et al., 2020; Garro, Minniti, Alessi, et al., 2022; Garro, Minniti, M. Gómez, Alonso-García, Ripepi, et al., 2022; Garro, Minniti, M. Gómez, Alonso-García, Palma, et al., 2021; Minniti, Fernández-Trincado, et al., 2021; Minniti, Palma, Camargo, et al., 2021; Gran, Zoccali, Saviane, et al., 2022). The current population of globular clusters is likely to merely represent the leftovers of an initially more numerous and more massive one that had been depopulated as a result of many disruptive processes (Gnedin & Ostriker, 1997; Murali & Weinberg, 1997b; Murali & Weinberg, 1997a; Vesperini & D. C. Heggie, 1997; Fall & Q. Zhang, 2001). One of the main processes affecting the globular cluster population and its evolution in number, mass, and size is tidal stripping.

As all stellar systems are characterized by a finite size and defined orbit of the Galaxy, globular clusters are subject to tidal effects, which arise because the opposite sides of these systems experience a different gravitational acceleration. The long-term effect of this process strips the system of its most loosely bound stars, which redistribute themselves onto orbits similar to those of their progenitor, forming so-called "tidal tails" or streams around it (see Grillmair, Freeman, et al., 1995; Leon et al., 2000, for some of the earliest studies). Some spectacular tails have been discovered and studied over the past twenty years around Milky Way globular clusters, ranging from the long tails (of roughly 30° degrees) departing from the Palomar 5 cluster (Odenkirchen, Grebel, Rockosi, et al., 2001; Odenkirchen, Grebel, Dehnen, H.-W. Rix, et al., 2003; Grillmair & Dionatos, 2006a; Odenkirchen, Grebel, Kayser, et al., 2009; G. F. Thomas, R. Ibata, et al., 2016; Starkman et al., 2020; R. Ibata, Malhan, N. Martin, et al., 2021) to those of NGC 5466 (Belokurov, Evans, et al., 2006), Palomar 14 (Sollima, Martínez-Delgado, et al., 2011), and the GD-1 stream, whose parent cluster has still to be discovered (or has already been completely destroyed, leaving behind the stream as the only vestige of its past existence; see Grillmair & Dionatos, 2006b; Webb & Bovy, 2019; Bonaca, Conroy, et al., 2020). These studies have been boosted in the last few years thanks to the publication of the ESA Gaia mission catalogues (Gaia Collaboration, Prusti, et al., 2016; Gaia Collaboration, Brown, Vallenari, Prusti, de Bruijne, Babusiaux, Bailer-Jones, et al., 2018; Gaia Collaboration, Brown, Vallenari, Prusti, de Bruijne, Babusiaux, Biermann, et al., 2021a; Gaia Collaboration, Brown, Vallenari, Prusti, de Bruijne, Babusiaux, Biermann, et al., 2021b) which has been delivering parallaxes, proper motions, and magnitudes for about 1.4 billion stars, as well as the radial velocities for several million, and thus allowing for searches of stars with coherent distances and motions in the Galaxy, revealing the existence of a number of new and spectacular streams, as well as rediscovering and confirming already known ones (Navarrete et al., 2017; Malhan, R. A. Ibata & N. F. Martin, 2018; Malhan, R. A. Ibata, Goldman, et al., 2018; R. A. Ibata, Malhan, N. F. Martin & Starkenburg, 2018; Piatti, 2021; Shipp, Drlica-Wagner, et al., 2018; R. A. Ibata, Bellazzini, et al., 2019; R. A. Ibata, Malhan & N. F. Martin, 2019; Kaderali et al., 2019; Bianchini, R. Ibata, et al., 2019; Malhan, R. A. Ibata, Carlberg, Bellazzini, et al., 2019; Malhan, R. A. Ibata, Carlberg, Valluri, et al., 2019; Palau & Miralda-Escudé, 2019; Piatti & Carballo-Bello, 2019; Caldwell et al., 2020; R. Ibata, G. Thomas, et al., 2020; Piatti, Carballo-Bello, et al., 2020; Piatti & Carballo-Bello, 2020; Piatti & Carballo-Bello, 2020; Shipp, Price-Whelan, et al., 2020; G. F. Thomas, R. Ibata, et al., 2016; Boldrini & Vitral, 2021; R. Ibata, Malhan, N. Martin, et al., 2021; Malhan, Valluri & Freese, 2021; Jensen et al., 2021; Palau & Miralda-Escudé, 2021; Piatti, 2021; Piatti, Mestre, et al., 2021; Yuan, Malhan, et al., 2022; S. Zhang et al., 2022; Nie et al., 2022; Piatti, 2022). For a general overview, Mateu (2023) provides a recent compilation of known stellar streams.

All these studies are unraveling a very complex and rich set of stellar structures in the Milky Way that are mainly distributed in the halo, where their identification is the easiest because of the low density of the background stellar field.

From a numerical and theoretical point of view, many studies over the years have been focused on the formation and evolution of tidal streams around globular clusters (Keenan & Innanen, 1975; Oh, Lin & S. J. Aarseth, 1992; Oh & Lin, 1992; Grillmair, 1998; Combes et al., 1999; R. A. Ibata, Lewis, M. J. Irwin, et al., 2002; Johnston, Spergel, et al., 2002; Yim & H. M. Lee, 2002; Capuzzo Dolcetta et al., 2005; Di Matteo, Capuzzo Dolcetta, et al., 2005; Montuori et al., 2007; Siegal-Gaskins & Valluri, 2008; Küpper, Kroupa, et al., 2010; R. R. Lane, Kiss, et al., 2010; Küpper, R. R. Lane, et al., 2012; Mastrobuono-Battisti, Di Matteo, et al., 2012; Sanders & Binney, 2013; Bovy, 2014; Amorisco et al., 2016; Erkal, Belokurov, et al., 2016; Sanders, Bovy, et al., 2016; Pearson, Price-Whelan, et al., 2017; Carlberg, 2018; G. F. Thomas, Famaey, R. Ibata, et al., 2018; Carlberg, 2020; Vitral & Boldrini, 2022). These studies have contributed to understanding how these structures form and evolve, to what extent they trace the globular cluster orbit, and how their shape, extension, and morphology depend on the orbital phase and characteristics of the Galactic potential, as well as on the potential tidal shocks experienced by the cluster itself when it crosses the Galactic disk.

Some works have presented models and simulations for specific streams (Dehnen et al., 2004; Mastrobuono-Battisti, Di Matteo, et al., 2012; Banik & Bovy, 2019; Bonaca, Hogg, et al., 2019; Banik, Bovy, et al., 2021; Bonaca, 2021), contributing to an understanding of their morphology, density variations, and their extent. From these works, it is clear that the tidal loss of stars from globular clusters and the formation of related structures are important for several reasons: (1) in quantifying to what extent globular clusters have contributed to the field stellar populations, from the halo to the disk to the bulge, and to what extent they still do; (2) reconstructing the properties (in terms of numbers and masses) of the early Galactic globular clusters, through their current mass loss; and (3) using globular cluster streams as a probe of the Galactic potential and, more generally, of the physical laws governing gravity (see, e.g., G. F. Thomas, Famaey, R. Ibata, et al., 2018; Bianchini, R. Ibata, et al., 2019; Naik et al., 2020; Banik, Bovy, et al., 2021).

In this chapter, we wish to contribute to the current discourse on this matter by presenting the first complete catalog of simulated extra-tidal features around globular clusters. We emphasize that we are speaking generically on their features, rather than specifically on tails or streams, because the latter are but one of the morphologies that extra-tidal material can reveal, as we go on to show in this work. This project is motivated, on the one hand, by the aforementioned discoveries of many numerous new streams and tails in the Galaxy and, on the other hand, by the availability of the full 6D phase information and internal parameters (masses and sizes) for more than 150 Galactic globular clusters (Baumgardt & Hilker, 2018; Baumgardt & Vasiliev, 2021; Vasiliev, Belokurov, et al., 2021). The aims of this project are manifold: (1) to obtain a complete view of the expected distribution of globular clusters tidal structures in the sky; (2) to inform the interpretation of recent and future discoveries; (3) to support the search for new extra-tidal features in the data; (4) to offer the community a repository of all these models to be compared to other theoretical and numerical predictions, which adopt different Galactic potentials and/or gravity laws.

2 Numerical method

To model the formation and evolution of extra-tidal features around Galactic globular clusters, we use a set of codes, called Globular Clusters' Tidal Tails (GCsTT) developed by our group. It comprises two python codes, for the backward and forward integration of a stellar system, made of N test-particles (see Sect. 2.1). These codes are separated for data organization and management, while the (computationally) most expensive part, namely, the calculation of the accelerations acting on the N particles and the orbits integration, is realized by means of a Fortran module written by our group. This module is interfaced to python by means of f2py directives from NumPy. The use of test-particle methods for modeling the tidal stripping process is widespread in the literature, where these methods are usually applied to one or few clusters at a time (see, e.g., R. R. Lane, Küpper, et al., 2012; Mastrobuono-Battisti, Di Matteo, et al., 2012; Palau & Miralda-Escudé, 2019; Piatti, 2021; Grillmair, 2022). In this work, we apply a test-particle methodology to the whole set (159) of Galactic globular clusters for which this is currently possible, also taking into account, for each cluster, the errors on astrometry, line-of-sight velocities[1] and distances. In the following, we describe the two main steps of the procedure used by GCsTT to simulate the tidal stripping process (Sect. 2.1), the initial conditions adopted for the clusters' parameters and their mass distribution (Sect. 2.2), as well as the Galactic potentials (Sect. 2.3).

2.1 Simulations of the tidal stripping process: Two-step procedure

To model the formation and evolution of extra-tidal features around Galactic globular clusters, and predict their current properties, we proceed as follows:

Step i: Backward integration. Reconstructing the globular cluster orbit over the last 5 Gyr: First, for each Galactic globular cluster for which the distances from the Sun, proper motions, line-of-sight velocities, and structural parameters are available (see Sect. 2.2), we determine their current positions and velocities in a Galactocentric reference frame, in which the Sun is at $(x_\odot, y_\odot, z_\odot) = (-8.34, 0., 0.027)$ kpc (B. Chen et al., 2001; M. J. Reid et al., 2014) and at a given velocity for the local standard of rest, $v_{LSR} = 240$ km/s (M. J. Reid et al., 2014), and a peculiar velocity of the Sun with respect to the LSR, $(U_\odot, V_\odot, W_\odot) = (11.1, 12.24, 7.25)$ km/s (Schönrich et al., 2010). We then integrate the orbit of a single point mass, representing the cluster barycenter, backwards in time for 5 Gyr, and in this way, we retrieve its position and velocity at that time in the chosen Galactic potential (see Sect. 2.3). We notice that other choices for the Sun's position or velocity with respect to the Galactocentric frame would have been possible. For example, Piatti (2021) adopted the same values as ours for the v_{LSR} and for the peculiar velocity

---

[1] Note: the term "line-of-sight velocities" adopted in this paper corresponds to the term "radial velocities" often used in the literature, as well as in the Gaia catalogues. We prefer the use of the first term, since the second is usually used also to indicate the (Galactocentric) radial velocities and can introduce some ambiguity, especially when different coordinate systems are used. We emphasize that the choice to use the term "line-of-sight velocity" is not new (see, e.g., Vasiliev & Baumgardt, 2021).

of the Sun but with a different distance to the Galactic center (8.1 kpc in their work, see GRAVITY Collaboration et al., 2018). The difference in the adopted position of the Sun is, however, generally smaller than the uncertainties affecting our knowledge of the distance of Galactic globular clusters to the Sun. For this reason, we do not to explore the dependency of the results presented in this paper with regard to these choices.

Step ii: Forward integration. Test-particle streams from the past to the present day: Once the positions and velocities of the barycenter of each cluster, 5 Gyr ago, have been determined, we build the corresponding N-body system, with N = 100 000 particles. The phase-space coordinates of these particles are generated following a Plummer distribution, with the total mass and half-mass radius as described in Sect. 2.2. The barycenter of this N-body cluster is then assigned initial positions and velocities in the Galactic model, as those retrieved at step (i), and the cluster is then integrated forward in time until the present day. Particles in this N-body system are modeled as test-particles, that is, they experience the gravitational field exerted by the globular cluster itself (see Sect. 2.2) and by the Galaxy (see Sect. 2.3), but do not generate any gravitational field themselves. This allows us to maintain a computational time which scales as $O(N)$ and not as $O(N^2)$, as would be the case for a direct N-body self-consistent computation.

In the following, we refer to these simulations, made by using the most probable values on distances, proper motions, and line-of-sight velocities, as the "reference simulations." In addition, for each globular cluster, we also take into account the errors on its distance, proper motions, and line-of-sight velocity, assuming Gaussian distributions of the errors, treated independently, and by generating 50 random realizations of these parameters. For each of these realizations, we repeat the steps described above, that is: (*step i*) we determine the associated current positions and velocities in the chosen Galactocentric reference frame, we integrate the orbit of the single-point mass (representing the cluster barycenter) backwards in time, retrieving the corresponding values 5 Gyr ago, (*step ii*) we build an N-body cluster containing $N=$ 100 000 particles, with total mass and half-mass radius as those used for the reference simulation, and then we integrate the N-body cluster forwards in time until the present-day position.

To summarize, for a given Galactic potential, we run $159 \times (50+1) = 8109$ simulations, where 159 is the total number of clusters for which we currently have both 6D phase-space information and structural parameters. As we discuss in the following section, the whole set of globular clusters has been evolved in three different Galactic potentials, which implies that a total of 24 327 simulations have been run.

For the orbit integration, a leap-frog algorithm is used, with a fixed time-step, Δt, and a total number of steps, N_{steps}, such that the total simulated time is $\Delta t \times N_{steps} = 5$ Gyr. The choice of the value of Δt adopted to simulate each cluster in the Galactic potential has been based on the energy conservation of the corresponding cluster evolved in isolation (i.e., without the effect of the Galactic gravitational field for 5 Gyr). For the majority of the clusters (109/159), this value was set to $\Delta t = 10^5$ yr (for a corresponding value of $N_{steps} = 50\,000$), while for the remaining clusters (50/159) a $\Delta t = 10^4$ yr (for a corresponding value of $N_{steps} = 500\,000$) was used. We refer to Supplemental Material 5.1 (and in particular to Table 4.3) for additional details on the choice of Δt for the whole set of clusters. As for the total simulated time, while globular clusters are much older than 5 Gyr, we chose this time limit because the longer back in time we could go, the less certain we would be of the Galactic environment. In addition, the last significant mergers in the Galaxy happened between 9 and 11 Gyr ago (see Belokurov, Erkal, et al., 2018; Helmi, Babusiaux, et al., 2018; Di Matteo, Haywood, et al., 2019; Gallart et al., 2019; Kruijssen, Pfeffer, et al., 2020) – well before the time interval simulated in this study. Other more recent interactions, such as the accretion of Sagittarius and of the Magellanic Clouds, may perturb the Galactic potential as well (see, e.g., Vasiliev, Belokurov, et al., 2021) and we plan to investigate their impact on the properties of globular cluster streams in the future.

For each realization, we generate an output file in an hdf5 format[2] containing the values for the right ascension (α), declination (δ), distance from the Sun (D), along with the components for proper motion in the equatorial coordinate system ($\mu_\alpha \cos(\delta)$ and μ_δ), the line-of-sight velocity ($\mathrm{v}_{\ell\mathrm{os}}$), longitude ($\ell$), latitude ($b$), as well as the components for proper motion in the Galactic coordinate system ($\mu_\ell \cos(b)$ and μ_b) and the Galactocentric positions (x, y, z), velocities (v_x, v_y, v_z) and energy, E, of each particle in the simulated system. We used Astropy (Astropy Collaboration, Robitaille, et al., 2013; Astropy Collaboration, Price-Whelan, et al., 2018) to convert the Galactocentric positions and velocities in the equatorial and Galactic quantities $\alpha, \delta, D, \mu_\alpha \cos(\delta), \mu_\delta, \mathrm{v}_{\ell\mathrm{os}}, \ell, \mathrm{b}, \mu_\ell \cos(b)$, and μ_b.

For each particle, we also save its escape time t_esc, defined as the time at which the particle escapes from the cluster, that is, the time, t, at which the particle satisfies the relation[3]:

$$E_{GC} = 0.5 \times \left((v_x - v_{x,GC})^2 + (v_y - v_{y,GC})^2 + (v_z - v_{z,GC})^2 \right) + \Phi_{GC} > 0, \tag{4.1}$$

with E_{GC} being the total specific energy of the particle relative to the cluster, that is, the sum of the potential energy, Φ_{GC}, due to the gravitational field of the cluster (see Eq. 4.2), and of the kinetic energy, relative to the cluster barycenter, $T_{GC} = 0.5 \times \left((v_x - v_{x,GC})^2 + (vy - v_{y,GC})^2 + (vz - v_{z,GC})^2 \right)$, where v_x, v_y, and v_z are its velocity components at time, t, and $v_{x,GC}, v_{y,GC}$, and $v_{z,GC}$ of the cluster barycenter at the same time. A positive value of E_{GC} implies that the particle is no longer gravitationally bound to the cluster and, hence, it is lost in the field. Overall, the total volume of the whole set

---

[2] `https://www.hdfgroup.org/solutions/hdf5/`

[3] If the particle is gravitationally bound to the cluster until the end of the simulation, t_esc is set equal to -9999.

of 24 327 simulations, saved in hdf5 format, amounts to about 370 Gb.

2.2 Simulations of the tidal stripping process: Globular clusters' current and initial conditions and their gravitational potential

Steps (*i*) and (*ii*) described in the previous section require some input conditions to be adequately executed. The current distances from the Sun, proper motions, and line-of-sight velocities, as well as the related uncertainties, of all 159 globular clusters considered in this study are taken respectively from Baumgardt & Vasiliev (2021) and Vasiliev & Baumgardt (2021). These values are then converted into Galactocentric positions and velocities by making use of Astropy and used as initial conditions to execute step (*i*).

Step (*ii*) requires generating an N-body system, representing the globular cluster, whose initial total mass and half-mass radius are assigned on the basis of their current values, as given by Baumgardt & Hilker (2018) [4] and reported in Table 4.4. As anticipated at step (*ii*) in Sect. 2.1, the phase-space coordinates of each N-body cluster are generated by assuming a Plummer distribution of total mass, M_{GC}, and half-mass radius, r_h, for which the corresponding potential is:

$$\Phi_{GC}(r) = -\frac{GM_{GC}}{\sqrt{r^2 + {r_c}^2}}, \tag{4.2}$$

where r_c is the cluster scale radius and it is related to the half-mass radius, r_h, through $r_h \simeq 1.305 r_c$ (D. Heggie & Hut, 2003). The variable r here indicates the distance of the test particle from the center of the cluster. For each cluster, the same Plummer distribution used to generate the N-body system is also used to calculate the accelerations exerted on each particle as the system moves through time. The Plummer sphere, representing the cluster potential, indeed moves through the Galaxy along the orbit retrieved at step (i), traveling this time in the opposite direction, from 5 Gyr ago to the present day.

It might be noted that this implies that the globular cluster density profile and its internal parameters (total mass and characteristic radius) are constant over time in these models. This is, of course, a crude approximation, because in reality both the internal parameters and the density profile itself can change over time. We consider these assumptions to be acceptable within the scope of our work given that we are primarily interested in the distribution of extra-tidal stars, which had once escaped from the cluster have dynamics primarily dictated by the Galactic potential rather than the globular cluster itself. Of course, the density of stars along the extra-tidal structures, as well as the total mass lost, depend on these assumptions. That is to say that if the mass of the cluster was

---

[4] In particular, the adopted values have been taken from the edition available at `https://people.smp.uq.edu.au/HolgerBaumgardt/globular/parameter.html`, up to January 14, 2022.

Table 4.1 – Parameters of the Galactic mass models adopted in this work. Masses are in units of $2.32 \times 10^7 M_\odot$, distances given in units of kpc.

Parameters	M_{bulge}	M_{bar}	M_{thin}	M_{thick}	M_{halo}	b_{bulge}	a_{bar}	b_{bar}	c_{bar}	a_{thin}	b_{thin}	a_{thick}	b_{thick}	a_{halo}
PI	460.0	0.0	1700.0	1700.0	6000.0	0.3	–	–	–	5.3000	0.25	2.6	0.8	14.0
PII	0.0	0.0	1600.0	1700.0	9000.0	–	–	–	–	4.8000	0.25	2.0	0.8	14.0
PII-0.3-SLOW	0	990.0	1120.0	1190.0	9000.0	–	4.0	1.	0.5	4.8000	0.25	2.0	0.8	14.0

not assumed constant over time, but could possibly decrease, the gravitational attraction exerted by the cluster itself on its stars would be weaker and this would lead to an increasing mass loss and density along the tails. We could have proceeded with diminishing the mass over time, based on some assumptions on the temporal behavior of this relation, however, we did not find this approach satisfying. In this way. we would have taken into account a temporal evolution of the mass, but not of the size of the cluster, adding a supplementary hypothesis to the problem. For these reasons, we decided to maintain the simplest approach. We emphasize that other groups have followed the same methodology, maintaining masses and sizes that remain constant over time (see, e.g., Palau & Miralda-Escudé, 2019).

The summary tables giving both the current internal parameters of the clusters (total mass and half-mass radius), their astrometric quantities of relevance for this study and the line-of-sight velocities are publicly available[5]. We have made use of these tables for our work and we report them in a unique table in our paper for the sake of the completeness and self-consistency of the data used (see Table 4.4).

2.3 Simulations of the tidal stripping process: Galactic potentials

As for the Galactic mass distribution, we make use of the two axisymmetric Galactic mass models presented in Pouliasis et al. (2017) and of an asymmetric mass model, containing a central stellar bar, and we present it here for the first time. We recall the main properties of the two models of Pouliasis et al. (2017) below and we describe the asymmetric Galactic mass model, presented here for the first time, in more detail.

2.3.1 Model I by Pouliasis et al. (2017): An axisymmetric mass model for the Galaxy including a spherical bulge

Model I by Pouliasis et al. (2017) (abbreviated name: PI) consists of four components: two disks (thin and thick), both described by Miyamoto & Nagai potentials, a dark matter halo, and a central bulge. Its total potential is:

$$\Phi_{tot}(R,z) = \Phi_{thin}(R,z) + \Phi_{thick}(R,z) + \Phi_{halo}(r) + \Phi_{bulge}(r), \tag{4.3}$$

---

[5] All data can be found here `https://people.smp.uq.edu.au/HolgerBaumgardt/globular`.

with $r = \sqrt{R^2 + z^2}$,

$$\Phi_{thin}(R,z) = \frac{-GM_{thin}}{\left(R^2 + \left[a_{thin} + \sqrt{z^2 + b_{thin}^2}\right]^2\right)^{1/2}}, \tag{4.4}$$

$$\Phi_{thick}(R,z) = \frac{-GM_{thick}}{\left(R^2 + \left[a_{thick} + \sqrt{z^2 + b_{thick}^2}\right]^2\right)^{1/2}}, \tag{4.5}$$

$$\begin{aligned}\Phi_{halo}(r) =& \frac{-GM_{halo}}{r} - \frac{M_{halo}}{1.02a_{halo}} \times \\ & \left[\frac{-1.02}{1+\left(\frac{r}{a_{halo}}\right)^{1.02}} + \ln\left(1 + \left(\frac{r}{a_{halo}}\right)^{1.02}\right)\right]_R^{100},\end{aligned} \tag{4.6}$$

and

$$\Phi_{bulge}(r) = -\frac{GM_{bulge}}{\sqrt{r^2 + b_{bulge}^2}}, \tag{4.7}$$

where M_{thin}, M_{thick}, M_{halo}, and M_{bulge} are the masses of the disks, halo, and bulge. Also, $a_{thin}, b_{thin}, a_{thick}, b_{thick}, a_{halo}, b_{bulge}$ are the characteristic scale lengths of the thin and thick disks, the halo, and the central bulge, respectively (see Table 4.1).

This model is a modification of the classical Allen & Santillan (1991) model, made to include also the presence of a thick disk. As it has been discussed in detail by Pouliasis et al. (2017), the choice to include a massive spheroid in this model, as well as in the original Allen & Santillan (1991) model, is dictated by the need to reproduce CO/HI-based velocity curves, as those provided by Sofue (2012), which show a rise and then a sudden decrease of the velocity curve in the inner Galactic regions ($R \leq 2 - 3$ kpc). In an axisymmetric model, such a rise can be reproduced only if a central spheroidal component, with a typical mass greater than 10% of that of the disk(s), is added. However, as shown by Chemin et al. (2015), the central rise observed in the rotation of the molecular gas in the inner Galaxy may be an effect of non-circular motions generated by large-scale asymmetries such as the bar. Moreover, this feature is not reported in all the observational studies (see, e.g., M. J. Reid et al., 2014, on which model PII is based). In other words, if we do not assume that the mass distribution of the inner Galaxy is axisymmetric, the need for a massive spheroidal component to reproduce velocity curves, such as those from Sofue (2012), no longer persists. In addition to that, in the last decade, a number of works have shown that if a spheroidal bulge exists in the central regions of our Galaxy, it has to be small (few percents of the mass of the disk at the most, see among others Shen et al., 2010; Kunder et al., 2012; Di Matteo, A. Gómez, et al., 2015; A. Gómez et al., 2018). All these arguments suggest to employ this model (as well as all models including a massive central spheroid; see, e.g., Irrgang et al., 2013) with care when dealing with the central parts of the Galaxy. Since models with a massive central spheroid, however, are still used in the literature, we have included model PI here, as a term of comparison.

2.3.2 Model II by Pouliasis et al. (2017): An axisymmetric, bulge-less mass model for the Galaxy

Model II by Pouliasis et al. (2017) (abbreviated name: PII) consists of a spherical dark matter halo, with the same functional form adopted in the Allen & Santillan (1991) model, and of two disk components (a thin and a thick disk), with same functional form as PI. This model does not include any central spheroid (i.e., it is a bulge-less model) and thus its total potential is the sum of three components only:

$$\Phi_{tot}(R,z) = \Phi_{thin}(R,z) + \Phi_{thick}(R,z) + \Phi_{halo}(r), \tag{4.8}$$

with the thin, thick disks, and dark matter halo having the same functional forms adopted in PI.

As it has been shown in Pouliasis et al. (2017), this model satisfies a number of observational constraints, such as the stellar density at the solar vicinity, thin- and thick-disk scale lengths and heights, the rotation curve as provided by M. J. Reid et al. (2014) and the absolute value of the perpendicular force, K_z, as a function of distance to the Galactic centre (see Sect. 2.5 in Pouliasis et al., 2017). As it is, however, an axisymmetric model, it fails to accurately describe the inner few kpc of the Galaxy, where the stellar mass distribution has been shown to be asymmetric.

2.3.3 Model II with a massive, slowly rotating stellar bar

The third mass model (abbreviated name: PII-0.3-SLOW) that we use in this paper is a version of PII by Pouliasis et al. (2017) modified to include a rotating stellar bar, whose mass has been assigned to be 30% of the (thin+thick) disk mass of PII. We assume that the bar rotates with a constant pattern speed of $\Omega_{bar} = 38\text{km s}^{-1}\text{kpc}^{-1}$ and that it is currently inclined of 25° with respect to the Sun-Galactic center direction (see Bland-Hawthorn & Gerhard, 2016). We model it as a triaxial distribution, whose gravitational potential is given by Long & Murali (1992):

$$\Phi_{bar}(x,y,z) = \frac{GM_{bar}}{2a_{bar}} \ln\left(\frac{x - a_{bar} + T_-}{x + a_{bar} + T_+}\right), \tag{4.9}$$

with $T_\pm = \left[(a_{bar} \pm x)^2 + y^2 + (b_{bar} + \sqrt{c_{bar}^2 + z^2})^2\right]^{1/2}$ and $a_{bar}, b_{bar}, c_{bar}$ the characteristic bar parameters. The total gravitational potential generated by this model thus takes the form:

$$\Phi_{tot}(x,y,z) = \Phi_{thin}(R,z) + \Phi_{thick}(R,z) + \Phi_{halo}(r) + \Phi_{bar}(x,y,z). \tag{4.10}$$

with all characteristic values given in Table 4.1. Practically, to include the bar, we reduced the mass of the disks in such a way to maintain the total stellar mass of this model as that of PII. Long & Murali (1992) provide the formulas of the accelerations generated by this triaxial distribution in the reference frame of the bar. To calculate and add them to the accelerations generated by the disks and dark matter halo, at each time step, we converted the positions of all particles in the rotating, non-inertial reference frame of the bar, computed the corresponding accelerations on each particle, and then transformed these accelerations back in the inertial reference frame described in Sect. 2.1. In this way, the accelerations due to the bar are added to those generated by the other terms of the Galactic mass distribution.

We emphasize that we do not consider this model as the best possible representation of the Galactic mass distribution, especially in the central region. It can, however, provide a first indication on how the inclusion of a rotating asymmetric component in the inner Galaxy can affect the globular cluster streams, near and far from the Galactic center.

Moreover, since the exact characteristics of the Milky Way bar are still subject to debate (see, e.g., Bland-Hawthorn & Gerhard, 2016), it is important to explore how varying the parameters adopted in this paper, such as the pattern speed, the mass, or the length of the bar, can affect the characteristics of the whole set of streams. More complex shapes for the bar can also be explored, for example, by substituting the inner parts of the triaxial bar with a boxy-peanut-shaped morphology, which has been shown to characterize the inner Milky Way (see, e.g., Wegg & Gerhard, 2013; Wegg, Gerhard & Portail, 2015). These topics are, however, beyond the scope of the present paper. In sum, given the uncertainties on the bar's physical extent and how it can change over the time span investigated here, its affect on the streams presented here are purely indicative.

3 Results

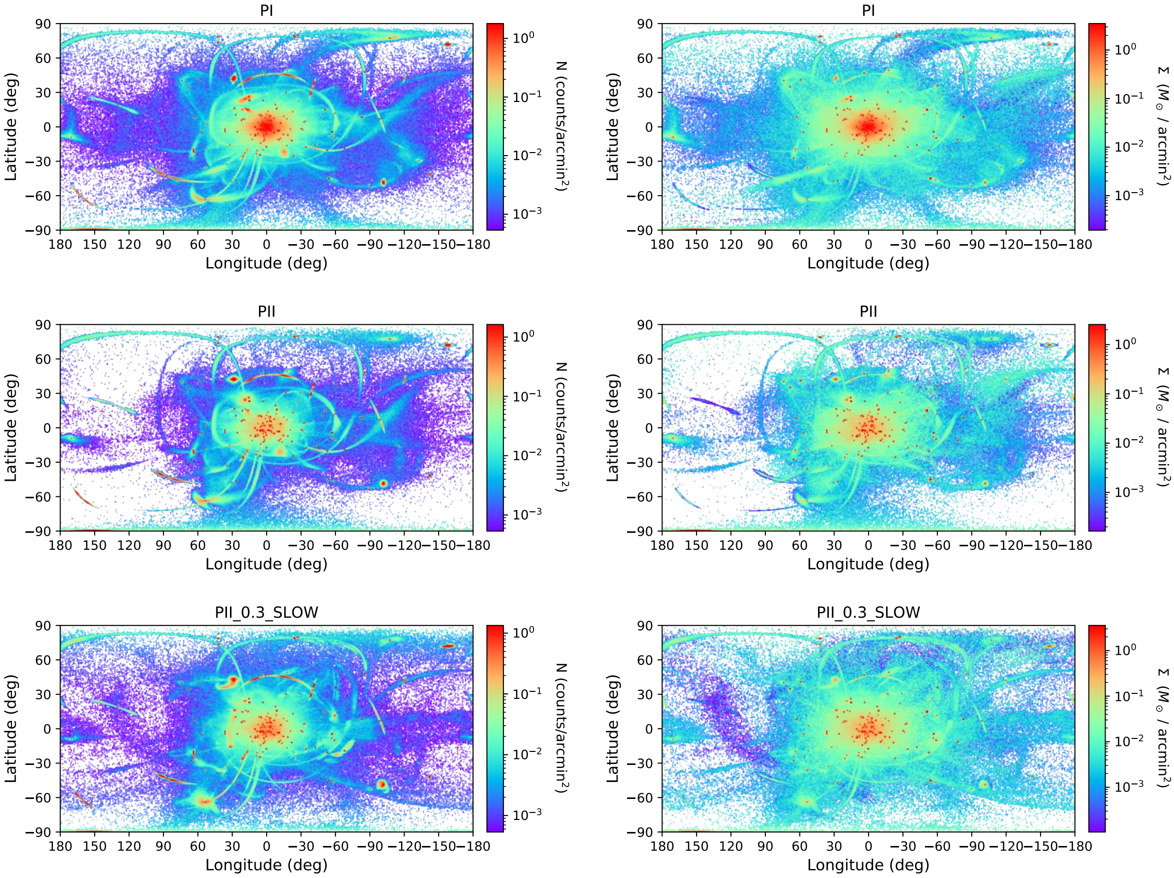

Figure 4.1 – The stellar surface density of the *ensemble* of extra-tidal features around the entire population of Galactic globular clusters at the current time, as predicted by our models. *Left:* Surface number density. *Right:* Surface mass density. Top row corresponds to model PI, the middle to model PII, and the bottom column to model PII-0.3-SLOW, as indicated. All densities are expressed in a logarithmic scale. The red point-like density maxima correspond to the current positions of the globular clusters. Values of higher density are overplotted. Thus in the case of mass density, diffuse tidal debris of more massive globular clusters covers the entire (ℓ, b) space and occults delicate tidal features, which are more visible when considering number density counts. In all panels, only the reference simulations are shown for clarity.

A few basic premises: Given the large number of simulations carried out and the wealth of information contained in them, it is not possible to exhaust all possible applications of this simulation database in this paper. We have therefore chosen to proceed as follows.

In Section 3.1, we present an overview of the distribution of all streams in Galactic coordinates. This coordinate space will be the one used in the remainder of the entire article. This first section allows us to show qualitatively how the global distribution of streams varies, depending on the Galactic potential used.

We then move on (Section 3.2) to present the global system of streams as a function of their distance from the Sun. In this section, we also show the kinematic properties of the streams, such as proper motions and line-of-sight velocities, that can be directly compared to Gaia data or other astrometric and spectroscopic surveys. This section also allows us to show the variety of morphologies that the stars which escaped from globular clusters can take. In Section 3.3, we explore this issue in more detail, showing how these morphologies depend primarily on the orbital characteristics of the clusters and their distance from the Galactic center. For the most interesting cases, we compare the tidal structures predicted by our simulations with streams found in observational data. For this purpose, we make use of the *galstreams* library of stellar streams in the Milky Way (Mateu, 2023), which constitutes a unique and public database summarizing angular positions, distances, proper motions, and line-of-sight velocity tracks for nearly a hundred Galactic stellar streams. Any stream that is not included in this library is not be compared to our simulations in the context of this paper.

We note that the tidal features associated with each of the 159 simulated clusters are presented in Supplemental Material 5.2. To avoid making this Supplemental Material too long, the tidal features above are presented only in the case of the potential PII. However, all the data are available on a dedicated site[6] where it is possible to the way the characteristics of these streams change, for any cluster, in the three chosen potentials.

3.1 A sky full of streams

Figure 4.1 shows the number and mass density distributions of the whole set of simulated globular clusters and their extra-tidal features in Galactic longitude and latitude for the three Galactic potentials.

For all Galactic mass models adopted, a striking characteristic among the plots in Figs. 4.1 is the variety of features that our models predict, which are reminiscent of the tidal tails, stellar streams, and shells that are produced by interacting and merging galaxies in the process of mass assembly (see, e.g., Mancillas et al., 2019). Some clusters have very thin and elongated streams, which describe arcs that can extend up to 180°

---

[6] `http://etidal-project.obspm.fr/`

in longitude, or tens of kpc in physical space. In some other cases, extra-tidal features appear shorter (a few up to ten degrees) and sometimes also thicker (about 10° in the sky) than others. Finally, in some cases, clusters are surrounded by extended structures, such as halos, rather than coherent and thin streams.

This variety of properties depends on several factors: the distance of the stream to the Sun (due to projection; i.e., for a given physical thickness, the closer the stream is to the Sun, the more extended it appears in the (ℓ, b) plane), its orbital phase (towards the peri-center or the apo-center of the orbit), and the orbital properties of the parent globular cluster. We also see from these figures that stellar particles stripped from their parent clusters do not only redistribute in coherent structures, but in some cases, they can also contribute to a more diffuse density distribution.

Because of the large number of simulated clusters, we have chosen not to present the corresponding extra-tidal features one-by-one in the main part of this paper, but we have rather decided to describe these extra-tidal features with a global approach, by first adopting a criterion based on the distance of these features to the Sun (see Sect. 3.2) and then discussing the types of distributions tidal debris can have and how these depend on the cluster orbital parameters (see Sect. 3.3). All the extra-tidal structures generated by the 159 globular clusters simulated in this paper, and their corresponding uncertainties, are reported in Supplemental Material 5.2. Among them, we include clusters with thin and elongated tails, such as IC 4499, NGC 3201, NGC 4590, NGC 5024, NGC 5053, Pal 5, to cite a few, as well as clusters such as AM 1, Pal 14, Pal 4, and Pal 15, whose extra-tidal material shows a halo-like configuration, and clusters such as NGC 1261, NGC 4147, NGC 6356, and UKS 1, whose stripped stars show a remarkable diffuse distribution in the field.

Finally, even when our models are not tailored to accurately reproduce the mass loss from globular clusters, since (as described in Sect. 2.2) we have adopted a test-particle approach with a time-constant globular cluster potential, it is however tempting to estimate, to a first order, the total mass associated with the tidally stripped population and compare it to the current mass. By calculating the mass lost in the field in the past 5 Gyr as the sum of the mass of all particles[7] that have escaped the cluster ($t_{\rm esc} > 0$), we find that the PI model sheds $2.1 \times 10^7 M_\odot$, which is 55% of the GC population's current mass. The PII model shed is $2.7 \times 10^6 M_\odot$, which is 7% of the current mass. Similarly, the PII-0.3-SLOW model lost $3.7 \times 10^6 M_\odot$, which is 10% of the current mass and gives a half mass radius of 6.3 kpc.

This mass roughly constitutes one-hundredth to one-tenth of the total stellar halo mass (Bland-Hawthorn & Gerhard, 2016) and it is probably only a lower limit on the mass of

---

[7] To estimate the mass of particles in each cluster we have quantified the number of particles, N_{bound}, bound to the cluster at the end of the simulation and calculated the corresponding particle mass as $m_p = M_{GC}/N_{bound}$, where M_{GC} is the current mass of a cluster given in Table 4.4.

escaped stars in the field, since a number of clusters initially in the Galaxy must have been destroyed over time (see introduction) and are thus no longer identifiabl as globular clusters today. It is also interesting to note that escaped stars are mostly redistributed in the inner Galaxy, with the half-mass radius of the PI model being 4.0 kpc and that of the PII and PII-0.3-SLOW models being 6.3 kpc.

The total mass lost from the clusters, as well as its spatial distribution, thus depends on the Galactic potential adopted: the variations between the PI model and both the PII and PII-0.3-SLOW models are of course caused by the PI's inclusion of the bulge, which leads to larger tidal forces in the center of the galaxy and subsequently drives larger mass loss.

Despite the differences in the modeling approach, it is interesting to compare our results to those of Baumgardt (2017). Briefly, our experiments differ in the following ways: they employ N-body simulations while we use our test-particle approach; they have an integration time of 12 Gyrs compared to our 5 Gyrs; lastly, their clusters have circular orbits in a Galactic potential modeled as an isothermal sphere as compared to the more realistic orbits and Galactic potentials considered in this work. Interestingly, the authors find that over 12 Gyrs their population of globular clusters lose two-thirds of their initial mass. This is roughly consistent with our application of the PI model, whose globular clusters shed 35% of their initial mass in 5 Gyrs, which is roughly half the mass found by Baumgardt (2017) in a period that is also about half as long.

3.2 From the nearest to the furthest extra-tidal structures

The analysis presented in this section along with the corresponding information are given in Figures 4.2, 4.3, 4.4, and 4.5 are restricted to the PII model.

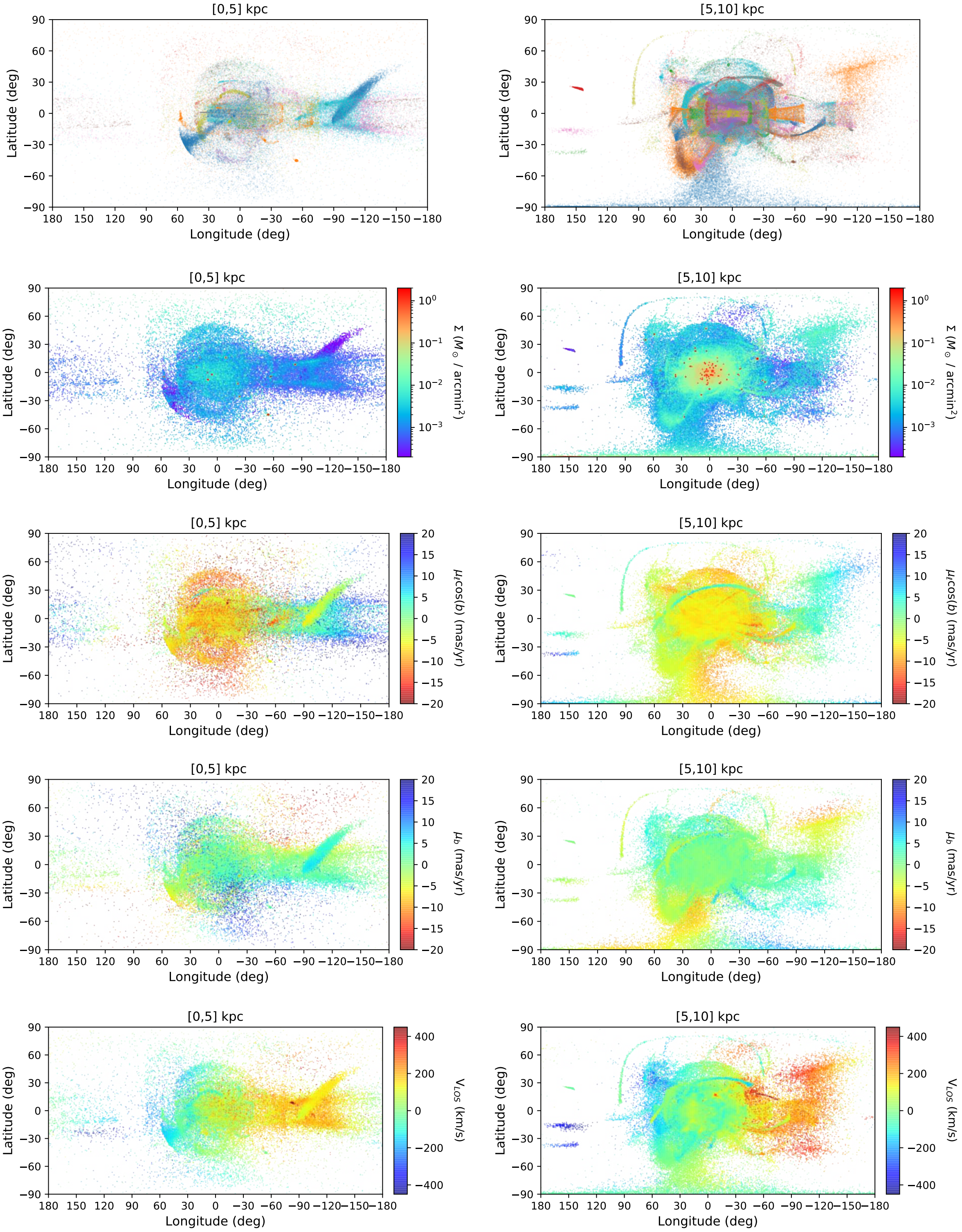

Figure 4.2 – The extra-tidal features colored and weighted by various quantities within limited distance bins from the Sun projected in the (ℓ, b) plane. All outputs arrise from using the PII galactic potential model and only the reference simulation is shown in order to preserve clairty. *Left column*: Extra-tidal features found at a distance of [0,5] kpc from the Sun. *Top row:* Scatter plot, with different colors indicating different progenitor clusters. *Second row:* Mass density map in logarithmic scale. *Third row:* Map color-coated by proper motions in longitudinal direction. *Fourth row:* Map color-coated by proper motions in latitudinal direction. *Bottom row:* Map color-coded by line-of-sight velocities. *Right column*: Same as left column, but for the tidal features found at a distance of [5, 10] kpc from the Sun. Note: the 10 colors used in the top panels are recycled between the 159 clusters, thus, all particles from the same cluster share one color, but a color is not unique to a cluster.

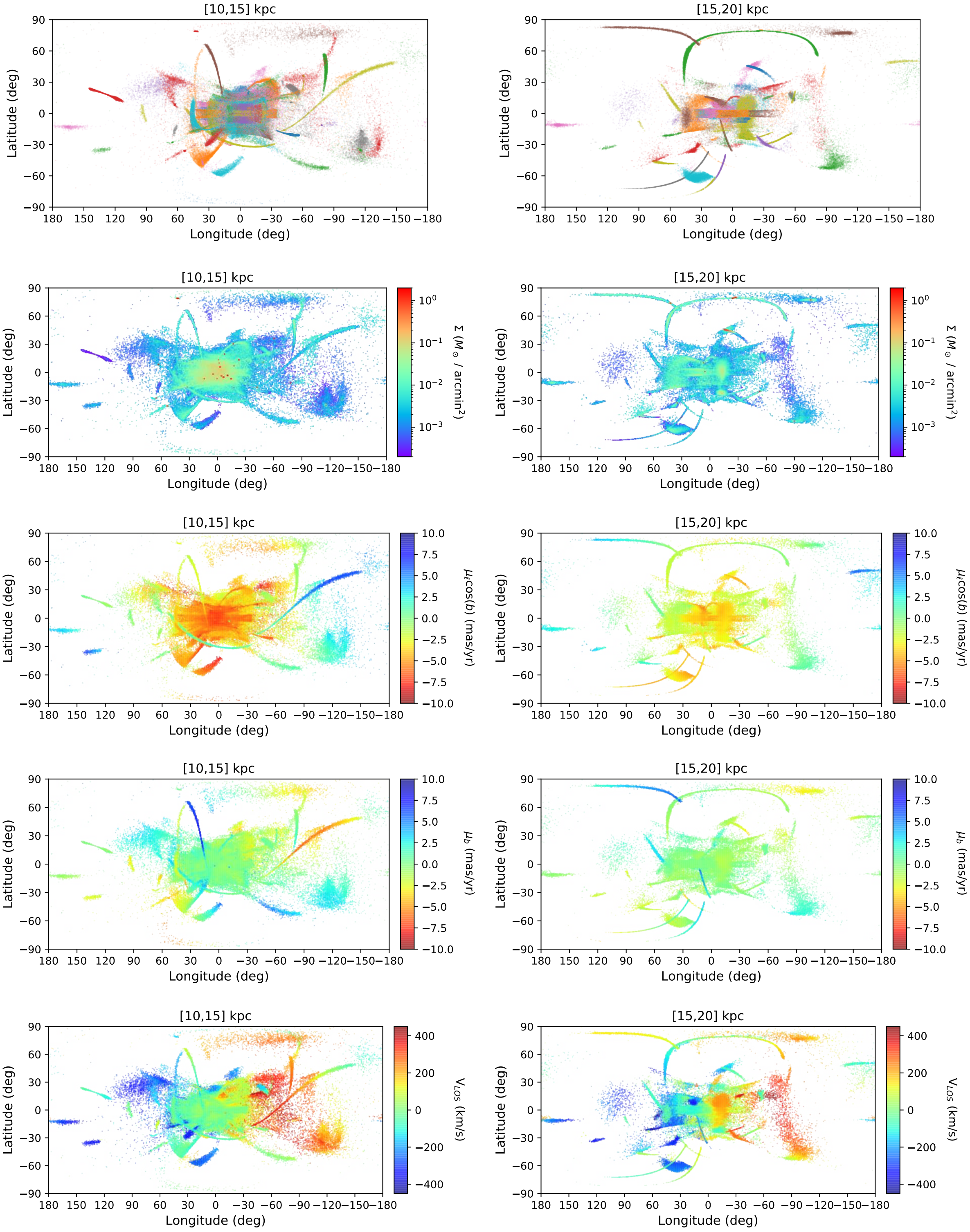

Figure 4.3 – As for Fig. 4.2, but for two father distance bins. Here, we are beyond the galactic nuclues and tidal debris are less diffuse in nature and more often stream-like. The *left column* shows debris at distances between [10, 15] kpc from the Sun while the *right column* shows debris at distances between [15, 20] kpc from the Sun.

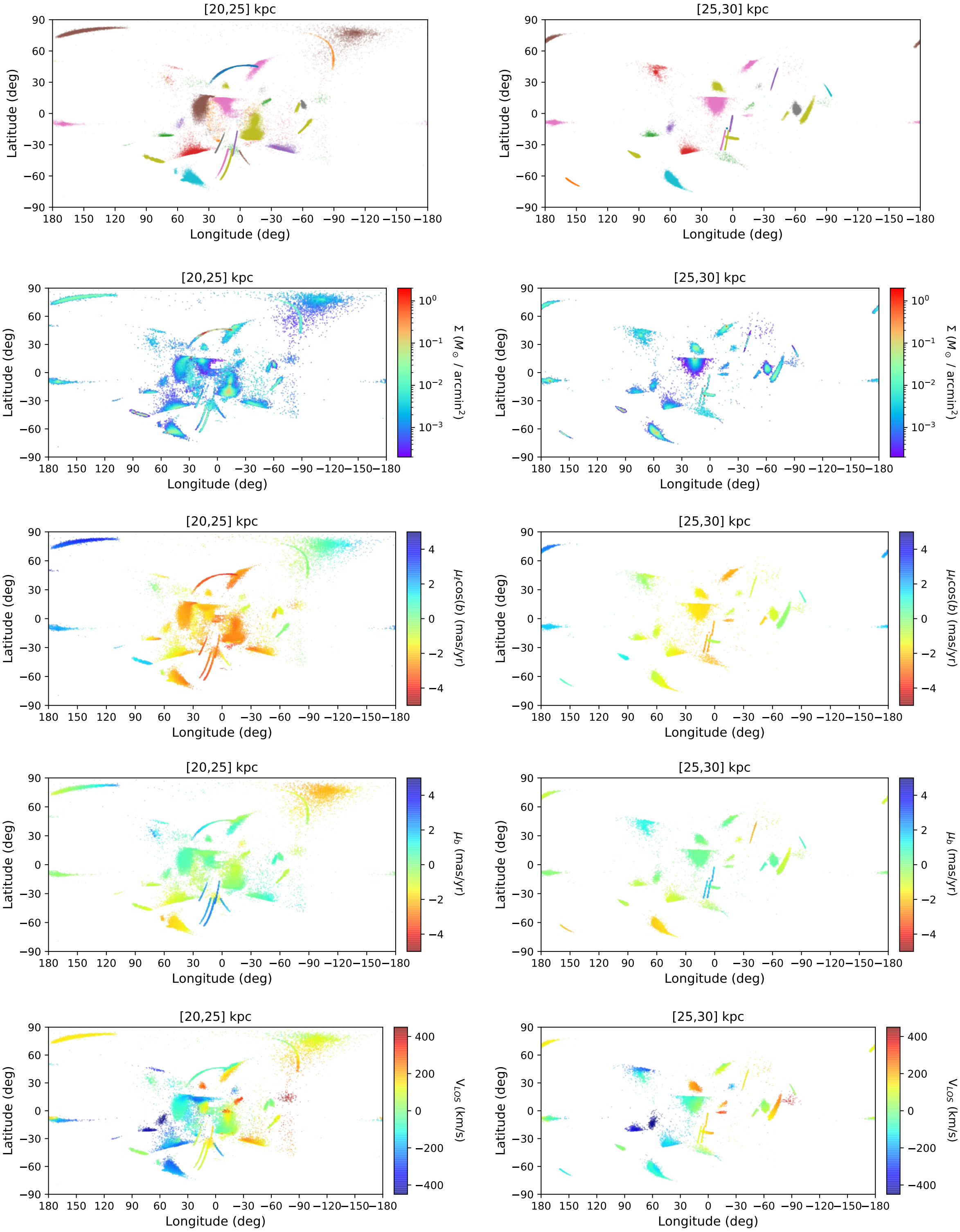

Figure 4.4 – As for Fig. 4.2 & 4.3, but for increased distances from the Sun. Here we notice that the tidal debris becomes more sparse as we move even father away from the galactic center. The *left column* shows debris at distances between [20, 25] kpc from the Sun while the *right column* shows debris at distances between [25, 30] kpc from the Sun.

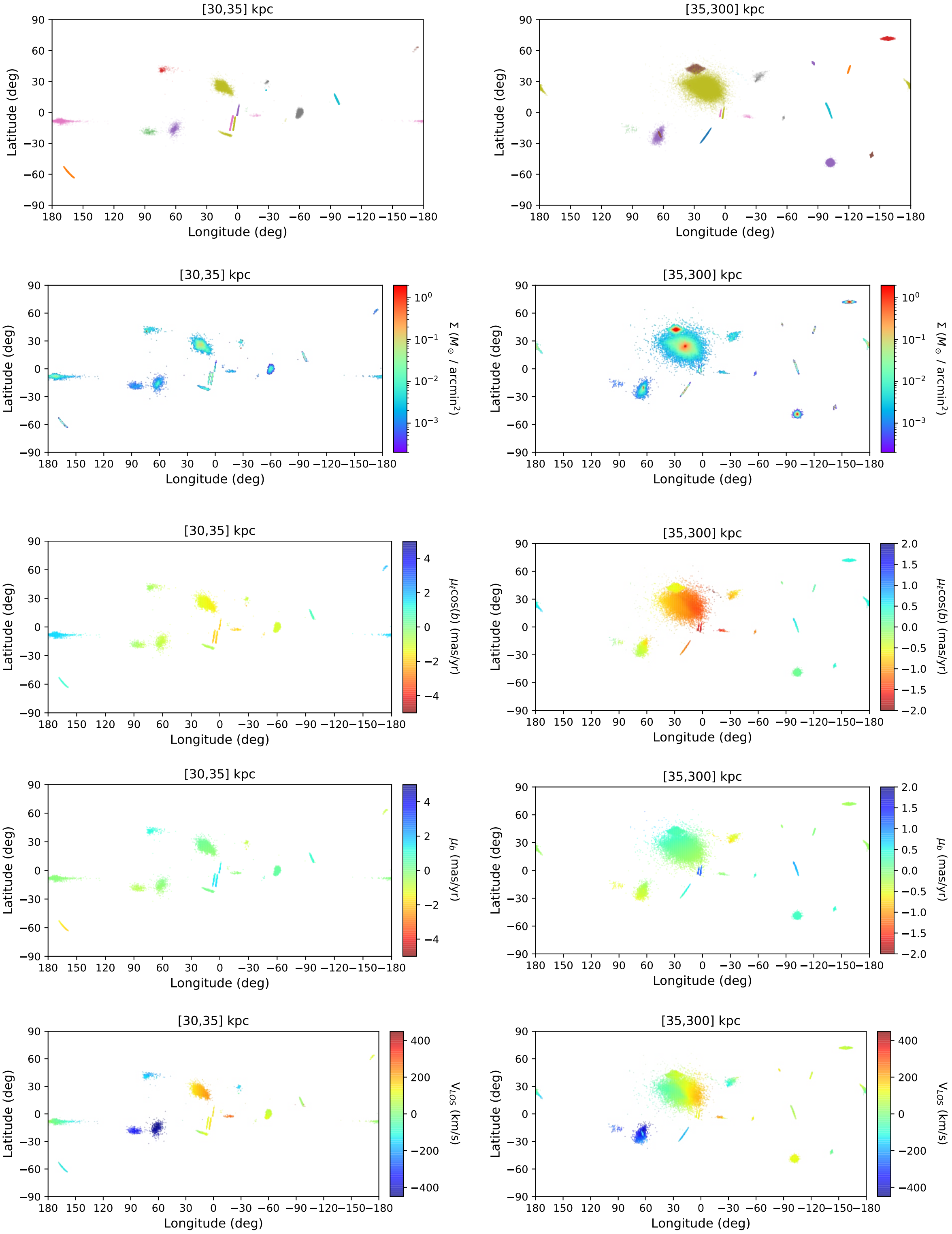

Figure 4.5 – As for Fig. 4.2-4.4, but now we include debris from the most outer extent of the galaxy. The *left column* shows debris at distances between [30, 35] kpc from the Sun while the *right column* shows debris at distances between [35, 300] kpc from the Sun.

In this section, we analyze structures located at different distances from the Sun. We identify structures as main or secondary on the basis of the fraction of stars they represent. If, for example, a cluster contributes more than 10% of its stripped stars in a given distance range, we consider the associated structure to be significant and we define it as a main structure in this distance range. If, on the other hand, the fraction of stripped stars from a cluster is between 1% and 10%, we define the associated structure as being "secondary". Structures that constitute less than 1% of the cluster mass are considered insignificant in that range. The main and secondary structures for each distance bin are reported in Table 4.2, where they are named by their progenitor cluster. Below, we describe the structures encountered at different distances from the Sun, from the closest to the most distant. For the following discussions, we refer to Figs. 4.2 to 4.5, where we report the different streams in a given distance range (top row in each figure), the corresponding mass density generated by all the structures found in that bin (second row), the longitudinal and latitudinal proper-motions map (third and fourth rows), and the line-of-sight velocities (bottom row).

The [0–2] kpc distance range: Among the 159 simulated clusters, only NGC 6121 is currently at a distance of less than 2 kpc from the Sun. In addition to stars stripped from this cluster within this distance-to-the-Sun range, we have identified very diffuse and low density extra-tidal stars associated with five other clusters, which are currently several kpc away from the Sun, as reported in Table 4.2. Of these, only UKS 1 and NGC 6121 have a significant fraction of their stripped mass in this distance range. All the others contribute with only a few percent. None of these clusters seem to show well-defined, stream-like features in the (ℓ, b) plane. This extra-tidal material appears indeed quite uniformly redistributed, in a latitude range mostly inside $-30°$ to $30°$, and is mostly found at negative longitudes. Because in this interval range there is no remarkable extra-tidal structure found on the sky, we decided to plot this distance bin together with the [2–5] kpc bin (see Fig. 4.2, left column).

The [2–5] kpc distance range: As the distance from the Sun increases, many more tidal structures are intercepted. Eleven globular clusters are found at a distance between 2 and 5 kpc from the Sun; and together with structures emanating from these clusters, we also find extra-tidal material associated with other 48 clusters, 19 of which are significant (as listed in Table 4.2). Some extra-tidal structures are clearly identifiable, even when over-plotted with all the others: this is the case, for example, for the tidal material associated with the E 3 cluster, which appears as an extended thick stream (as shown in Fig. 4.2) at approximately $-100°$ longitude. This is also the case for the complex tidal structure associated with BH 140, which resembles a ribbon in the sky, with a bifurcation at negative longitudes whose edges extend to about $-30°$ and $30°$ latitude. In addition to these, there are a series of circular halos concentric about the Galactic center, with abrupt drop-offs in density tracing the furthest extent of diffuse debris emanating from a variety of clusters. Overall, few streams are immediately recognizable in this range, although plenty of debris is present. This is expected given that this range samples a bite of the Sun-side of the Galactic disk and that this range has a relatively small volume. In this, as in the following distance ranges, the $v_{\ell os}$ maps show that the tidal material at negative Galactic longitudes has, on average, positive $v_{\ell os}$ while material at positive Galactic longitudes has, on average, negative $v_{\ell os}$, which is due to the solar reflex velocity. This is the same trend observed for the whole set of radial (i.e., line-of-sight) velocities in Gaia DR3; for instance, we refer to the bottom panel of Fig. 5 from Katz et al. (2023), although less extreme velocities are reported in their plot since their dataset is dominated by disk stars, whereas our maps have a high proportional contribution of halo stars (additionally, they use median values in their bins, while we use an average). In order to quantify the net rotation of the system of streams, we calculated the mean angular momentum about the Galactic pole as $\langle L_z \rangle = \sum_i L_{z,i} m_{p,i} / \sum_i m_{p,i}$, where $m_{p,i}$ is the mass of each star particle indexed by i (as discussed in footnote 7) and $L_{z,i}$ is the corresponding particle's angular momentum. The mean angular momentum is found to be $\langle L_z \rangle = -300$ kpc km s^{-1}, which shows a slight co-rotation of the system of streams with the disk though there is much dispersion about this value – as shown in bottom right panel of Fig. 4.34 in the Supplemental Material.

The [5–10] kpc distance range: The [5–10] kpc distance range, which includes the Galactic center, contains much more material. A total of 79 clusters are found in this range, together with tidal structures associated with 131 different progenitors redistributed among main and secondary structures. Some tiny streams are visible in the density maps as well as in proper motions and line-of-sight velocity spaces (see Fig. 4.2, right column): the trailing portion of the tail of the globular cluster Pal 1, at $(\ell, b) \sim (140°, 25°)$; the most extreme portion of the trailing tail of NGC 3201 at $(\ell, b) \sim (150°, -37°)$; the waterfall-like shape of NGC 288, particularly evident at $b \lesssim -60°$; the thin inverted U-shape of NGC 4590 at positive latitudes spanning a large longitude extent from $\ell \simeq -60°$ to 100°; the portion of the E 3 tails the closest to the cluster at $(\ell, b) \sim (-75°, -15°)$, which continues from the more easily recognizable portion in the [0–5] kpc bin.

The [10–15] kpc distance range: In the [10–15] kpc range, we find tidal structures associated with 134 progenitors, as listed in Table 4.2 and reported in Fig. 4.3 (left column), 27 of which are related to globular clusters that are also found in this distance bin. We note that at these distances from the Sun, the distribution of tidal features in directions towards the Galactic center, from $-30°$ to $30°$ longitude, appears less fuzzy than the one characterizing the [0–5] and [5–10] kpc distance bins. Tidal features here are beyond the Galactic center, and are mostly associated with disk or halo clusters.

Among the thinnest structures, we find the stream associated with Pal 1, at $(\ell, b) \sim (120°, 15°)$, which is also visible in the distance bin [5–10] kpc (see previous discussion), but which is even more elongated here. NGC 6101 shows the nearest portion of its long thin diagonal tidal tail that spans negative longitudes and ranges from $-15°$ to $45°$ latitude. Additionally, this stream is also unique against its counter parts in proper motion space. NGC 5053's nearest portion appears as a vertical tidal tail at $-80°$ longitude. Similarly, NGC 5466 is shown vertically at 25° longitude.

Among the thickest structures, we can recognize general diffuse and bowtie-like shapes. There are also spoke-like structures departing radially from the Galactic center. For instance, we can associated the extra-tidal material with NGC 7078 at $(\ell, b) \sim (60°, -28°)$, as well as NGC 7089, which is nearly parallel to the previous structure, but at lower latitudes at $(\ell, b) \sim (50°, -40°)$.

The [15–20] kpc distance range: At larger distances ([$15 - -20$] kpc range, see Fig. 4.3), some of the most striking features are associated with the clusters NGC 5024 and NGC 5053, whose long thin tails essentially overlap in this distance, with the latter covering the former, and appearing at high latitudes spanning a longitudinal range from $\ell \sim -90°$ to $\ell \sim 45°$. Again, the long thin stream of NGC 5466 appears in this range (as will be the case for the next) and is at high latitudes at roughly 85° and positive longitudes. There is also the thicker extended structure of NGC 4147 whose diffuse structure emanates from about $(\ell, b) \sim (-100°, 80°)$.

In this distance bin, we find long tidal tails emanating from globular clusters associated with the Sagittarius dwarf galaxy, which are particularly visible at negative longitudes: a long thin stream is associated with Pal 12 at positive longitudes and latitudes $b \leq -15°$, as well as two overlapping structures at $0° \lesssim \ell \lesssim 30°$ longitude, namely, Ter 7 (and Ter 8 in the next distance bin). A word of caution is needed here: the mass loss from these clusters may be incorrect, since we do not include the presence of the Sagittarius dwarf galaxy itself. The potential well associated with this latter could change the tidal effects experienced by clusters associated with Sagittarius, especially in the case of NGC 6715, which sits at the center of this dwarf galaxy. The inclusion of the Sagittarius dwarf will be the subject of future investigations. Overall, in this distance bins, we find 11 clusters and 61 streams, all listed in Table 4.2.

The [20–25] and [25–30] kpc distance ranges: In the following distance bins (at [20–25] kpc and [25–30]; see Fig. 4.4), globular clusters and extra-tidal structures become less numerous, although some are still visible, such as Pal 5 at $(\ell, b) \sim (0°, 45°)$. In more detail, in the [20–25] kpc bin we find tidal features associated with 37 different progenitors, 8 of which are associated with globular clusters whose current positions are in the same distance bin; in the [25–30] kpc bin, 7 clusters are found, together with tidal features associated with 30 other progenitor clusters which do not lie in this same distance range. In both bins, the streams emanating from globular clusters associated with the Sagittarius dwarf galaxy are still visible, as well as the most extreme portion of the tail associated with NGC 5466.

The [30–35] and [35–300] kpc distance ranges: Finally, in the last distance bins (see Fig. 4.5), thin streams become rare. Some small streams are visible: Pyxis at $(\ell, b) \sim (-100°, 0°)$; NGC 2419 at $(\ell, b) \sim (-180°, 30°)$; Pal 4 at $(\ell, b) \sim (-160°, 75°)$; Pal 3 at $(\ell, b) \sim (-120°, 45°)$. Many more have a diffuse and halo-like structure. For instance, the blob associated with Pal 15, centered at $(\ell, b) \sim (15°, 20°)$; AM 1 at $(\ell, b) \sim (-100°, -55°)$; Eridanus at $(\ell, b) \sim (-140°, -45°)$; Pal 14 at $(\ell, b) \sim (30°, 45°)$; Laevens 3 at $(\ell, b) \sim (65°, -20°)$, which is completely enveloped by NGC 7006. In total, in these two distance bins, we find 4 and 12 clusters, respectively, along with their associated streams, together with extra-tidal material associated with 14 and 19 progenitors in total.

3.3 Disks of inner and outer halo clusters: A variety of morphologies and shapes for extra-tidal structures

The analysis presented in the previous section allows us to appreciate the variety of morphologies found for extra tidal structures, from padlocks to "Easter eggs," disks, ribbons, and canonical streams. Moreover, some structures are limited in latitude and longitude, while some others fill nearly the entire sky.

To more easily capture the similarity and differences in the morphology of the extra-tidal features surrounding Galactic globular clusters, we can group the latter on the basis of their orbital parameters[8](see Supplemental Material 5.4 for more details), as follows: *Disk clusters*: A cluster is classified as a disk cluster if $\arctan(z_{max}/R_{max}) \leq 10°$, where z_{max} and R_{max} are, respectively, the maximum height above or below the Galactic plane reached by its orbit in the last 5 Gyr and its maximum in-plane distance from the Galactic center. *Inner clusters*: All clusters with $r_{max} \leq R_{\odot}$ that are not classified as disk clusters enter this group. Contrary to R_{max}, which is the maximum in-plane distance that a cluster reaches from the Galactic center, r_{max} is the maximum 3D distance, that is, $r_{max} = \max(\sqrt{R^2 + z^2})$, with the maximum calculated over the whole cluster orbit. *Outer clusters*: All clusters with $r_{max} > R_{\odot}$ that are not classified as disk clusters are included in this group.

By using the orbital radius of the Sun as the criterion for inner and outer clusters,

---

[8] We caution the reader that the classification of disk, inner and outer clusters made in this Section is based on the orbital parameters of the clusters, as found when their orbits are integrated in model PII. This classification may slightly change if model PI or model PII-0.3-SLOW were adopted.

Table 4.2 – List of tidal structures found in different intervals of distance to the Sun. The tidal structures are named by their progenitor clusters. If the parent cluster is also in the distance range under consideration, the name of the tidal structure is shown in bold. Second column reports the main structures found in a given distance bin. The third column list secondary structures. The numbers in parenthesis in the second column and third column (numbers with normal font) correspond to the total number of main and secondary structures found in a given distance range. The number of clusters in each distance bin is also reported in the second column (bold numbers in parenthesis).

Distance (kpc)	Main tidal structures	Secondary tidal structures
[0-2]	(**1**,2) **NGC6121**, UKS1	(4) BH140, Djor1, NGC6333, NGC6356
[2-5]	(**11**,30) **NGC6397**, **NGC6544**, **NGC3201**, **BH140**, **NGC104**, **NGC6838**, **NGC6366**, **NGC6752**, **IC1276**, **NGC6656**, **2MASS-GC01**, NGC6284, NGC6356, NGC6287, VVV-CL001, NGC6254, NGC5927, E3, NGC6121, VVV-CL001, Djor1, UKS1, Ter10, 2MASS-GC02, Pal10, NGC5139, NGC6333, NGC6441, NGC6541, NGC288	(29) FSR1716, FSR1758, NGC1851, NGC1904, NGC2298, NGC2808, NGC362, NGC4372, NGC4833, NGC5897, NGC5986, NGC6205, NGC6218, NGC6235, NGC6273, NGC6316, NGC6352, NGC6388, NGC6496, NGC6681, NGC6749, NGC6760, NGC6809, NGC6864, NGC7078, Pal2, Pal8, Ter12, Ton2
[5-10]	(**79**,124) **VVV-CL001**, **NGC7099**, **NGC6362**, **Ton2**, **Djor1**, **VVV-CL001**, **NGC6496**, **Djor2**, **NGC6535**, **NGC6528**, **NGC6539**, **NGC6540**, **NGC6553**, **2MASS-GC02**, **Ter12**, **BH261**, **Ter9**, **NGC6712**, **NGC6717**, **NGC6723**, **NGC6749**, **NGC6760**, **Pal10**, **HP1**, **Ter4**, **Ter2**, **Ter3**, **NGC2298**, **E3**, **NGC4372**, **NGC4833**, **NGC5904**, **NGC5927**, **FSR1716**, **Lynga7**, **NGC6144**, **NGC6171**, **NGC6352**, **ESO452-SC11**, **NGC6218**, **FSR1735**, **NGC6254**, **NGC6256**, **NGC6287**, **NGC6293**, **NGC6304**, **NGC6355**, **NGC6809**, **NGC6637**, **NGC6402**, **NGC6325**, **NGC6341**, **NGC6342**, **NGC6380**, **NGC6401**, **NGC6440**, **NGC6517**, **NGC6522**, **NGC6541**, **NGC6558**, **NGC6624**, **NGC6626**, **NGC6638**, **NGC6642**, **NGC6652**, **NGC6681**, **Pal6**, **Ter1**, **Ter5**, **Ter6**, **NGC6333**, **NGC288**, **NGC362**, **NGC6273**, **NGC6266**, **NGC6205**, **NGC5139**, **Liller1**, **NGC5946**, NGC5897, NGC1904, NGC6752, NGC6656, NGC6121, NGC1851, NGC6864, NGC7078, NGC7089, NGC6316, NGC5272, NGC6779, NGC2808, NGC4590, Rup106, NGC104, NGC4147, NGC3201, Pal11, Pal1, NGC1261, BH140, NGC6235, Ter10, NGC6569, UKS1, NGC6453, NGC6139, NGC6426, NGC6397, NGC6093, NGC6388, FSR1758, IC1276, NGC6838, NGC6366, NGC5986, NGC6441, NGC6356, NGC6584, NGC5286, NGC6544, NGC6284, Pal8, NGC6981	(7) 2MASS-GC01, IC1257, NGC5634, NGC5694, NGC6229, NGC7006, Pal2
[10-15]	(**27**,115) **NGC6453**, **NGC5272**, **NGC6584**, **Pal8**, **NGC6316**, **NGC5897**, **NGC6284**, **NGC6139**, **NGC6093**, **NGC5986**, **NGC5286**, **NGC6235**, **NGC2808**, **NGC1904**, **NGC1851**, **NGC6101**, **NGC6779**, **NGC6388**, **Pal11**, **Pal1**, **Ter10**, **NGC4590**, **NGC7089**, **NGC6569**, **NGC7078**, **FSR1758**, **NGC6441**, NGC6304, NGC6254, FSR1735, NGC6426, NGC6397, NGC6362, Ton2, NGC6256, NGC6366, NGC6287, NGC6352, NGC6355, NGC6356, NGC6218, NGC6293, VVV-CL001, NGC6171, NGC5024, NGC1261, NGC2298, E3, NGC3201, NGC4147, NGC4372, Rup106, BH140, NGC4833, NGC5053, Ter3, NGC5466, NGC5634, IC4499, NGC5904, NGC5927, FSR1716, UKS1, NGC6121, NGC6144, Lynga7, NGC6553, VVV-CL001, NGC6496, NGC5946, NGC6205, NGC6266, NGC6273, NGC6333, NGC6341, NGC6342, NGC6401, NGC6402, NGC6517, NGC6541, NGC6544, NGC6558, NGC6626, NGC6652, NGC6656, NGC6681, NGC6864, Pal6, Ter1, Ter5, NGC5139, NGC362, NGC104, Ter12, Djor2, NGC6535, NGC6528, NGC6539, NGC6540, 2MASS-GC01, Ter9, 2MASS-GC02, IC1276, BH261, NGC7099, NGC6712, NGC6723, NGC6749, NGC6752, NGC6760, NGC6809, NGC6838, NGC6934, NGC6981, NGC288	(18) Djor1, ESO280-SC06, ESO452-SC11, HP1, IC1257, NGC5694, NGC5824, NGC6229, NGC6325, NGC6380, NGC6638, NGC6642, NGC6717, NGC7006, NGC7492, Pal10, Pal2, Ter6
[15-20]	(**11**,46) **NGC6356**, **NGC5466**, **NGC1261**, **UKS1**, **NGC4147**, **IC4499**, **NGC5024**, **NGC5053**, **Pal12**, **NGC6981**, **NGC6934**, NGC6101, NGC5904, Pal5, NGC5824, NGC5634, NGC7089, FSR1758, NGC4833, BH140, NGC4590, Rup106, NGC3201, Pal2, NGC5272, Djor1, NGC6426, NGC7078, NGC6864, NGC6715, NGC6656, NGC6341, NGC6333, NGC5286, NGC362, NGC2808, NGC1851, NGC104, NGC7492, Pal10, Ter7, NGC6779, NGC6584, IC1276, ESO280-SC06, NGC288	(15) 2MASS-GC02, IC1257, NGC1904, NGC2298, NGC4372, NGC5139, NGC5694, NGC6121, NGC6205, NGC6229, NGC6838, NGC7006, NGC7099, Pal13, Ter8
[20-25]	(**8**,29) **Pal5**, **NGC7492**, **Pal13**, **Rup106**, **NGC6864**, **NGC6426**, **ESO280-SC06**, **Ter7**, NGC5466, IC4499, NGC5634, NGC7089, NGC5824, NGC5024, NGC4590, NGC4147, NGC3201, NGC5272, IC1257, NGC5904, NGC6101, NGC6584, Arp2, Ter8, NGC6934, NGC6981, Pal12, NGC6229, Pal2	(9) Djor1, FSR1758, NGC1261, NGC1851, NGC1904, NGC2298, NGC2808, NGC5694, NGC7006
[25-30]	(**7**,20) **NGC6715**, **Pal2**, **AM4**, **NGC5634**, **Ter8**, **Arp2**, **IC1257**, NGC5824, Rup106, NGC5694, IC4499, NGC6101, NGC5904, NGC6229, Ter7, NGC6934, NGC6981, Pal13, NGC7492, Whiting1	(10) NGC1851, NGC1904, NGC3201, NGC4147, NGC4590, NGC5466, NGC7006, NGC7089, Pal15, Pyxis
[30-35]	(**4**,11) **NGC6229**, **NGC5824**, **NGC5694**, **Whiting1**, NGC7006, Ter8, Arp2, Ter7, Rup106, Pyxis, Pal2	(3) NGC6101, NGC6934, Pal15
[35-300]	(**12**,15) **Laevens3**, **NGC7006**, **SagittariusII**, **Pal15**, **Pal14**, **Crater**, **Pal4**, **Pal3**, **Pyxis**, **NGC2419**, **Eridanus**, **AM1**, NGC6715, NGC5824, NGC5694	(4) Arp2, NGC6934, Pal2, Ter8

debris from outer clusters can span the whole sky while inner clusters must be restricted in longitude and latitude. With these definitions, 21 clusters are disk clusters, 71 are inner clusters, and 67 are outer clusters (see Table 4.5 in Supplemental Material 5.4). We emphasize that this classification does not aim to suggest any specific origin for these systems (e.g., whether they are in-situ or accreted, see Massari et al., 2019), but it is uniquely based on their current orbital characteristics and helps in capturing some of the properties in the extension (projected in to the sky) and shape of their extra-tidal material, as we discuss in the following.

3.3.1 Extra-tidal features originating from disk clusters: ribbons in the Galactic plane

Disk clusters are defined on the basis of the flatness of their orbits (i.e., on their z_{max}/R_{max} ratio). As a result, they typically are restricted to low latitudes, though the exact distribution depends on the relationship of their orbit to the solar radius. To specify, clusters whose R_{max} are interior to the Solar radius generate tidal debris in a limited range in longitude and latitude. For instance, the material associated with clusters as Ter 1, Ter 5, Ter 6, and Ter 9 has a disk-like shape and is completely confined to $|\ell| < 30°$ and $|b| < 10°$. If R_{max} is greater than the solar radius, material can cover the full longitude space and most of the material will still appear at low latitudes. This is the case, for example, of BH 140, whose escaped stars diffusely occupy all longitudes and most of them are found at $|b| \leq 30°$, while for Pal 2 and Pal 10, their extra-tidal stars have a very limited latitudinal extension and appear as ribbons in the sky. In the following, we discuss some of the structures associated with NGC 6121, Pal 2, and Pal 10. We refer to Supplemental Material 5.2 for the tidal structures generated by the whole set of disk clusters.

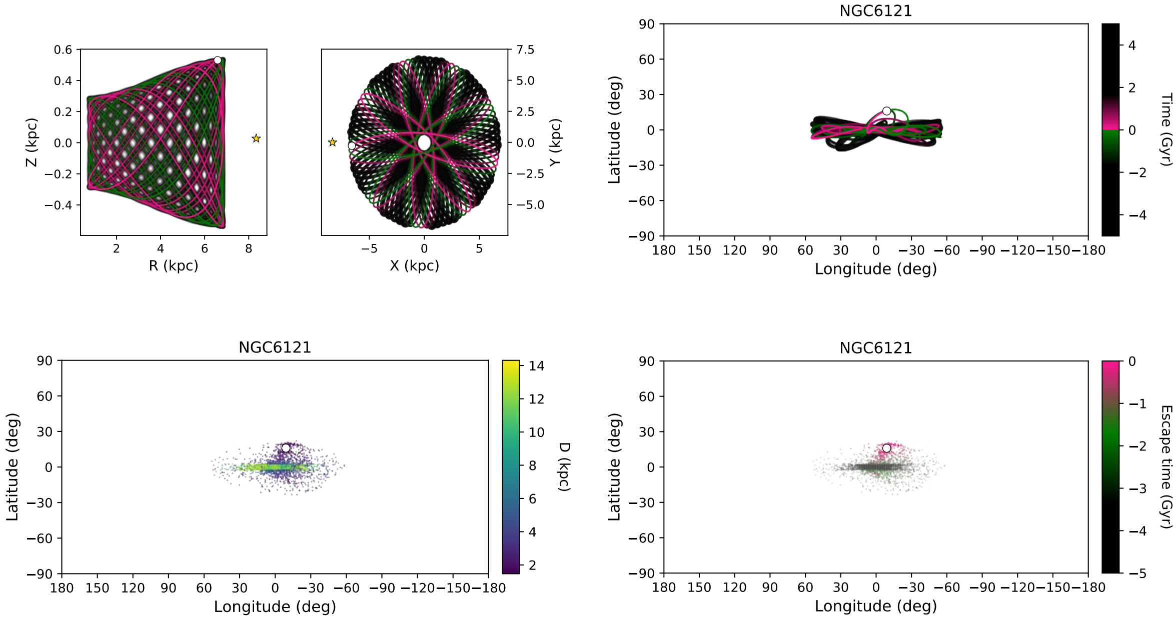

Figure 4.6 – *Top-left panel:* Projection of the orbit of NGC 6121 in the meridional R − z plane. Colors trace time, from 5 Gyr ago (negative values) to 5 Gyr forward in time (positive values). *Top-right panel:* Projection of the orbit of NGC 6121 in the Galactic $x - y$ plane. *Second row:* Projection of the NGC 6121 orbit for the past and future 5 Gyr, in the longitude-latitude plane. *Third row:* Projection in the longitude-latitude plane of the extra-tidal material lost by NGC 6121. Colors indicate the average distance of the stripped material from the Sun. *Bottom panel:* Projection in the longitude-latitude plane of the extra-tidal material lost by NGC 6121. Colors indicate the average time at which stellar particles become gravitationally unbound to the cluster, from 5 Gyr ago (negative time) to the current time (escape time = 0). In the bottom and middle panels, only the reference simulation without errors is shown for clarity. In all plots, the current position of the cluster is given by the white circle with a black outline. The yellow star, when present, indicates the position of the Sun.

NGC 6121: With a current position at $x = -6.58$, $y = -0.28$ and $z = 0.53$ kpc, NGC 6121 is the closest globular cluster to the Sun in our list. This cluster has a remarkably planar orbit, with a maximal vertical excursion from the Galactic plane of only 0.5 kpc (see Fig. 4.6), and an eccentricity $e = 0.80 \pm 0.01$, which makes it oscillate between an apo-center at $R_{\max} = 6.81 \pm 0.02$ kpc and a peri-center at $R_{min} = 0.76 \pm 0.04$ kpc. Because this cluster lies inside the solar circle, its orbit is limited to a longitude interval from −60° to 60°; because the cluster currently lies very close to the Sun, and is at its highest height above the Galactic plane, the orbit forms a hook-like pattern in longitude-latitude space. This hook-like portion of the orbit, nearest to the cluster, is traced by the recently stripped tidal material (see Fig. 4.6), with a leading tail oriented mostly in a vertical direction in the (ℓ, b) plane, from the current cluster location, up to approximately 0° latitude. This portion of the stripped material lies at less than 2 kpc from the Sun, and it constitutes the nearest stream found in our simulations.

To our knowledge, no extra-tidal structure has been discovered around NGC 6121 thus far. Recently, Kundu et al. (2019) used RR-Lyrae stars to trace the extra-tidal material around NGC 6121, without finding any clear evidence of structures. The current position of the cluster in the sky, at a latitude of roughly 20° and at a longitude close to 0°, makes this search difficult due to the strong contamination of field disk stars, despite the fact that this portion of the stream is expected to be very close to the Sun.

Pal 10 and Pal 2: Pal 10 and Pal 2 are two disk clusters whose orbit crosses the solar radius. While for Pal 10, the maximal in-plane distance, $R_{\max}$, is approximately 12 kpc, in the case of Pal 2, the orbit can reach about 40 kpc from the Galactic center. The fact that both these clusters have a radial excursion of the orbit which is beyond the solar radius implies that their stripped stars can redistribute over the whole longitudinal range and, thus, is also in the anti-center direction. The fact that both clusters have orbits confined close to the disk plane implies that the escaped material redistributes in very thin structures (i.e., confined in a limited latitude interval), which resemble typical "ribbons" in the sky. Our models predict that both clusters are surrounded by a long stream of tidal material, which is however probably very difficult to identify because in both cases, these extra-tidal stars are confined close to the Galactic plane. No tidal streams emanating from these two clusters, to our knowledge, have been identified in the observational data so far. Because the tidal structures associated with these two clusters have similar properties, we report only the case of Pal 10 in Fig. 4.7.

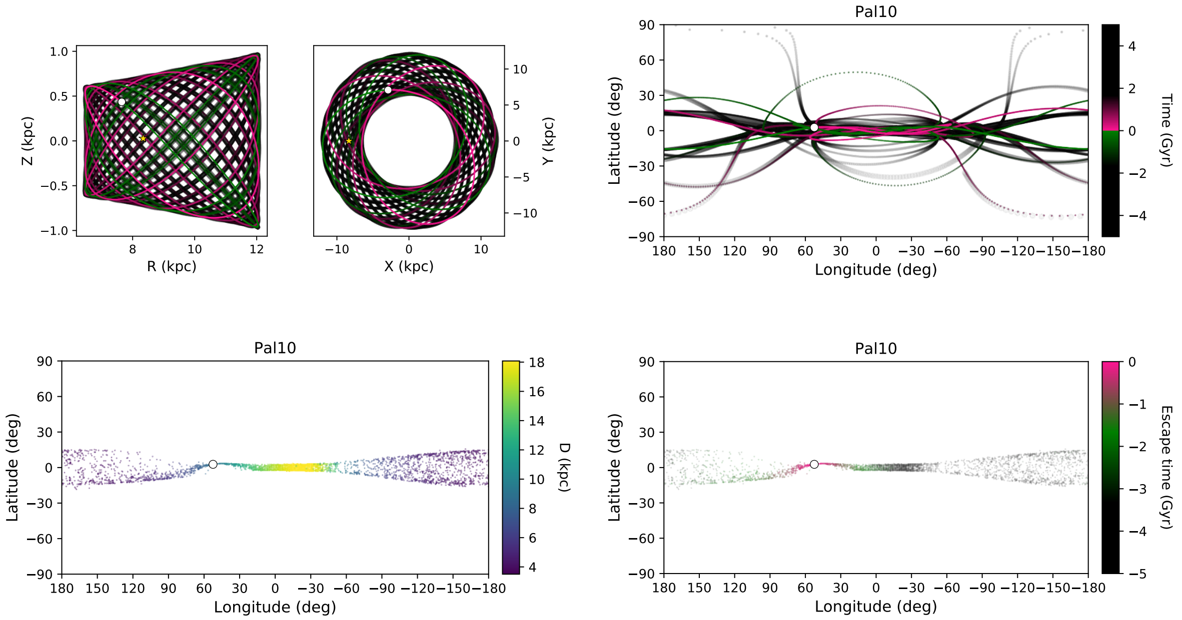

Figure 4.7 – Various projections of the host globular cluster orbit with its accompaning tidal debris as Fig. 4.6, but for the cluster Pal 10.

3.3.2 Extra-tidal features originating from inner clusters: Bow-ties and more complex shapes

We have defined inner globular clusters as systems that are not disk clusters (their orbit is not confined close to the Galactic plane) but that are confined inside the solar radius. Seventy-one clusters are found in this category (see Table 4.5). We discuss some of them in the following.

NGC 5946 & NGC 5986: These are inner-non disk clusters whose escaped stars redistribute in a characteristic "bow-tie" shape. These stars are all confined in a relatively narrow longitudinal range (typically within $-30°$ to $30°$). Towards the edges of the longitude interval, the distribution of extra-tidal stars tends to flare, whereas it instead shrinks at zero longitude. These trends can be explained as an effect of the projection of the orbits of these clusters in the (ℓ, b) plane. Moreover, because these clusters always stay in the inner region of the Galaxy, where the dynamical timescales are short, their orbit - and consequently their stripped stars - can experience many disk crossings over the whole duration of the simulation, filling the whole (ℓ, b) space allowed by their orbital parameters. An example of such a distribution is given in Fig. 4.8 for the extra-tidal material associated with the cluster NGC 5986.

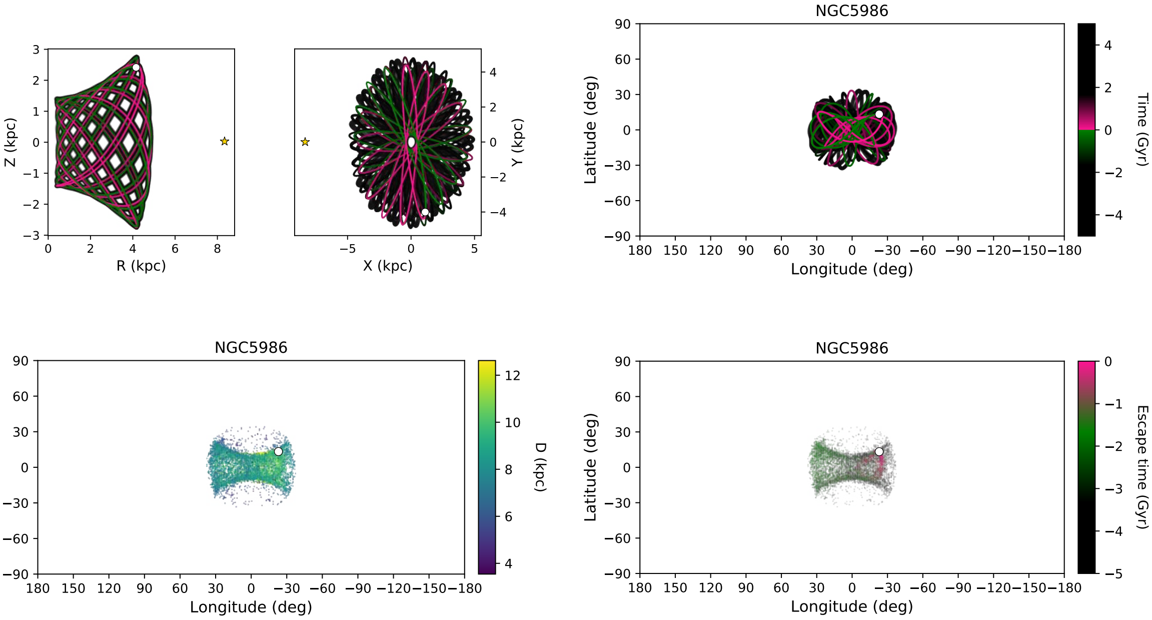

Figure 4.8 – Various projections of the host globular cluster orbit with its accompaning tidal debris as in Fig. 4.6 & 4.7, but for the cluster NGC 5986.

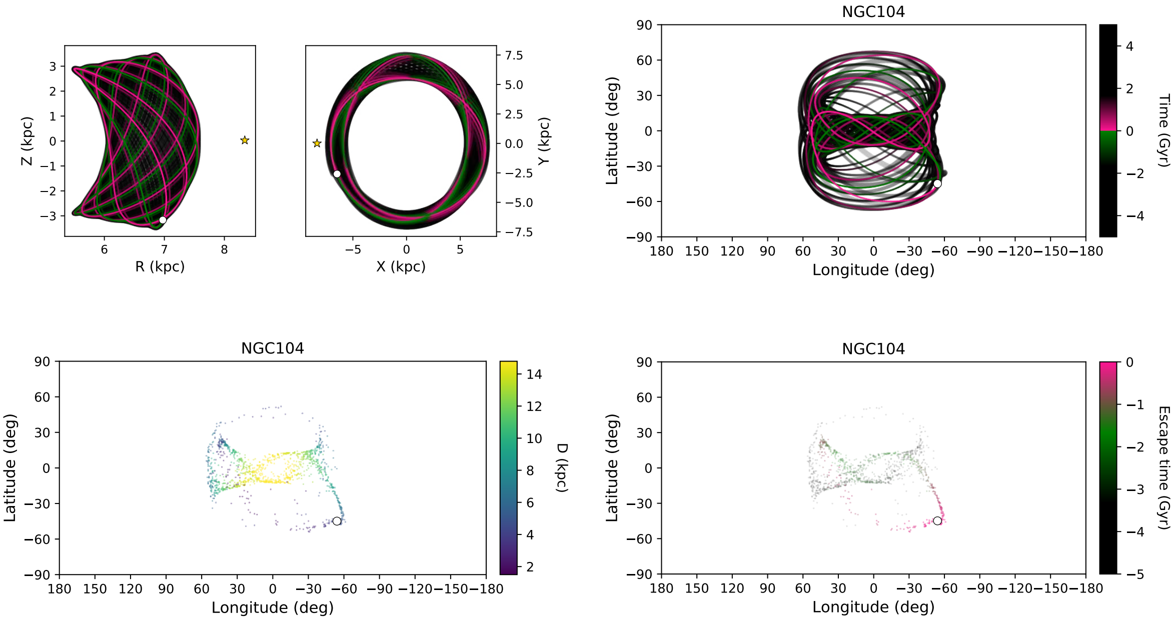

Figure 4.9 – Various projections of the host globular cluster orbit with its accompaning tidal debris as in Fig. 4.6-4.8, but for the cluster NGC 104.

There are also clusters such as NGC 104 (47 Tuc) for which the morphology of the extra-tidal material can take on more complex shapes. This cluster has an orbit confined inside the solar radius, but which, at its apocenter, can reach a distance of less than 1 kpc from the Sun (see Fig. 4.9). The projection of the past and future orbit in the (ℓ, b) plane gives rise to a kind of figure-eight shape, with the stars stripped more recently from the cluster tracing the portion of this shape that extends to negative latitudes. Our model of NGC 104 is in agreement with the conclusions reached by R. R. Lane, Küpper, et al. (2012), who suggested that two clear tidal tails should emanate from this cluster, however, the orientation of these tails in the (ℓ, b) plane differs slightly between the two works. The models of R. R. Lane, Küpper, et al. (2012) do indeed suggest that the leading tail of NGC 104 should extend a bit beyond $\ell < -70°$ (see Fig. 4 in their paper, as an example), while our model predicts a minimum longitude of about $-60°$. The exact comparison between these two works is however difficult, since the model of the Galactic potential, the distance to the Sun, proper motions, and line-of-sight velocities of NGC 104 used in their study are different from ours. To date, clear tails around NGC 104 have not been found yet, with the most recent observational works pointing to the possibility of the presence of a diffuse extended halo-like structure around this cluster (see Piatti, 2017). We note that we only find a more diffuse distribution of extra-tidal material in the case of the PII-0.3-SLOW model. Additional work for comparing the current observational data with simulations will be needed to resolve this apparent discrepancy between theoretical predictions and observational findings.

Other shapes found in this category include "Easter eggs", which are generated by clusters whose orbits are confined to the innermost kpc of the Galaxy and show significant variations in the z-coordinates that are at least as large as those found in the radial direction. Among clusters whose extra-tidal material shows these peculiar shapes we have found: HP1, NGC 6093, NGC 6273, NGC 6293, NGC 6723, and NGC 6809.

3.3.3 Extra-tidal features originating from outer clusters: "canonical" tidal tails

Caveat: In this group, there are some elongated streams emanating from such clusters as NGC 6715, Pal 12, Ter 7, and Ter 8, which are associated with the Sagittarius dwarf galaxy. As a caution, we add that for these clusters the elongation and shape of the streams may be severely modified if the gravitational potential generated by the Sagittarius dwarf galaxy itself was included in the model. For completeness, we decided to include these streams in the paper, and to report them in Supplemental Material 5.2. In future works, we plan to investigate how the inclusion of the Sagittarius dwarf may alter these streams and possibly affect also those of other clusters that are not necessarily associated with this dwarf galaxy.

Among the extra-tidal structures emanating from outer globular clusters, we find some of the most beautiful and elongated tidal tails, of which those associated with Pal 5 were the first to be discovered (Odenkirchen, Grebel, Rockosi, et al., 2001). In this category, we note the stream associated with the E 3 cluster that extends about 120° in longitude based on our models prediction; the thin stream emanating from IC 4499, which we predict has an extension of about 150° in longitude. To recap, the finest and thinnest stellar streams have been predicted from: AM 4, Arp 2, IC 4499, NGC 1261, NGC 3201, NGC 4590, NGC 5024, NGC 5053, NGC 5272, NGC 5466, NGC 5694, NGC 5824, NGC 5904, NGC 6101, NGC 6426, NGC 6584, NGC 6934, Pal 1, Pal 5, Pyxis, Rup 106, Sagittarius II, Ter 7, Ter 8, and Whiting 1.

Many of the above-cited streams have been discovered and also found in observational data, but in many cases, the extent of the tails, as predicted by our models, is larger. Of these observed streams, many tracks are available in the *galstreams* (Mateu, 2023) library. In the following, we compare our model predictions to some of these tracks in the three different Galactic potentials adopted in this paper. More specifically, we compare the projected density distribution of the simulated stream to observations in the (ℓ, b), $(\ell, \mu_\ell \cos(b))$, $(\ell, \mu_{\rm b})$, and $(\ell, {\rm D})$ planes. As for the projected density distributions derived from the models, we calculated them by taking into account all the 51 simulations realized for each cluster, that is, both the reference simulation and those realized by a Monte-Carlo sampling of the uncertainties. Overall, the agreement between models and observational data is excellent for all Galactic models used. By looking at more extended regions in the sky than those covered by current observations, it should be possible to better constrain the streams, as well as favor or otherwise disfavor some of these models.

NGC 3201: NGC 3201 is an outer cluster at a distance of about 4.7 kpc from the Sun. It has received a great deal of attention in the last couple of years, followng the suggestion by Riley & Strigari (2020) that part of its tidal tails could be associated with the Gjöll stream, discovered by R. A. Ibata, Malhan & N. F. Martin (2019). The association of the Gjöll and NGC 3201 streams has been further confirmed by Hansen et al. (2020) on the basis of the similarity of the chemical abundances of stars in the Gjöll stream and in NGC 3201. More recently, Palau & Miralda-Escudé (2021) conducted an extensive study of the tidal tails emanating from this cluster, discovering a long stream, with an overall length of 140° in the sky. Our models suggest that the tails emanating from NGC 3201 may, in fact, be even more extended than those found by Palau & Miralda-Escudé (2021). To further illustrate this point, in Fig. 4.10 we compared our model predictions to the tracks available for this stream in the *galstreams* library as well as those taken from R. Ibata, Malhan, N. Martin, et al. (2021), from Palau & Miralda-Escudé (2021), and from the Gjöll stream, as reported by R. Ibata, Malhan, N. Martin, et al. (2021). All models represent the portion of the stream discovered so far very well, specifically, in terms of the distribution of the stream in the sky, distance, and proper motion spaces. Our models indeed predict that for this cluster, the differences in the stream properties change very little with the mass model adopted. The most striking difference is found for the elongation of the stream at $\ell > 0$: in the case of the barred potential, the stream associated with NGC 3201 does extend to smaller values of ℓ (up to $\ell \sim 70^\circ$), which are not reached in the case of the axisymmetric models. This portion of the stream is expected to be found at distances greater than 20 kpc from the Sun (see bottom panels in Fig. 4.10).

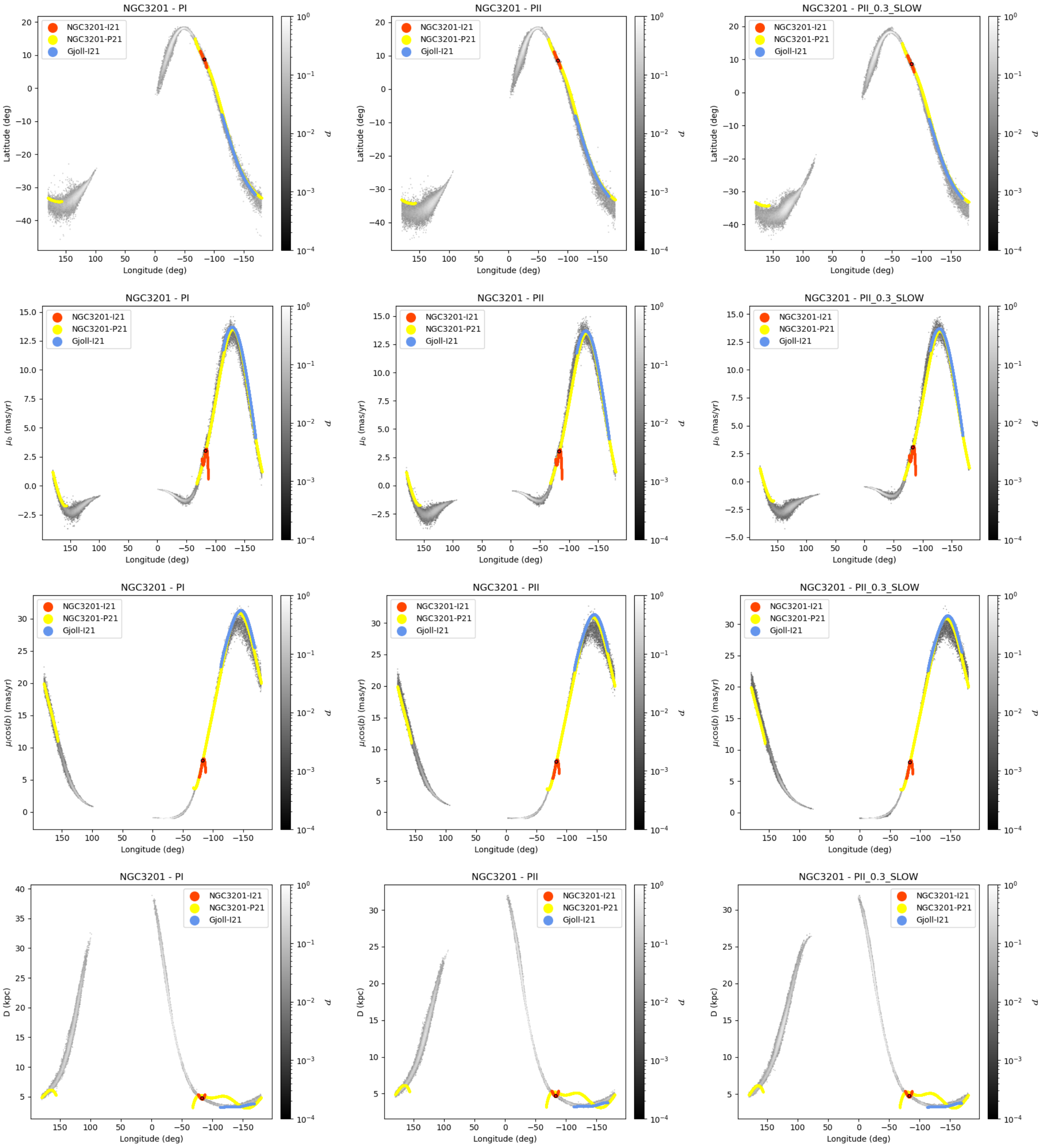

Figure 4.10 – Projected density distribution of the NGC 3201 stream, as predicted by our simulations, in the (ℓ, b), (ℓ, μ_{b}), $(\ell, \mu_\ell\cos(b))$ and (ℓ, D) planes, shown from top to bottom. The model predictions are shown for the three Galactic potentials PI (*left column*), PII (*middle column*), and PII-0.3-SLOW (*right column*) and are compared to the tracks available in the *galstreams* library for this cluster, and which are taken from R. Ibata, Malhan, N. Martin, et al. (2021) (NGC3201-I21, red lines), Palau & Miralda-Escudé (2021) (NGC3201-P21, yellow lines) and from R. Ibata, Malhan, N. Martin, et al. (2021), as for the Gjöll stream (Gjöll-I21, blue lines). For each panel, the color bar indicates the 2D probability density quantified by taking into account all the particles from the 51 realizations, which is then normalized to its maximum value. In all panels, the current position of the cluster is indicated by a red dot.

NGC 4590: NGC 4590 (M 68) is an outer cluster at a current distance of about 10 kpc from the Sun. This cluster is surrounded by a very extended stream (Palau & Miralda-Escudé, 2019; R. Ibata, Malhan, N. Martin, et al., 2021), a long portion of which is represented by the Fjörm stream, discovered by R. Ibata, Malhan, N. Martin, et al. (2021). The comparison between our model predictions and the tracks available in *galstreams* is shown in Fig. 4.11. Interestingly (and differently from the case of NGC 3201), not all the Galactic potentials adopted in this paper seem to represent the stream distribution in the sky equally well. While the axisymmetric models PI and PII predict generally a good match – with model PI describing the stream at positive longitudes even more accurately than model PII – the model PII-0.3-SLOW fails to reproduce the stream in its observed extension: the modeled stream in this case appears quite thick in the (ℓ, b) plane and, moreover, it is much shorter than the stream found in the observational data. Interestingly, the axisymmetric models capture very well also the proper motions and distance-to-the-Sun trends as a function of longitude, as found by R. Ibata, Malhan, N. Martin, et al. (2021) (for Fjörm) and by Palau & Miralda-Escudé (2019), while the NGC 4590 as reported by R. Ibata, Malhan, N. Martin, et al. (2021) (and named "M68-I21" in Fig. 4.11) tends to be off in all models – and also off when compared to the other observational tracks. As suggested by Mateu (2023), it is possible that the stellar stream that was associated with NGC 4590 by R. Ibata, Malhan, N. Martin, et al. (2021)does indeed have a different progenitor. Finally, the failure of the barred model to reproduce the extension of the NGC 4590 stream (and in particular Fjörm) might be due to the choice of the pattern speed adopted or that of the bar length. We will explore these topics in future work. Here, we simply note that given the sensitivity of NGC 4590 stream to the choice of the barred potential, this stream is potentially very interesting for determining the parameters of the latter.

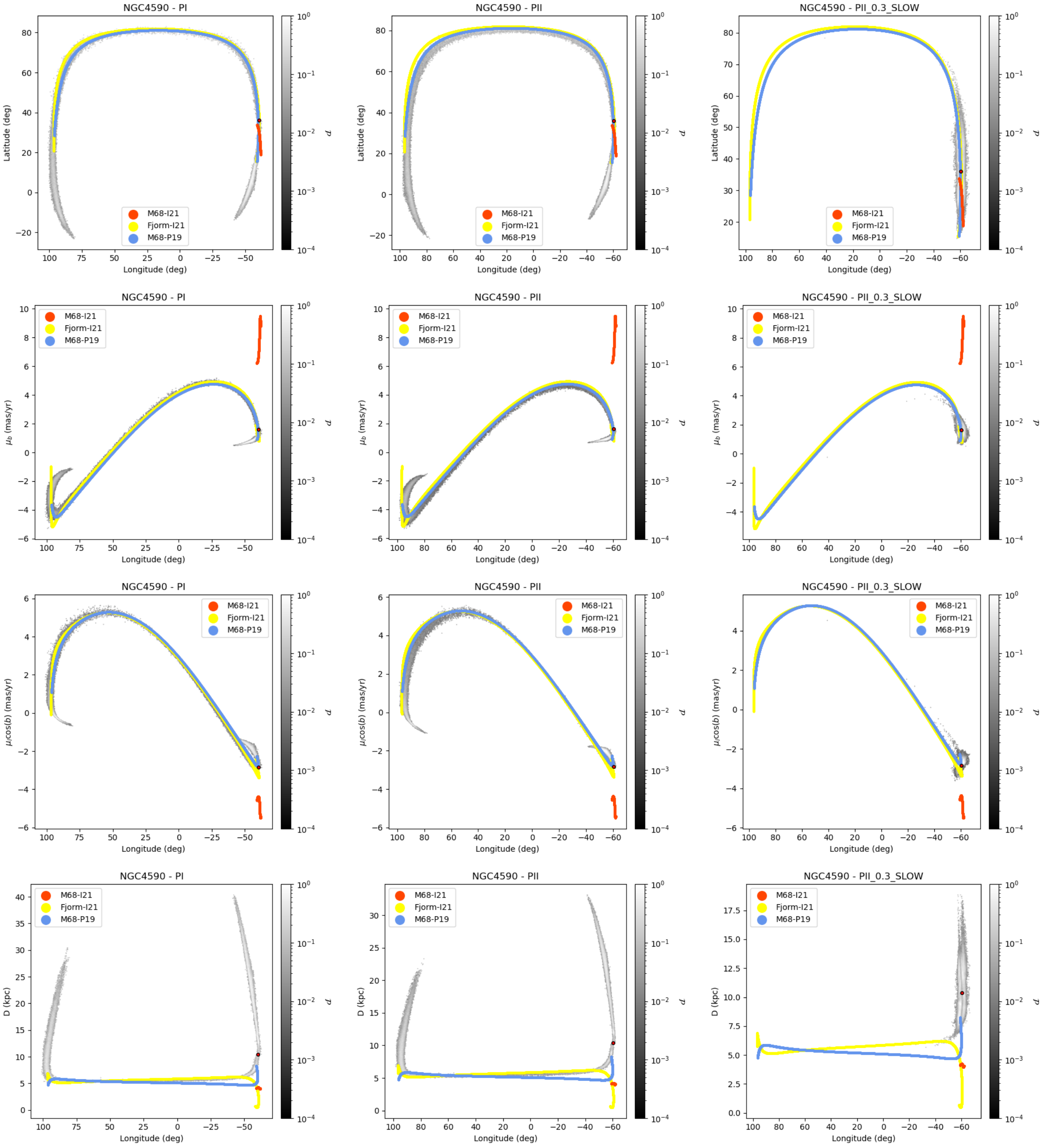

Figure 4.11 – The probability density maps arising from our simulations plotted against observed stellar streams as in Fig. 4.10, but for the NGC 4590 cluster. The tracks come from the work by Palau & Miralda-Escudé (2019) (M68-P19, blue lines), R. Ibata, Malhan, N. Martin, et al. (2021) (M68-I21, red lines) and from R. Ibata, Malhan, N. Martin, et al. (2021) as for the Fjörm stream (Fjorm-I21, yellow lines).

NGC 5466: NGC 5466 is another cluster known to be surrounded by a thin and very extended stream, as shown by Grillmair & R. Johnson (2006) and Belokurov, Evans, et al. (2006). More recently, Jensen et al. (2021) used Gaia DR2 data to study the stream, finding an extension of about 30 degrees on the sky and a somewhat different orientation than that suggested by Grillmair & R. Johnson (2006). Also, R. Ibata, Malhan, N. Martin, et al. (2021) confirmed the existence of an elongated stream around this cluster, even if it appears somewhat less extended than what was found by Grillmair & R. Johnson (2006). In Fig. 4.12, we show the comparison of our model predictions to the tracks available in *galstreams*, taken from the works by Grillmair & R. Johnson (2006) and R. Ibata, Malhan, N. Martin, et al. (2021). The comparison is excellent for all the Galactic potentials used in this paper. We note that there is a slight offset between the modeled streams and the track by R. Ibata, Malhan, N. Martin, et al. (2021) in the $(\ell - D)$ plane (of about 1 kpc at a fixed longitude) – which is maybe less evident for the case of the PII-0.3-SLOW potential than in the axisymmetric cases. We emphasize that all our models predict that the stream should be more extended than that discovered so far in the observations. In particular, there is a portion of the leading tail at $0 < \ell < 42°$ that has not yet been discovered, lying at distances from the Sun closer or similar to that of the known stream.

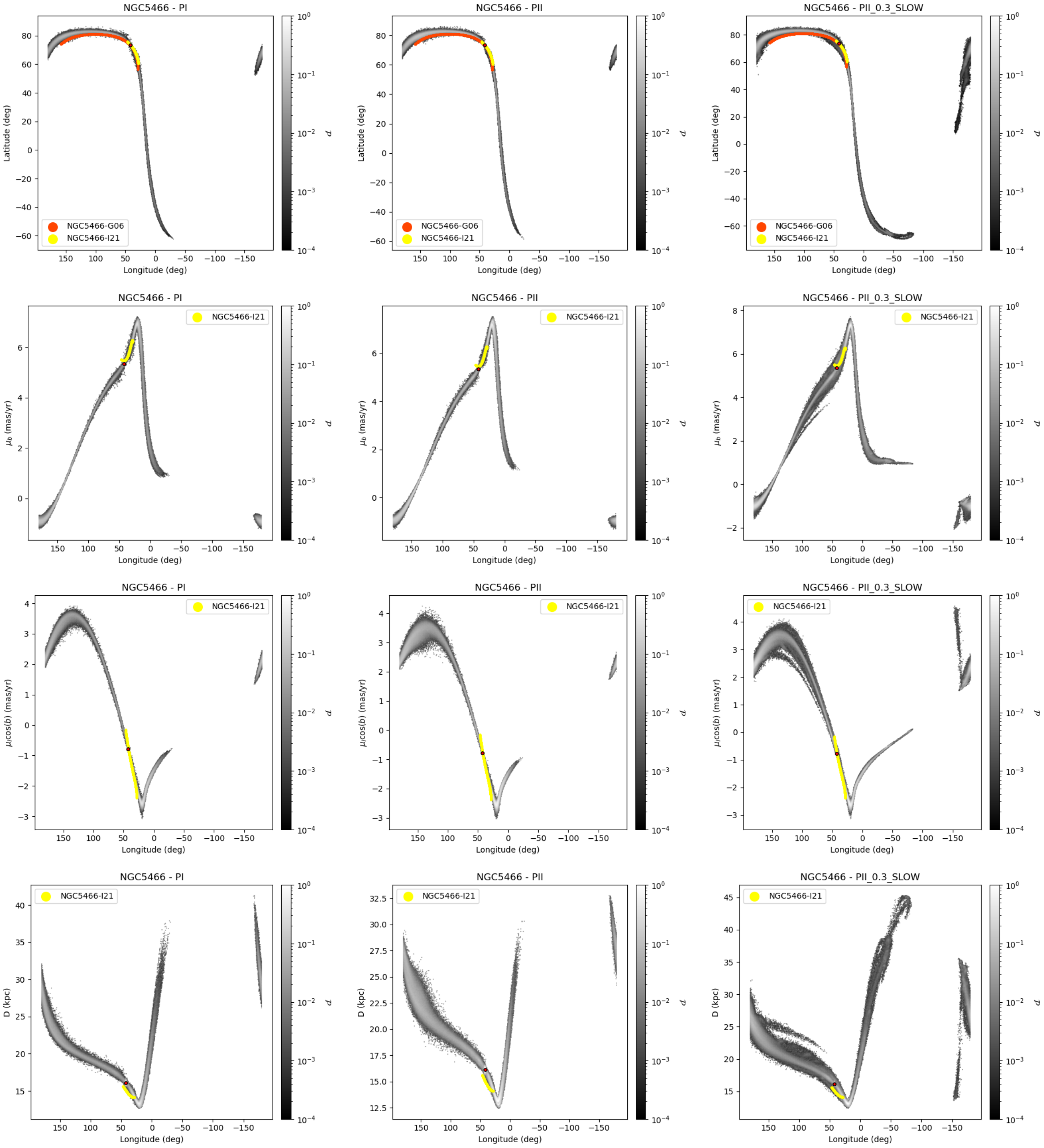

Figure 4.12 – The probability density maps arising from our simulations plotted against observed stellar streams as in Figs. 4.10, & 4.11, but for the case of the NGC 5466 cluster. Model predictions are compared to the tracks available in the *galstreams* library and those coming from the work by Grillmair & R. Johnson (2006) (red lines) and R. Ibata, Malhan, N. Martin, et al. (2021) (yellow lines). Note: proper motions and distances are available only for the NGC5466-I21 track. We also note that the variations in the streams, specifically the different stripes, originate from the errors considered in the simulations.

Pal 5: About 20 years after the discovery of its tidal tails (Odenkirchen, Grebel, Rockosi, et al., 2001; Odenkirchen, Grebel, Dehnen, H.-W. Rix, et al., 2003), Pal 5 still represents the prototype cluster surrounded by thin and extended streams of stars. The extension, morphology, kinematics, and chemical composition of its tails have been extensively studied, both observationally and numerically (Odenkirchen, Grebel, Dehnen, H.-W. Rix, et al., 2003; Rockosi et al., 2002; Dehnen et al., 2004; Koch, Grebel, et al., 2004; Grillmair & Dionatos, 2006a; Odenkirchen, Grebel, Kayser, et al., 2009; Mastrobuono-Battisti, Di Matteo, et al., 2012; Küpper, Balbinot, et al., 2015; Kuzma, Da Costa, et al., 2015; Fritz & Kallivayalil, 2015; R. A. Ibata, Lewis & N. F. Martin, 2016; Ishigaki et al., 2016; G. F. Thomas, R. Ibata, et al., 2016; Koch & Côté, 2017; R. A. Ibata, Lewis, G. Thomas, et al., 2017; Pearson, Price-Whelan, et al., 2017; Price-Whelan, Mateu, et al., 2019; Starkman et al., 2020; Bonaca, Pearson, et al., 2020; R. Ibata, Malhan, N. Martin, et al., 2021; Phillips et al., 2022; Kuzma, Da Costa, et al., 2015). In Fig. 4.13, we report the comparison of our model predictions to the tracks available for this cluster in *galstreams* and those coming from the work by Price-Whelan, Mateu, et al. (2019), Starkman et al. (2020), and R. Ibata, Malhan, N. Martin, et al. (2021). Projected in the (ℓ, b) plane, the observed streams are in excellent agreement with the model predictions for all the Galactic potentials adopted. Interestingly, all potentials suggest more extended streams than those discovered so far. In the case of the barred potential, we note that the prediction of the stream position in the sky at large angular distances from the cluster center is still highly uncertain. This is due to the fact that the uncertainties are still affecting the current distance of Pal 5 to the Sun, combined with the impact of the rotating bar, which can be more or less efficient in perturbing the stream depending on the torques experienced by the latter at pericenter; these, in turn, depend on the orbital parameters of the cluster itself. Pearson, Price-Whelan, et al. (2017) already explored the effect of a rotating bar on the extension and morphology of Pal 5 tails. While we can confirm the Pearson, Price-Whelan, et al. (2017) findings, namely, that both characteristics are affected by a rotating bar, we also emphasize that both the extension of the leading tail (i.e., the portion of the stream at negative longitudes) and its morphology depend on the choice of the bar pattern speed. For example, we do not find a density drop in the leading tail as reported by Pearson, Price-Whelan, et al. (2017). These authors adopted a higher bar pattern speed than the one adopted in this work ($\Omega_b = 60$ kms^{-1}kpc^{-1} for the example discussed in Fig. 2 of their work, right panel, while $\Omega_b = 38$ kms^{-1}kpc^{-1} in our PII-0.3-SLOW model). Additionally, taking into account the uncertainties in the cluster distance, proper motions, and line-of-sight velocity is also important for obtaining robust predictions on the stream characteristics. Some of our solutions, for example, predict a very extended leading tail that is significantly more extended than those found for the axisymmetric potentials.

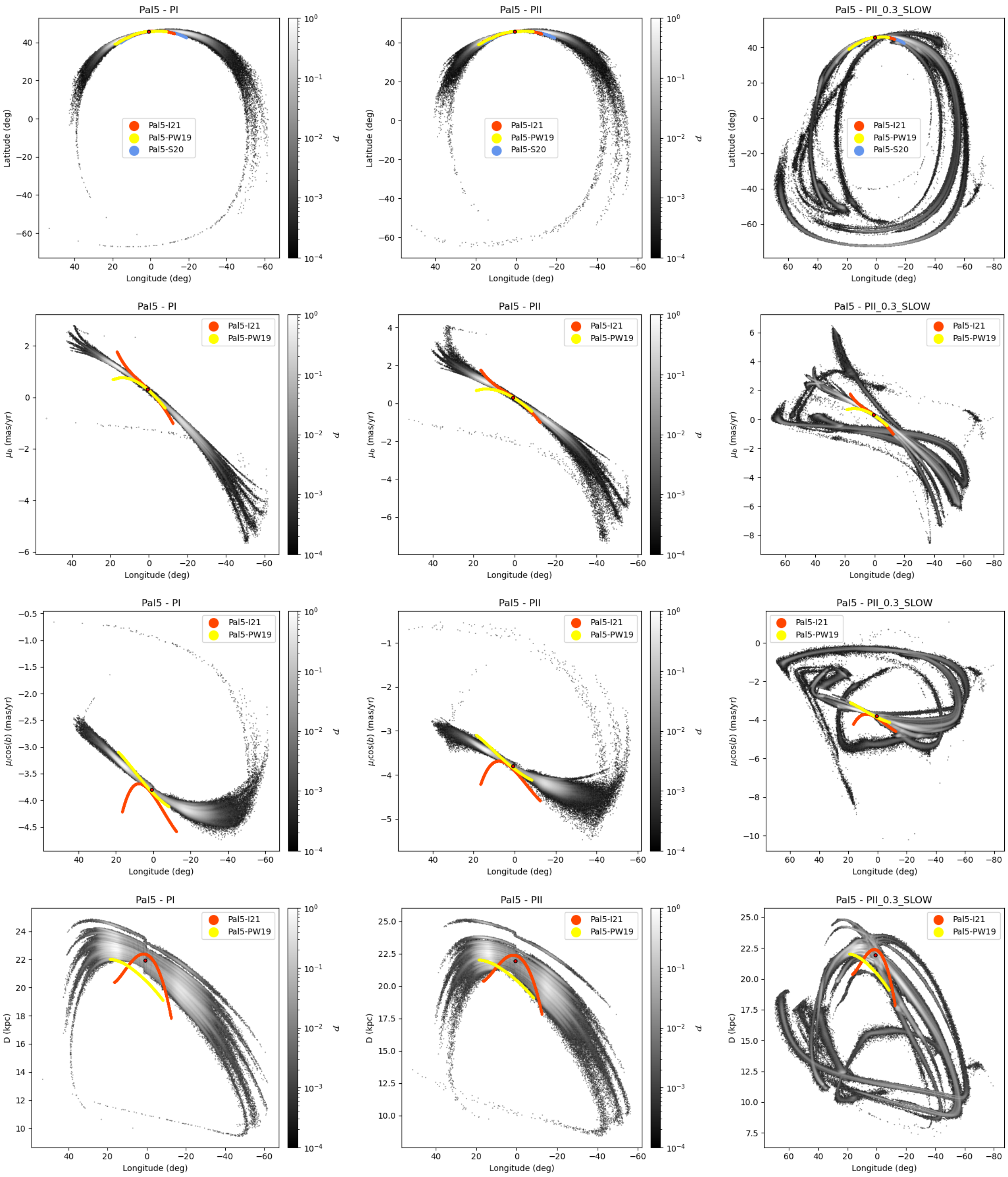

Figure 4.13 – The probability density maps arising from our simulations plotted against observed stellar streams as in Figs. 4.10, 4.11, and 4.12, but for the case of the Palomar 5 cluster. Model predictions are compared to the tracks available in the *galstreams* library and those coming from the work by R. Ibata, Malhan, N. Martin, et al. (2021) (red lines), Price-Whelan, Mateu, et al. (2019) (yellow-lines), and Starkman et al. (2020) (blue lines). Note: proper motions and distances are not available for the Pal5-S20 track.

4 Conclusion

In this work, we have presented the first simulated catalogue of all Galactic globular clusters for which 6D phase-space information, along with masses and sizes are available. A total of 159 globular clusters has been simulated in three Milky Way-like potentials, modeling the process of tidal stripping that these clusters have experienced over the past 5 Gyr. As a result, for all clusters, we can predict the distribution of the extra-tidal material in the sky, their proper motions, distances to the Sun, and line-of-sight velocities. Errors on 6D phase-space information have been taken into account by generating 50 complementary simulations for each cluster, with a Monte-Carlo sampling of the uncertainties. This catalogue currently contains 24 327 simulations, for a total volume of about 370 Gb. It will be made publicly available [9], with the intention to provide the community with an instrument that allows for: a more complete view of the expected distribution of globular clusters tidal structures in the sky, helping in formulating the interpretation of recent and future discoveries, supporting the search for new extra-tidal features in the data, and offering the community a repository of all these models to be compared to other theoretical and numerical predictions, which employ different Galactic potentials and/or gravity laws.

In this first paper, we have presented the distribution in the (ℓ, b) plane of all the simulated extra-tidal features. A striking result is the variety of extra-tidal shapes that globular clusters can give rise to. The canonical tidal tails à la Palomar 5 are only some of the multiple morphologies these structures can have. Ribbons, bow-ties, padlocks, and halo-shapes are also common. This variety of shapes that these stripped stars can show in the sky depends on the characteristics of the cluster orbit, on its current position in the orbit itself, and on the distance of the extra-tidal material from the Sun. Any search for the left-overs of globular clusters in the field should take into account this richness of distributions and morphologies.

These simulations have also allowed us to derive an estimate of the expected mass of stars that have escaped from the clusters in the last 5 Gyr and now in the field. Although these are approximations, given the limitation of our models, our estimate of the mass lost from the Galactic globular cluster system over the last 5 Gyr is between $2 - 21 \times 10^6 M_\odot$, which is comparable to up to half of the total stellar mass found nowadays in the Galactic globular cluster system itself.

This work is intended to be the first of a series which investigates the properties of globular clusters streams in a variety of realistic Galactic potentials, including the perturbations induced by close dwarf satellites (Sagittarius and the Large and Small Magellanic Clouds), as well as more complex and time-varying distributions for the dark matter component.

---

[9] All data are available on a dedicated website (`http://etidal-project.obspm.fr/`)

5 Supplementary material

5.1 Choice of the time-step for orbit integration

To choose the optimal time-step Δt for the simulations, we quantified the energy conservation of the orbit integration, in the case where the 159 clusters evolve in isolation, that is, the case where each test-particle in a cluster feels the gravitational attraction of the cluster itself – but not that of the Galaxy. Since in the case of an isolated cluster, the gravitational potential is time-independent, the total energy, E_i, of each particle in the system (sum of the particle kinetic and potential energy) must be conserved. Any departure from energy conservation is thus a check of the quality of the integration and in particular of the choice of the adopted time-step.

For the isolated simulations, we thus proceeded as follows. We modeled each cluster as a set of N=100 000 test-particles, subject to the cluster potential, only. To model this latter, for each cluster we adopted the same Plummer sphere distribution, with same characteristic radius r_c and total masse M_{GC}, as those adopted for the simulations described in Sect. 2 (see in particular Sect. 2.2). A first set of 159 isolated simulations was run adopting a $\Delta t = 10^5$ yr and a total number of steps $N_{steps} = 50000$ for all clusters, for a total simulated time interval of 5 Gyr. We then quantified the energy conservation by calculating the median error per time-step, m_{err}, of $(\Delta E/E)_i = |(E_{fin,i} - E_{ini,i})/E_{ini,i}|$, where $E_{ini,i}$ and $E_{fin,i}$ are, respectively, the initial (time $t = 0$) and final (time t=5 Gyr) energy of each particle in the system.

While for most of the simulated clusters (109 over 159), this choice of the time-step was sufficient to guarantee an excellent energy conservation (with m_{err} typically of the order of $10^{-11} - 10^{-12}$) for 50 clusters the corresponding m_{err} values were found to be above 10^{-10}. This was the case for all clusters with crossing times $t_{cross} = \sqrt{{r_c}^3/GM_{GC}}$ lower than 2×10^5 yr, that is about twice the time-step. For these clusters, we hence reduced the Δt of a factor 10, rerunning the simulations with $\Delta t = 10^4$ yr and $N_{steps} = 500000$. With such a choice, the corresponding energy conservation turned out to be excellent (below 10^{-10} per step). In Table 4.3, we summarize the result of this study, reporting the cluster name, crossing time, and median error, m_{err}, in energy conservation obtained for all isolated cluster simulations. Clusters for which a $\Delta t = 10^4$ yr, and a corresponding number N_{steps} have been used, are indicated in the Table with an asterisk. The values of Δt adopted for the isolated simulations, and the associated number of time steps, N_{steps}, are also those used to run the simulations of the same clusters orbiting in the gravitational field of the Milky Way.

Table 4.3 – Crossing time, t_{cross}, and median error in energy conservation, m_{err}, for all 159 clusters evolved in isolation. All "isolated" simulations have been run with a $\Delta t = 10^5$ yr, and for a total of $N_{steps} = 50000$ steps, except for clusters marked with (*), for which a $\Delta t = 10^4$ yr and a a total of $N_{steps} = 500000$ steps have been used.

Cluster	t_{cross}	m_{err}	Cluster	t_{cross}	m_{err}	Cluster	t_{cross}	m_{err}
2MASS-GC01	5.6×10^5	2.1×10^{-12}	2MASS-GC02	3.9×10^5	4.4×10^{-12}	AM1	6.5×10^6	5.4×10^{-13}
AM4	2.2×10^7	8.6×10^{-13}	Arp2	4.2×10^6	6.1×10^{-13}	BH140	1.2×10^6	5.3×10^{-13}
BH261	6.9×10^5	1.7×10^{-12}	Crater	1.3×10^7	4.4×10^{-13}	Djor1	4.8×10^5	1.0×10^{-12}
Djor2	3.4×10^5	3.9×10^{-12}	E3	2.9×10^6	3.3×10^{-14}	ESO280-SC06	3.5×10^6	1.1×10^{-13}
ESO452-SC11	7.9×10^5	7.9×10^{-13}	Eridanus	7.2×10^6	1.3×10^{-12}	FSR1716	4.7×10^5	3.4×10^{-13}
FSR1735	1.9×10^5	4.9×10^{-11}	FSR1758	9.1×10^5	7.4×10^{-13}	HP1	2.1×10^5	4.0×10^{-11}
IC1257	9.9×10^5	1.5×10^{-14}	IC1276	4.5×10^5	3.4×10^{-12}	IC4499	1.5×10^6	9.0×10^{-13}
Laevens3	6.5×10^6	4.7×10^{-13}	Liller1 (*)	3.0×10^4	6.0×10^{-13}	Lynga7	4.2×10^5	2.3×10^{-13}
NGC104 (*)	1.7×10^5	2.4×10^{-13}	NGC1261	2.96×10^5	1.4×10^{-11}	NGC1851 (*)	9.0×10^4	3.8×10^{-13}
NGC1904 (*)	1.6×10^5	6.8×10^{-10}	NGC2298	2.6×10^5	1.2×10^{-11}	NGC2419	1.4×10^6	1.2×10^{-12}
NGC2808 (*)	8.4×10^4	1.6×10^{-12}	NGC288	8.1×10^5	6.5×10^{-13}	NGC3201	4.5×10^5	1.6×10^{-12}
NGC362 (*)	1.4×10^5	1.9×10^{-13}	NGC4147	4.2×10^5	5.2×10^{-14}	NGC4372	5.7×10^5	4.8×10^{-13}
NGC4590	6.1×10^5	4.3×10^{-13}	NGC4833	2.3×10^5	1.8×10^{-12}	NGC5024	4.9×10^5	3.0×10^{-12}
NGC5053	2.7×10^6	4.4×10^{-13}	NGC5139 (*)	1.8×10^5	1.1×10^{-12}	NGC5272	2.6×10^5	2.0×10^{-12}
NGC5286 (*)	1.3×10^5	1.5×10^{-13}	NGC5466	2.2×10^6	1.0×10^{-12}	NGC5634	4.3×10^5	4.6×10^{-12}
NGC5694	1.9×10^5	6.9×10^{-11}	NGC5824	1.9×10^5	5.2×10^{-11}	NGC5897	9.4×10^5	2.5×10^{-13}
NGC5904	2.2×10^5	8.3×10^{-12}	NGC5927	2.4×10^5	1.9×10^{-11}	NGC5946 (*)	1.4×10^5	1.1×10^{-12}
NGC5986 (*)	1.5×10^5	7.7×10^{-13}	NGC6093 (*)	7.5×10^4	7.9×10^{-13}	NGC6101	1.3×10^6	3.5×10^{-13}
NGC6121	2.5×10^5	9.1×10^{-12}	NGC6139 (*)	7.0×10^4	3.9×10^{-13}	NGC6144	4.0×10^5	3.9×10^{-12}
NGC6171	2.9×10^5	1.7×10^{-13}	NGC6205 (*)	1.7×10^5	1.7×10^{-13}	NGC6218	2.5×10^5	3.0×10^{-12}
NGC6229 (*)	1.8×10^5	2.5×10^{-14}	NGC6235	3.3×10^5	3.1×10^{-12}	NGC6254	2.4×10^5	9.0×10^{-12}
NGC6256	3.1×10^5	7.1×10^{-12}	NGC6266 (*)	5.0×10^4	1.1×10^{-13}	NGC6273 (*)	1.1×10^5	8.0×10^{-13}
NGC6284	2.1×10^5	1.3×10^{-11}	NGC6287	1.9×10^5	3.1×10^{-11}	NGC6293	1.8×10^5	9.9×10^{-11}
NGC6304	2.5×10^5	5.9×10^{-12}	NGC6316 (*)	1.9×10^5	1.3×10^{-13}	NGC6325 (*)	1.2×10^5	4.4×10^{-13}
NGC6333 (*)	1.5×10^5	2.2×10^{-13}	NGC6341 (*)	1.6×10^5	5.6×10^{-13}	NGC6342 (*)	1.5×10^5	3.4×10^{-13}
NGC6352	3.9×10^5	2.2×10^{-12}	NGC6355	2.2×10^5	4.8×10^{-11}	NGC6356	2.4×10^5	3.0×10^{-11}
NGC6362	5.6×10^5	8.1×10^{-13}	NGC6366	6.9×10^5	4.0×10^{-13}	NGC6380 (*)	1.6×10^5	2.1×10^{-13}
NGC6388 (*)	8.3×10^4	6.0×10^{-13}	NGC6397	2.5×10^5	4.1×10^{-12}	NGC6401 (*)	1.6×10^5	6.5×10^{-13}
NGC6402 (*)	1.5×10^5	9.7×10^{-13}	NGC6426	8.6×10^5	8.6×10^{-13}	NGC6440 (*)	4.6×10^4	1.1×10^{-13}
NGC6441 (*)	5.7×10^4	2.6×10^{-14}	NGC6453	1.9×10^5	5.2×10^{-11}	NGC6496	6.3×10^5	2.7×10^{-13}
NGC6517 (*)	8.0×10^4	3.8×10^{-13}	NGC6522 (*)	1.2×10^5	5.9×10^{-13}	NGC6528	1.9×10^5	5.7×10^{-11}
NGC6535	4.8×10^5	2.9×10^{-12}	NGC6539	2.6×10^5	2.5×10^{-12}	NGC6540	6.8×10^5	2.0×10^{-13}
NGC6541 (*)	1.7×10^5	6.1×10^{-13}	NGC6544 (*)	1.0×10^5	6.4×10^{-13}	NGC6553	1.9×10^5	7.8×10^{-11}
NGC6558 (*)	1.4×10^5	7.0×10^{-13}	NGC6569 (*)	1.6×10^5	1.5×10^{-13}	NGC6584	4.0×10^5	4.7×10^{-13}
NGC6624 (*)	1.8×10^5	4.3×10^{-13}	NGC6626 (*)	6.4×10^4	2.5×10^{-12}	NGC6637	1.8×10^5	5.4×10^{-11}
NGC6638 (*)	9.7×10^4	7.8×10^{-13}	NGC6642 (*)	1.0×10^5	1.3×10^{-12}	NGC6652 (*)	1.3×10^5	3.3×10^{-13}
NGC6656 (*)	1.8×10^5	1.5×10^{-13}	NGC6681 (*)	1.5×10^5	4.3×10^{-13}	NGC6712	1.9×10^5	4.5×10^{-11}
NGC6715 (*)	9.1×10^4	1.4×10^{-12}	NGC6717	4.7×10^5	7.4×10^{-13}	NGC6723	2.8×10^5	2.1×10^{-11}
NGC6749	4.2×10^5	7.0×10^{-13}	NGC6752	2.4×10^5	2.9×10^{-11}	NGC6760	2.4×10^5	6.7×10^{-12}
NGC6779	2.3×10^5	1.3×10^{-11}	NGC6809	4.3×10^5	1.7×10^{-12}	NGC6838	6.7×10^5	7.0×10^{-14}
NGC6864 (*)	8.6×10^4	9.1×10^{-13}	NGC6934	3.2×10^5	6.4×10^{-12}	NGC6981	5.7×10^5	7.0×10^{-13}
NGC7006	5.1×10^5	9.1×10^{-13}	NGC7078 (*)	1.1×10^5	4.1×10^{-13}	NGC7089 (*)	1.4×10^5	1.3×10^{-13}
NGC7099	3.0×10^5	5.2×10^{-14}	NGC7492	1.9×10^6	6.0×10^{-13}	Pal1	2.1×10^6	3.0×10^{-13}
Pal10	4.0×10^5	4.6×10^{-13}	Pal11	2.0×10^6	3.5×10^{-13}	Pal12	4.4×10^6	1.1×10^{-12}
Pal13	1.3×10^7	3.0×10^{-13}	Pal14	1.7×10^7	7.4×10^{-13}	Pal15	6.3×10^6	9.2×10^{-14}
Pal2	4.9×10^5	4.1×10^{-13}	Pal3	1.1×10^7	8.1×10^{-13}	Pal4	8.8×10^6	6.6×10^{-13}
Pal5	1.5×10^7	6.2×10^{-13}	Pal6 (*)	1.6×10^5	1.0×10^{-12}	Pal8	5.6×10^5	1.1×10^{-12}
Pyxis	7.2×10^6	6.0×10^{-13}	Rup106	2.2×10^6	9.4×10^{-13}	SagittariusII	1.9×10^7	7.3×10^{-13}
Ter1 (*)	8.3×10^4	7.1×10^{-13}	Ter10	1.8×10^5	7.3×10^{-11}	Ter12	2.1×10^5	3.1×10^{-11}
Ter2	2.4×10^5	1.2×10^{-11}	Ter3	9.8×10^5	1.2×10^{-12}	Ter4	3.4×10^5	5.9×10^{-12}
Ter5 (*)	7.7×10^4	3.5×10^{-13}	Ter6 (*)	4.9×10^4	1.5×10^{-12}	Ter7	3.2×10^6	7.4×10^{-13}
Ter8	4.1×10^6	9.4×10^{-13}	Ter9 (*)	7.7×10^4	4.7×10^{-13}	Ton2	3.8×10^5	1.1×10^{-13}
UKS1	2.8×10^5	2.0×10^{-12}	VVV-CL001 (*)	1.4×10^5	1.1×10^{-12}	Whiting1	1.4×10^7	1.6×10^{-13}

5.2 Extra-tidal features generated by all the simulated clusters

In this section, we report all the extra-tidal features as predicted by our models. For each cluster, we show (from Figs. 4.14 to 4.33) the probability density of finding associated extra-tidal features in the sky, by calculating the 2D histogram of the escaped particles. Each particle per cluster is present, meaning that all 100,000 particles originating each of the 50 Monte-Carlo realizations are included, plus the case with the best values (see Sect. 2.1). Thus, each map is a 500x500 histogram that bins 5.1×10^6 particles. The retrieved cumulative 2D histogram is then normalized to its maximum value and plotted in the following figures in logarithmic scale.

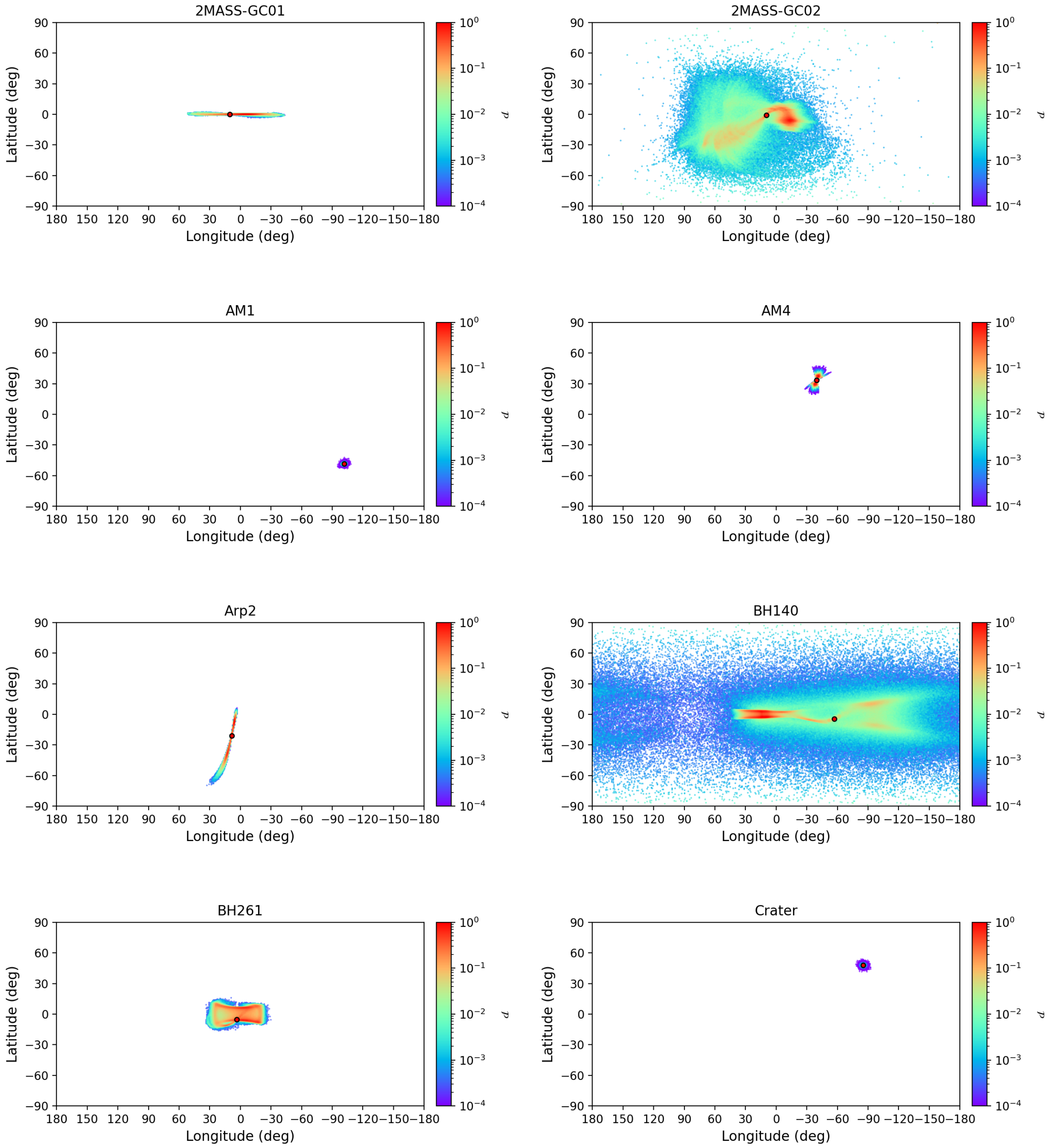

Figure 4.14 – Projected density distribution in the (ℓ, b) plane of a subset of simulated globular clusters, as indicated at the top of each panel. In each panel, the red circle indicates the current position of the cluster. The densities have been normalized to their maximum value.

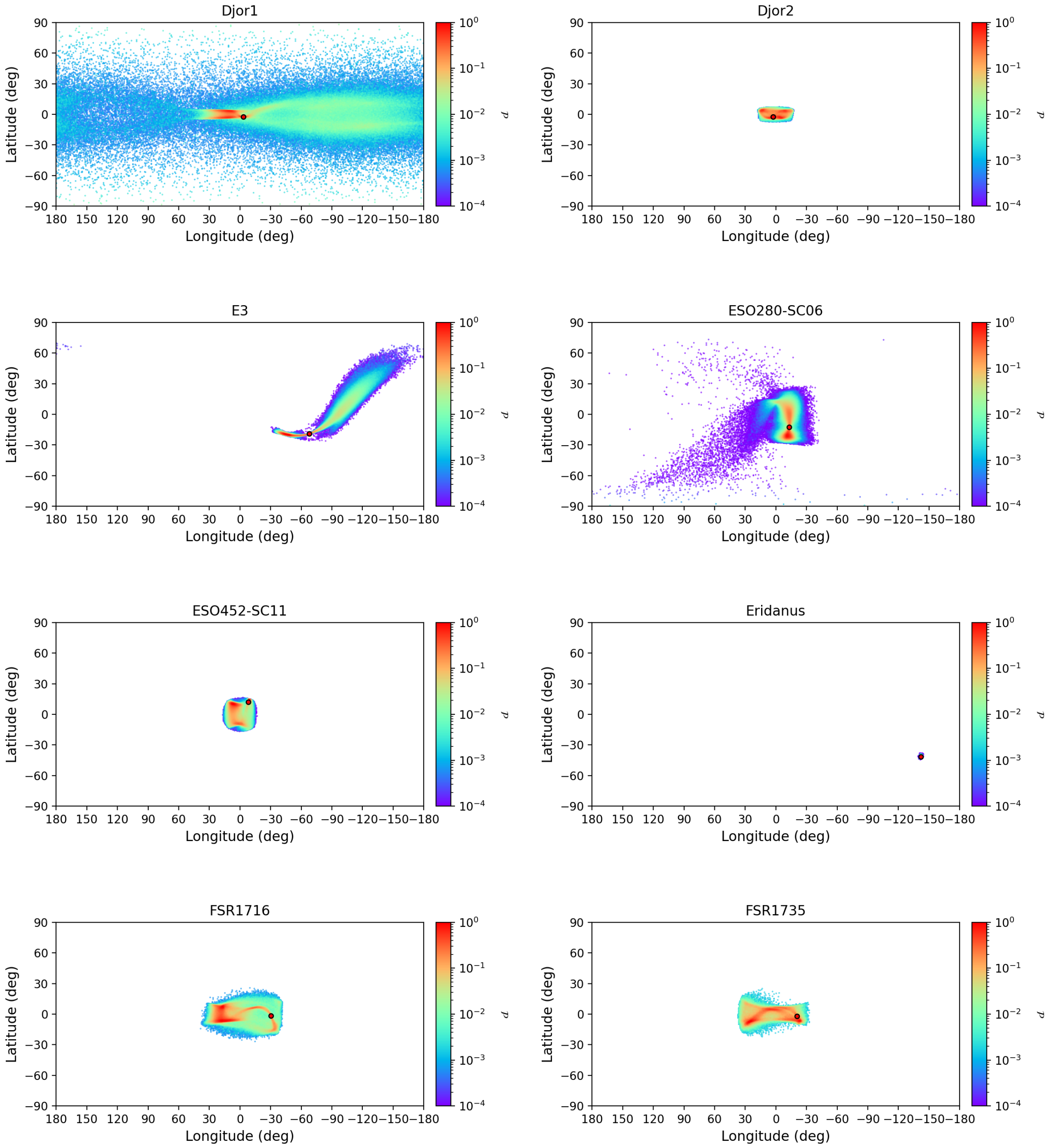

Figure 4.15 – Projected density distribution in the (ℓ, b) plane of a subset of simulated globular clusters, as indicated at the top of each panel. In each panel, the red circle indicates the current position of the cluster. The densities have been normalized to their maximum value.

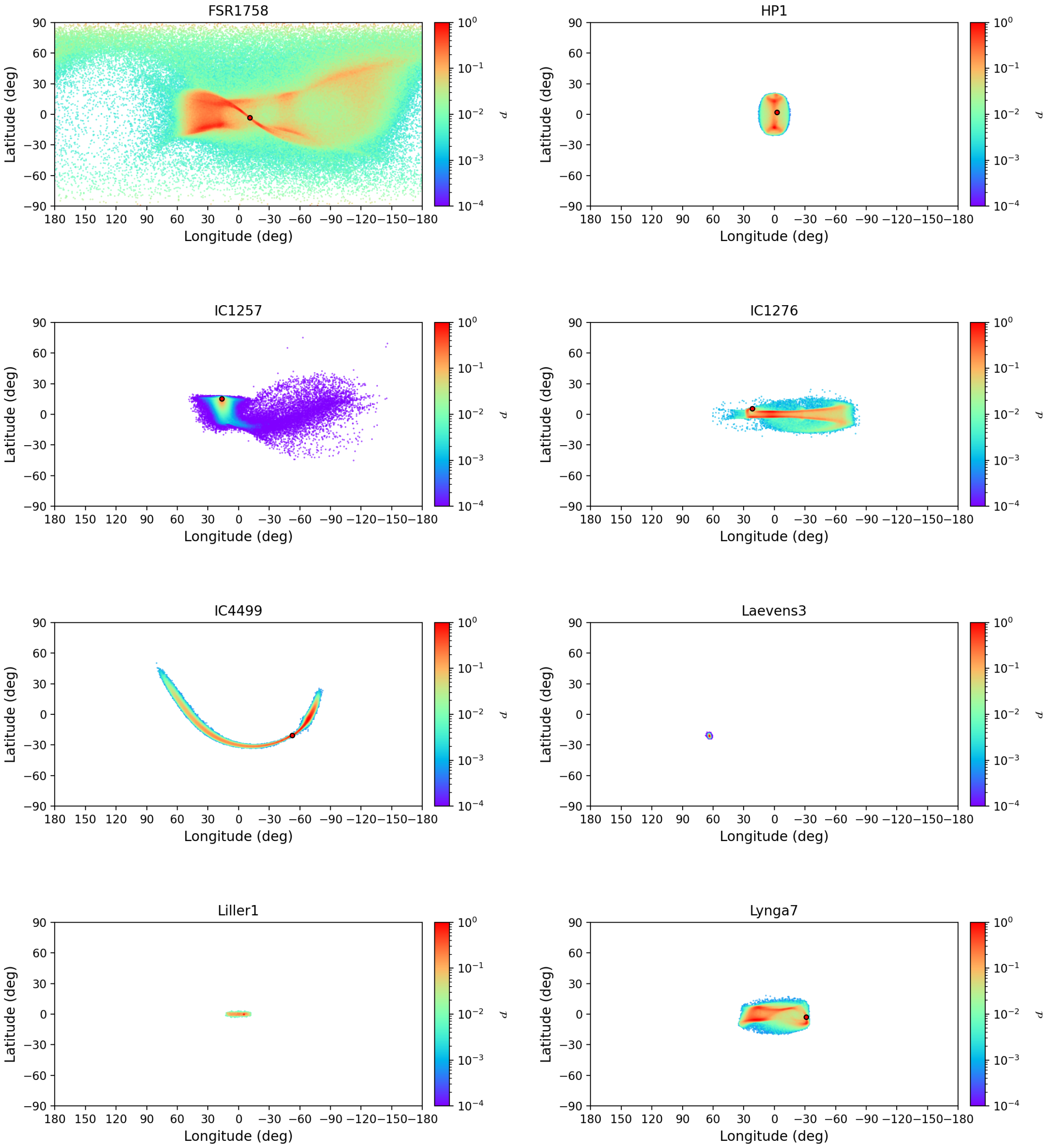

Figure 4.16 – Projected density distribution in the (ℓ, b) plane of a subset of simulated globular clusters, as indicated at the top of each panel. In each panel, the red circle indicates the current position of the cluster. The densities have been normalized to their maximum value.

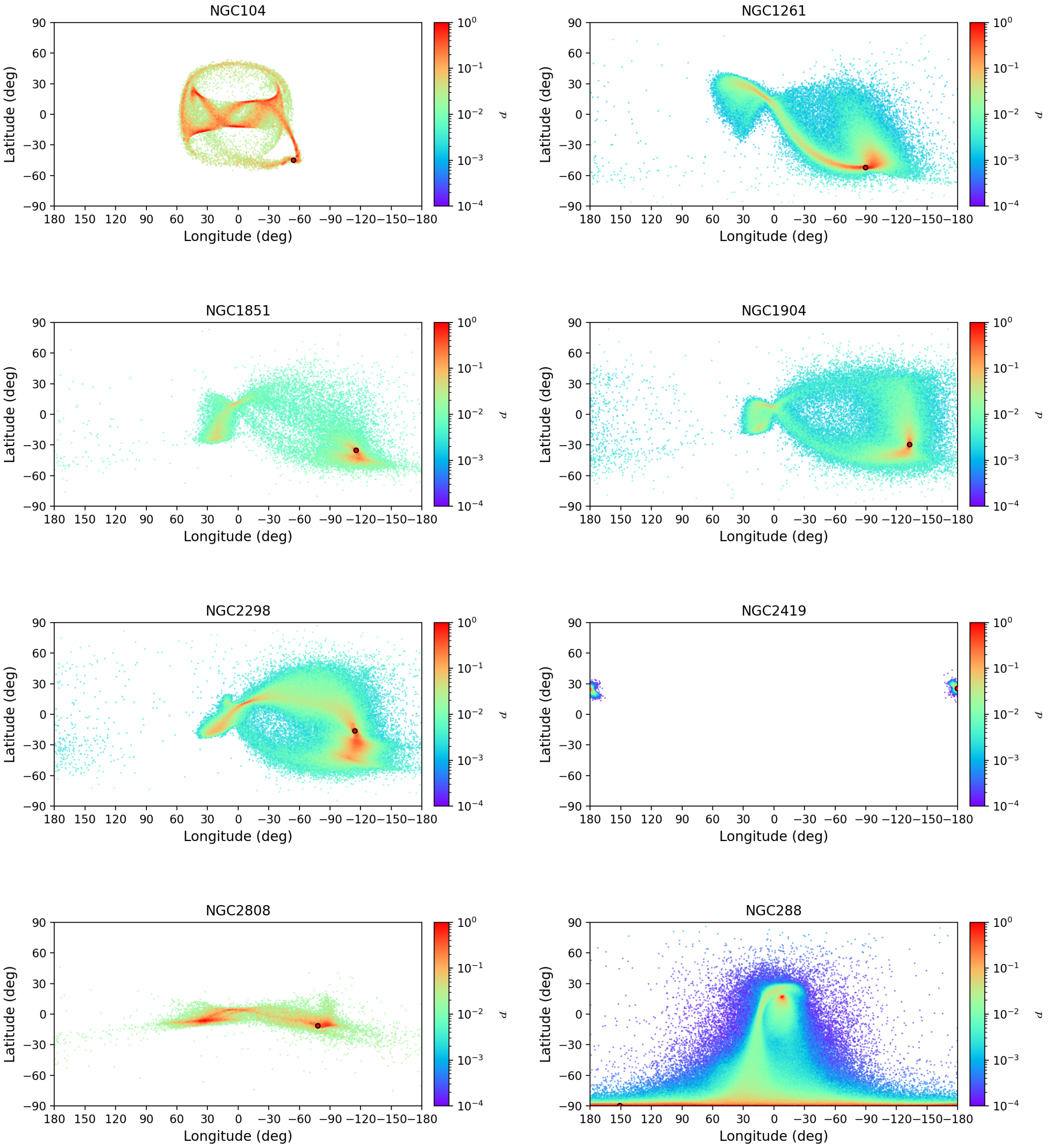

Figure 4.17 – Projected density distribution in the (ℓ, b) plane of a subset of simulated globular clusters, as indicated at the top of each panel. In each panel, the red circle indicates the current position of the cluster. The densities have been normalized to their maximum value.

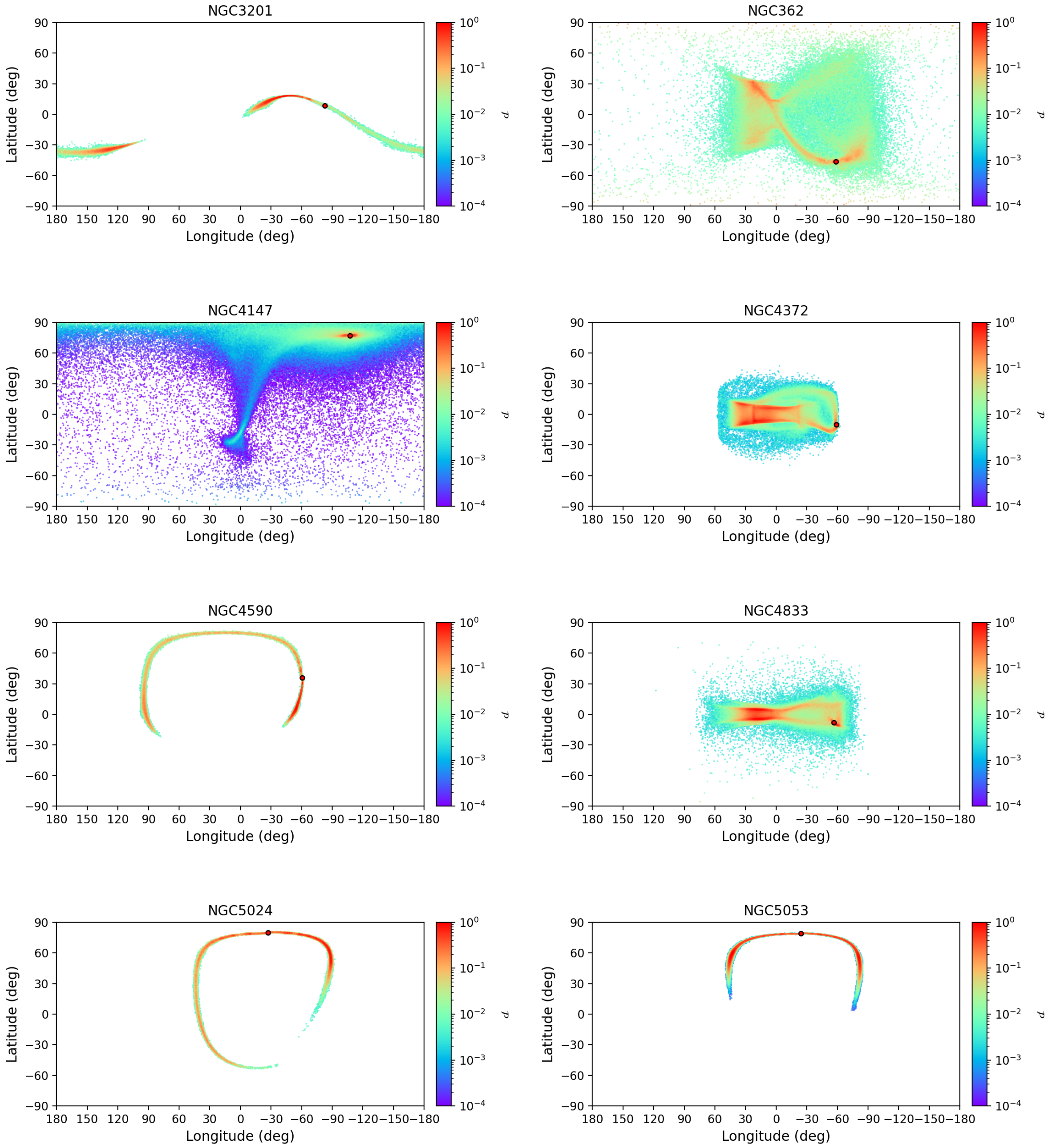
NGC3201

NGC362

NGC4147

NGC4372

NGC4590

NGC4833

NGC5024

NGC5053

Figure 4.18 – Projected density distribution in the (ℓ, b) plane of a subset of simulated globular clusters, as indicated at the top of each panel. In each panel, the red circle indicates the current position of the cluster. The densities have been normalized to their maximum value.

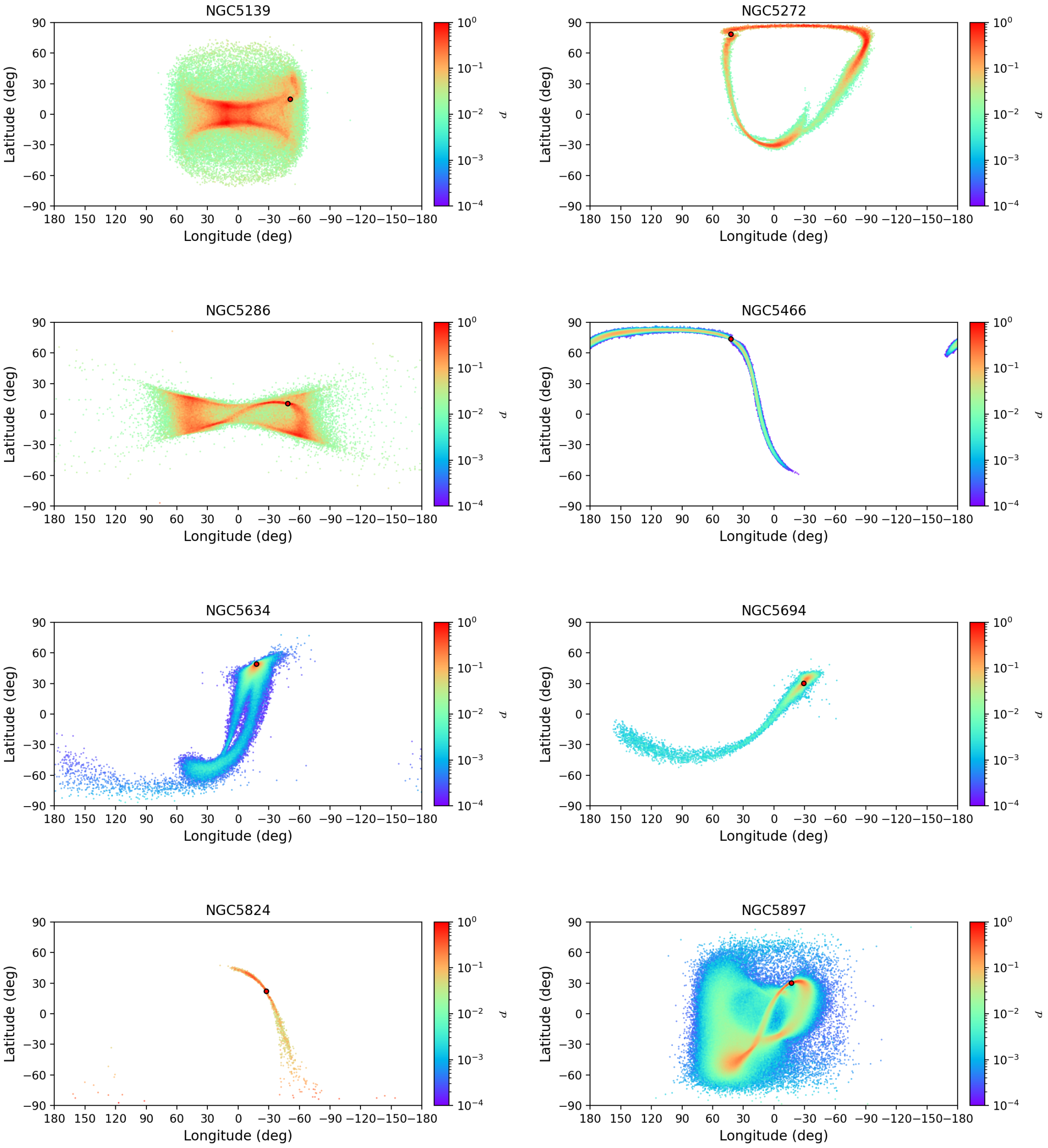

Figure 4.19 – Projected density distribution in the (ℓ, b) plane of a subset of simulated globular clusters, as indicated at the top of each panel. In each panel, the red circle indicates the current position of the cluster. The densities have been normalized to their maximum value.

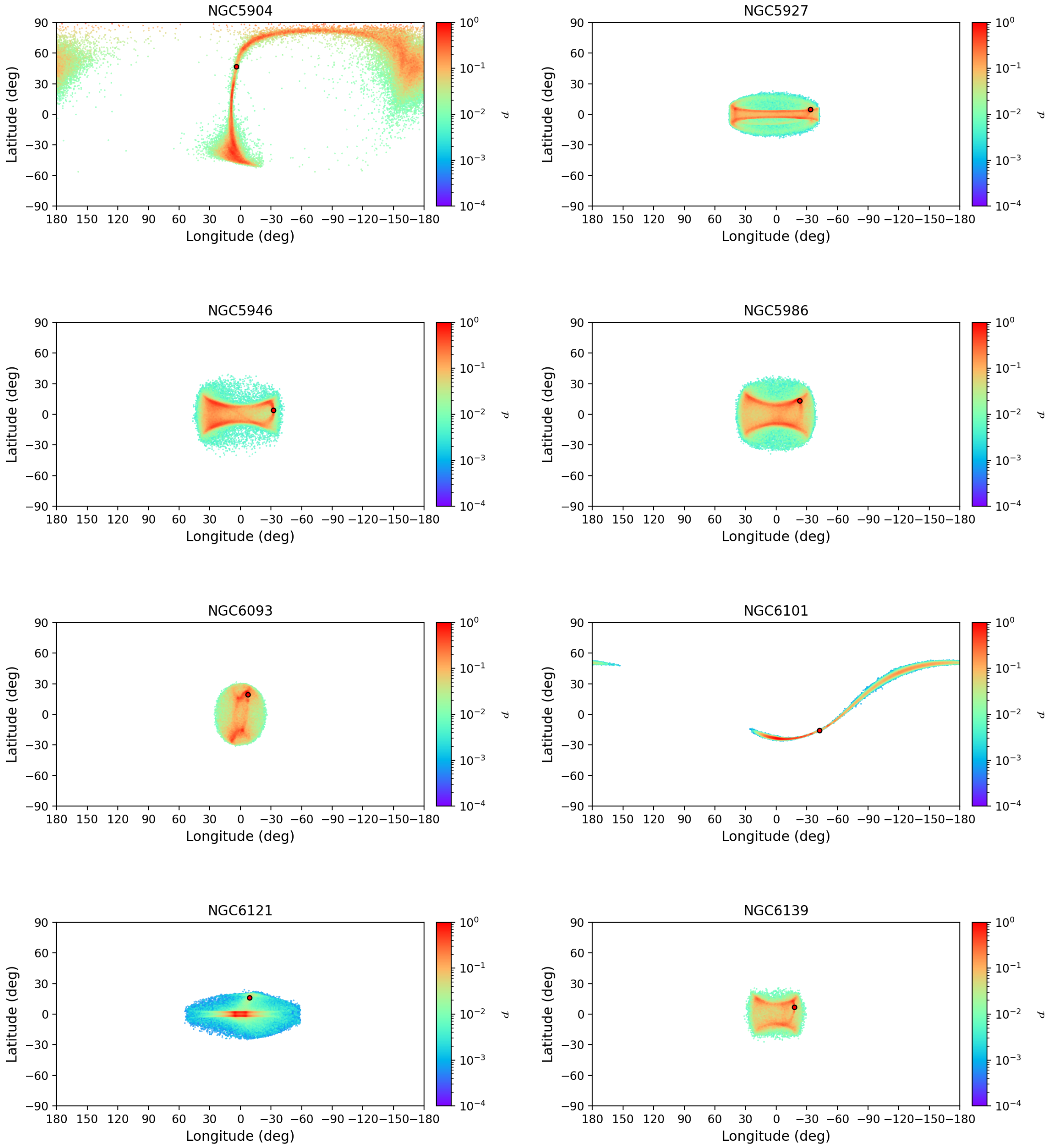

Figure 4.20 – Projected density distribution in the (ℓ, b) plane of a subset of simulated globular clusters, as indicated at the top of each panel. In each panel, the red circle indicates the current position of the cluster. The densities have been normalized to their maximum value.

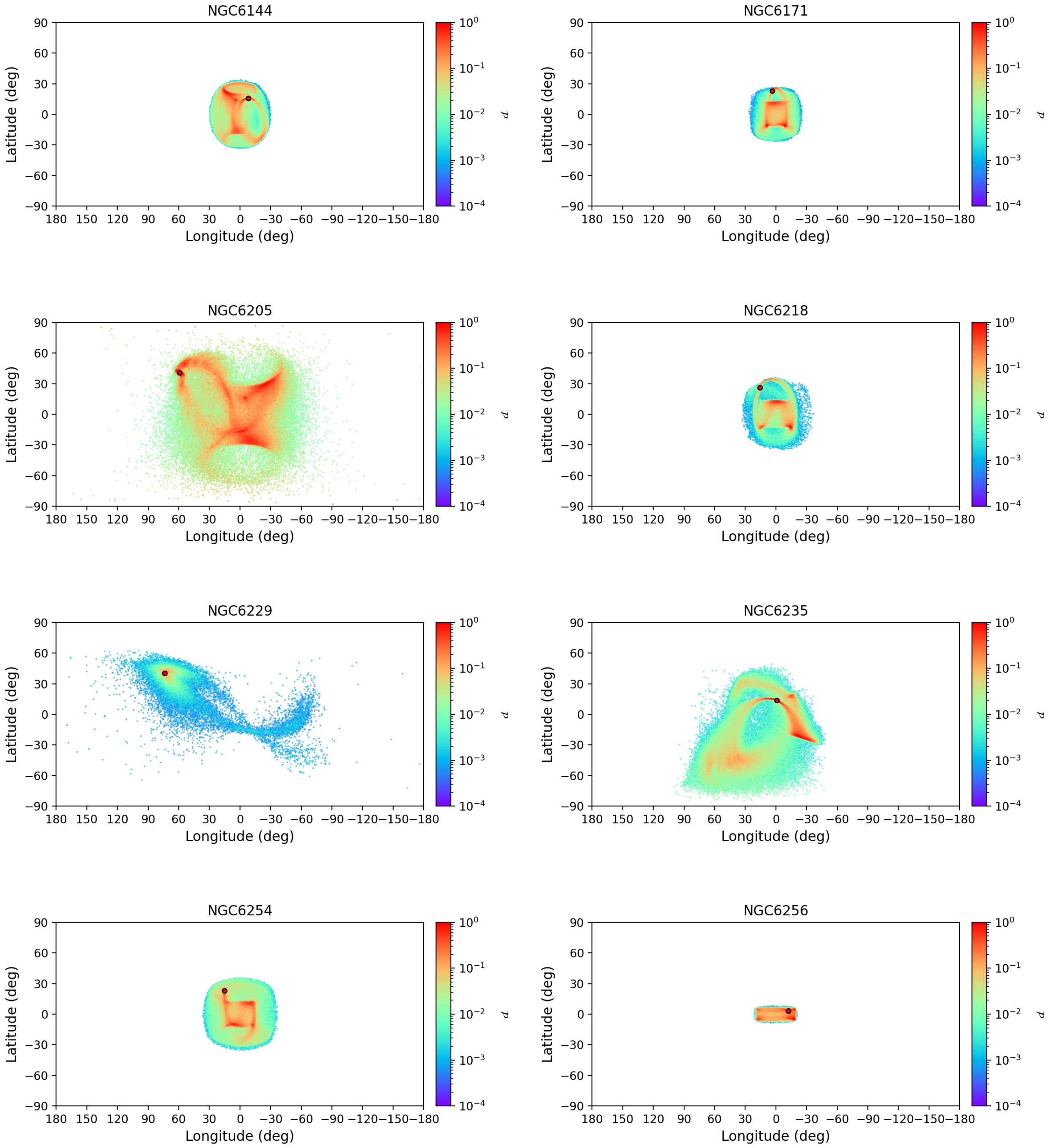

Figure 4.21 – Projected density distribution in the (ℓ, b) plane of a subset of simulated globular clusters, as indicated at the top of each panel. In each panel, the red circle indicates the current position of the cluster. The densities have been normalized to their maximum value.

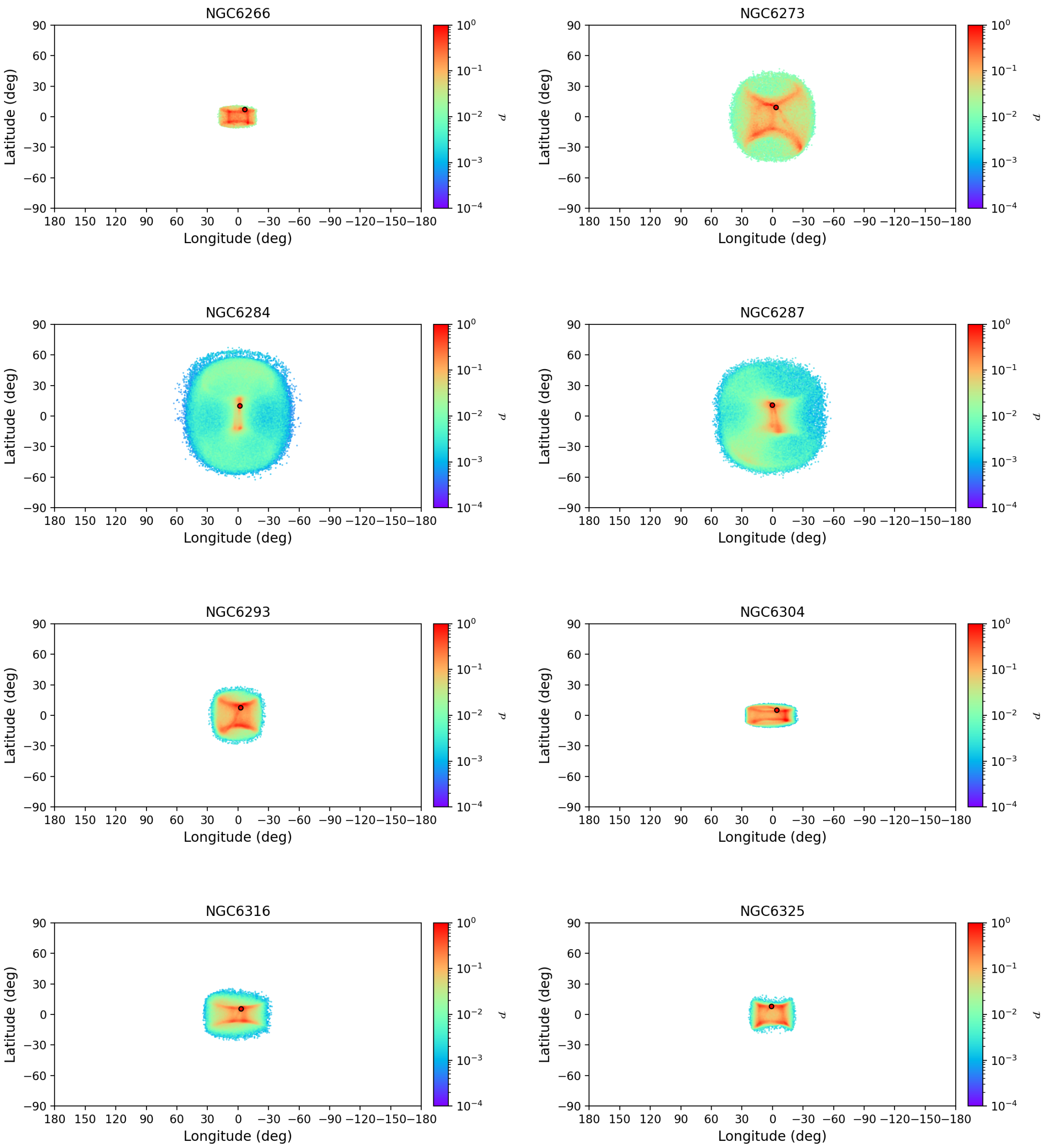

Figure 4.22 – Projected density distribution in the (ℓ, b) plane of a subset of simulated globular clusters, as indicated at the top of each panel. In each panel, the red circle indicates the current position of the cluster. The densities have been normalized to their maximum value.

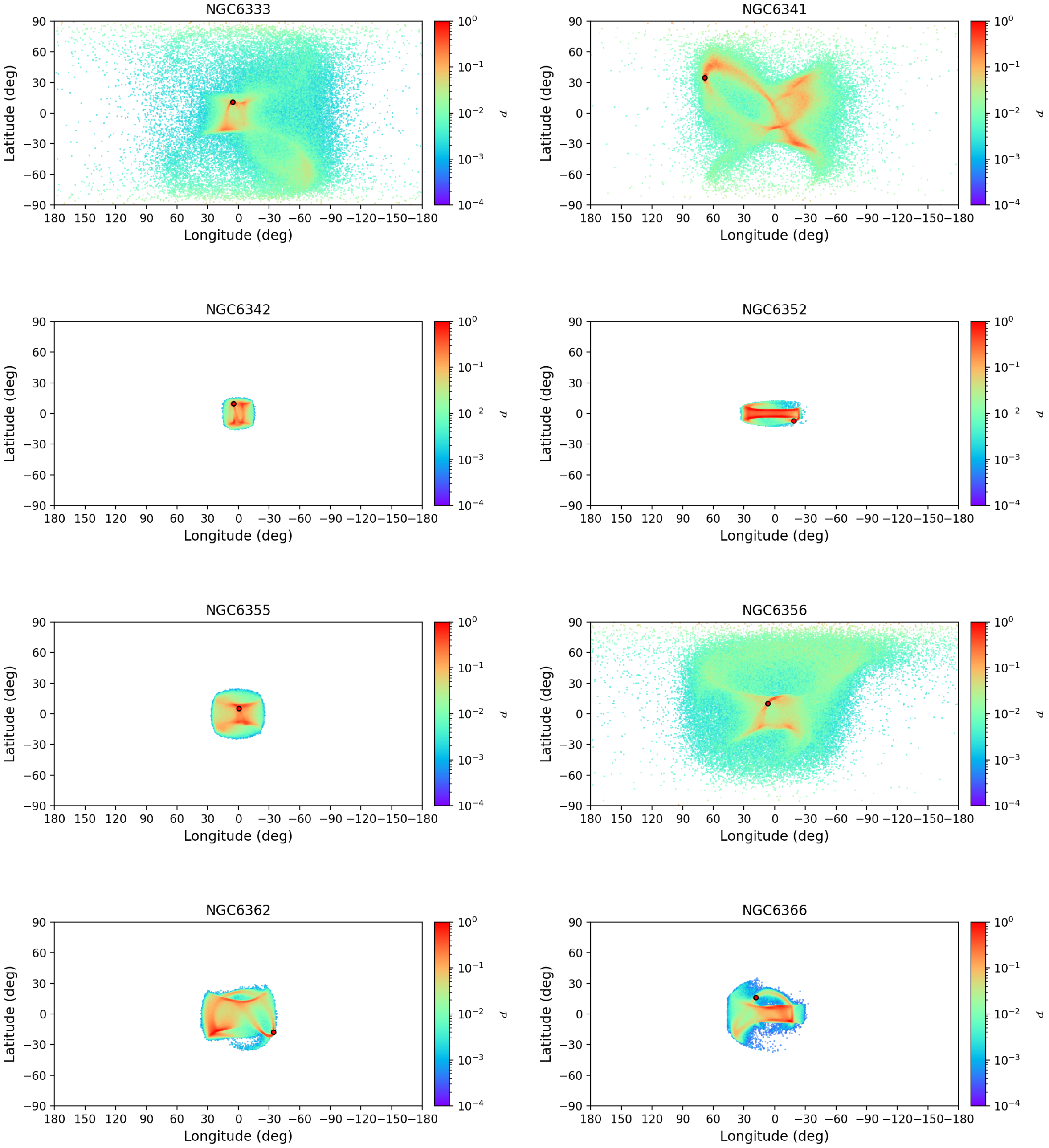
NGC6333 NGC6341 NGC6342 NGC6352 NGC6355 NGC6356 NGC6362 NGC6366

Figure 4.23 – Projected density distribution in the (ℓ, b) plane of a subset of simulated globular clusters, as indicated at the top of each panel. In each panel, the red circle indicates the current position of the cluster. The densities have been normalized to their maximum value.

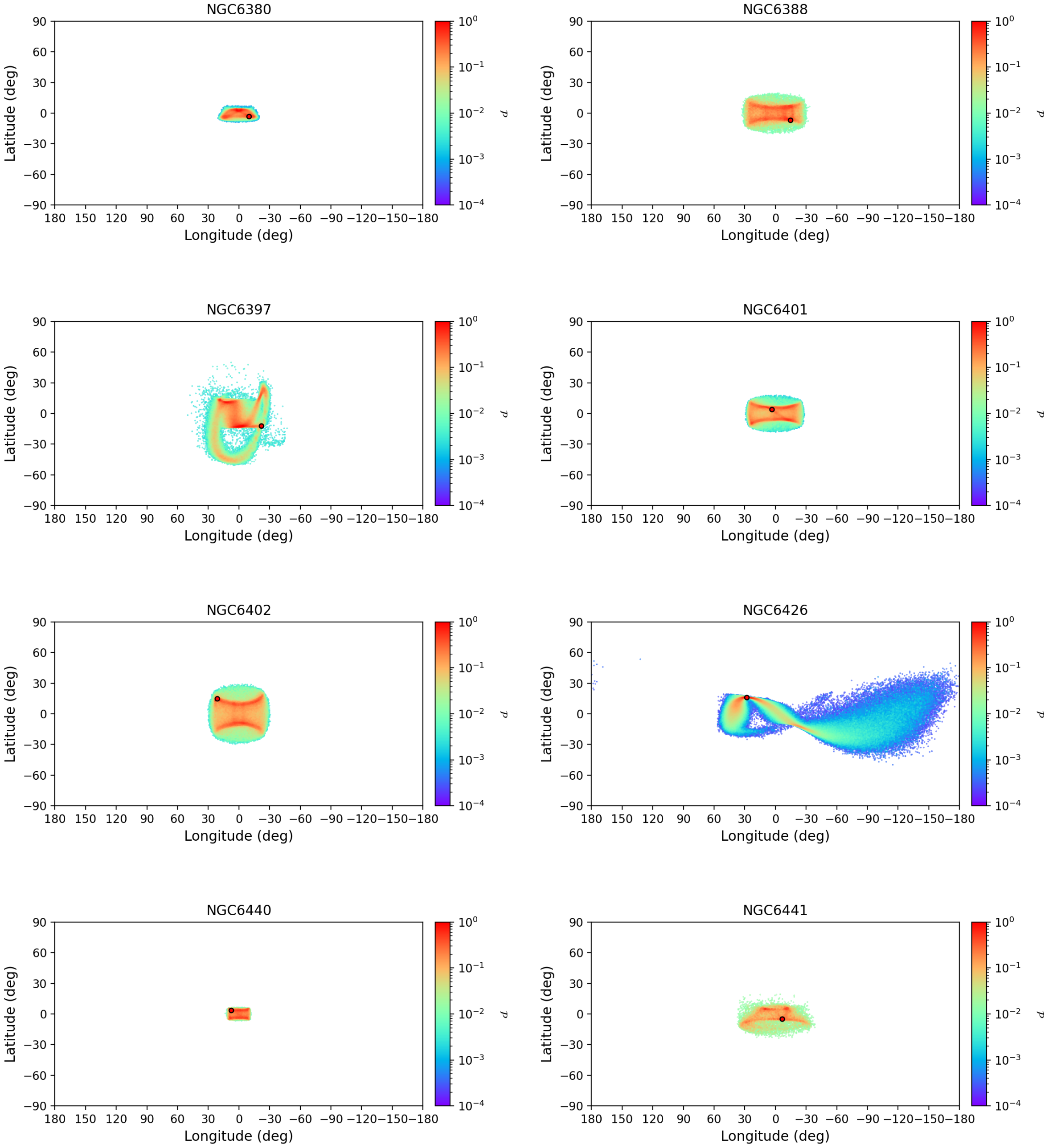

Figure 4.24 – Projected density distribution in the (ℓ, b) plane of a subset of simulated globular clusters, as indicated at the top of each panel. In each panel, the red circle indicates the current position of the cluster. The densities have been normalized to their maximum value.

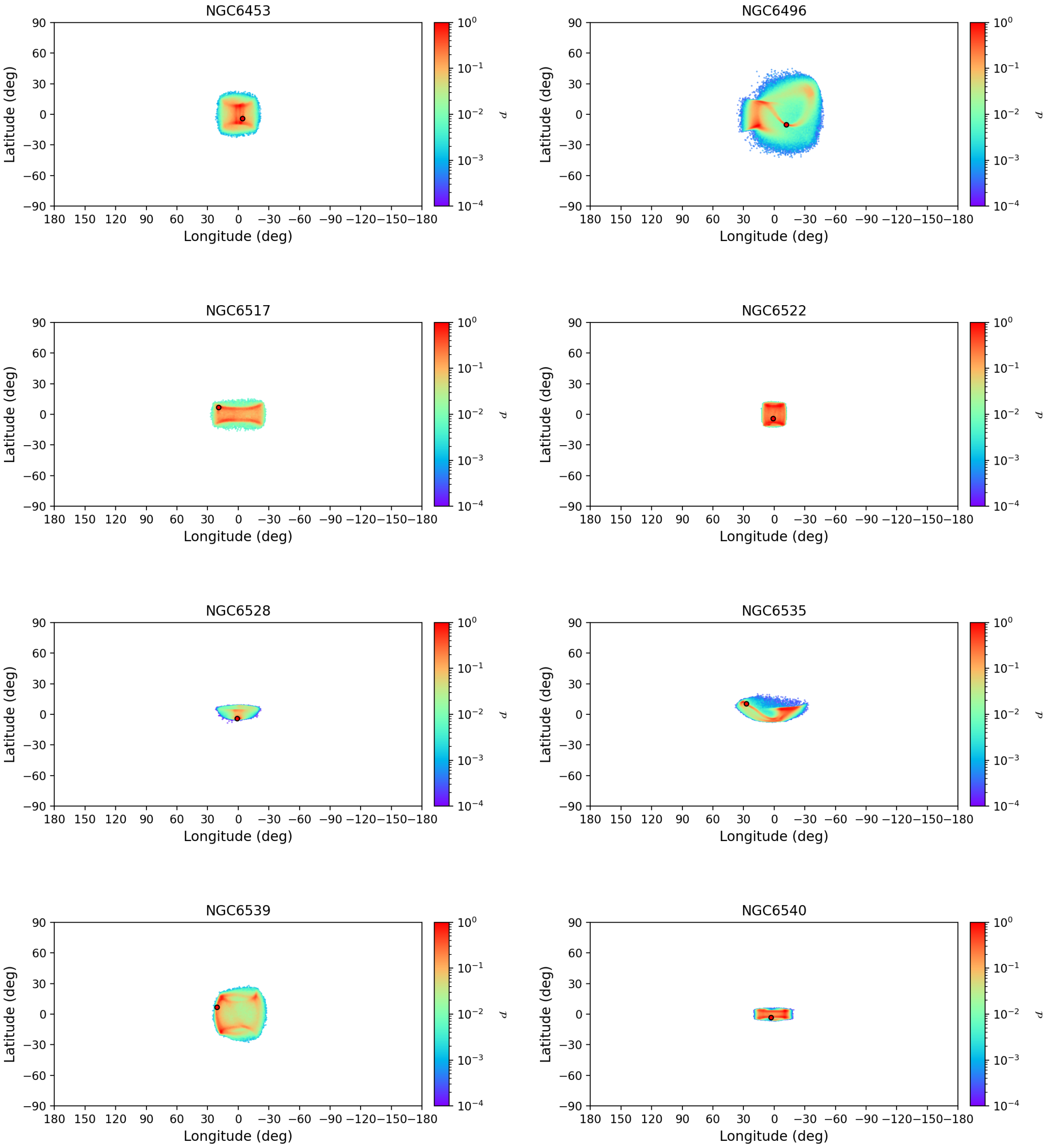
NGC6453
NGC6496
NGC6517
NGC6522
NGC6528
NGC6535
NGC6539
NGC6540

Figure 4.25 – Projected density distribution in the (ℓ, b) plane of a subset of simulated globular clusters, as indicated at the top of each panel. In each panel, the red circle indicates the current position of the cluster. The densities have been normalized to their maximum value.

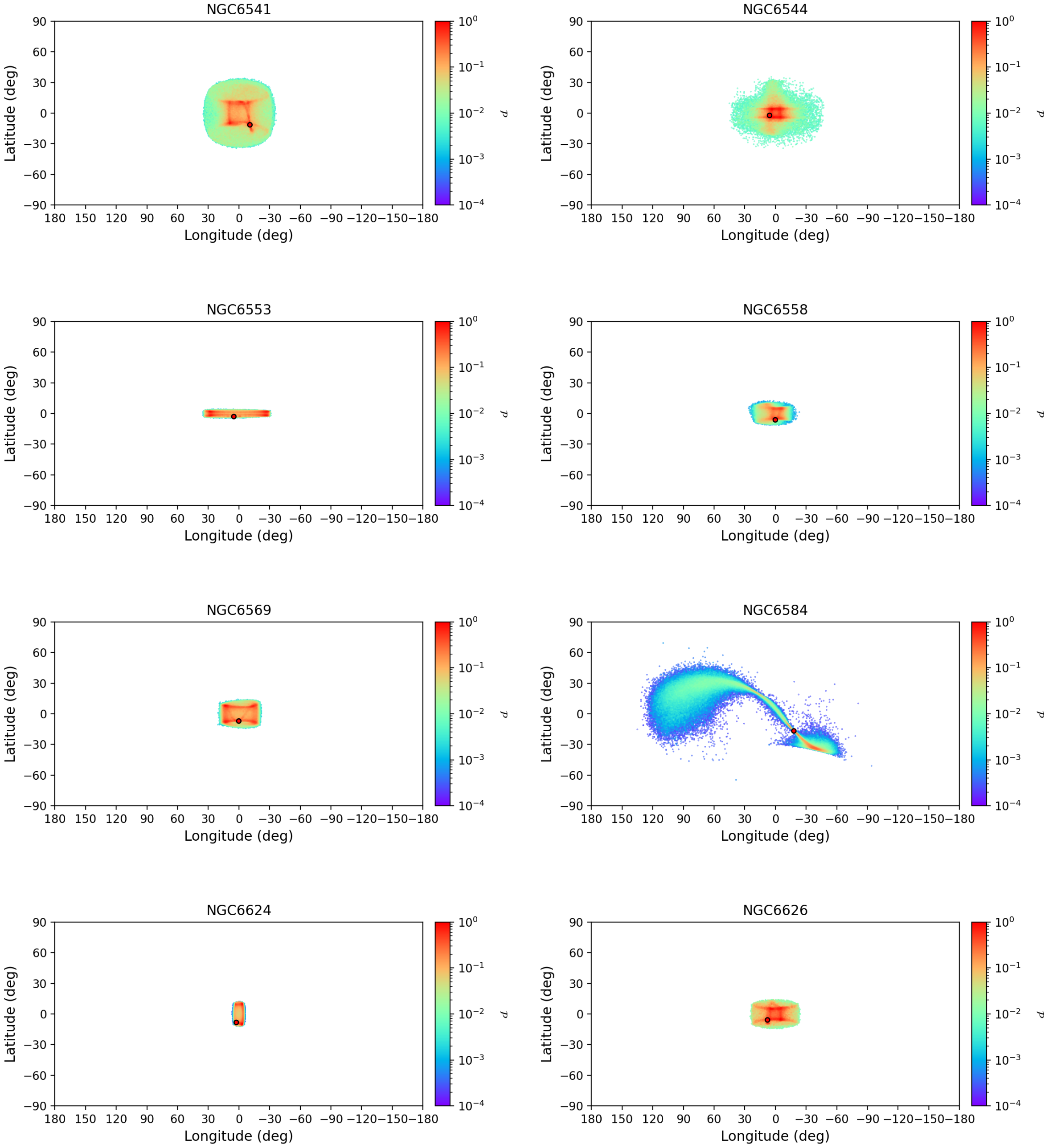

Figure 4.26 – Projected density distribution in the (ℓ, b) plane of a subset of simulated globular clusters, as indicated at the top of each panel. In each panel, the red circle indicates the current position of the cluster. The densities have been normalized to their maximum value.

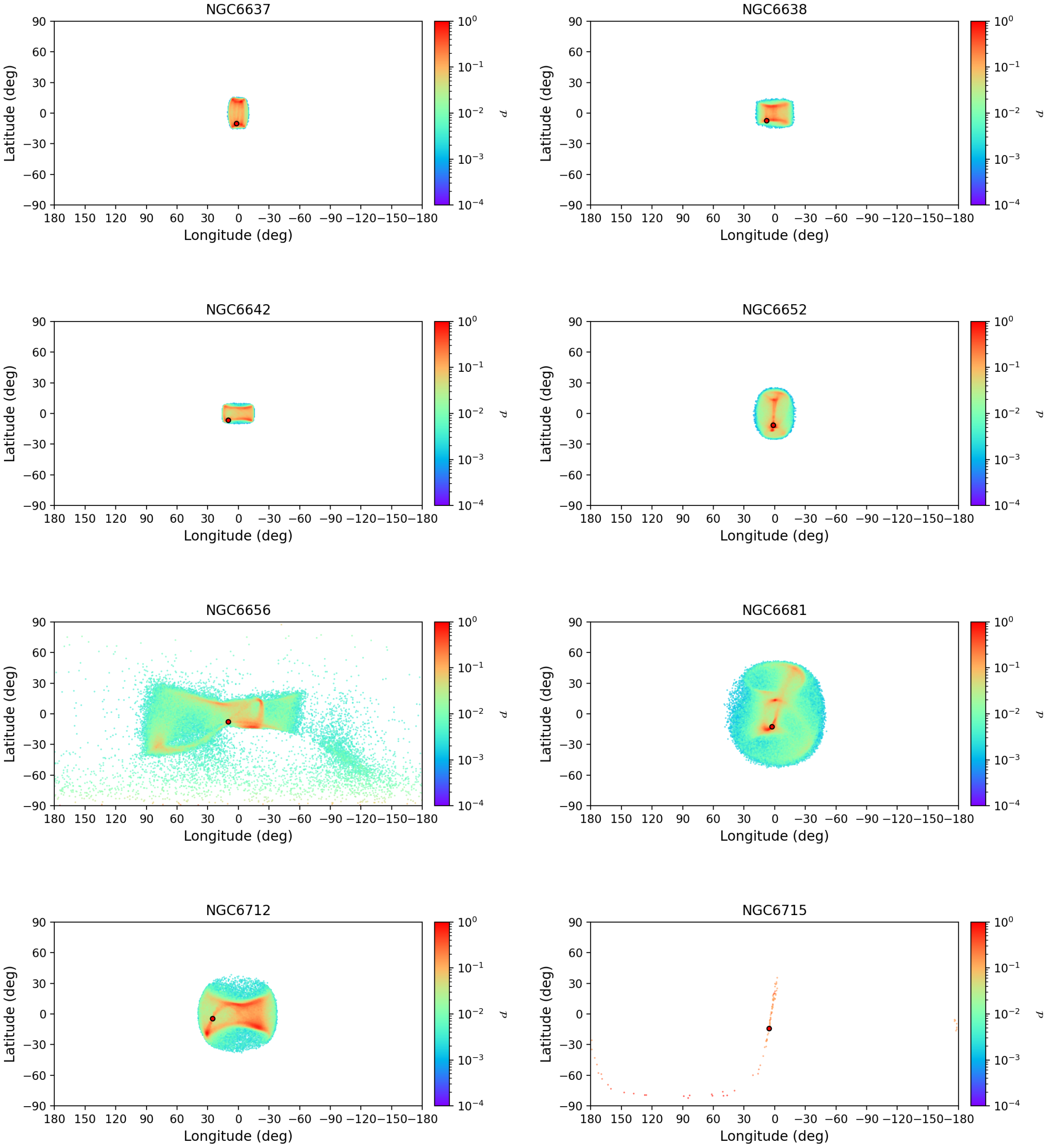

Figure 4.27 – Projected density distribution in the (ℓ, b) plane of a subset of simulated globular clusters, as indicated at the top of each panel. In each panel, the red circle indicates the current position of the cluster. The densities have been normalized to their maximum value.

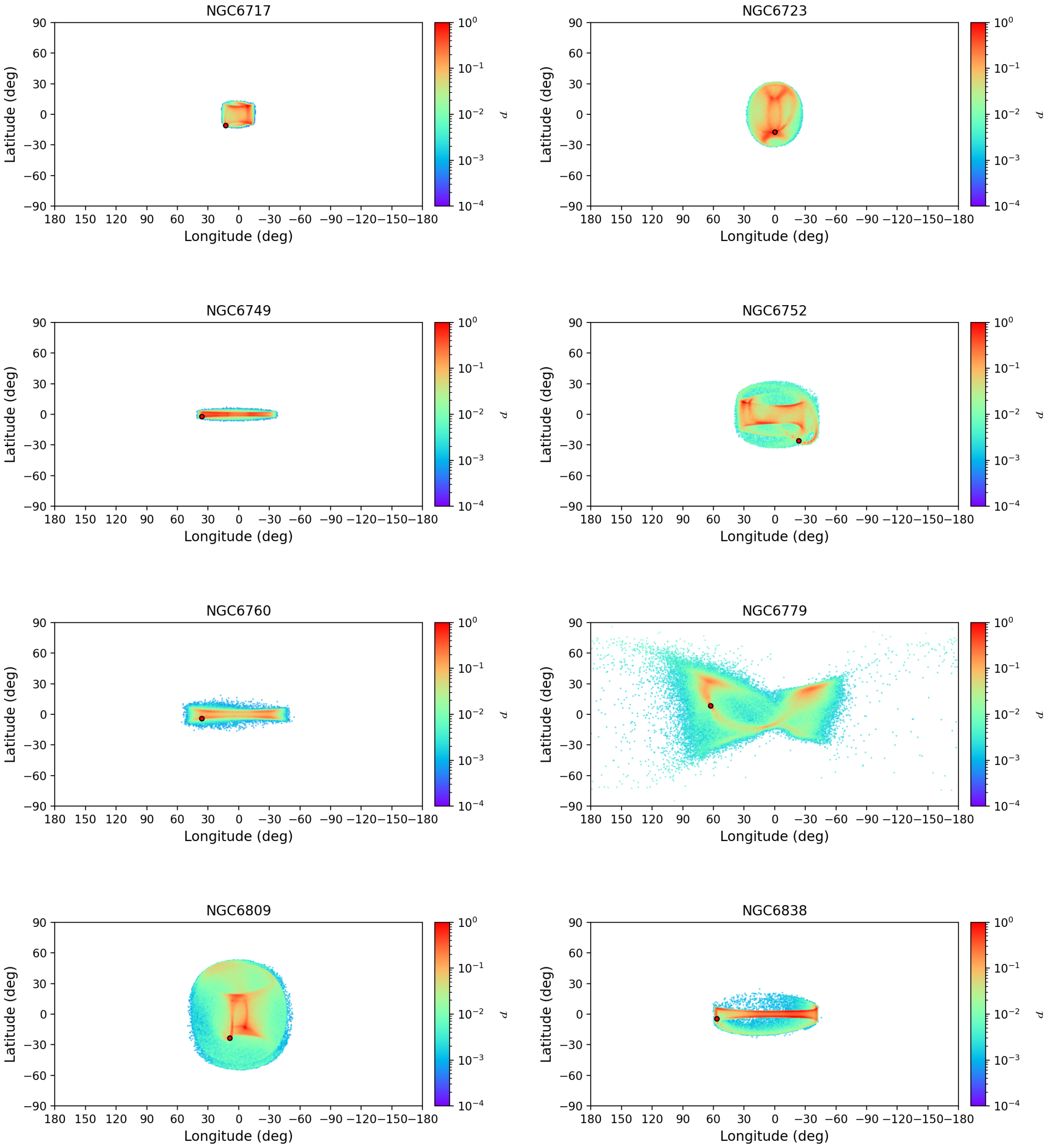

Figure 4.28 – Projected density distribution in the (ℓ, b) plane of a subset of simulated globular clusters, as indicated at the top of each panel. In each panel, the red circle indicates the current position of the cluster. The densities have been normalized to their maximum value.

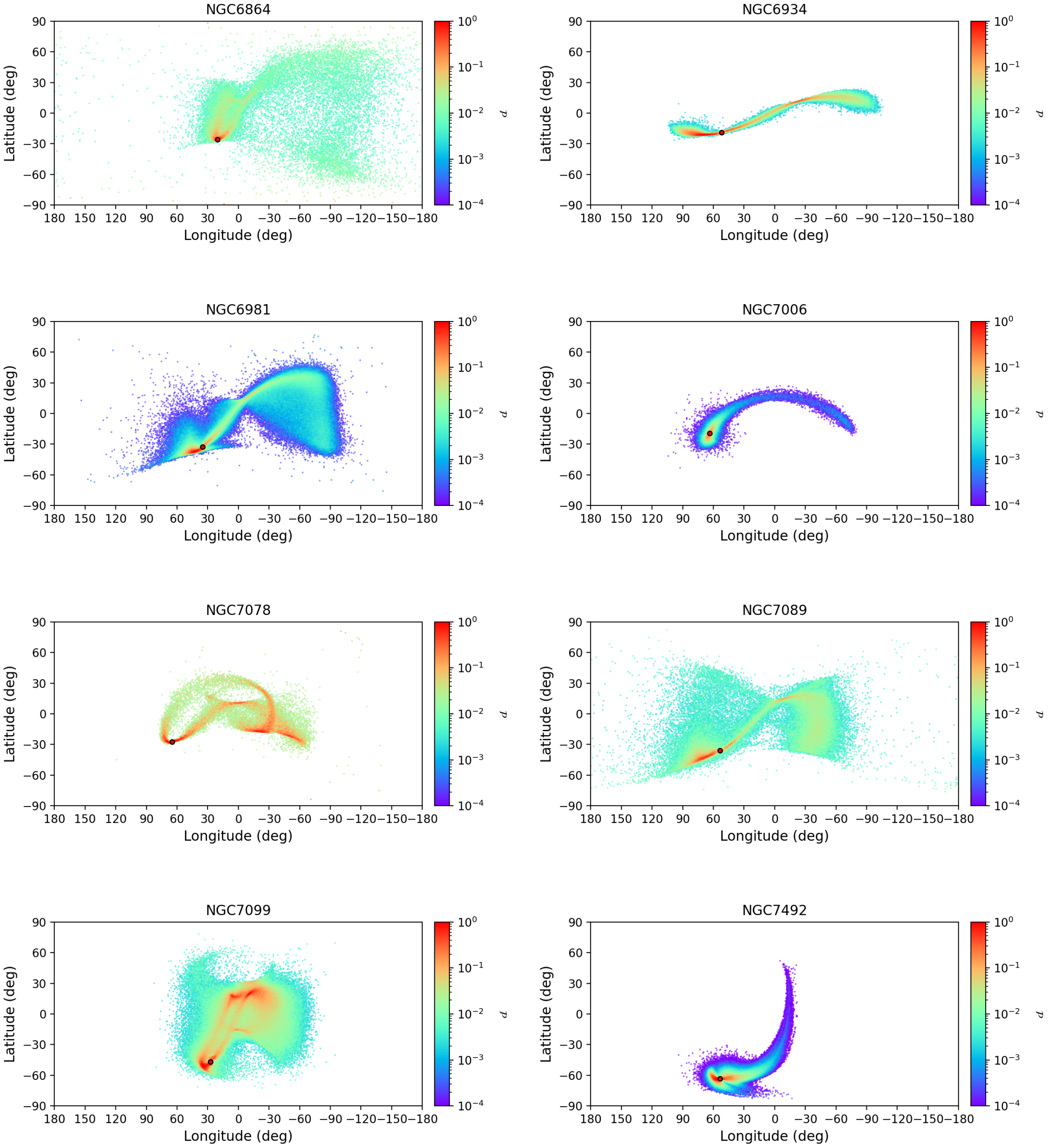

Figure 4.29 – Projected density distribution in the (ℓ, b) plane of a subset of simulated globular clusters, as indicated at the top of each panel. In each panel, the red circle indicates the current position of the cluster. The densities have been normalized to their maximum value.

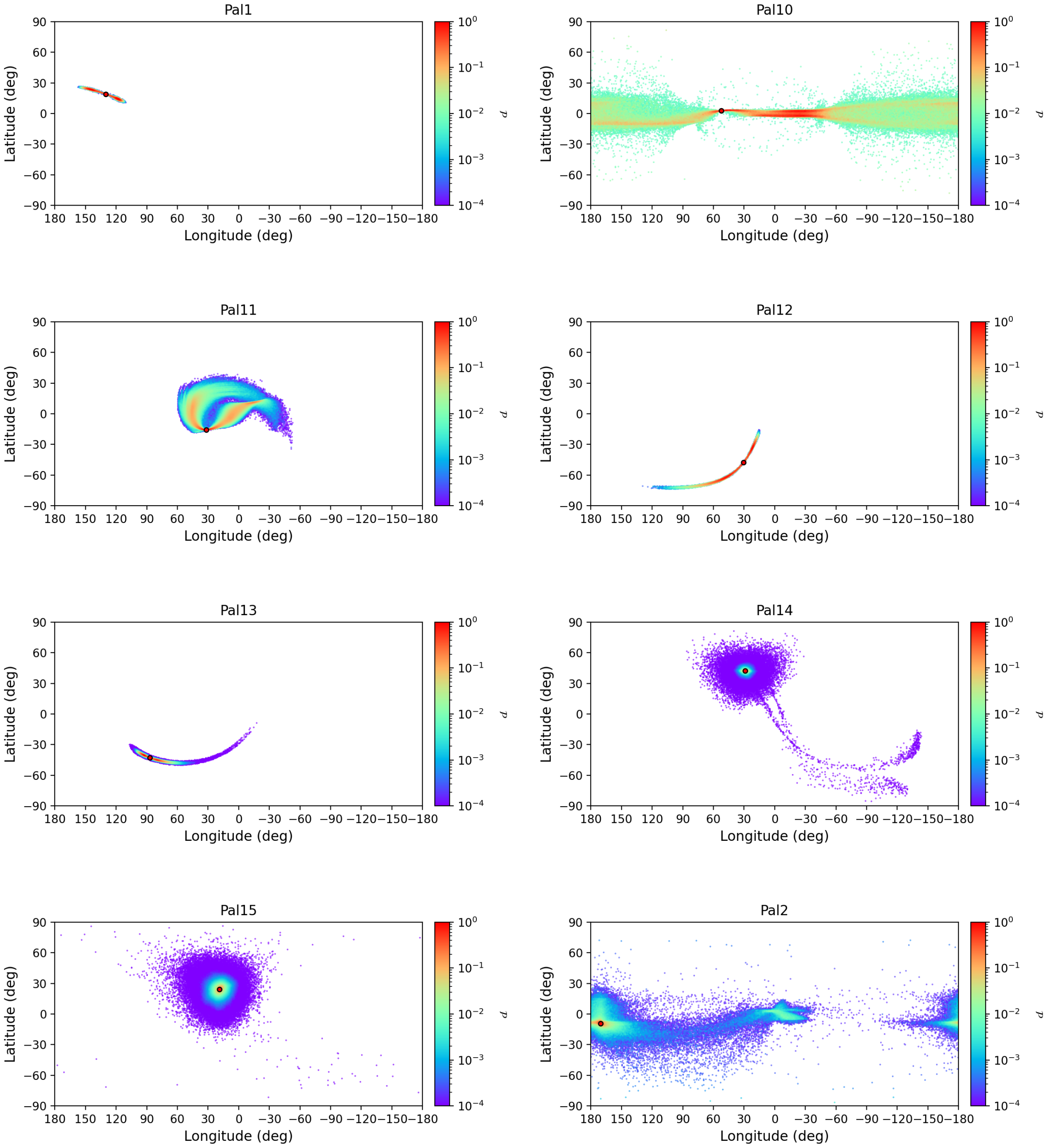

Figure 4.30 – Projected density distribution in the (ℓ, b) plane of a subset of simulated globular clusters, as indicated at the top of each panel. In each panel, the red circle indicates the current position of the cluster. The densities have been normalized to their maximum value.

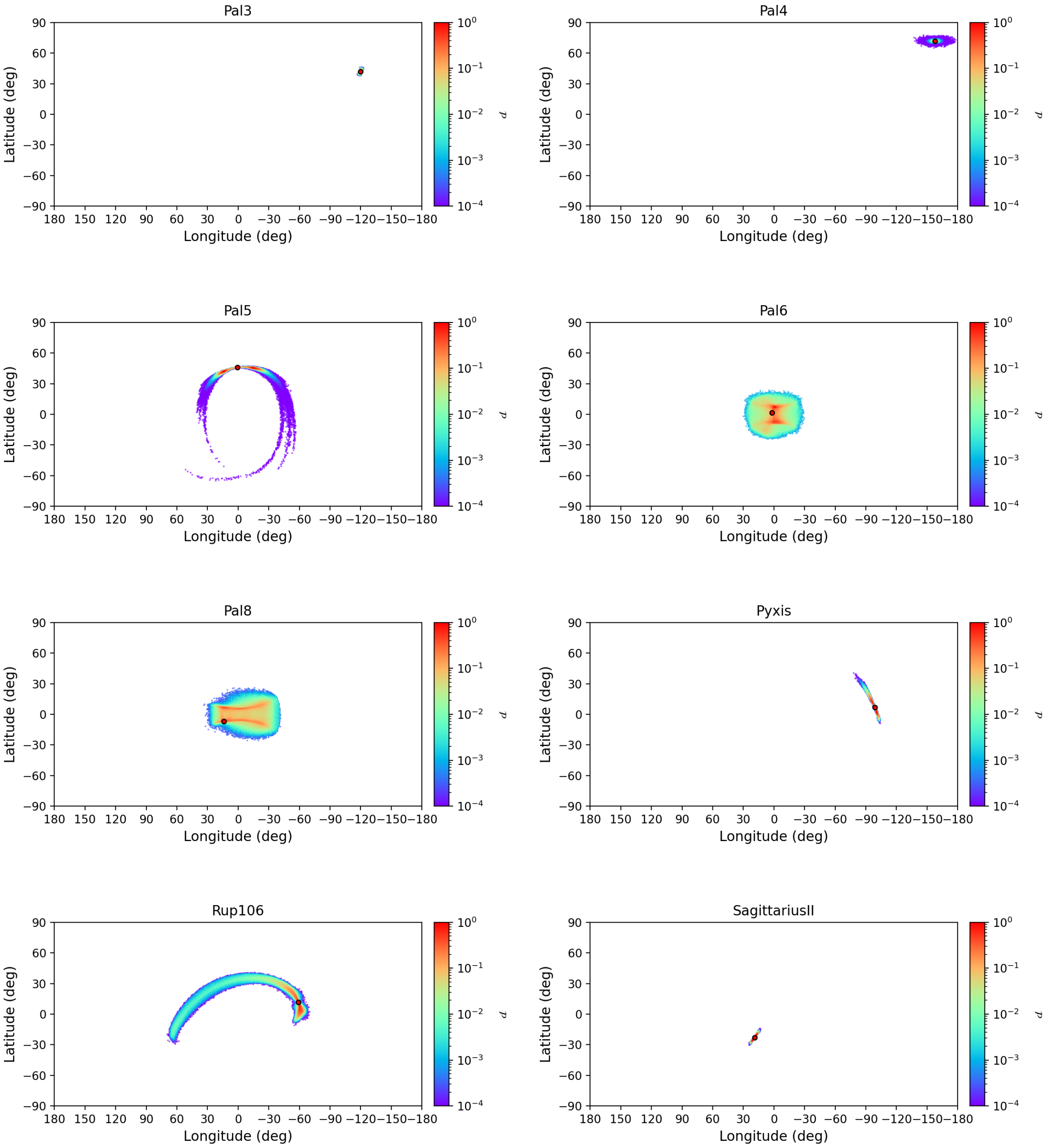

Figure 4.31 – Projected density distribution in the (ℓ, b) plane of a subset of simulated globular clusters, as indicated at the top of each panel. In each panel, the red circle indicates the current position of the cluster. The densities have been normalized to their maximum value.

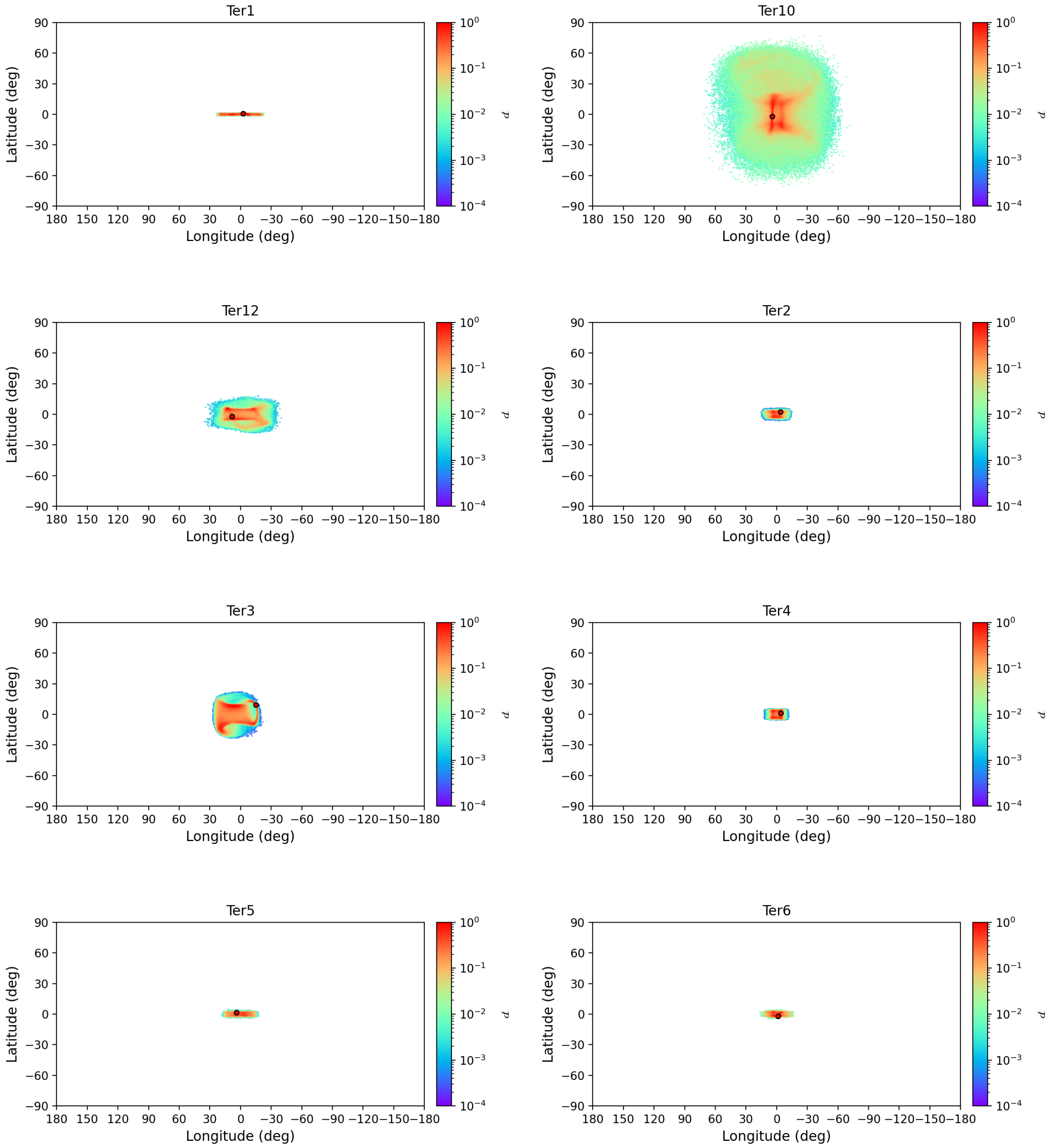

Figure 4.32 – Projected density distribution in the (ℓ, b) plane of a subset of simulated globular clusters, as indicated at the top of each panel. In each panel, the red circle indicates the current position of the cluster. The densities have been normalized to their maximum value.

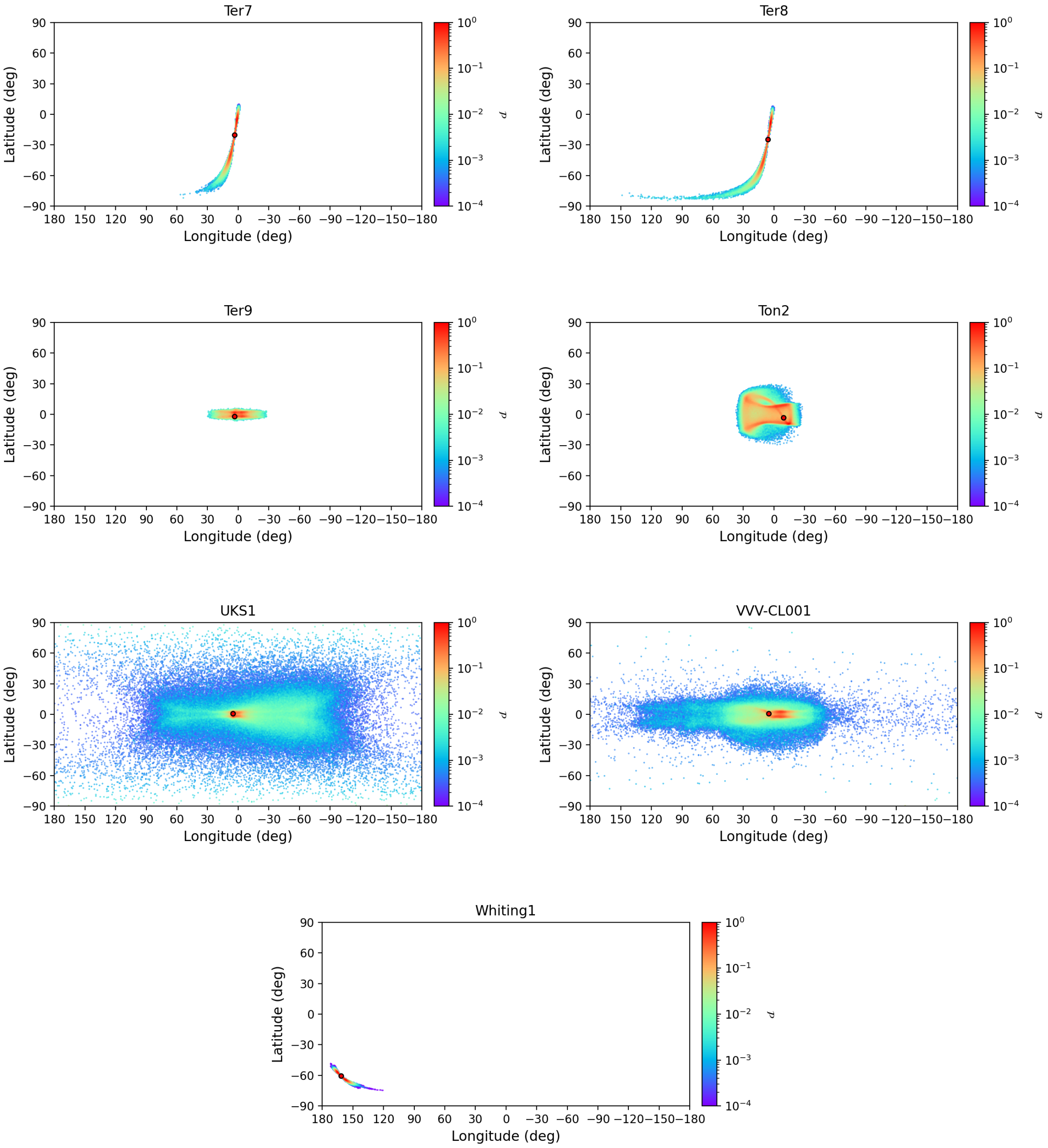

Figure 4.33 – Projected density distribution in the (ℓ, b) plane of a subset of simulated globular clusters, as indicated at the top of each panel. In each panel, the red circle indicates the current position of the cluster. The densities have been normalized to their maximum value/

5.3 Globular cluster initial conditions

Table 4.4 – Current positions in the sky, proper motions, line-of-sight velocities, distances and relative uncertainties, masses, and half-mass radii for all globular clusters analyzed in this study.

Cluster	D kpc	err D kpc	α degrees	δ degrees	μ_α mas/yr	err μ_α mas/yr	μ_δ mas/yr	err μ_δ mas/yr	$v_{\ell os}$ km/s	err $v_{\ell os}$ km/s	M_{GC} $M_\odot$	r_h pc
2MASS-GC01	3.37	0.62	272.0909	-19.8297	-1.121	0.296	-1.881	0.235	-31.28	0.50	35100	4.70
2MASS-GC02	5.50	0.44	272.4021	-20.7789	4.000	0.900	-4.700	0.800	-237.75	10.10	15800	2.85
AM1	118.91	3.40	58.7596	-49.6153	0.291	0.107	-0.177	0.086	118.00	14.14	19200	19.86
AM4	29.01	0.94	209.0891	-27.1652	-0.291	0.445	-2.512	0.344	151.19	2.85	756	15.00
Arp2	28.73	0.34	292.1838	-30.3556	-2.331	0.031	-1.475	0.029	122.64	0.29	37000	18.45
BH140	4.81	0.25	193.4729	-67.1773	-14.848	0.024	1.224	0.024	90.30	0.35	59900	9.53
BH261	6.12	0.26	273.5275	-28.6350	3.566	0.043	-3.590	0.037	-45.00	15.00	22000	4.66
Crater	147.23	4.27	174.0687	-10.8770	-0.059	0.125	-0.116	0.116	148.10	0.65	10800	25.74
Djor1	9.88	0.65	266.8696	-33.0664	-4.693	0.046	-8.468	0.041	-359.18	1.64	79700	5.57
Djor2	8.76	0.18	270.4544	-27.8258	0.662	0.042	-2.983	0.037	-149.75	1.10	125000	5.16
E3	7.88	0.25	140.2378	-77.2819	-2.727	0.027	7.083	0.027	11.71	0.34	2890	6.14
ESO280-SC06	20.95	0.65	272.2750	-46.4233	-0.688	0.039	-2.777	0.033	93.20	0.34	7800	9.65
ESO452-SC11	7.39	0.20	249.8542	-28.3992	-1.423	0.031	-6.472	0.030	16.37	0.44	8260	3.68
Eridanus	84.68	2.89	66.1856	-21.1868	0.510	0.039	-0.301	0.041	-23.15	0.73	11600	17.91
FSR1716	7.43	0.27	242.6250	-53.7489	-4.354	0.033	-8.832	0.031	-30.70	0.98	64300	5.16
FSR1735	9.08	0.53	253.0442	-47.0581	-4.439	0.054	-1.534	0.048	-69.85	4.88	72300	2.97
FSR1758	11.09	0.74	262.8000	-39.8080	-2.881	0.026	2.519	0.025	227.31	0.59	628000	17.04
HP1	7.00	0.14	262.7717	-29.9817	2.523	0.039	-10.093	0.037	39.76	1.22	124000	3.74
IC1257	26.59	1.43	261.7854	-7.0931	-1.007	0.040	-1.492	0.032	-137.97	2.04	18100	5.54
IC1276	4.55	0.25	272.6844	-7.2076	-2.553	0.026	-4.568	0.026	155.06	0.69	73900	5.21
IC4499	18.89	0.25	225.0772	-82.2138	0.466	0.025	-0.489	0.025	38.41	0.31	155000	14.96
Laevens3	61.77	1.65	316.7267	14.9805	0.172	0.101	-0.666	0.080	-70.30	0.82	2120	9.46
Liller1	8.06	0.34	263.3523	-33.3896	-5.403	0.109	-7.431	0.077	60.36	2.44	915000	2.01
Lynga7	7.90	0.16	242.7652	-55.3178	-3.851	0.027	-7.050	0.027	17.86	0.83	79600	5.16
NGC104	4.52	0.03	6.0238	-72.0813	5.252	0.021	-2.551	0.021	-17.45	0.16	895000	6.30
NGC1261	16.40	0.19	48.0675	-55.2162	1.596	0.025	-2.064	0.025	71.34	0.21	182000	5.23
NGC1851	11.95	0.13	78.5282	-40.0466	2.145	0.024	-0.650	0.024	321.40	1.55	318000	2.90
NGC1904	13.08	0.18	81.0458	-24.5244	2.469	0.025	-1.594	0.025	205.76	0.20	139000	3.21
NGC2298	9.83	0.17	102.2475	-36.0053	3.320	0.025	-2.175	0.026	147.15	0.57	55800	3.31
NGC2419	88.47	2.40	114.5353	38.8819	0.007	0.028	-0.523	0.026	-21.10	0.31	971000	26.50
NGC2808	10.06	0.11	138.0129	-64.8635	0.994	0.024	0.273	0.024	103.57	0.27	864000	3.89
NGC288	8.99	0.09	13.1885	-26.5826	4.164	0.024	-5.705	0.024	-44.45	0.13	93400	8.37
NGC3201	4.74	0.04	154.4034	-46.4125	8.348	0.022	-1.958	0.022	493.65	0.21	160000	6.78
NGC362	8.83	0.10	15.8094	-70.8488	6.694	0.025	-2.535	0.024	223.12	0.28	284000	3.79
NGC4147	18.54	0.21	182.5263	18.5426	-1.707	0.027	-2.090	0.027	179.35	0.31	39000	4.03
NGC4372	5.71	0.21	186.4391	-72.6591	-6.409	0.024	3.297	0.024	75.59	0.30	198000	8.53
NGC4590	10.40	0.10	189.8666	-26.7441	-2.739	0.024	1.779	0.024	-93.11	0.18	122000	7.58
NGC4833	6.48	0.08	194.8913	-70.8765	-8.377	0.025	-0.963	0.025	201.99	0.40	206000	4.76
NGC5024	18.50	0.18	198.2302	18.1682	-0.133	0.024	-1.331	0.024	-63.37	0.25	455000	10.18
NGC5053	17.54	0.23	199.1129	17.7003	-0.329	0.025	-1.213	0.025	42.82	0.25	74200	17.31
NGC5139	5.43	0.05	201.6970	-47.4795	-3.250	0.022	-6.746	0.022	232.78	0.21	3640000	10.36
NGC5272	10.18	0.08	205.5484	28.3773	-0.152	0.023	-2.670	0.022	-147.20	0.27	406000	6.34
NGC5286	11.10	0.14	206.6117	-51.3742	0.198	0.025	-0.153	0.025	62.38	0.40	353000	3.79
NGC5466	16.12	0.16	211.3637	28.5344	-5.342	0.025	-0.822	0.024	106.82	0.20	59800	14.03
NGC5634	25.96	0.62	217.4053	-5.9764	-1.692	0.027	-1.478	0.026	-16.07	0.60	228000	7.39
NGC5694	34.84	0.74	219.9012	-26.5388	-0.464	0.029	-1.105	0.029	-139.55	0.49	317000	4.86
NGC5824	31.71	0.60	225.9942	-33.0681	-1.189	0.026	-2.234	0.026	-25.24	0.52	762000	6.51
NGC5897	12.55	0.24	229.3517	-21.0101	-5.422	0.025	-3.393	0.025	101.31	0.22	157000	10.99
NGC5904	7.48	0.06	229.6384	2.0810	4.086	0.023	-9.870	0.023	53.50	0.25	394000	5.68
NGC5927	8.27	0.11	232.0029	-50.6730	-5.056	0.025	-3.217	0.025	-104.09	0.28	275000	5.28
NGC5946	9.64	0.51	233.8691	-50.6597	-5.331	0.028	-1.657	0.027	137.60	0.94	93100	2.59
NGC5986	10.54	0.13	236.5125	-37.7864	-4.192	0.026	-4.568	0.026	101.18	0.43	334000	4.25
NGC6093	10.34	0.12	244.2600	-22.9761	-2.934	0.027	-5.578	0.026	10.93	0.39	338000	2.62
NGC6101	14.45	0.19	246.4505	-72.2022	1.756	0.024	-0.258	0.025	366.33	0.32	178000	14.06
NGC6121	1.85	0.02	245.8967	-26.5257	-12.514	0.023	-19.022	0.023	71.21	0.15	87100	3.69
NGC6139	10.04	0.45	246.9185	-38.8488	-6.081	0.027	-2.711	0.026	24.41	0.95	323000	2.47
NGC6144	8.15	0.13	246.8078	-26.0235	-1.744	0.026	-2.607	0.026	194.79	0.58	79200	4.91
NGC6171	5.63	0.08	248.1328	-13.0538	-1.939	0.025	-5.979	0.025	-34.71	0.18	74900	3.94
NGC6205	7.42	0.08	250.4218	36.4599	-3.149	0.023	-2.574	0.023	-244.90	0.30	545000	5.26
NGC6218	5.11	0.05	251.8091	-1.9485	-0.191	0.024	-6.802	0.024	-41.67	0.14	107000	4.05
NGC6229	30.11	0.47	251.7452	47.5278	-1.171	0.026	-0.467	0.027	-137.89	0.71	286000	4.41
NGC6235	11.94	0.38	253.3557	-22.1774	-3.931	0.027	-7.587	0.027	126.68	0.33	107000	4.78
NGC6254	5.07	0.06	254.2877	-4.1003	-4.758	0.024	-6.597	0.024	74.21	0.23	205000	4.81
NGC6256	7.24	0.29	254.8861	-37.1210	-3.715	0.031	-1.637	0.030	-99.75	0.66	125000	4.82
NGC6266	6.41	0.10	255.3042	-30.1134	-4.978	0.026	-2.947	0.026	-73.98	0.67	610000	2.43
NGC6273	8.34	0.16	255.6575	-26.2680	-3.249	0.026	1.660	0.025	145.54	0.59	697000	4.21
NGC6284	14.21	0.42	256.1201	-24.7648	-3.200	0.029	-2.002	0.028	28.62	0.73	129000	3.78
NGC6287	7.93	0.37	256.2889	-22.7080	-5.010	0.029	-1.883	0.028	-294.74	1.65	145000	3.65

Table 4.4 – continued.

Cluster	D kpc	err D kpc	α degrees	δ degrees	μ_α mas/yr	err μ_α mas/yr	μ_δ mas/yr	err μ_δ mas/yr	$v_{\ell os}$ km/s	err $v_{\ell os}$ km/s	M $M_\odot$	r_h pc
NGC6293	9.19	0.28	257.5425	-26.5821	0.870	0.028	-4.326	0.028	-143.66	0.39	205000	4.05
NGC6304	6.15	0.15	258.6344	-29.4620	-4.070	0.029	-1.088	0.028	-108.62	0.39	126000	4.26
NGC6316	11.15	0.39	259.1554	-28.1401	-4.969	0.031	-4.592	0.030	99.65	0.84	318000	4.77
NGC6325	7.53	0.32	259.4963	-23.7677	-8.289	0.030	-9.000	0.029	29.54	0.58	58900	2.05
NGC6333	8.30	0.14	259.7991	-18.5163	-2.180	0.026	-3.222	0.026	310.75	2.12	323000	4.17
NGC6341	8.50	0.07	259.2808	43.1359	-4.935	0.024	-0.625	0.024	-120.55	0.27	352000	4.49
NGC6342	8.01	0.23	260.2916	-19.5877	-2.903	0.027	-7.116	0.026	115.75	0.90	42200	2.06
NGC6352	5.54	0.07	261.3713	-48.4222	-2.158	0.025	-4.447	0.025	-125.63	1.01	64700	4.56
NGC6355	8.65	0.22	260.9935	-26.3528	-4.738	0.031	-0.572	0.030	-195.85	0.55	101000	3.55
NGC6356	15.66	0.92	260.8958	-17.8130	-3.750	0.026	-3.392	0.026	48.18	1.82	600000	6.86
NGC6362	7.65	0.07	262.9791	-67.0483	-5.506	0.024	-4.763	0.024	-14.58	0.18	127000	7.23
NGC6366	3.44	0.05	261.9344	-5.0799	-0.332	0.025	-5.160	0.024	-120.65	0.19	37600	5.56
NGC6380	9.61	0.30	263.6186	-39.0695	-2.183	0.031	-3.233	0.030	-1.48	0.73	334000	4.40
NGC6388	11.17	0.16	264.0718	-44.7355	-1.316	0.026	-2.709	0.026	83.11	0.45	1250000	4.34
NGC6397	2.48	0.02	265.1754	-53.6743	3.260	0.023	-17.664	0.022	18.51	0.08	96600	3.90
NGC6401	8.06	0.24	264.6522	-23.9096	-2.748	0.035	1.444	0.034	-105.44	2.50	145000	3.28
NGC6402	9.14	0.25	264.4007	-3.2459	-3.590	0.025	-5.059	0.025	-60.71	0.45	592000	5.14
NGC6426	20.71	0.35	266.2280	3.1701	-1.828	0.026	-2.999	0.026	-210.51	0.51	71700	8.00
NGC6440	8.25	0.24	267.2202	-20.3604	-1.187	0.036	-4.020	0.035	-69.39	0.93	489000	2.14
NGC6441	12.73	0.16	267.5544	-37.0514	-2.551	0.028	-5.348	0.028	18.47	0.56	1320000	3.47
NGC6453	10.07	0.22	267.7155	-34.5985	0.203	0.036	-5.934	0.037	-99.23	1.24	165000	3.85
NGC6496	9.64	0.15	269.7654	-44.2659	-3.060	0.027	-9.271	0.026	-134.72	0.26	68900	6.42
NGC6517	9.23	0.56	270.4608	-8.9588	-1.551	0.029	-4.470	0.028	-35.06	1.65	195000	2.29
NGC6522	7.29	0.21	270.8920	-30.0340	2.566	0.039	-6.438	0.036	-15.23	0.49	211000	3.08
NGC6528	7.83	0.24	271.2067	-30.0558	-2.157	0.043	-5.649	0.039	211.86	0.43	56700	2.73
NGC6535	6.36	0.12	270.9604	-0.2976	-4.214	0.027	-2.939	0.026	-214.85	0.46	21900	3.65
NGC6539	8.16	0.39	271.2073	-7.5859	-6.896	0.026	-3.537	0.026	35.19	0.50	209000	5.18
NGC6540	5.91	0.27	271.5357	-27.7653	-3.702	0.032	-2.791	0.032	-16.50	0.78	34500	5.32
NGC6541	7.61	0.10	272.0098	-43.7149	0.287	0.025	-8.847	0.025	-163.97	0.46	293000	4.34
NGC6544	2.58	0.06	271.8338	-24.9982	-2.304	0.031	-18.604	0.030	-38.46	0.67	91400	2.07
NGC6553	5.33	0.13	272.3153	-25.9078	0.344	0.030	-0.454	0.029	-0.27	0.34	285000	4.56
NGC6558	7.47	0.29	272.5740	-31.7645	-1.720	0.036	-4.144	0.034	-195.12	0.73	26500	1.70
NGC6569	10.53	0.26	273.4117	-31.8269	-4.125	0.028	-7.354	0.028	-49.83	0.50	236000	3.85
NGC6584	13.61	0.17	274.6566	-52.2158	-0.090	0.026	-7.202	0.025	260.64	1.58	102000	5.37
NGC6624	8.02	0.11	275.9188	-30.3610	0.124	0.029	-6.936	0.029	54.79	0.40	156000	3.69
NGC6626	5.37	0.10	276.1370	-24.8698	-0.278	0.028	-8.922	0.028	11.11	0.60	299000	2.26
NGC6637	8.90	0.10	277.8463	-32.3481	-5.034	0.028	-5.832	0.028	47.48	1.00	155000	3.69
NGC6638	9.78	0.34	277.7337	-25.4975	-2.518	0.029	-4.076	0.029	8.63	2.00	118000	2.20
NGC6642	8.05	0.20	277.9760	-23.4756	-0.173	0.030	-3.892	0.030	-60.61	1.35	34400	1.51
NGC6652	9.46	0.14	278.9401	-32.9907	-5.484	0.027	-4.274	0.027	-95.37	0.86	48100	1.96
NGC6656	3.30	0.04	279.0998	-23.9047	9.851	0.023	-5.617	0.023	-148.72	0.78	476000	5.29
NGC6681	9.36	0.11	280.8032	-32.2921	1.431	0.027	-4.744	0.026	216.62	0.84	116000	2.89
NGC6712	7.38	0.24	283.2680	-8.7060	3.363	0.027	-4.436	0.027	-107.45	0.29	96300	3.21
NGC6715	26.28	0.33	283.7639	-30.4799	-2.679	0.025	-1.387	0.025	143.13	0.43	1780000	5.20
NGC6717	7.52	0.13	283.7752	-22.7015	-3.125	0.027	-5.008	0.027	30.25	0.90	35800	4.23
NGC6723	8.27	0.10	284.8881	-36.6322	1.028	0.025	-2.418	0.025	-94.39	0.26	177000	5.06
NGC6749	7.59	0.21	286.3141	1.8998	-2.829	0.028	-6.006	0.027	-58.44	0.96	211000	7.09
NGC6752	4.12	0.04	287.7171	-59.9846	-3.161	0.022	-4.027	0.022	-26.01	0.12	276000	5.27
NGC6760	8.41	0.43	287.8003	1.0305	-1.107	0.026	-3.615	0.026	-2.37	1.27	269000	5.22
NGC6779	10.43	0.14	289.1482	30.1835	-2.018	0.025	1.618	0.025	-136.97	0.45	186000	4.51
NGC6809	5.35	0.05	294.9988	-30.9647	-3.432	0.024	-9.311	0.024	174.70	0.17	193000	6.95
NGC6838	4.00	0.05	298.4437	18.7792	-3.416	0.025	-2.656	0.024	-22.72	0.20	65600	6.57
NGC6864	20.52	0.45	301.5198	-21.9212	-0.598	0.026	-2.810	0.026	-189.08	1.12	370000	2.96
NGC6934	15.72	0.17	308.5474	7.4045	-2.655	0.026	-4.689	0.026	-406.22	0.73	136000	5.16
NGC6981	16.66	0.18	313.3654	-12.5373	-1.274	0.026	-3.361	0.026	-331.39	1.47	68900	5.96
NGC7006	39.32	0.56	315.3726	16.1873	-0.128	0.027	-0.633	0.027	-383.47	0.73	136000	6.99
NGC7078	10.71	0.10	322.4930	12.1670	-0.659	0.024	-3.803	0.024	-106.84	0.30	633000	4.30
NGC7089	11.69	0.11	323.3626	-0.8233	3.435	0.025	-2.159	0.024	-3.78	0.30	620000	4.77
NGC7099	8.46	0.09	325.0921	-23.1799	-0.737	0.025	-7.299	0.024	-185.19	0.17	143000	4.99
NGC7492	24.39	0.57	347.1112	-15.6115	0.756	0.028	-2.320	0.028	-176.70	0.27	26600	9.89
Pal1	11.18	0.32	53.3335	79.5811	-0.252	0.034	0.007	0.037	-75.72	0.29	1030	3.56
Pal10	8.94	1.18	289.5069	18.5790	-4.322	0.029	-7.173	0.029	-31.70	0.23	162000	6.33
Pal11	14.02	0.51	296.3100	-8.0072	-1.766	0.030	-4.971	0.028	-67.64	0.76	11900	7.72
Pal12	18.49	0.30	326.6618	-21.2526	-3.220	0.029	-3.333	0.028	27.91	0.28	6270	10.52
Pal13	23.48	0.40	346.6852	12.7715	1.748	0.049	0.104	0.047	25.30	0.22	3020	16.95
Pal14	73.58	1.63	242.7525	14.9578	-0.463	0.038	-0.413	0.038	72.30	0.14	18900	36.70
Pal15	44.10	1.14	254.9626	-0.5390	-0.592	0.037	-0.901	0.034	72.27	1.74	50900	26.86
Pal2	26.17	1.28	71.5246	31.3815	1.045	0.034	-1.522	0.031	-135.97	1.55	231000	8.06
Pal3	94.84	3.23	151.3816	0.0717	0.086	0.060	-0.148	0.071	94.04	0.80	18900	27.44
Pal4	101.39	2.57	172.3183	28.9734	-0.188	0.042	-0.476	0.041	72.40	0.24	12900	21.30
Pal5	21.94	0.51	229.0192	-0.1210	-2.730	0.028	-2.654	0.027	-58.61	0.15	9980	27.64
Pal6	7.05	0.45	265.9258	-26.2250	-9.222	0.038	-5.347	0.036	177.00	1.35	94500	2.89
Pal8	11.32	0.63	280.3773	-19.8289	-1.987	0.027	-5.694	0.027	-31.54	0.21	67400	5.86
Pyxis	36.53	0.66	136.9869	-37.2266	1.030	0.032	0.138	0.035	40.46	0.21	24600	22.83
Rup106	20.71	0.36	189.6675	-51.1503	-1.254	0.026	0.401	0.026	-38.36	0.26	34200	11.57

Table 4.4 – continued.

Cluster	D kpc	err D kpc	α degrees	δ degrees	μ_α mas/yr	err μ_α mas/yr	μ_δ mas/yr	err μ_δ mas/yr	$v_{\ell os}$ km/s	err $v_{\ell os}$ km/s	M $M_\odot$	r_h pc
SagittariusII	66.53	1.56	298.1647	-22.0653	-0.804	0.044	-0.882	0.028	-175.73	0.37	18500	39.31
Ter1	5.67	0.17	263.9467	-30.4818	-2.806	0.055	-4.861	0.055	56.75	1.61	150000	2.15
Ter10	10.21	0.40	270.7408	-26.0669	-6.827	0.059	-2.588	0.050	211.37	2.27	302000	4.60
Ter12	5.17	0.38	273.0658	-22.7419	-6.222	0.037	-3.052	0.034	95.61	1.21	87200	3.28
Ter2	7.75	0.33	261.8879	-30.8023	-2.170	0.041	-6.263	0.038	134.56	0.96	136000	4.16
Ter3	7.64	0.31	247.1625	-35.3398	-5.577	0.027	-1.760	0.026	-135.76	0.57	40400	7.19
Ter4	7.59	0.31	262.6625	-31.5955	-5.462	0.060	-3.711	0.048	-48.96	1.57	200000	6.06
Ter5	6.62	0.15	267.0202	-24.7791	-1.989	0.068	-5.243	0.066	-82.57	0.73	935000	3.77
Ter6	7.27	0.35	267.6932	-31.2754	-4.979	0.048	-7.431	0.039	136.45	1.50	104000	1.33
Ter7	24.28	0.49	289.4330	-34.6577	-3.002	0.029	-1.651	0.029	159.85	0.14	24000	13.21
Ter8	27.54	0.42	295.4350	-33.9995	-2.496	0.027	-1.581	0.026	148.43	0.17	62100	21.53
Ter9	5.77	0.34	270.4117	-26.8397	-2.121	0.052	-7.763	0.049	68.49	0.56	120000	1.90
Ton2	6.99	0.34	264.0393	-38.5409	-5.904	0.031	-0.755	0.029	-184.72	1.12	69100	4.60
UKS1	15.58	0.56	268.6133	-24.1453	-2.040	0.095	-2.754	0.063	59.38	2.63	77000	3.84
VVV-CL001	8.08	1.48	268.6771	-24.0147	-3.487	0.144	-1.652	0.107	-327.28	0.90	135000	2.94
Whiting1	30.59	1.17	30.7375	-3.2528	-0.228	0.065	-2.046	0.056	-130.41	1.79	1970	15.49

5.4 Globular cluster classification

In Fig. 4.34 (top panel), we show the distribution of the arctangent of the z_{max}/R_{max} ratio, with z_{max} and R_{max} being (respectively) the maximum height above or below the Galactic plane and their maximum in-plane distance from the Galactic center that was reached in the past 5 Gyr of orbital evolution in the Galactic potential adopted in this paper (see Sect. 2.3). As was already noticed for field stars (see Haywood, Di Matteo, Lehnert, Snaith, et al., 2018), the GC distribution also shows a dip at about 10°, which separates clusters with flattened orbits ($\arctan(z_{max}/R_{max}) \leq 10°$) from thicker ones. We thus define a first set of clusters (the *disk GCs*) as that containing all globular clusters with $\arctan(z_{max}/R_{max}) \leq 10°$. This first set contains 21 clusters. Of the remaining 138, we distinguish between an “inner” *GCs* sample and an “outer” *GCs* sample, on the basis of the maximum 3D distance (r_{max}) that the cluster reaches from the Galactic center. Inner GCs are those with $r_{max} \leq 10$ kpc and outer GCs are those with $r_{max} > 8.34$ kpc, which is the value of the distance of the Sun to the Galactic Center used in this experiment. Such a value allows us to discriminate between two classes of tidal debris, for inner clusters are necessarily restricted in latitude and longitude, whereas outer cluster can fill the sky.

Finally, the third and bottom panels of Fig. 4.34 show the distribution of these three defined groups in the $R_{max} - z_{max}$ and $E - L_z$ planes. We note that since disk clusters are uniquely defined on the basis of the ratio between the maximum vertical and in-plane orbital excursion – and not on the circularity of their orbits (as seen, e.g., in Massari et al., 2019), some of our disk GCs have elongated (i.e., radial) orbits ($L_z \sim 0$) or even retrograde ones ($L_z > 0$). Our definition of disk clusters is purely related to a morphological criterium: disk GCs are those whose orbits are confined close to the Galactic plane, independently of their eccentricity.

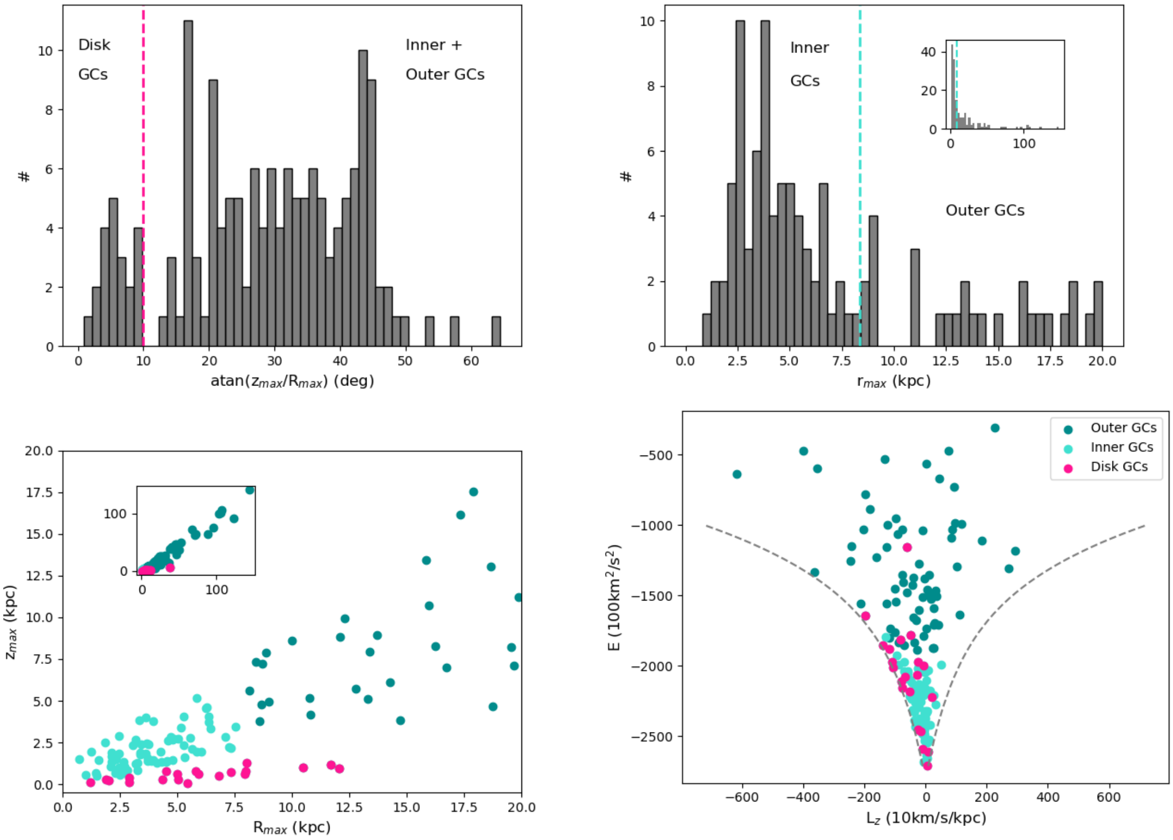

Figure 4.34 – A series of plots describing the categorization of disk, inner, and outer globular clusters. *From the top left to the bottom right: First panel*: Distribution of the arctangent of the z_{max}/R_{max} ratio for all simulated GCs. The values are expressed in degrees. The vertical dashed line at 10° separates disk clusters ($\arctan(z_{max}/R_{max}) \leq 10°$) from the rest of the population of GCs. *Second panel* Distribution of the maximum 3D distance, r_{max}, from the Galactic center, reached by the GCs orbits in the last 5 Gyr. The main plot shows this distribution for $r_{max} \leq 20$ kpc, where (as the inset shows) the whole distribution is extended at $r_{max} > 100$ kpc. In both panels, the vertical dashed line, at the solar radius $r_\odot$, separates the group of inner GCs from the group of outer GCs. We note that the clusters in one of these two groups which also satisfy the criterion to be disk clusters are classified as disk GCs and are not in the inner or outer GC groups. *Third panel*: Distribution of disk GCs (magenta points), inner GCs (turquoise points), and outer GCs (dark turquoise points) in the $R_{max} - z_{max}$ plane. The main panel shows the distribution of the GCs having $R_{max} \leq 20$ kpc, the inset the distribution of the whole GC sample. *Fourth panel*: Distribution of the disk GCs (magenta points), inner GCs (turquoise points), and outer GCs (dark turquoise points) in the $E - L_z$ plane. The dashed grey lines correspond, for any given energy E, to the angular momentum of the corresponding circular orbit. Prograde orbits correspond to negative L_z values, retrograde orbits to positive L_z.

Table 4.5 – Classification of the 159 globular clusters studied in this paper in disk clusters (“D”), inner clusters (“I”) and outer clusters (“O”). The values of r_{max} and the angle in degrees of the $arctan(z_{max}/R_{max})$ are also given.

Cluster	r_{max}	angle	class	Cluster	r_{max}	angle	class	Cluster	r_{max}	angle	class
2MASS-GC01	5.45	0.85	D	2MASS-GC02	7.38	17.15	I	AM1	123.19	36.56	O
AM4	26.97	43.53	O	Arp2	42.44	44.54	O	BH140	10.52	5.54	D
BH261	3.83	21.02	I	Crater	147.37	44.46	O	Djor1	11.74	5.77	D
Djor2	2.39	16.74	I	E3	12.91	24.07	O	ESO280-SC06	13.82	33.04	O
ESO452-SC11	2.53	41.47	I	Eridanus	109.07	44.83	O	FSR1716	5.46	17.07	I
FSR1735	4.43	17.10	I	FSR1758	14.35	23.13	O	HP1	2.70	53.56	I
IC1257	19.69	19.93	O	IC1276	7.98	5.71	D	IC4499	27.17	42.77	O
Laevens3	70.74	41.35	O	Liller1	1.20	5.84	D	Lynga7	4.69	17.18	I
NGC104	7.71	24.70	I	NGC1261	20.99	36.68	O	NGC1851	19.94	29.46	O
NGC1904	19.57	22.81	O	NGC2298	16.69	26.93	O	NGC2419	96.76	38.13	O
NGC2808	14.92	14.57	O	NGC288	12.50	39.00	O	NGC3201	25.53	22.62	O
NGC362	12.27	36.03	O	NGC4147	24.90	45.18	O	NGC4372	7.36	16.30	I
NGC4590	27.99	32.55	O	NGC4833	8.13	9.07	D	NGC5024	22.32	44.24	O
NGC5053	18.08	44.39	O	NGC5139	7.14	21.89	I	NGC5272	16.02	40.27	O
NGC5286	13.32	21.11	O	NGC5466	41.16	43.51	O	NGC5634	22.18	43.13	O
NGC5694	51.29	35.50	O	NGC5824	32.44	40.00	O	NGC5897	9.18	41.61	O
NGC5904	24.76	42.83	O	NGC5927	5.83	7.91	D	NGC5946	5.31	23.80	I
NGC5986	5.00	29.36	I	NGC6093	4.04	49.12	I	NGC6101	32.24	30.56	O
NGC6121	6.84	4.48	D	NGC6139	3.72	34.95	I	NGC6144	4.41	43.66	I
NGC6171	3.95	33.40	I	NGC6205	8.96	39.68	O	NGC6218	4.95	31.01	I
NGC6229	30.26	37.44	O	NGC6235	8.37	34.55	O	NGC6254	4.98	29.32	I
NGC6256	2.68	14.83	I	NGC6266	2.57	21.99	I	NGC6273	5.56	37.78	I
NGC6284	6.51	36.21	I	NGC6287	6.50	30.33	I	NGC6293	3.40	37.21	I
NGC6304	3.38	14.75	I	NGC6316	3.80	22.98	I	NGC6325	2.57	32.34	I
NGC6333	9.07	28.89	O	NGC6341	10.90	40.72	O	NGC6342	2.48	38.09	I
NGC6352	4.53	9.72	D	NGC6355	3.55	29.38	I	NGC6356	8.83	28.77	O
NGC6362	5.41	33.16	I	NGC6366	6.04	17.80	I	NGC6380	2.35	16.74	I
NGC6388	3.91	19.73	I	NGC6397	6.61	27.48	I	NGC6401	3.70	21.02	I
NGC6402	3.99	32.64	I	NGC6426	16.84	22.68	O	NGC6440	1.53	25.31	I
NGC6441	4.67	16.48	I	NGC6453	2.71	36.68	I	NGC6496	5.71	26.65	I
NGC6517	3.31	21.34	I	NGC6522	1.97	42.54	I	NGC6528	2.89	16.38	I
NGC6535	4.92	16.72	I	NGC6539	3.64	39.67	I	NGC6540	2.54	12.61	I
NGC6541	4.78	29.39	I	NGC6544	5.93	18.30	I	NGC6553	4.36	4.14	D
NGC6558	2.75	21.35	I	NGC6569	2.85	26.50	I	NGC6584	20.31	35.07	O
NGC6624	1.61	64.40	I	NGC6626	3.22	20.88	I	NGC6637	2.11	56.81	I
NGC6638	2.34	31.98	I	NGC6642	2.20	26.61	I	NGC6652	3.15	49.58	I
NGC6656	10.87	21.01	O	NGC6681	6.33	41.70	I	NGC6712	5.15	28.49	I
NGC6715	38.71	45.11	O	NGC6717	2.48	33.11	I	NGC6723	4.26	47.80	I
NGC6749	5.05	3.24	D	NGC6752	5.72	20.72	I	NGC6760	5.95	6.19	D
NGC6779	13.46	30.72	O	NGC6809	6.50	36.15	I	NGC6838	7.34	5.82	D
NGC6864	16.06	33.89	O	NGC6934	37.41	20.95	O	NGC6981	21.54	35.97	O
NGC7006	47.26	32.50	O	NGC7078	10.86	25.72	O	NGC7089	18.77	34.91	O
NGC7099	8.76	40.99	O	NGC7492	25.78	45.99	O	Pal1	18.77	13.96	O
Pal10	12.06	4.56	D	Pal11	8.69	23.83	O	Pal12	41.33	42.80	O
Pal13	49.09	42.54	O	Pal14	88.95	35.97	O	Pal15	46.62	44.52	O
Pal2	38.20	8.94	D	Pal3	104.49	43.88	O	Pal4	105.89	43.58	O
Pal5	17.54	42.94	O	Pal6	3.53	27.77	I	Pal8	3.99	20.14	I
Pyxis	73.65	47.40	O	Rup106	32.08	31.98	O	SagittariusII	75.32	41.80	O
Ter1	2.92	2.13	D	Ter10	6.55	32.40	I	Ter12	4.23	17.31	I
Ter2	1.49	18.30	I	Ter3	3.81	26.97	I	Ter4	1.11	28.72	I
Ter5	2.04	7.10	D	Ter6	1.93	8.77	D	Ter7	41.39	45.10	O
Ter8	47.16	45.55	O	Ter9	2.92	7.94	D	Ton2	4.39	24.81	I
UKS1	7.95	4.51	D	VVV-CL001	5.04	7.09	D	Whiting1	52.30	43.09	O

Chapter 5

Gaps in stellar streams

reference

Ferrone, Salvatore, Marco Montuori, Paola Di Matteo, Alessandra Mastrobuono-Battisti, Rodrigo Ibata, Paolo Bianchini, Sergey Khoperskov, et al. 2025. “Gaps in stellar streams as a result of globular cluster flybys: The case of Palomar 5” 699 (July):A289. https://doi.org/10.1051/0004-6361/202553923.

In this work, we investigated the possibility that globular clusters can create gaps in the Palomar 5 stellar stream. This project began during the development phase of our code, when we first introduced perturbers. Initially, we intended these perturbers to represent dark matter subhalos or giant molecular clouds. However, before generating a new dataset, we tested the code using the catalog of globular clusters. To our surprise, we found that several clusters produced clear gaps in the Palomar 5 stream, which motivated us to carry out a detailed analysis. Here, we report the frequency of interactions that generate significant gaps, and identify the clusters responsible for these perturbations. Finally, in the supplementary material, we discuss the persistence of these gaps in light of the velocity distribution within the stream.

1 Introduction

Stellar streams are several-kiloparsecs-long structures formed by the tidal disruption of globular clusters or dwarf galaxies orbiting a host galaxy. These tidal forces arise due to differential gravitational pulls across extended objects, causing stars farther from the galactic center to lag behind, while those closer to the center speed up. This stretching creates two tidal tails that trace the cluster's orbit unless in the closest vicinity to the object (Montuori et al., 2007).

Numerical predictions of this phenomenon have existed since the 1970s (see, e.g., Keenan & Innanen, 1975). These predictions occurred well before the first detections of Galactic globular cluster tidal tails (Grillmair, Freeman, et al., 1995). Interestingly, Grillmair, Freeman, et al. (1995)'s detections were made nearly contemporaneously with the discovery of the Sagittarius stellar stream by R. A. Ibata, Gilmore, et al. (1994), which is the closest example of a stream emerging from a dwarf satellite currently interacting with the Milky Way.

Subsequent studies[1] extended Grillmair's findings to other globular cluster streams but were often limited to the detections of stars still close to the cluster tidal radius, until the discovery made by Odenkirchen, Grebel, Rockosi, et al. (2001), Odenkirchen, Grebel, Dehnen, H. W. Rix, et al. (2002), and Odenkirchen, Grebel, Dehnen, H.-W. Rix, et al. (2003) of long and thin tails outside the Palomar 5 globular cluster. With a mass of $1.34 \pm 0.24 \times 10^4 M_\odot$ (Baumgardt, Hilker, et al., 2019), Palomar 5 is one of the least massive globular clusters in the Galaxy. Odenkirchen, Grebel, Dehnen, H.-W. Rix, et al. (2003) showed that its tails contain more mass than the cluster. The works of Grillmair & Dionatos (2006a) and Kuzma, Da Costa, et al. (2015) showed that the tails have an extent

---

[1] For more subsequent observation detections of tidal debris, i.e., globular cluster stars beyond the tidal radius see the works of: Lehmann & Scholz (1997), Testa et al. (2000), Leon et al. (2000), Siegel (2001), K. H. Lee et al. (2003), Sollima, Martínez-Delgado, et al. (2011), Sollima, Martínez Delgado, et al. (2018), and Sollima (2020).

of more than 20° degrees in the sky. The discovery of its prominent tails stimulated a vigorous and successful search in the following years. New streams were discovered, mostly taking advantage of Sloan Digital Sky Survey data, but Pan-STARRS and ATLAS were also used (Grillmair & Dionatos, 2006b; Belokurov, Evans, et al., 2006; Grillmair, 2009; Bonaca, Geha, et al., 2012; Grillmair, Cutri, et al., 2013; Grillmair, 2014; Grillmair, L. Hetherington, et al., 2015; Bernard, Ferguson, Schlafly, Abbas, et al., 2014; Bernard, Ferguson, Schlafly, N. F. Martin, et al., 2016; Grillmair, 2017; Koposov, M. Irwin, et al., 2014).

Bonaca & Price-Whelan (2025) provides a review of stellar stream astronomy, which has entered a new era since the publication of the data from the Gaia astrometric mission (Gaia Collaboration, Prusti, et al., 2016). Gaia's characterization of billions of stars in the Milky Way enables the search for these structures by coupling photometry, astrometry, and spectroscopy for the brightest stars. The possibility given by Gaia to track stars with coherent movements over the entirety of the sky has led to the discovery of dozens of new streams. In addition, Malhan & R. A. Ibata (2018) developed the `streamfinder` algorithm and applied it across a series of works (Malhan, R. A. Ibata & N. F. Martin, 2018; R. A. Ibata, Malhan, N. F. Martin & Starkenburg, 2018; R. A. Ibata, Malhan & N. F. Martin, 2019) to discover a multitude of streams.

The possibility of combining Gaia data with spectroscopic surveys has extended the study of stellar streams beyond the quantification of their orbital properties to a full chemical characterization (T. S. Li, Koposov, Zucker, et al., 2019; Ji et al., 2020; T. S. Li, Koposov, Erkal, et al., 2021; T. S. Li, Ji, et al., 2022; Usman et al., 2024). Currently, about a hundred stellar streams are known in our Galaxy. Mateu (2023) compiled their tracks on the sky into a catalog. Interestingly, only about 20 streams are associated with known Galactic globular clusters.

One of the interests in studying stellar streams is that they can constrain the gravitational field of their host galaxies, particularly the Milky Way. Compared to the measurement of the HI rotation curve, stellar streams offer the opportunity to investigate the potential of the host galaxy over a wide range of distances, reaching the outermost regions of the halo. For example, Varghese et al. (2011) demonstrated how stellar streams can be used to infer the mass and scale parameters of dark matter halos, utilizing various amounts of observational data, ranging from basic right ascension and declination to full six-dimensional phase space information. Bonaca & Hogg (2018) reviewed this concept from an information-theoretic point of view, identifying which orbits and configurations of stellar streams yield the most information about the Galactic potential. However, using single streams to constrain the potential led to ambiguous and non-converging results. For example, Law & Majewski (2010) made use of the Sagittarius stream to infer that the dark matter halo of our Galaxy has a triaxial shape (see also Helmi, 2004; Johnston, Law, et al., 2005; Law, Johnston, et al., 2005), but Bovy et al. (2016) concluded that the dark matter halo of our Galaxy is nearly spherical at the distances of the Palomar 5 and GD-1 streams. The two contrasting results could indicate that the halo is triaxial at one distance but spherical at another, highlighting the need for streams at different distances to map the halo shape. Recently, R. Ibata, Malhan, Tenachi, et al. (2024) constructed a Milky Way model by applying a Markov chain Monte-Carlo (MCMC) fitting procedure. This method identified the set of potential parameters in an axisymmetric model of the Milky Way that best reproduces all observed stellar streams.

Beyond the global visible and dark mass distribution streams, streams can also be used to infer the granularity of the dark matter, that is, the mass and density of the subhalos populating our Galaxy. According to simulations by Springel et al. (2008), the Λ cold dark matter (ΛCDM) model predicts that galaxies grow hierarchically, with dark matter clumps forming at a wide range of masses and sizes. These clumps, or subhalos, are predicted to follow a mass distribution with a power-law slope slightly shallower than -2.0. Vegetti et al. (2012) detected the smallest observed dark matter halo through gravitational lensing in an Einstein ring with a mass of 10^8 solar masses. However, some models predict that dark matter clumps could exist down to at least the mass of Earth-like planets (Green et al., 2005; Amorisco, 2021, see).

R. A. Ibata, Lewis, M. J. Irwin, et al. (2002) first suggested that dark matter subhalos could influence stellar streams by diffusing their orbital elements. Later, Carlberg (2012) expanded this idea, proposing that subhalos could create gaps in stellar streams during flyby encounters, where a subhalo approaches closely enough to a segment of a stream and significantly changes the orbits of the closest stars. Carlberg & Grillmair (2013) applied this idea and looked for the presence of gaps in the well-known Palomar 5 and GD-1 streams, concluding that the density variations found in their streams were consistent with expectations from ΛCDM models. Bonaca, Hogg, et al. (2019) provided further observational evidence for this idea, identifying a gap and a spur in the GD-1 stream that they could not explain by known objects, such as globular clusters, and which they suggested was due to the close passage of a dark matter subhalo. Interestingly enough, as stated in Bonaca, Hogg, et al. (2019), the recovered properties of this subhalo (mass and size) were denser than those with the ΛCDM mass-size relationship presented in Moliné et al., 2017. The works mentioned are only a few examples of the extensive literature that has explored the impact of dark matter subhalos in simulated streams (Helmi & Koppelman, 2016; Hermans et al., 2021; Banik, Bovy, et al., 2021; Hilmi et al., 2024; Nibauer et al., 2025) or searched for their traces in observed streams (G. F. Thomas, R. Ibata, et al., 2016; Erkal, Koposov, et al., 2017; Bonaca, Pearson, et al., 2020; Bonaca, Conroy, et al., 2020).

In contrast, a limited number of works have explored whether other structures, such as those from baryonic matter, can cause variations in the density of streams and gaps that can be confused with those produced by dark matter subhalos. Among these works, it is worth mentioning the results of Pearson, Price-Whelan, et al. (2017), which suggest that the presence of the bar at the center of the Galaxy can perturb the characteristics of a stream, such as Palomar 5, and generate gaps along its tail. That the Galactic bar could have an influence on stream morphology was also discussed by Hattori et al. (2016) and Price-Whelan, Sesar, et al. (2016), in the case of the Ophiuchus stream (Bernard, Ferguson, Schlafly, Abbas, et al., 2014). Besides the Galactic bar, giant molecular clouds can also produce gaps in stellar streams, as shown by Amorisco et al. (2016). All of these works thus indicate that baryonic structures can play an important role in tail morphology. In this context, an extensive numerical study specifically focused on modeling the tails of Palomar 5 under the influence of the Galactic bar, spiral arms, giant molecular clouds, and globular clusters, has been realized by Banik & Bovy (2019), who concluded that both the influence of the bar and that of the giant molecular clouds can leave imprints on Palomar 5 tidal tails similar to those left by dark matter subhalos. In contrast, they found the effect of globular clusters to be negligible.

Few studies have specifically investigated the effect of globular clusters on stellar streams. Erkal, Koposov, et al. (2017) concluded that globular clusters could not be responsible for the observed density variations in the tails of Palomar 5. Their analysis focused on the characteristics of the observed gaps and involved constraining progenitor properties using reconstructive modeling. By trial and error, they identified a specific configuration of masses, sizes, impact parameters, times of impact, and relative velocities for two perturbers that successfully reproduced the observed density distribution. However, as we do in this work, their method does not perform full forward modeling of the entire globular cluster system on Palomar 5's stream. While they suggest that the impact rate of globular clusters is likely less significant—given their lower abundance compared to the expected dark matter subhalos population—they do not explore this aspect in detail. However, they state that it is an avenue for future investigation.

More recently, Doke & Hattori (2022) have examined the possibility that gaps in the GD-1 stellar stream could be due to the close passage of globular clusters, concluding that this scenario is improbable. These first works suggest that the impact of globular clusters on stellar streams is negligible. This result does not necessarily need to be the general case, especially for streams of clusters such as Palomar 5, which live in the inner 20 kpc of the Galaxy, where many other globular clusters also orbit. For example, Khoperskov, Mastrobuono-Battisti, et al. (2018), Mastrobuono-Battisti, Khoperskov, et al. (2019), and Ishchenko, Sobolenko, Berczik, Omarov, et al. (2023) showed that globular clusters can even collide with other clusters, which implies that cluster stream collisions should happen much more frequently since streams are far more extended than clusters.

In this study, we aim to fill this gap in the literature on numerically modeling cluster-stream interactions. We seek to quantify the impact of passing globular clusters in the vicinity of streams to understand whether these systems can also be effective and how

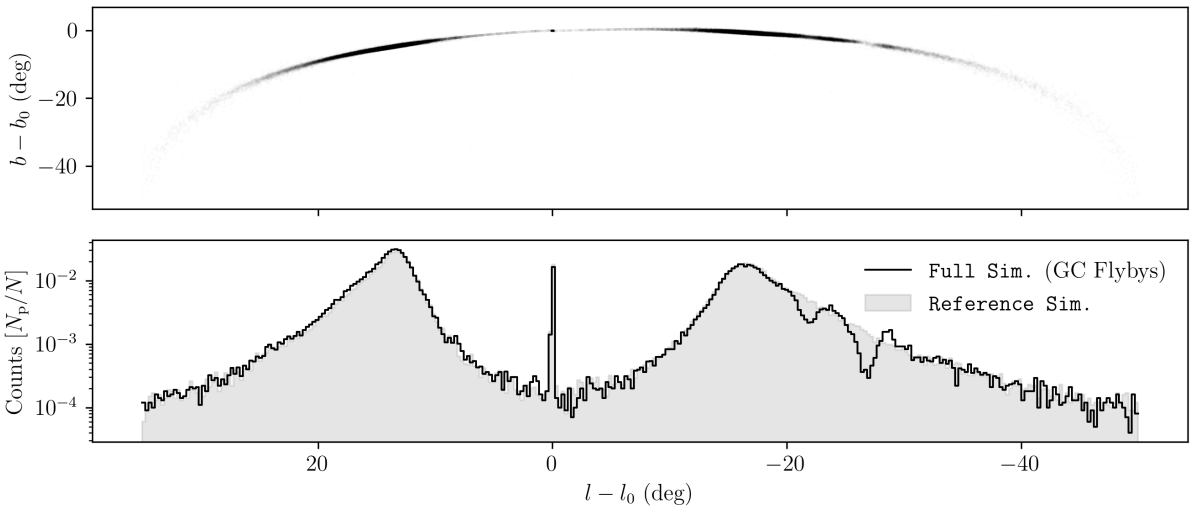

Figure 5.1 – Simulated Palomar 5 stream created by modeling the host cluster as a Plummer sphere disrupting within an axis-symmetric Galactic potential plus the gravitational effect of 164 other Galactic globular clusters. The top panel shows the distribution of star particles that escaped the cluster due to tidal forces. The bottom panel shows the 1D density profile marginalized over longitude. The gray fill shows a reference simulation that uses the same conditions to produce the stream but does not include the other globular clusters. The large central peak in density is composed of particles still bound to Palomar 5. ℓ_0, b_0 are located Palomar 5's cluster's center of mass. Two large gaps are present due to the passage of two globular clusters. N_p indicates the number of particles in a bin, while N is the total number of particles, which is 100,000.

frequently they alter the distribution of stars in the tails, producing underdense regions or gaps. To this end, in the following pages, we present the results of simulations of the streams of Palomar 5 subject to the gravitational interaction with the set of 165 Galactic globular clusters for which positions and velocities are known to date and for which orbits can therefore be reconstructed (Baumgardt & Vasiliev, 2021). We chose to simulate streams formed from a cluster with the current characteristics of Palomar 5 because it is a halo cluster with extended tails, and because it is a cluster for which the effect of baryonic structures on its stream has already been studied. As we show, and in tension with previous claims, the close passage of other clusters with such a stream is not rare. Indeed, in the 50 simulations we ran, we found the formation of numerous gaps, averaging 1.5 gaps per simulation, generated by 18 different clusters across the entire system of Galactic globular clusters.

2 Methods

The most accurate model of the Palomar 5 stream would involve full modeling of the internal dynamics of the cluster, which would mean computing N-body interactions with a

$\mathcal{O}(N^2)$ computation time, stellar evolution, supernovae, an initial mass distribution, treatment of binary star systems, etc. (for such an example, see Gieles et al., 2021; L. Wang, Spurzem, S. Aarseth, Giersz, et al., 2016). Instead, we opt for solving the restricted-three-body problem, also known as the particle-test method, as we did for S. Ferrone, Di Matteo, et al. (2023), which we describe here for completeness. As demonstrated by Mastrobuono-Battisti, Di Matteo, et al. (2012), although the restricted three-body problem neglects the internal evolution of the cluster, it still reproduces very similar stream properties since the model captures key extracluster physics, such as disk shocking and epicyclic stripping.

Below, we first present the approach used to include the Galactic globular cluster system in our modeling (Sect. 2.1), highlighting the similarities and differences with respect to what we did in S. Ferrone, Di Matteo, et al. (2023); we then summarize the method used to model the mass loss from the cluster (Sect. 2.2) and finally discuss the quality of the numerical integration (Sect. 2.3).

2.1 Numerical methodology

We begin by extracting positions in the sky, proper motions, line-of-sight velocities, and distances, as well as masses and half-mass radii, of 165 globular clusters from the Galactic globular cluster catalog by Baumgardt & Vasiliev, 2021.[2] We then convert the initial conditions from sky coordinates into a Galactocentric reference frame, by adopting a velocity for the local standard of rest of $v_{\mathrm{LSR}} = 240$ km s^{-1} and a peculiar velocity of the Sun equal to $(U_\odot, V_\odot, W_\odot) = (11.1, 12.24, 7.25)$ km s^{-1}, as reported by Schönrich (2012). We set the Sun's position to $(x_\odot, y_\odot, z_\odot) = (-8.34, 0, 0.027)$ kpc. We took the vertical position above the disk from B. Chen et al. (2001) and the distance of the Sun to the Galactic center from M. J. Reid et al. (2014). These transformations were performed using `astropy` (Astropy Collaboration, Robitaille, et al., 2013).

For the Galactic potential, we employed the second model from Pouliasis et al. (2017), a superposition of a thin disk, thick disk, and dark matter halo, with masses and scale lengths provided in Table 1 of S. Ferrone, Di Matteo, et al. (2023). This model is time-independent throughout our simulations. This model satisfies a series of observational constraints such as local solar, stellar density, the Galactic rotation curve, similarly to other Galactic models such as `MWpotential2014` from Bovy (2015) and `McMillian2017` from McMillan (2017). However, we use only one Galactic potential to balance data volume and computation time, which should suffice. Vasiliev & Baumgardt (2021) found that only a few outer globular clusters are strongly affected by different potential models.

---

[2] The Baumgardt catalog has been assembled across a series of works, see: Baumgardt, Sollima, et al., 2020; Baumgardt, Hilker, et al., 2019; Baumgardt & Hilker, 2018. The catalog can be found on the World Wide Web at https://people.smp.uq.edu.au/HolgerBaumgardt/globular/.

Generally, kinematic uncertainties are the dominant factor in differences between orbital solutions per cluster. Similarly, Grondin, Webb, J. M. M. Lane, et al. (2024) generated a globular cluster mass-loss catalog using seven different potential models and found that their debris distributions were rather model-independent, similar to those of S. Ferrone, Di Matteo, et al. (2023). While the clusters' exact positions in time may depend on the model, we assert that interaction rates and stream formation are largely independent of the choice of the Galactic potential model.

Lastly, we select an integration time of 5 Gyr as a compromise between maximizing interaction statistics and modeling the Galaxy as a time-independent, constant mass distribution. Ishchenko, Sobolenko, Berczik, Khoperskov, et al. (2023) analyzed the orbits of the Galactic cluster population using the same initial conditions as in this work within five live Milky Way-like potentials from IllustrisTNG (Pillepich et al., 2018). They found that in all sampled potentials, orbital changes remain minimal over 5 Gyr, becoming significant only at earlier look-back times when the host galaxy had significantly less mass or was undergoing a merger event.

2.1.1 `Full` simulations

There is a primary methodological departure from S. Ferrone, Di Matteo, et al. (2023). In that work, globular clusters evolved under the gravitational effect of the Galaxy alone. In contrast, now we also consider the effect of all other Galactic globular clusters by taking into account the direct N-body interactions between them. First, all clusters are represented by Plummer spheres, each with its own mass and half-mass radius as reported in the Baumgardt catalog (Baumgardt & Vasiliev, 2021). For the remainder of this paper, the `full` simulations consider the gravitational forces from the globular cluster interactions.

For these simulations, we proceeded in two steps:

1. First, starting from the Galactocentric positions and velocities of all 165 Galactic globular clusters, we integrate their orbits back in time for 5 Gyr under the influence of the Galaxy itself and their mutual influence. In the backward integration, the system of equations of motion for the globular clusters is thus:

$$\ddot{\vec{r}}_i = -\nabla\Phi + \sum_{j\neq i}^{N_{GC}} \frac{Gm_j}{\left(|\vec{r}_j - \vec{r}_i|^2 + b_j^2\right)^{3/2}} \left(\vec{r}_j - \vec{r}_i\right), \tag{5.1}$$

   where $\vec{r}$ indicates the Galactocentric position vector, the index i indicates the globular cluster of interest; the index j indicates the other globular clusters that are summed over. N_{GC} is the total number of globular clusters, which in this study is 165, m_j is the mass of the j-th cluster in the sample, b_j is its Plummer scale radius, and $\vec{r_j}$ is its Galactocentric position. Φ represents the same Galactic smooth potential that we discussed previously (Pouliasis et al., 2017, Model II, in the present case). Note that the masses and sizes of the globular clusters are kept constant in these simulations and are not allowed to vary with time, which means that we do not consider their internal evolution. In sec. 4, we discuss the implications of the modeling limitations.

2. Once we found the positions and velocities of the entire globular cluster, we sampled Palomar 5 with 100,000 particles from a Plummer distribution, taking the mass and half-mass radius from the Baumgardt catalog: 1.3×10^4 $M_\odot$ and 27.6 pc. We then integrated the evolution of these particles forward in time to the present day, taking into account that each particle feels the gravitational potential of the Galaxy, its host cluster, and that of all the other clusters in the Galaxy. Note that we do not account for self-gravity among particles. The particles experience the gravitational field yet do not contribute to it, a common assumption in galactic dynamics, as the mass of an individual star is negligible compared to the mass of the larger dynamical system. The equation of motion of a generic particle among the 100,000 that populate Palomar 5 is thus:

$$\ddot{\vec{r}}_p = -\nabla\Phi + \sum_j^{N_{GC}} \frac{Gm_j}{\left(|\vec{r}_j(t) - \vec{r}_p|^2 + b_j^2\right)^{3/2}} \left(\vec{r}_j(t) - \vec{r}_p\right), \tag{5.2}$$

where the index p represents one of the 100,000 particles of interest, $\vec{r_p}$ being its position, and j indexes over the globular clusters as in Eq. 1. We note that in Eq. 2, the positions of the globular clusters are time-dependent since they are being loaded during this step and not computed, unlike Eq. 1.

The procedure described so far has been repeated 50 times, generating a new set of initial conditions each time, given the uncertainties on proper motions, line-of-sight velocities, distances to the Sun, and masses of all clusters, as reported in the Baumgardt catalog. We handle these uncertainties through a Monte-Carlo approach by sampling them with a Gaussian distribution and considering the covariance term between the proper motions. We use the most probable values for the initial conditions in the first simulation. We sample the uncertainties for all globular clusters. Additionally, for each resampling of Palomar 5's mass, we also resample the distribution of the 100,000 star particles.

During the integration, we save intermediate snapshots to facilitate the analysis of stellar streams and the effects of cluster impacts. Specifically, for each realization of the Palomar 5 stream, we saved 5000 in snapshots, equivalent to a temporal resolution of 1 million years. We provide the parameters that specify our data volume in Table 5.1.

Using single precision floating point numbers, the size of our simulations is approximately:

$$N_p \times N_{\text{ts}} \times N_{\text{phase}} \times N_{\text{sampling}} \times 4 \text{ bytes} \approx 600 \text{ Gb}. \tag{5.3}$$

Table 5.1 – Parameters determining the data volume. N_p is the number of particles, N_{ts} is the number of time-steps saved, N_{phase} is the number of phase space coordinates, and N_{sampling} is the number of Monte-Carlo samplings of the initial conditions.

N_p	N_{ts}	N_{phase}	N_{sampling}
100000	5000	6	50

2.1.2 `Reference` simulations

To quantify the impact of globular cluster passages on the density of the Palomar 5 stream, we performed a second set of simulations, which we refer to as the `reference` simulations in this paper. These `reference` simulations use the same 50 sets of initial conditions as the `full` simulations, the same Galactic potential, but exclude mutual interactions between globular clusters. The approach adopted for this second set of simulations is thus equivalent to that adopted already in S. Ferrone, Di Matteo, et al. (2023). In Eq. 1, only the gradient of the Galactic potential is considered. In Eq. 2, of the second term on the right side of the equation, only the influence of Palomar 5's Plummer sphere on Palomar 5's particles is considered. In other words, the sum iterates over only one globular cluster, the host. We omit all interactions with the other clusters.

2.2 Mass loss

Each of the 100,000 particles that initially populate the cluster undergoes experiences the forces from Pal 5 and the Galactic potential. The mass and radius of Pal 5 are held constant over time. At each time step, a certain number of particles will therefore acquire sufficient energy to no longer be gravitationally bound to the cluster itself and thus go on to populate the streams, whose mass and spatial extent grow over time. It is important to note that in the approach used:

1. The masses and sizes of the clusters (and therefore the parameters of the Plummer potentials) do not change over time, which is an oversimplification, because in a self-consistent approach, these parameters would vary.
2. We use the same initial conditions for Pal 5 progenitor as it has today, and this is also a simplification, since Pal 5 - 5 Gyr years ago - must have contained at least

part of the mass estimated today in its tails[3].

The assumption in point 2 is a direct consequence of the approach described in point 1. Starting from a cluster with a mass and size similar to the current ones can lead to streams with lower velocity dispersions than those we would obtain if we had used a self-consistent approach. In a future article, we will report on the study of gap survival times depending on the masses and sizes of progenitor clusters (Ferrone et al, in prep). We note, however, that simplifications of this kind are not uncommon in literature. Pearson, Price-Whelan, et al. (2017) discussed the formation of gaps in the Pal 5 tails and assumed a time-independent mass of $50,000$ $\mathrm{M}_{\odot}$ for Pal 5, over the last 4 Gyr; Erkal, Koposov, et al. (2017) adopted a N-body approach to simulate Pal 5 stream, but used Pal 5 current conditions as their progenitor's initial conditions; Banik & Bovy (2019) simulated the Pal 5 stream as emerging from a stellar system with a velocity dispersion of 0.5 km/s (similar to that of particles escaping from our cluster, as we have verified).

The characteristics of the streams modeled in this paper may be considered more representative of those of clusters that are now completely dispersed, i.e., it is conceivable that completely dispersed globular clusters that left behind a population of 'orphan' streams passed through characteristics similar to those of Pal 5 today (small masses and extended radii). In this sense, the initial conditions chosen (in terms of internal parameters) may be more representative of those of streams for which the progenitor is now dissolved (see, for example, the population of streams without progenitors described by R. Ibata, Malhan, Tenachi, et al., 2024) than those currently typical of Galactic globular clusters than those currently typical of Galactic globular clusters.[4]

2.3 Numerical stability

We used a leapfrog integrator because of its ability to preserve phase-space volume and conserve the Hamiltonian with each integration step. For instance, this method is preferable to a Runge-Kutta scheme, which can introduce non-physical and significant numerical errors in systems that require long-term stability and energy conservation. One drawback of the leapfrog integrator is that it requires a uniform time step throughout the entire computation, resulting in unnecessary computations for a particle after it has escaped from the host cluster. However, energy conservation and phase-space volume preservation are paramount when modeling stellar streams. The time step was therefore set to be small enough to conserve energy for the most interior particles within the cluster—ensuring that a higher mass loss did not arise from numerical error. We found

---

[3] We used the same approach (i.e., time-independent masses and sizes) to model the whole set of globular clusters.

[4] In this regard, we recall that Bovy (2014) modeled the GD-1 stream as the result of the dissolution of a cluster with a mass of $2 \times 10^4 M_{\odot}$, and a tidal radius of 0.07 kpc.

that a time-step of 10,000 years was adequate to maintain energy conservation, with a median variation of $10^{-12}\frac{\Delta E}{E_0}$, where E_0 is a particle's initial energy, and ΔE is the difference between its final and initial energy.

We also checked the reverse integrability of the globular cluster system for the `reference` simulations. By reverse integrability, we mean the integrator's capability to track the cluster backward in time and then re-integrate it forward along the same trajectory. Integrating point masses in a static axis-symmetric potential conserves L_z and E, which create regular periodic and non-chaotic orbits. Therefore, any drift would arise from purely numerical error. We selected a timestamp for which the drift in the final position after forward integration, compared to the initial position from the backward integration, was consistently at least two orders of magnitude smaller than the Plummer scale radius used for Palomar 5. This high precision ensures that no fictitious numerical forces influence the system, preventing any artificial mass loss or retention of star particles.

3 Results

3.1 Overview

The presence of the other globular clusters affects the properties of the Palomar 5 stream. Fig. 5.1 presents an obvious example of this effect, which we selected for its prominent gaps. Two of these gaps are visible in Galactic coordinates and become even more apparent when marginalizing over latitude to reconstruct the 1D density profile of the stream as a function of longitude.

Regarding the shape of the density distribution, the central peak corresponds to the still-intact globular cluster whose stars have not yet escaped. The stream's density peaks are of the same order as the cluster itself, which is inconsistent with reality; the cluster's peak density should be higher than that of the stream. Of course, this discrepancy is a result of our modeling choices. Since we use the present-day mass and radius for Palomar 5 for the whole simulation duration, the system is less dense than it should have been. In turn, our simulations have a strong initial mass loss, which adds to the amplitudes of the profile density peaks of Fig. 5.1. This inaccuracy is acceptable for the scope of this work. First, Palomar 5's tails indeed have more mass than the cluster itself. R. A. Ibata, Lewis, G. Thomas, et al. (2017) reports that there could be three times as much mass in Palomar 5's tails as the cluster itself. Secondly, the exact form of the density distribution is less important than having a population of particles present that can probe a cluster flyby event.

To compare the `reference` and `full` simulations more quantitatively, we work in the tail coordinate system, in which the stream's central axis aligns with the cluster's orbit. We based this coordinate system on the work of Dehnen et al. (2004) and present

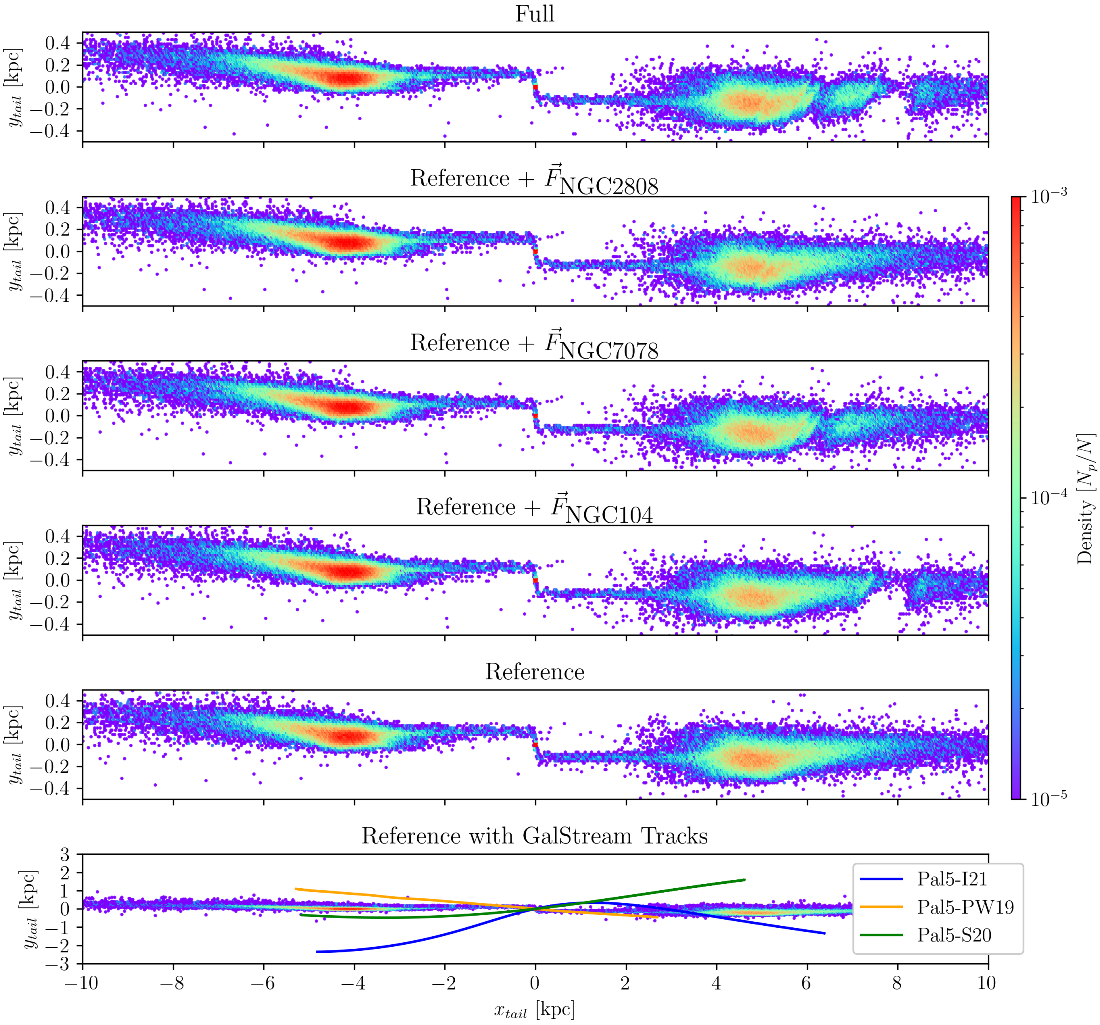

Figure 5.2 – Density maps of Palomar 5's stream in the tail coordinate system, where $x\prime$ is the integrated arc length along the cluster's orbit and $y\prime$ is the distance within the orbital plane. The color scale represents normalized particle counts (total: 100,000). The top panel shows the `full` simulation with three gaps on the stream's right-hand side. The next three panels depict simulations with identical initial conditions but exclude the gravitational influence of all clusters except those forming a given gap. The `Reference` simulation omits the influence from other globular clusters. The bottom panel compares Palomar 5's observed stream length to the `Reference` simulation, using the same Monte-Carlo realization as Fig. 5.1 and `Sampling 009` (as seen in the online appendix).

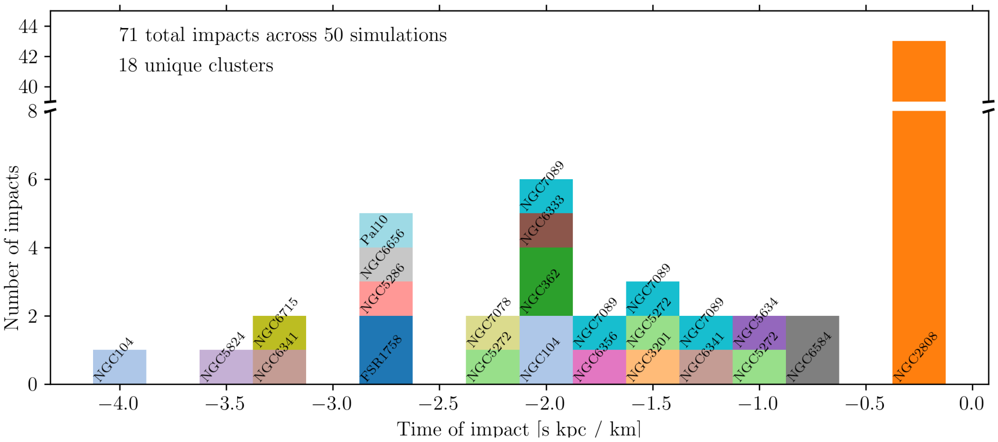

Figure 5.3 – Simulation time when the impacts occurred for all gap-causing flybys summed over all 50 simulations. Each perturbing cluster is labeled and color-consistent. We report the time axis in simulation units, with 1 s kpc km $^{-1}$ corresponding to roughly 1 Gyr. We note that the plot breaks the y-axis to accommodate the large number of encounters from NGC 2808 without overshadowing the other interactions.

it in Fig. 5.9. Briefly, in this system, the x_{tail} coordinate represents the position of a particle along the orbit relative to the globular cluster. Positive values of x_{tail} are ahead of the cluster, while negative x_{tail} is behind the cluster. The y_{tail} coordinate measures the particle's distance within the orbital plane, where positive values indicate that the particle is farther from the Galactic center and negative values indicate that it is closer. Fig. 5.2 shows a comparison between one of the 50 realizations of the Palomar 5 stream, taking into account the gravitational interactions with all other globular clusters in the Galaxy (top panel) and omitting them (bottom panel). This comparison clearly shows the presence of two wide ($\sim$100 pc and $\sim$1 kpc) gaps in the leading tail and of a more subtle underdensity at $x_{\text{tail}} \sim 5$ kpc (we refer the reader to Supplemental Material 6.1 for a detailed description of the underdensities and gaps detection method).

To determine which globular clusters were responsible for creating these gaps and when close passages occurred, we estimated the gravitational acceleration along the orbit of Palomar 5. We represented it in the (t, τ) space. t is the simulation time, and τ indicates how long it will take for Palomar 5 to reach a given point in its orbit or how long ago it passed. The use of τ is advantageous because the growth of the stream is approximately linear in τ.

On the other hand, streams in physical space are modulated by their orbital eccentricity with periodic expansion and contraction depending on the orbital phase (see the top panel of Fig. 5. Sanders, Bovy, et al., 2016, for an example). Adopting this time-space and reporting the gravitational acceleration along the Palomar 5 orbit in this space, identifying the globular clusters that produced the perturbation and the time at which it occurred becomes straightforward. We refer the reader to Supplemental Material 6.2 for a detailed description of the procedure. In this way, we can identify that the clusters responsible for creating gaps in the simulation of the Palomar 5 stream, as reported in Fig. 5.2, are NGC 2808, NGC 7078, and NGC 104. Their close passages occurred 200 Myr, -1.9, and -2.1 Gyr ago, respectively.

To further investigate whether the three clusters above are responsible for producing the gaps observed in this simulation, we conducted additional experiments by including only the perturbation of each cluster at a time, while neglecting the gravitational perturbations of all the other clusters in the Galaxy.

To verify that the three suspected clusters are responsible for producing the gaps, we conducted experiments by including one perturbed at a time and excluding all others. We present these results in the middle panels of Fig. 5.2 and clearly show that NGC 2808, NGC 7078, and NGC 104 are the clusters responsible for creating the underdense regions observed in the leading tails of Palomar 5. It is worth noting that the times at which the passages of these clusters occurred, according to our analysis, are in agreement with the observed width of the corresponding gaps: the encounter with NGC 2808 being very recent (only 200 Myr ago), its induced gap is still very thin, because it takes time for a perturbation to grow into an extended gap, as it is the case for those induced by the passages of NGC 7078 and NGC 104, which occurred in earlier times. It is also interesting to emphasize that gaps as thin as those generated by the passage of NGC 2808, 200 Myr ago, can be detected by working in the tail coordinate system and by making a comparative analysis (`full` versus `reference` simulations): they are so thin that they cannot be directly identified in Galactic coordinates (see Fig. 5.1).

The analysis presented in Fig. 5.2 has been repeated for the whole set of simulations, and online appendix reports all of them for completeness. For all the streams, morphologically speaking, the only changes appear to be the existence of gaps or their absence. We do not observe a thickening of the streams due to an increased velocity dispersion.

From this analysis, we can derive a statistical view of (1) the number of gaps generated on the Palomar 5 stream by the system of Galactic globular clusters, (2) the clusters that generated these gaps, and the time history of these perturbations. From this, we can then quantify (3) the properties of the perturbers (their masses, sizes, and orbital parameters) as well as (4) the impact geometry of the encounters, which allows us to understand which encounters are more favorable for generating gaps in the Palomar 5 stream. In the following, we will present the results of this analysis, addressing points (1) and (2).

3.2 The history and statistics of gap creations in the Palomar 5 stream

By applying the methodology described above to the whole set of simulations, we can reconstruct the history of close passages of Galactic globular clusters to Palomar 5's stream in the last 5 Gyr, which – we remind the reader – is the time interval investigated in our simulations. Fig. 5.3 and Table 5.2 present results of this analysis. NGC 2808 impacted Palomar 5's stream about 200 Myr ago in 44 out of 50 simulations, creating a small gap at a similar position to the one reported in Fig. 5.2 in each case. Since this interaction occurred less than one orbital period ago, despite the uncertainties, the orbital solutions remain similar and thus produce consistent results across all simulations. However, as we continue to turn back time further, the uncertainties in the initial conditions allow the various orbital solutions to diverge from one another. Thus, in one configuration, a cluster can impact the stream at a given time, and yet at the same moment, in a different set of initial conditions, it could be on the other side of the Galaxy. We will discuss the necessary conditions for creating a gap in Supplemental Material 6.4.

Table 5.2 – Number of gaps created by each perturber across all 50 simulations. These data are color-coded and illustrated in Fig. 5.3.

NGC2808	44	NGC7089	5	NGC5272	4
NGC6584	3	NGC6341	2	NGC6656	2
NGC104	2	NGC3201	1	NGC5634	1
NGC5286	1	NGC362	1	NGC5824	1
NGC6356	1	NGC6333	1	NGC6715	1
FSR1758	1	NGC7078	1	Pal10	1

In total, we report the finding of 73 gaps across our 50 simulations, which averages to 1.5 gaps per simulation. Eighteen different perturbers provoke the gaps. Table 5.3 presents the distribution of the number of gaps appearing per simulation. If we consider NGC 2808 an outlier and exclude it from the experiment, we observe an average of 0.6 gaps per simulation.

Table 5.3 – Occurrence of gaps in Palomar 5 streams, in our simulations. More specifically, the table reports the number of simulations (second row) for a given number of gaps (first row).

Number of Gaps	0	1	2	3	4
Number of Sims.	4	25	16	4	1

We need a more sophisticated statistic to compare our results to other simulations, so we turn to the gap creation rate developed by Carlberg (2012). The gap creation rate is

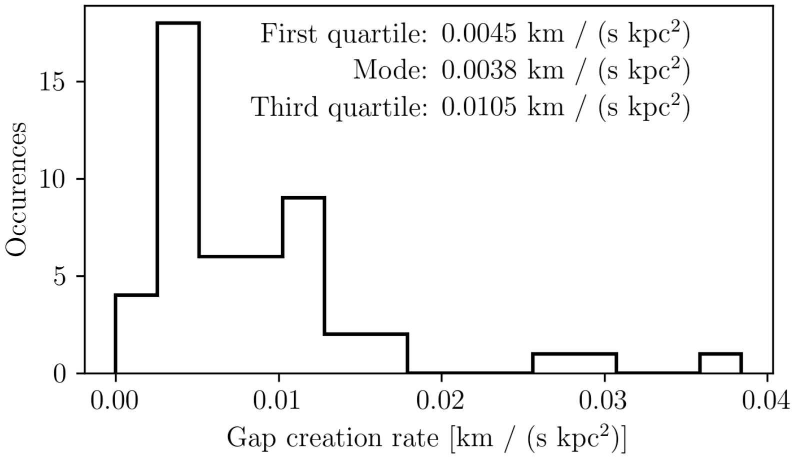

Figure 5.4 – Distribution of the number of gaps normalized over the total integration time and unit stream length as described by Eq. 5.4 for the whole set of 50 `full` simulations.

the number of gaps that appear per unit time and is normalized by the stream's length. For our simulations, this rate is given by:

$$\mathcal{R}_{\text{Pal5}} = \frac{1}{T}\int_0^T l^{-1}(t)\sum_i \delta(t-t_i)dt, \tag{5.4}$$

where T is the total integration time, $l(t)$ is the length of the stream, and $\sum_i \delta(t-t_i)$ sums over the gap occurrences, with i indexing over the number of gaps in a given simulation. Here, δ represents the Dirac delta function. This expression can be simplified to:

$$\mathcal{R}_{\text{Pal5}} = \frac{1}{T}\sum_i \frac{1}{l(t_i)}. \tag{5.5}$$

This computation allowed us to analyze the distribution of gap creation rates across all simulations. Notice that since the gap creation rate adds in parallel, naturally, gaps that occur at earlier times when the stream was shorter are weighted higher than those that occur when the stream is longer. Fig. 5.4 presents these results which are is roughly consistent with a simple estimate of the average gap creation rate: with 73 gaps over 5 Gyr of integration time for a stream about 20 kpc in length, the naive estimate is approximately 0.015 km s^{-1} kpc^{-2} (which is roughly equivalent to 0.015 Gyr^{-1}kpc^{-1}). This naive estimate is about double the weighted mean gap creation rate of 0.009 km s^{-1} kpc^{-2} and is higher because it does not account for the growth of the stream over time, unlike Eq. 5.4.

Lastly, we note that of the 73 observed gaps, only eight are in the trailing tail, and the rest are in the leading tail, which is a surprising result. A priori, since the star particles escape at similar rates from the L_1 and L_2 Lagrange points, each tail is of similar length and density. The main difference between the two tails is that the leading tail is closer to the Galactic center than the trailing tail by about 400 pc. Since the lengths are equal, and the offset between the tails is slight compared to the Galactocentric distance of about 10 kpc, we expected the gaps in each tail to be more or less the same. We can compute the probability of observing the unequal occurrences through the binomial distribution. First, since the 44 gaps linked to NGC 2808 are the result of the same flyby, they are not independent events. We remove them from this consideration, which leaves 21 gaps in the leading tail and 8 in the trailing. The probability of observing up to 8 successes in 29 trials, given a 50% chance of success, is 1.2%–unlikely, but possible. Additionally, other perturbers impact at consistent times, which may violate the assumption of independent events, as seen with NGC 2808.

3.3 Impact geometry and parameters of the perturbers

With the perturbers identified, we perform statistical analysis to understand the conditions necessary for a globular cluster to induce a gap in the Palomar 5 stream. We turn to impact theory, which in its simplest form is presented in works such as Binney & Tremaine (2008). Consider two particles: one stationary and the other moving past it. The impact parameter is the distance between the two particles at the point of their closest approach. The impulse approximation is employed, which assumes that the velocity of the perturber remains unchanged during the interaction. This assumption simplifies the computation.

To understand how the impacted particle is perturbed, one needs to compute its change in momentum, which is determined by integrating the force acting on the particle throughout the interaction. A useful approximation for this change in momentum, per unit mass, is the force at the closest approach multiplied by an estimate of the interaction time:

$$\Delta p \approx \text{Force} \times \text{interaction time} = \frac{GM}{b^2} \times 2\frac{b}{\delta v} = 2\frac{GM}{b\delta v}, \tag{5.6}$$

where M is the mass of the perturber, b is the impact parameter, δv is the relative velocity of the perturber with respect to the particle, and G is the gravitational constant.

This equation asserts that a more massive perturber, passing closer to the particle and moving more slowly, will have a greater impact. It is important to note that the momentum change is inversely proportional to the velocity of the perturber. Note that this contrasts with the intuition from elastic collisions, such as those between billiard balls, where higher velocities result in greater impacts.

Erkal & Belokurov (2015) extended this impact theory from one point mass impacting another to studying how an extended body impacts a stream by quantifying the change in momentum of a given particle as a function of its distance from the point of greatest impact along the stream. Erkal & Belokurov (2015) models their perturber as a Plummer sphere,

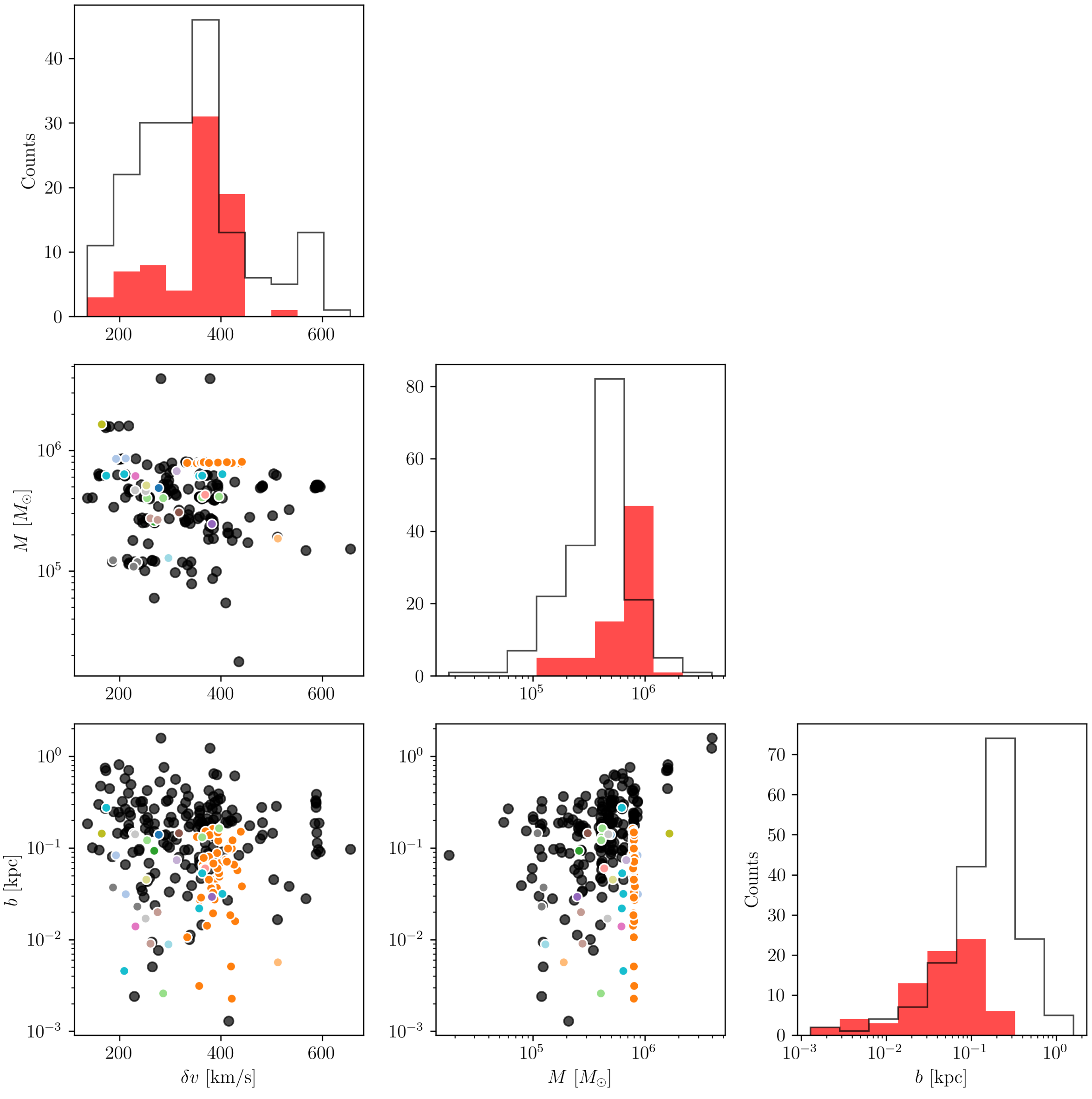

Figure 5.5 – Distribution and relationship between the impact variables from Eq. 5.6 for all close flybys considered. The colors indicate the encounters that cause gaps and are the same as Fig. 5.3, with white edges for visibility and binned in red for the histograms. The black histogram shows the close encounters that did not lead to gaps. Indeed, no obvious trend has emerged that delimits these planes into gap-producing or non-gap-producing ones.

like in our simulations. Since a stream is not a point but has length and an orientation in space, one needs to consider the parallel and perpendicular components of the velocity to describe the impact fully. Consequently, five parameters determine the change in velocity of a given stream particle: M, r_p, b, $W_{\|}$, and $W_{\perp}$, which are the mass of the perturber, size of the perturber, impact parameter, parallel and perpendicular components of the relative velocity. As detailed in Supplemental Material 6.3, we calculated these parameters for all our `full` simulations by selecting – for each of them – the strongest five flybys of a perturber with the Palomar 5 stream. Thus, we compute 250 impacts and flag those that give way to gaps.

Visual inspection of the five key impact parameters (M, r_p, b, $W_{\|}$, and $W_{\perp}$) did not reveal a clear distinction between flybys that create gaps and those that do not. Therefore, we only present the quantities from Eq. 5.6 in Fig. 5.5.

Note that this figure displays the total relative velocity rather than separating the parallel and perpendicular components, as no specific trends were observed when plotting the two velocity components separately. We also excluded the characteristic cluster radius, which showed little correlation with the results, likely due to the narrow range of globular cluster radii (see Fig. 5.7). This factor might be more significant for dark matter subhalos, where size variation is greater.

While Fig. 5.5 demonstrates that mass, relative velocity, or impact parameter alone cannot predict gap formation, one interesting result emerges: impact parameters greater than 300 pc do not create gaps. The stream widths are roughly 200 pc, as seen in the online appendix. This finding is even more evident when examining the b-M plane. A series of perturbers at roughly $\sim 8 \times 10^5 M_\odot$ highlights NGC 2808's flybys, where all encounters with impact parameters under 200 pc result in gaps, while those beyond this distance do not. In other words, even the most massive globular clusters with masses greater than about $10^6 M_\odot$ cannot cause gaps if their impact parameters are greater than roughly 300 pc. Interestingly, even fast encounters ($\delta v > 300$ km/s) can produce gaps for impact parameter values below this threshold. Perhaps this is not surprising, since the range of possible relative velocities is much less than that of mass and impact parameters, which vary by two and three orders of magnitude, respectively. In contrast, the relative velocities only vary by about a factor of three.

Once all the key impact parameters are estimated, we can use Eq. 5.6 and calculate Δp, the change in momentum (per unit mass) imparted by a cluster flyby on Palomar 5 stream. Fig. 5.6 shows the distribution of imparted change in momentum for all impacts that produce a gap compared to those that do not. On average, encounters that lead to gap creation impart a change in momentum on stream particles, which is a factor of 10 higher than encounters that do not form gaps (but with some overlap in the low-velocity tail). Interestingly, changes in momentum, which lead to gap creations, extend over a large range in velocities. There is a factor of about 100 between the smallest and largest

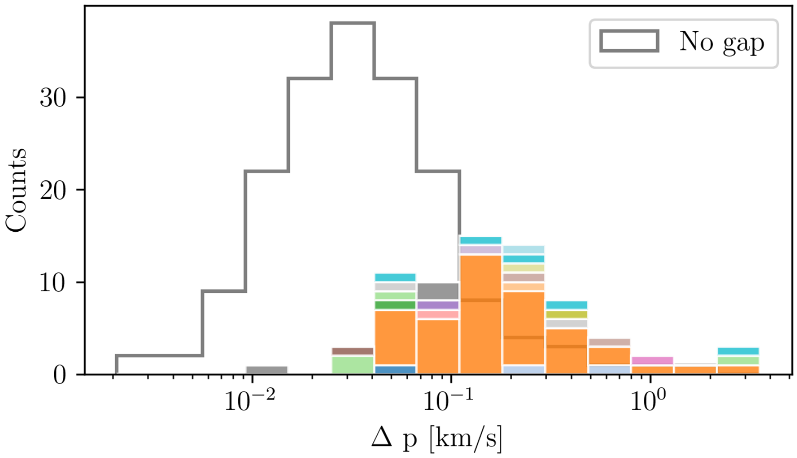

Figure 5.6 – Distribution of imparted change in momentum (per unit mass) from a cluster flyby given by Eq. 5.6. The data set includes the top 5 strongest flybys from each simulation. Those that cause gaps are colored, stacked, and overlaid atop those that do not — this is the gray distribution. We note the meaning of the colors is the same as in Fig. 5.3.

changes with NGC 2808 (orange color in the histogram) imparting changes in the velocity of stream particles, which redistribute over the whole range of Δp.

In addition to characterizing the parameters governing cluster encounters with the stream, since we know which clusters have produced gaps on the tail of Palomar 5, we can also verify their orbital and structural properties. Fig 5.7 shows just this, where we first show the clusters' mass and size (i.e., half-mass radius) that cause gaps on the tails of Palomar 5, dividing them from those that do not. As can be seen, no cluster with mass below $10^5 M_\odot$ causes gaps on the Palomar 5 stream, and all perturbers, except FSR 1758, have a half-mass radius below 10 pc. Even more interesting is their distribution in the E-L$_z$ plane, which shows that the clusters that cause gaps are on both direct and retrograde orbits (negative and positive values of L_z). However, all of the perturbers exist in an energy interval between -2 and -1×10^5 km^{2}s^{-2}, which is because only clusters within Palomar 5's orbital space can interact with the stream: clusters with higher orbital energies tend to have larger apocenters than that of Palomar 5 and thus spend most of their time away from Palomar 5's orbital volume.

Finally, it is worth noting the location of impacts with the stream, specifically whether they occur when Palomar 5 is near its pericenter. Fig. 5.7's bottom panel shows that encounters can occur at all orbital phases of Palomar 5, when it is close to the pericenter, but also very far away from it, at the outskirts of its orbital space. However, when taken all together, the location of gap-creating impacts shows a strong negative correlation with the Galactocentric radius r, with the number N of encounters favorable to gap formation going as $N = -2.5r + 50$ (with a Pearson coefficient of -0.86). While there

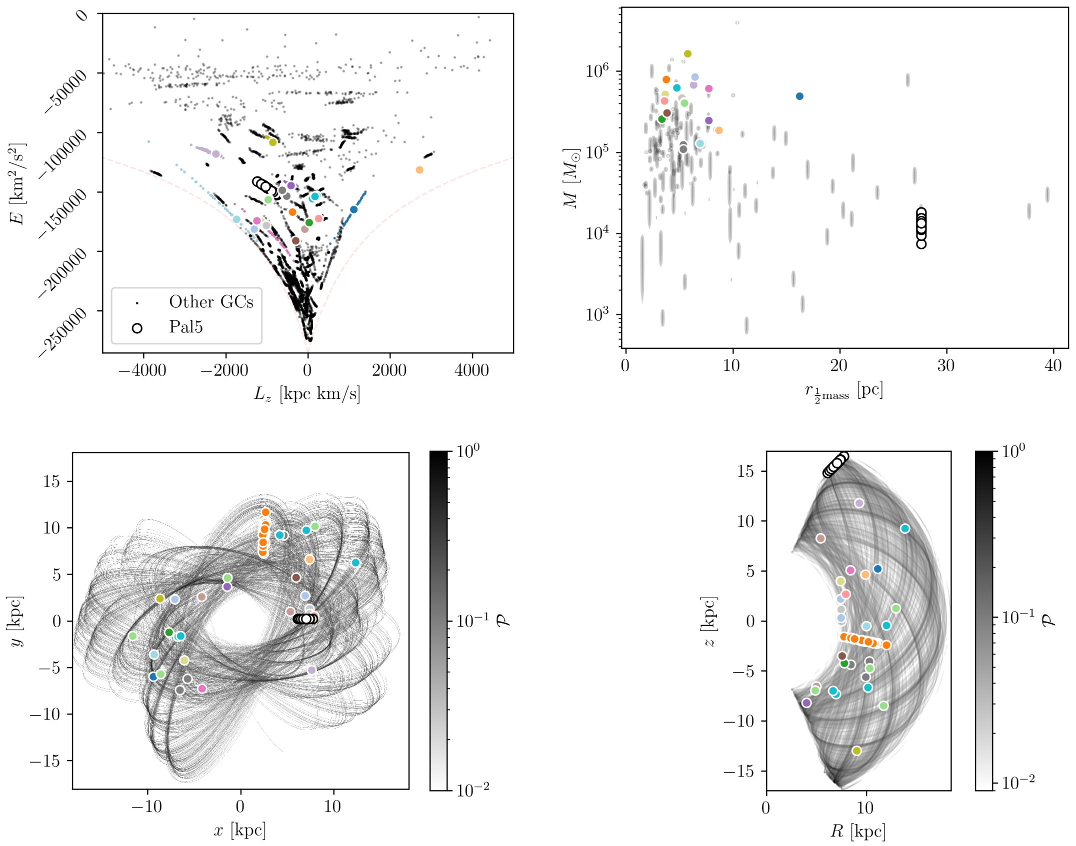

Figure 5.7 – *Top left:* Energy-angular momentum space of the globular clusters in the simulations, with 50 × 165 data points representing all sampled initial conditions. Clusters impacting Palomar 5 are shown with colored markers, large for the samplings that induce a gap and small for those that do not. The small gray dots represent the non-gap-causing clusters. The 50 white dots indicate Palomar 5's sampled initial conditions for the current day position. The light-pink dashed curve shows the circular velocity curve. *Top right:* Mass-size plane of the globular clusters in the simulations, with uncertainties on the masses indicated as vertical lines. We remind the reader that the globular cluster catalog currently does not provide uncertainties for the characteristic radii of clusters. *Bottom left:* Palomar 5's orbit in the Galactocentric xy plane. The gray scale represents all 50 stacked orbits, with $\mathcal{P}$ indicating the probability of Palomar 5's position, normalized to $\mathcal{P}_{\mathrm{max}} = 1$. The colored markers indicate the position of the perturber when it impacted the stream and *not* its present-day position. *Bottom right:* Same as the bottom left but in the meridional plane. In all panels, the colors of the markers and histogram bars correspond to specific perturbers as specified in Fig. 5.3.

are more clusters near the Galactic center, clusters naturally spend more time near their apocenters, and the lower relative velocities in these regions should favor gap creation. However, this result suggests that the cluster Galactic number density outweighs these factors when determining the number of gaps. The results are for Palomar 5 only, and a future study would need to investigate streams along various orbits before generalizing this conclusion.

3.4 Comparison to observations

We briefly compare our simulated gaps to the literature on Palomar 5. In the bottom panel of Fig. 5.2, we compare the tracks of Palomar 5 that were compiled in `galstreams` by Mateu (2023). The mid-point positions of the streams do not have the same Galactocentric positions as Palomar 5 from Baumgardt's catalog, and this difference creates an offset when projected into tail coordinates. Moreover, since we sample the distances to Palomar 5, the Galactocentric position within the Baumgardt catalog varies. To combat this, we position the mid-point of the `Galstream` tracks at the cluster's center of mass, allowing us to compare the length of the observed tracks to our simulated streams. We use the three tracks Pal5-PW19, Pal5-S20, and Pal5-I21 from Price-Whelan, Mateu, et al. (2019), Sollima (2020), and R. Ibata, Malhan, N. Martin, et al. (2021), respectively. For each track, we found the distance from the cluster in both directions, counting the number of gaps within this range, and we present this in Fig. 5.8. In the maximum limit, many gaps could appear at a rate of about one per realization. However, only a few gaps occur at the shortest reported stream length. We note that the gap generated by the recent perturbation induced on the stream by the passage of NGC 2808 (whose occurrence is very likely according to our models) sits in a portion of the simulated tail which is at the edge of the observed one (see bottom panel in Fig. 2). This element and the fact that this gap is skinny, because it is very recent, probably make its detection difficult.

We observe no gaps within 3 kpc of the cluster in our simulation. There may be a few reasons for the absence of gaps in the portion of the tails closer to the cluster center. First, as Sanders, Bovy, et al. (2016) demonstrated, the dispersion of action-frequencies in the stream plays a role. For instance, the frequency corresponding to the azimuthal action, J_ϕ, is $\dot{\theta}_\phi = -\frac{\partial \mathcal{H}}{\partial J_\phi}$ and where θ_ϕ is the angle describing the position of the particle phase space between momentum (p_ϕ) and position (ϕ) axes—where ϕ is the azimuthal angle between the x-y axes in physical space. Stream regions with well-separated frequencies are more susceptible to gap formation, while those with a wide frequency range (near the cluster) tend to erase the history of impacts. Thus, for a gap to form, the imparted change in frequency must exceed the range of frequencies in the impacted region. Therefore, the strong flybys close to the cluster were inconsequential for gap formation.

Another possible explanation is the different thicknesses of the simulated tails at dif-

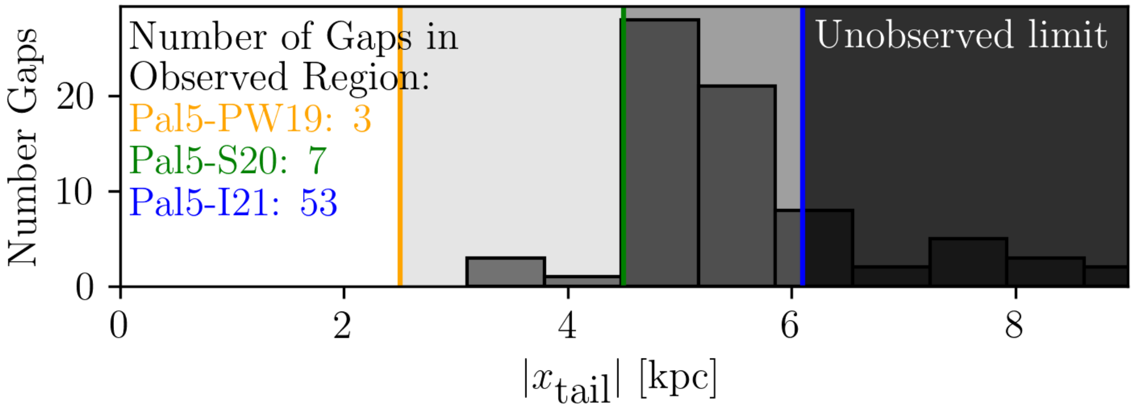

Figure 5.8 – Distribution of gaps as a function of absolute distance from the center of mass of Palomar 5's globular cluster. We count the number of gaps within the observable range on an individual track basis, with track lengths determined by the minimum and maximum x'-coordinates from the bottom panel of Fig. 5.2. The ranges for Price-Whelan, Mateu, et al. (2019), Sollima (2020), and R. Ibata, Malhan, N. Martin, et al. (2021) are shown for their respective dimensions, and the number of gaps within these ranges is indicated in the figure. Vertical bars mark the $x' > 0$ limit of the stream–we only show the right-hand side instead of both for clarity, as most gaps are located on the right-hand side of the stream in any case.

ferent distances from the cluster's center. At distances less than 3 kpc from Palomar 5, the tails are skinny, with a typical thickness of less than 100 pc. To cause gaps in these regions, the clusters would have to pass close to the stream, with impact parameters similar to the thickness itself. We note that the thinness of the tails at these distances is probably a direct consequence of the initial parameters we chose for the simulation. For Palomar 5, 5 Gyr years ago, we assumed the same internal parameters (mass and size) as the cluster today. With such parameters, after 5 Gyr of evolution, our system has lost most of its mass, and therefore, the part of the tails closest to the cluster itself, whose density depends mainly on the most recent mass loss (see, for example, Fig. A.3 in Mastrobuono-Battisti, Di Matteo, et al., 2012), is necessarily very thin because the simulated cluster has essentially no more mass to lose. This last point also has a consequence in the gap creation rate, which we derived at the end of Sect. 3.3: with only 70% of the tail ($\sim$ 14 kpc over 20 kpc, excluding the innermost ±3 kpc from the cluster center) suitable for forming gaps, the gap creation rates are about 50% higher than those estimated in the previous section, where values have been derived taking into account the full tail extent. This gap creation rate would still not be high enough to reproduce the number of gaps in Palomar 5's tails, as reported by Carlberg, Grillmair & N. Hetherington (2012). Their study suggested the presence of five gaps with a 99 % detection confidence, leading to a gap creation rate of 0.17 $\mathrm{Gyr}^{-1}\ \mathrm{kpc}^{-1}$. If correct, this rate would be too high to be explained by Galactic globular clusters only.

An additional explanation for the absence of gaps in the inner regions of a stream is given in App. 6.4. Briefly, the eccentricity of an orbit induces tidal shocking at the pericenter passages that cause episodes of increased mass loss where the escaped stars leave with a higher mean velocity and greater velocity dispersion. In essence, streams from progenitors on eccentric orbits are made of two components: a continuous flow of stars plus many packets of stars that burst out from pericenter passages. The gap impact occurs at a single position, creating a gap in each subpopulation. However, the gaps have different drift rates across the groups, and they eventually go out of phase, erasing the impact's signature. The packets of stars disperse with time. However, bursts contribute to more escaped stars as the simulation evolves than the continuous outflow. As a result, at late stages of the simulation, the region nearest to the globular cluster is made of distinct yet overlapping populations. After an impact in this location, the impact site between the groups quickly goes out of phase.

4 Discussion

The simulations presented in this paper suggest that, in the last 5 Gyr of evolution, Palomar 5's stream could have experienced multiple close encounters with other Galactic globular clusters, some of which can create gaps – even a few kiloparsecs wide – in its tails. Currently, the literature debates whether or not a gap exists in the observed portion of Palomar 5 tails. R. A. Ibata, Lewis & N. F. Martin (2016) found no statistically significant gap in Palomar 5 tails, while Erkal, Koposov, et al. (2017), analyzing the same dataset as R. A. Ibata, Lewis & N. F. Martin (2016), suggested the presence of a few dips and gaps in the tails, at angular distances between 2° and 9° from the cluster center (see also Bonaca, Pearson, et al., 2020). While our simulations produced 73 gaps across 50 realizations, only about 22 are beyond the current length of the observed portion of the stream, which means, on average, we obtain at least one gap from a globular cluster within the past 5 Gyr. However, we did not attempt to create mock observations or simulate a full detection process accounting for the challenges of disentangling field stars from stream stars. While such an analysis would be valuable, it is beyond the scope of this study.

Our simulations produce a stream for Palomar 5 that is longer than the currently observed extent. In simulations, stream detections are straightforward because we can use reference runs to clearly separate stream particles from the field and compare against a known "true" structure. In contrast, observational data are inherently more challenging due to magnitude limits, contamination from field stars, and the lack of a ground truth for comparison.

The factors mentioned above could lead one to conclude that the number of gaps identified in this study could represent an upper limit. However, this conclusion is incomplete. Globular clusters lose mass and evaporate over time, leading to an incomplete catalog of perturbers. Moreover, the present-day masses used in our simulations are likely lower than the historical masses of these clusters. For example, Pearson, Bonaca, et al. (2024) conducted a study simulating the dissolution of a realistic globular cluster population to identify how many stellar streams we should expect in the Milky Way and used a mock catalog of globular clusters with masses above $10^4 M_\odot$ totaling about 10,000 clusters. Their setup implies that more perturbers could have been present in the past, potentially increasing the frequency and number of gaps in Palomar 5's stream.

We note that our results seem to be in tension with the conclusions of Banik & Bovy (2019), who presented a numerical study of Palomar 5 tails, orbiting a Milky Way-like potential, where both dark matter subhalos and baryonic sub-structures (Galactic bar, spiral arms, giant molecular clouds, globular clusters) were taken into account to quantify the importance of these latter in density variations in Pal5 streams. While their methods are extremely similar to ours, their analysis diverges significantly. Specifically, Banik & Bovy (2019) focused on examining power spectra, analyzing variations in the one-dimensional stream density in stellar counts along the length of the stream. Upon comparison with our simulations, we observe that the power spectra from our `full` simulations that include globular clusters and the `reference` simulations that do not significantly differ. We suggest that this may be due to the signal from only one or two gaps caused by globular clusters not being sufficient to produce notable differences in the overall power spectrum. Additionally, Banik & Bovy (2019) may not have inspected the profiles for individual gaps, which may be why they did not report them. Further investigations would be needed to confirm this interpretation and thoroughly assess the impact of globular clusters on stream density profiles.

Erkal, Koposov, et al. (2017) also present a study about the impact of globular clusters in producing gaps on the Pal 5 stream. In section 6.3 of their article, Erkal, Koposov, et al. (2017) discuss the fact that globular clusters with masses greater than 10^6 $\mathrm{M}_\odot$ are rare in the Galaxy, especially at distances compatible with the orbit of Pal 5, while – based on previous works – they estimate that subhalos of dark matter of similar mass are at least three times greater in number. This difference leads them to conclude that the gaps they report in the Pal 5 streams are more likely to be induced by dark matter subhalos than by globular clusters.

However, as we show in this paper, even clusters with masses below 10^6 M$\odot$ can produce gaps. The clusters perturbing the Pal 5 stream are clusters with masses up to 10 times lower than those considered by Erkal, Koposov, et al. (2017). It is thus possible that Erkal, Koposov, et al. (2017) have underestimated the impact of globular clusters' close passages on a stream such as Pal 5. It is more difficult, however, to make a comparative analysis between the role of clusters and subhalos at equal stellar mass. Being less dense than globular clusters, subhalos should produce less intense perturbations on streams (for fixed impact parameters and relative velocities). We can derive from Sanders, Bovy, et al. (2016)'s third figure that a more concentrated system delivers a higher velocity kick but over a shorter distance, while a more spread out system will affect more stars yet perturb them less. A systematic comparative analysis to quantify the role of clusters and subhalos in producing gaps and perturbations in stellar streams still needs to be done.

The impact of globular clusters' close interactions with stellar streams has also been the object of another recent paper by Doke & Hattori (2022), who concluded that the chance for GD-1 gaps, which have been reported in several works (see, for example, Bonaca, Hogg, et al., 2019; T. J. L. de Boer et al., 2018; T. de Boer et al., 2020) to be produced by globular clusters is very low. This result is not necessarily in contradiction with ours since GD-1 has a pericenter which is almost twice that of Palomar 5 (see, for example Malhan & R. A. Ibata, 2019). As discussed in Sect. 3.3, the number, N, of close encounters that lead to gap creation is anti-correlated with the distance r to the Galactic center. If we naively use the same radial dependence of gaps from Palomar 5 for GD-1 by swapping a pericenter from 6 kpc to 16 kpc, we would reduce the number of gap-favorable impacts by more than a factor of 2. Moreover, we note that Doke & Hattori (2022) pre-selects the globular clusters that could have experienced a close encounter with the GD-1 stream by selecting only clusters that pass at a distance of less than 0.5 kpc from the stream, having a relative velocity smaller than 300 km/s. As shown in our Fig. 5.5, bottom-left panel, in the case of Palomar 5, this choice would lead to excluding most of the encounters favorable to gap creation, which turn out to have relative velocities above 300 km/s, reducing the total to just 19 gaps. It would be interesting to repeat a similar study as the one made by Doke & Hattori (2022) for GD-1, imposing no selection on possible candidate clusters.

As already suggested in previous works which have studied the impact of baryonic structures on Palomar 5 tails (Pearson, Price-Whelan, et al., 2017; Banik & Bovy, 2019), this cluster may lie in a region of the phase-space which is not favorable to distinguish gaps created by dark matter subhalos from gaps created by baryonic structures, such as the Galactic bar and giant molecular clouds. Our study shows that close encounters with globular clusters constitute a further element that confuses a simple interpretation of the observed Palomar 5 stream gaps (if any). Other clusters and streams in the orbital energy range of Palomar 5 may suffer from the same difficulty. Going to lower orbital energies worsens the situation because the effect of the Galactic bar, giant molecular clouds, and interactions with globular clusters becomes even more efficient. In the innermost regions of the Galaxy, where the density of dark matter subhalos is maximal, globular cluster streams are intrinsically more difficult to find, in addition to the fact that the dynamical times in these regions become so small that the stars lost from globular clusters do not redistribute themselves for the most part into thin structures (see S. Ferrone, Di Matteo, et al., 2023). It is thus probably only at larger distances from the Galactic center than those spanned by Palomar 5's orbit that the impact of dark matter subhalos may become dominant, but one should bear in mind that at these distances, the number density of subhalos also decreases. In the future, it will be interesting to apply the type of study conducted here to the whole set of streams to quantify the regime in which they are favorable to the creation of gaps from baryonic structures.

5 Conclusions

Our study demonstrates that globular cluster flybys can produce density gaps in the stellar streams of Palomar 5. The occurrence and characteristics of these gaps depend on the stream's dynamical and structural properties, the perturber's mass, and the impact parameter. While our simulations predict the formation of gaps in Palomar 5's tails, the predicted gaps do not align with the regions of the stream currently observed. Several factors contribute to the absence of simulated gaps in the observed portions of Palomar 5's tails, including the stream's varying thickness, the dispersion of action frequencies near the cluster, and the initial conditions adopted in our simulations.

The broader implications of our findings indicate that globular cluster interactions add a layer of complexity to interpreting stellar stream substructures, complicating efforts to distinguish between baryonic and dark matter-induced gaps. While Palomar 5's phase-space region may not be ideal for isolating the impact of dark matter subhalos, extending this analysis to other streams, particularly those at larger Galactocentric distances, could provide clearer insights.

Future work should involve a systematic comparison of gap creation rates across various Galactic potentials and extend the scope to a wider range of streams and globular clusters. Such a work could disentangle regimes where baryonic and dark matter-induced substructures can dominate gap creation, shedding light on the elusive influence of dark matter subhalos on stellar streams. Additionally, we can continue to add realistic physics to the Galactic environment, such as the merger of the Sagittarius dwarf galaxy, the passages of the Large and Small Magellanic clouds, as well as a time-evolving globular cluster population that compensates for the clusters' mass loss, evaporation, and similarly add members from the current incomplete census.

6 Supplementary Material

6.1 Gap detection

For each of the 50 simulations, we compare the final snapshots between the `reference` and `full` simulations using the tail coordinate system, as shown in Fig. 5.9. We only saved the `reference` simulations at the final time stamps, thus from Eq. 5.3 where N_{ts}=1, leading to a data volume of about one hundred measly megabytes. We inspected these differences by generating 2D density maps of the streams. Additionally, we marginalized over the y'-coordinate to produce 1D density profiles along the x'-axis. We show these comparisons in the results section (see Fig. 5.10).

To construct the 1D density profiles, we binned the data using the $\sqrt{N}$ rule, where N is the number of data points ($N_p = 10^5$). After binning the 1D profiles, we apply a median boxcar smoothing technique. At each bin, we select a number of adjacent data points from both sides, place them in a list, and replace the central value of the bin with the median. We use 10 adjacent points per side, corresponding to a smoothing length of approximately 1 kpc. This procedure reduces high-frequency noise and smooths the profiles. For instance, notice the absence of a high mass peak indicating the center of mass in the bottom panel of Fig. 5.10.

With the smoothed 1D density profiles in hand, we search regions where the `full` simulations are significantly underdense compared to `reference` simulations, surpassing stochastic fluctuations. We first impose a signal-to-noise ratio threshold, $\mathcal{SNR}$. The signal is the log of the counts per bin from the `reference` 1D density profile; we propagate errors assuming a Poisson distribution. We then compute a threshold for the number of counts in the `reference` simulation, N_v, using the transcendental equation:

$$\mathcal{SNR} = \ln(10)\log_{10}(N_v)\sqrt{N_v}. \tag{5.7}$$

By setting $\mathcal{SNR} = 5$, we solve for N using `scipy.optimize.fsolve`, finding that N must be greater than 7. After discarding insignificant bins (i.e., those with counts below the threshold), we computed the log ratio of the counts between the `reference` and `full` simulations:

$$\mathcal{R}_i = \log_{10}\left(\frac{N_{f,i}}{N_{v,i}}\right), \tag{5.8}$$

where $\mathcal{R}_i$ is the log ratio, $N_{f,i}$ are the counts from the `full` simulation, and $N_{v,i}$ are the counts from the `reference` simulation for each bin i. We then analyze the $\mathcal{R}_i$ distribution. If the differences between the density profiles are primarily due to stochastic processes of similar magnitude, this distribution should resemble a Gaussian, as expected from the central limit theorem. Thus, we flag all regions where the density is underdense by more than two standard deviations, which should highlight regions whose underdensity

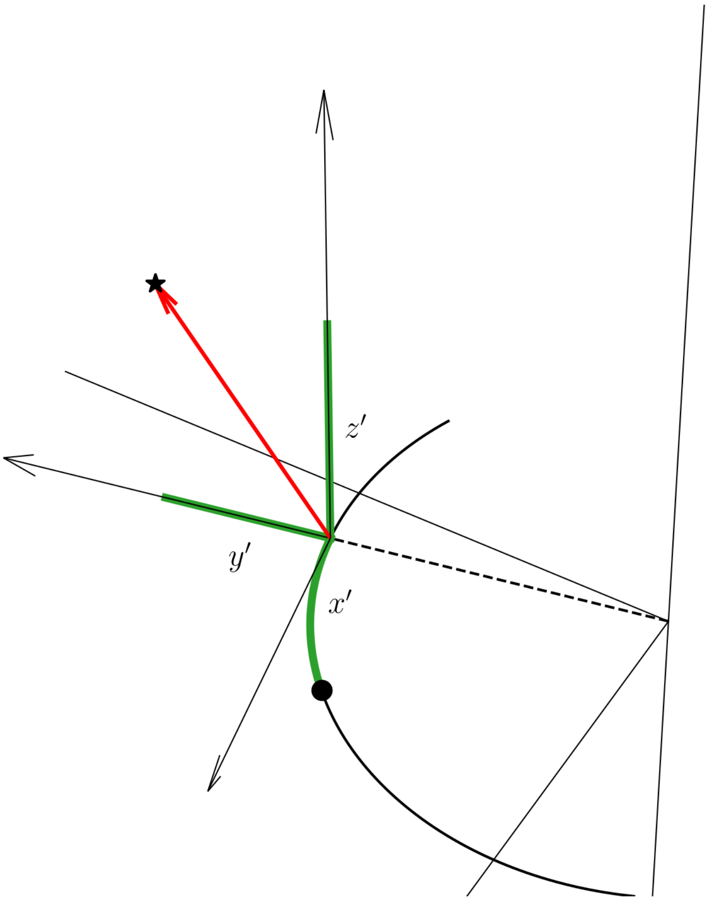

Figure 5.9 – Demonstration of the transformation from Galactocentric coordinates to tail coordinates. The black dot represents the globular cluster, while the thick black line shows a segment of its orbit. The star symbol indicates a star particle. The red vector points from the nearest point on the cluster's orbit to the star particle. The Galactocentric position vector is the y'-axis. The local orbital plane, the cross-product between the orbit's local position and velocity vector, defines the z'-axis. We project the red vector on each of these axes. We measure the x' coordinate as the path length along the orbit from the cluster to the nearest point. Positive x', y', z' indicate that a star is ahead of the cluster, farther from the Galactic center, and above the orbital plane, respectively.

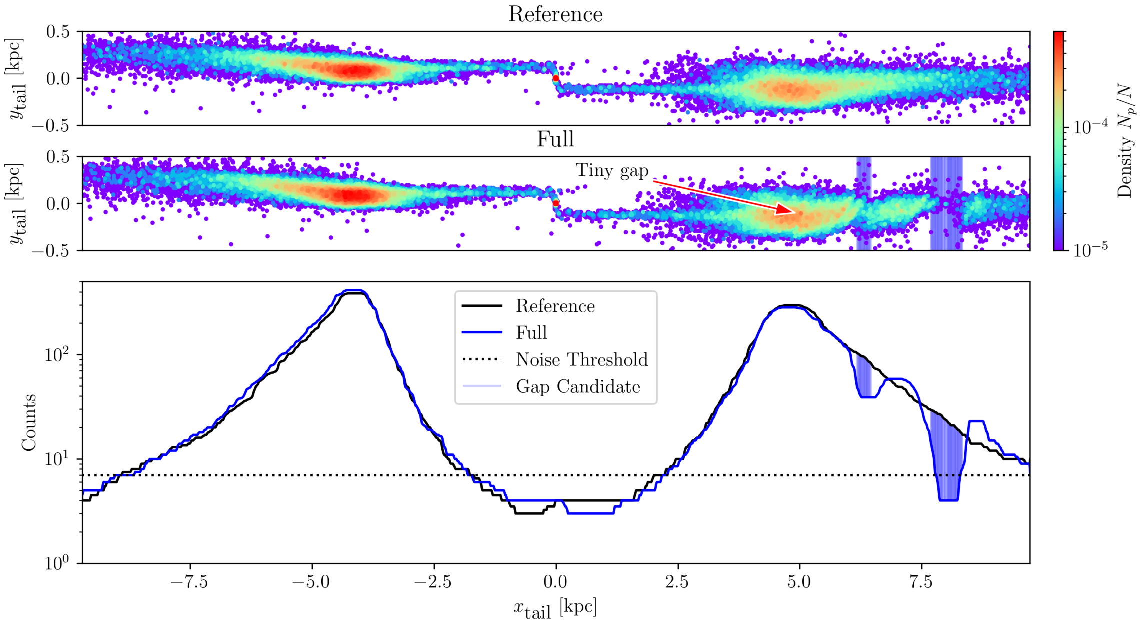

Figure 5.10 – Comparison between the density maps and profiles of the `full` and `reference` simulations is presented. The blue vertical bars highlight the locations where the `full` simulation is less dense than the `reference` simulation by 2-σ. We do not consider bins below the noise threshold when measuring the differences between the two 1D profiles. We smoothed the 1D profiles with a median box-car filter.

is unlikely to be the result of the sum of stochastic processes but rather the passage of another globular cluster.

However, this method has its limitations, especially when detecting smaller gaps. As outlined by Erkal & Belokurov (2015), since gap growth is a dispersion phenomenon, a small gap is not indicative of a weak impact but a recent one. Additionally, since our streams have finite width, some gaps are oblique with respect to the stream axis. In such cases, marginalizing over y' erases the gap's signal, making it impossible to detect in a 1D profile. This limitation is particularly evident in gaps caused by NGC 2808, as discussed in the results. Therefore, this quantitative analysis serves as an aid to visual inspection rather than a complete substitute for it. This method helps with significant, subtle gaps that the eye does not notice in the 2D maps. The online appendix presents these profiles.

6.2 Perturber identification

We aim to identify the origin of the gaps observed at the end of the simulation. To this end, we examine the evolution of stream density over time. Instead of using the x'-coordinate, we introduce τ, which represents time rather than distance. Specifically, τ indicates how long a cluster will take to reach a given point in its orbit or how long ago it passed. This choice of coordinates is advantageous because the growth of the stream is approximately linear in τ. In contrast, in physical space, streams on eccentric orbits expand and contract depending on the orbital phase.

Sanders, Bovy, et al. (2016) extended the analysis of Erkal & Belokurov (2015), demonstrating that action-angle variables provide a useful coordinate system for analyzing stream evolution, as actions are conserved quantities and their associated angles grow linearly over time. Although we became aware of this work only after completing our analysis, we note that τ is a suitable approximation and behaves similarly to the angle variable corresponding to the azimuthal action: $\tau \approx \theta_{\phi,i} - \theta_{\phi,\mathrm{GC}}$.

The core of our analysis is presented in Fig. 5.11. The bottom panel shows the evolution of the stream density over time. To avoid extremely low-density regions at the stream's edges, we applied the same density threshold as from Eq. 6.1 to focus on the more significant areas of the stream. Next, we modeled Palomar 5's orbit as a proxy for its stream and sampled points along the orbit to measure the gravitational force exerted by other globular clusters. The top panel of Fig. 5.11 shows how the total gravitational acceleration on Palomar 5's stream evolves over its length throughout the simulation.

We then used `scipy`'s `ndimage` (Virtanen et al., 2020) package to identify the top five local maxima in the data space of gravitational acceleration $\vec{g}$ as a function of time t and the stream coordinate τ. First, we smooth the data space by taking a 5-point moving average kernel. Secondly, we use a maximum filter to locate coordinates in the (t, τ) data plane that are local maxima to at least 10 adjacent data points. We order these locations

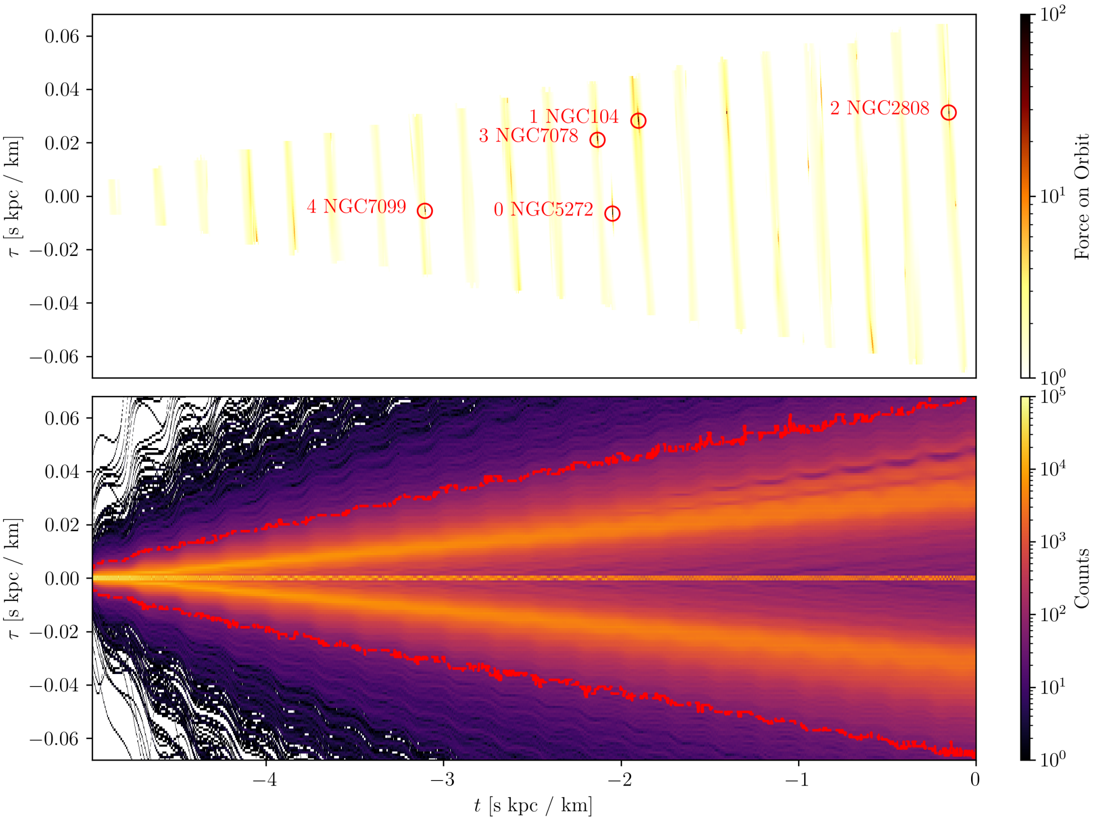

Figure 5.11 – Demonstration of how we determined which globular clusters were responsible for the gaps. The y-axis is τ, a coordinate in units of time that indicates how far ahead or behind it is from a globular cluster. The x-axis is the simulation time, t, where 0 s km kpc^{-1} indicates the present time. The bottom plot showcases the evolution of the stream density over simulation time. We used the density to determine a suitable stream length. Subsequently, we used this length to extract a piece of Palomar 5's orbit. This orbital segment approximates the stream. Then, we compute the gravitational force from all other stream stand-in clusters, shown in the top plot. The gravitational force is measured in acceleration and is given in integration units: km^2 kpc^{-1} s^{-2}. Moments of high acceleration indicate the passage of another cluster. The red circles indicate the top 5 strongest passages, as well as the names of the clusters. The example shown in this plot is the same simulation as Fig. 5.1.

and save the top five strongest interactions. Then, we iterated over the contributions of individual globular clusters to determine which cluster contributed the most to each peak in $\vec{g}$. We label each significant peak with the corresponding globular cluster.

Afterward, we cross-referenced these peaks with the locations of the gaps identified by studying the density maps and profiles from Fig. 5.10. The impact leaves a low-density wake in the (t, τ) plane for large gaps resulting from strong interactions. the bottom panel of Fig. 5.11 shows the wakes corresponding to the impacts of NGC 104 and NGC 7808.

Fig. 5.11 contains some interesting information. Notice the periodic ribbons of force in the (t, τ) plane. The ribbons are due to pericenter passages where Palomar 5 is getting closer to the center of mass of the globular cluster system. Additionally, for the impacts of NGC 104 and NGC 7078, wakes can be observed in the density map. Another important aspect is that the strongest peak in gravitational force does not necessarily create a gap. Notice how NGC 5272, which was labeled with 0 to indicate that it has the greatest local maxima, does not have a gap. The reason for this is manifold. For instance, the force needs to be modulated with time since the change in momentum is the determining factor and not the peak magnitude of the force. Additionally, there is an offset of about 200 pc between the stream and the orbit, as seen when viewing the stream in tail coordinates, so peaks upon the orbit are good proxies for the stream but are not definitive. We found that the top five greatest impacts accounted for all gaps, except for Sampling 014 as shown in Fig. 3 of our extended list of figures, whose gap from NGC 6584 corresponded to the 7th peak.

We compile the results of this analysis into a table. Each row of the table corresponds to a gap; its corresponding suspects are the columns. The culprit is labeled as `TRUE`. For a handful of simulations, to double-check that we make the correct verdict, we recompute the simulations, yet individually adding one globular cluster at a time. As a result, we can confirm that singular gaps arise from the suspected clusters. Fig. 5.2 shows one such example.

6.3 Reconstruction of the impact geometry

As discussed in Sect 3.3, five parameters determine the change in velocity of a given stream particle: M, r_p, b, $W_{\parallel}$, and $W_{\perp}$. In the following, we describe how we estimated these parameters during impacts in our simulations.

To achieve this, we identify the impact of the most significant clusters, as determined in the previous analysis in Sec. 6.2. Then, we refine these estimates to pinpoint the exact location of the impact along the stream and the precise moment it occurred. To do so, we fit a third-order parametric polynomial to the stream using the saved snapshots from our simulations:

$$\vec{s}(\tau) = \begin{cases} x(\tau) = a_0 + a_1\tau + a_2\tau^2 + a_3\tau^3 \\ y(\tau) = b_0 + b_1\tau + b_2\tau^2 + b_3\tau^3 \\ z(\tau) = c_0 + c_1\tau + c_2\tau^2 + c_3\tau^3, \end{cases} \tag{5.9}$$

where x, y, and z represent the parametric line describing the stream in Galactocentric coordinates, τ is the stream coordinate in time as described in the Supplemental Material 6.2, and is used as the independent variable to parameterize the position along the stream. The coefficients a_i, b_i, and c_i are the polynomial coefficients. We found that a second-order polynomial was insufficient to capture the curvature along the full length of the stream, with divergence at the ends of the tails. A third-order polynomial was sufficient and desirable, as the lowest order adequately captures the stream's path over the entire length under consideration.

In this analysis, we only consider one side of the stream. For instance, if the impact candidate was in the leading tail, only the star particles with $\tau > 0$ are used to constrain the stream track. The polynomial coefficients were determined through a minimization method using the Nelder-Mead algorithm from `scipy`'s optimization package.

Since we saved the simulation snapshots at a temporal resolution of 1 Myr–rather than at the integration time-step, which would have generated excessive data, we must interpolate between snapshots to more precisely estimate the impact geometry. We fit the stream's shape with a parametric third-order polynomial at the five time steps surrounding the approximate impact time. This time is a period of 5 Myr, sufficiently covering the interaction time. The interaction time can be estimated as $t \approx \frac{100 \text{ pc}}{300 \frac{\text{km}}{\text{s}}} \approx 0.3$ Myr.

Then, we used a cubic spline interpolation for the coefficients describing the stream's shape, which allows us to describe each polynomial coefficient as a function of time. Consequently, we can parameterize the stream as a function of both simulation time and position along the stream:

$$\vec{s}(t,\tau) = \begin{cases} x(t,\tau) = a_0(t) + a_1(t)\tau + a_2(t)\tau^2 + a_3(t)\tau^3 \\ y(t,\tau) = b_0(t) + b_1(t)\tau + b_2(t)\tau^2 + b_3(t)\tau^3 \\ z(t,\tau) = c_0(t) + c_1(t)\tau + c_2(t)\tau^2 + c_3(t)\tau^3. \end{cases} \tag{5.10}$$

The values of the coefficients as a function of time are obtained through linear interpolation, ensuring that the coefficients at the snapshot times match the values constrained by the simulation data.

Next, we fit the trajectory of the perturber with a second-order polynomial. With equations for both the stream and the perturber as functions of time, we identify the time and location of impact by minimizing a cost function, defined as the distance between the stream and the perturber:

$$b(t,\tau) = \|\vec{s}(t,\tau) - \vec{p}(t)\|\,, \tag{5.11}$$

where $\vec{s}(t,\tau)$ is the Galactocentric position of a point on the stream, $\vec{p}(t)$ is the position of the perturber, and b is the distance between the two. The minimum value of b, denoted as $\min(b)$, represents the impact parameter. We performed the minimization using `scipy`'s optimization package with the `L-BFGS-B` method, which allowed us to place bounds on t and τ, ensuring no extrapolation occurs (Davidon, 1991).

Once this minimization is done, determining the relative velocity becomes straightforward. Since the minimization provides the impact parameter, time of impact, and the corresponding value of τ, we can compute the derivatives of the parametric equations at $t_{\min}$ and $\tau_{\min}$. The parallel and perpendicular components of the perturber's velocity relative to the stream are given by:

$$\begin{aligned} \delta\vec{v} &= \vec{v_p} - \vec{v_s}, \\ w_{\parallel} &= (\delta\vec{v}) \cdot \hat{v_s}, \\ w_{\perp} &= \sqrt{\Delta v^2 - w_{\parallel}^2}, \end{aligned} \tag{5.12}$$

where $\vec{v}_p$ and $\vec{v}_s$ are the velocities of the perturber and the stream, respectively. We compute the strongest five flybys for each of the 50 simulations. Thus, we created a sample of 250 impacts and flagged those that give rise to gaps. We refer the reader to Sect. 3.3 for the presentation and discussion of the results.

6.4 Survival of gaps in streams emerging from more massive globular clusters

In Section 2.2, we emphasized that the conditions chosen to simulate the formation and evolution of streams around Pal 5 are probably unrealistic. By choosing, as we did, the same values for the mass and size of the cluster 5 billion years ago as the cluster has today, we did not take into account the loss of mass and internal evolution of the cluster over time. In particular, the velocity dispersion of the stars in a cluster and the velocity dispersion of the stars leaving the cluster and entering the stream depend on the cluster's mass. It is therefore legitimate to ask whether, using a progenitor with a different mass and/or size, the gaps survive and whether, in particular, gaps formed several billion years ago can still be visible today.

While we anticipate that a specific study on this aspect is in preparation (Ferrone et al., in prep), we would like to preview a few results here, particularly regarding the gap decoherence phenomenon presented in Fig. 5.12. First, Fig. 5.13 shows two streams with the same orbital parameters that were impacted by NGC 7078. The top panel shows a stream originating from a host mass of $10,000\ M_{\odot}$, while in the second panel we increased

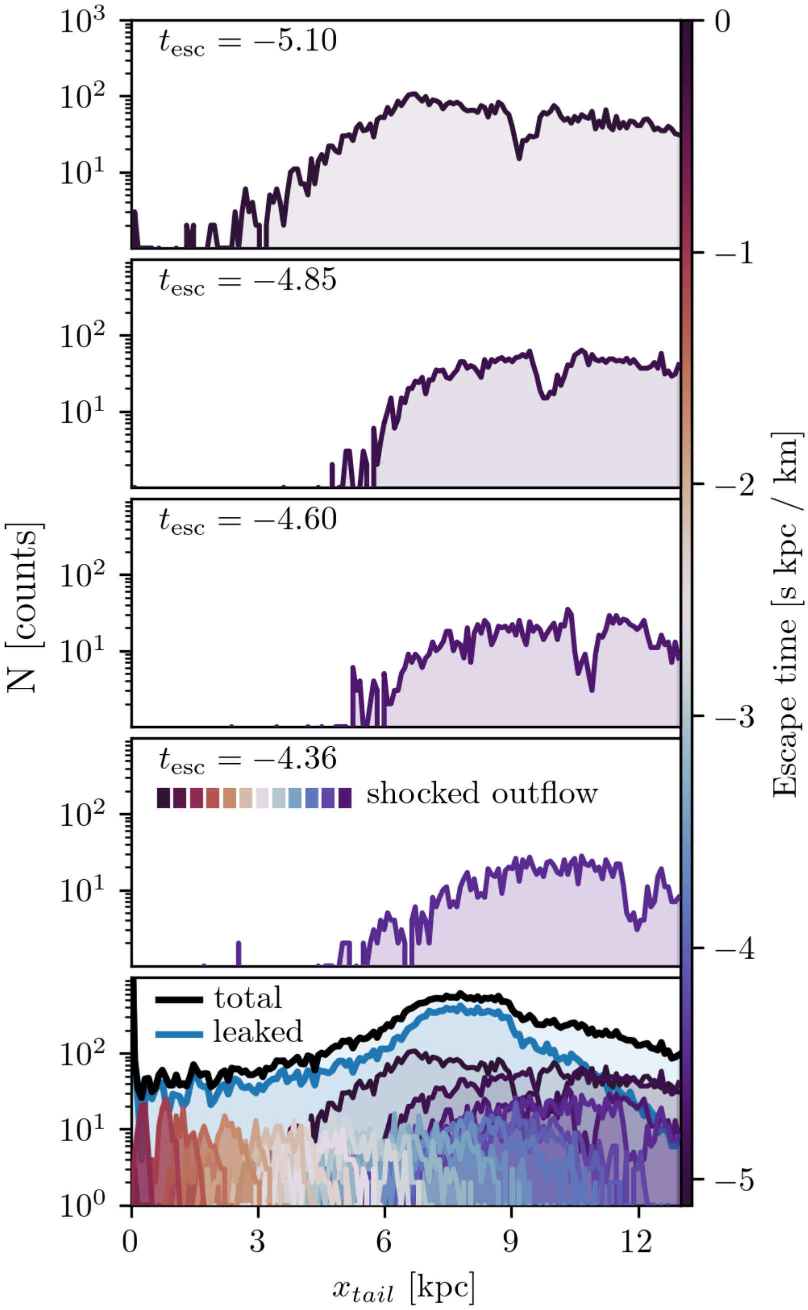

Figure 5.12 – We dissect the one-dimensional density of the stream from the bottom panel of Fig. 5.13. We divide the stars into two categories: the multiple groups that are shocked out at different pericenter passages, or those that leak out of the cluster continuously. The bottom panel shows the leaked population in blue, and each group that was shocked out at each pericenter passage is color-coded by the escape time. The sum of the leaked and shocked outflow gives the total profile density, which is shown in black. The top four panels display the first shocked groups from different pericenter passages, shown individually. Each group shows the gap resulting from the impact of NGC 7078 ∼2.5 Gyr ago, yet they are progressively offset as explained in the text.

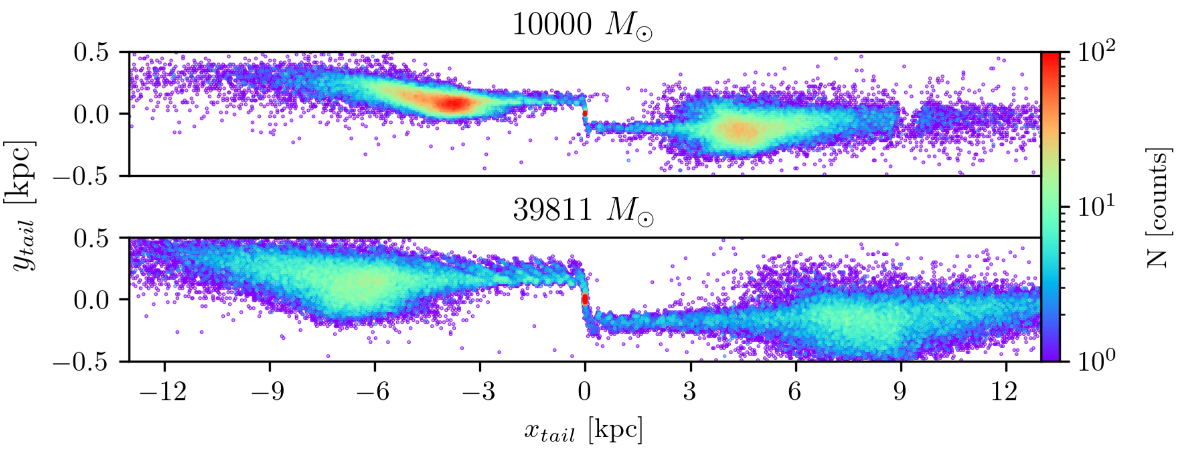

Figure 5.13 – Both simulations use identical orbital conditions for the globular clusters, with a half-mass radius of 27 pc. In the lower panel, Pal 5's mass is increased relative to the upper one. Although both streams are perturbed by NGC 7078 approximately 2.5 Gyr ago, the resulting gap is attenuated in the more massive model.

the mass to $\sim 40,000\ M_\odot$. For simplicity, both clusters have the same half-mass radius of 27 pc. The encounter occurred about two and a half billion years ago with NGC 7078, which has a mass of $5.16 \times 10^5\ M_\odot$. The gap persists for the lighter host, yet is barely visible in the case of the more massive host.

Fig. 5.12 dissects the more massive stream of Fig. 5.13 and explains why the gap does not persist. The bottom panel shows the total density distribution, decomposed into two profiles: stars that are either leaked or shocked out of the cluster. By shocked, we mean stars that are lost during pericenter passages. Tidal forces generally scale with r^{-3}, and thus significantly intensify during pericenter passages (see Fig. 3 of Dehnen et al. (2004) for an illustration of the magnitude of tidal forces along an orbit). A consequence of these passages is that many more stars escape, fleeing with higher mean velocity and velocity dispersion—this can be visualized in the "Christmas tree" illustration in Fig. A.3 of Mastrobuono-Battisti, Di Matteo, et al. (2012). We consider the continuous outflow of stars between pericenter passages to be leaked stars. We identify pericenter passages by computing each local minimum of the cluster's Galactocentric 3D radius using `scipy.signal.find_peaks`. The duration of each shock is given by $t_{\text{shock}} = 2\sqrt{r/|\nabla\Phi|}$, where r is the Galactocentric radius and $|\nabla\Phi|$ is the magnitude of the acceleration from the Galactic potential. Stars within this time range around a given pericenter passage are all given the same color and shown as individual groups in the first through fourth panels of Fig. 5.12.

Chapter 6

Conclusions

In this chapter, I summarize the works undertaken in this thesis and reconnect it to the broader literature with proposing more avenues for investigation.

1 Summary

In Chapter 1, I outlined the importance of stellar streams from globular clusters, highlighting both their intrinsic scientific interest and their role as probes for a wide range of astrophysical questions. These include the chemical enrichment of the Universe, the assembly history of the Milky Way, pathways of black hole formation, and constraints on the global and local properties of the Galactic gravitational field—particularly in relation to the detection of dark matter.

In Chapter 2, I presented the exact equations of motion used to model the formation of stellar streams from globular clusters, formulated as a restricted three-body problem. I then explained how these equations can be interpreted to describe the escape of stars through the Lagrange points under tidal forces, followed by their evolution via phase mixing to form the streams. I summarized the literature on the mechanisms by which perturbations can create gaps. I also discussed the limitations of our models: specifically, that without N-body simulations or analytical prescriptions for internal cluster dynamics, certain questions cannot be addressed.

In Chapter 3, I introduced my simulation code, `tstrippy`, describing its numerical solution of the equations of motion, its performance in terms of accuracy and computation time, and a comparison of two numerical schemes. I explained how the code is written in Fortran and interfaced with Python via `f2py`, and provided a minimal, non-working example illustrating the workflow from the user's perspective.

In Chapter 4, I presented S. Ferrone, Di Matteo, et al. (2023), in which we simulated the expected tidal debris from the entire globular cluster catalog. These simulations have been made publicly available and are now used by the community, including in searches for additional tidal debris beyond some of the clusters in our sample (Kuzma, Ishigaki, et al., 2025; S. Wang et al., 2025).

In Chapter 5, I present S. Ferrone, Montuori, et al. (2025), where we investigated how the Palomar 5 stellar stream responds to the granularity of the Milky Way's gravitational field—specifically, the presence of other globular clusters. We showed that the internal dynamics of globular clusters can strongly influence the morphology of their stellar streams. In particular, gap formation from the fly-by of a massive perturber requires very specific stream conditions: regions close to the progenitor, where the morphology is still dominated by epicyclic overdensities, are unfavorable for gap formation, as different stellar packets respond differently to the perturbation and subsequently drift out of phase. This is a new contribution, as previous studies primarily considered the effects of random motions, such as velocity dispersion.

2 Prospective

One of the main strengths of this work is its focus on Milky Way streams and globular clusters. While idealized toy models are invaluable for testing new ideas and exploring a wide range of theoretical phenomena, our emphasis on the Milky Way allows us to ask more grounded questions: how often should these phenomena occur in our Galaxy, with what significance, and how do they connect directly to what we observe? By anchoring our models to the Milky Way, we can close the loop between theory and data.

The ubiquity and sensitivity of stellar streams make them exceptional probes for inferring the properties of various mass distributions. This opens multiple avenues for future investigation. Some phenomena still require detailed numerical forward modeling—either to understand the underlying physical mechanisms or to obtain robust predictions for their expected occurrence rates. In other cases, where the theoretical picture is mature, we can turn directly to observations and begin the task of inference.

2.1 Dark Matter Subhalos

The prospect of detecting dark matter (DM) on scales smaller than those accessible in the extragalactic context is particularly compelling. One of my current interests consists in performing a study similar to that in Chapter 5, but rather than limiting ourselves to a population of Galactic globular clusters, we will also include a ΛCDM-motivated population of dark matter subhalos. Figure 6.1 shows an example of such a population from a cosmological simulation of a Milky Way analogue. Adams et al. (2024) recently carried out a similar analysis for the GD-1 stream and found that, over the last few billion years, GD-1 has on average one detectable gap from a DM subhalo encounter. Lu et al.

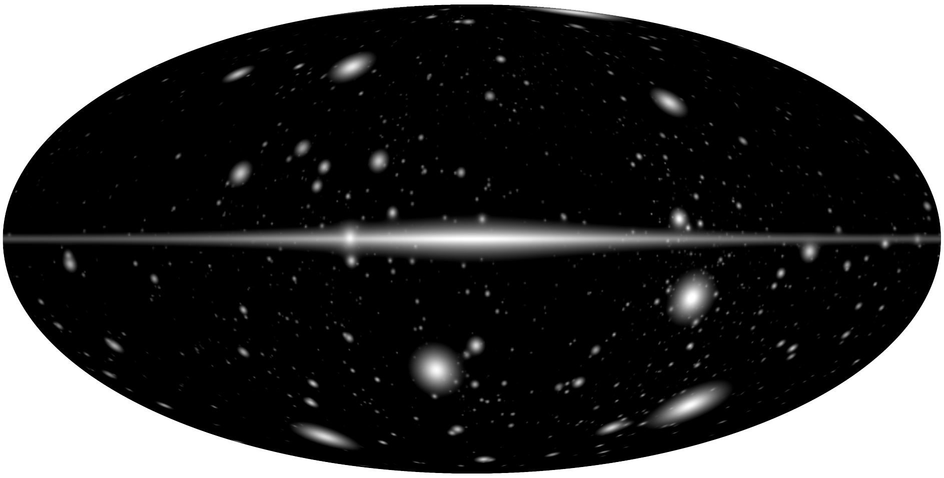

Figure 6.1 – Plausible ΛCDM dark matter subhalo population as “seen” from the Sun. The subhalos are modeled as Plummer spheres, with their light integrated along the line of sight from the Sun and scaled according to the total halo mass. Overlaid is the integrated surface light density profile of the Milky Way’s stellar disk, modeled with a Miyamoto-Nagai potential. DM simulation from Boldrini et al. (in prep).

(2025) adopted this rate of ~ 1 gap per stream to discuss the detectability of gaps in ~ 50 known Milky Way streams.

There is considerable modeling work on gap formation in stellar streams. While we aim to make theoretical predictions for the expected number of gaps, these must be set in the context of a realistic Milky Way potential that includes known time-dependent and non-axisymmetric features. To date, most studies have examined either subhalo encounters in isolation (Carlberg, 2013; Erkal & Belokurov, 2015; Erkal, Belokurov, et al., 2016; Sanders, Bovy, et al., 2016; Adams et al., 2024; Lu et al., 2025) or the effect of the Galactic bar alone (Hattori et al., 2016; Price-Whelan, Sesar, et al., 2016; Pearson, Price-Whelan, et al., 2017; G. F. Thomas, Famaey, Monari, et al., 2023). However, it is known that perturbations from baryonic structures can also generate gap-like signals, potentially mimicking the effects of DM subhalos (R. Ibata, G. Thomas, et al., 2020). To correctly frame the inference problem, the false positive rate must therefore be quantified and calibrated.

Ultimately, the inversion of this problem is a case study in Bayesian hierarchical modeling (Ivezić et al., 2020). Each gap detection is under-determined (Erkal & Belokurov, 2015): even in the absence of measurement uncertainties, a single gap cannot uniquely constrain the perturber’s mass, size, time of impact, and relative velocity simultaneously.

Nevertheless, with a sufficiently large sample of gaps and posterior distributions for each encounter, we can begin to infer statistical properties of the DM subhalo population.

This is a challenging problem. We must account for other astrophysical processes that can erase gap signatures or create false positives, quantify their rates, and embed them in a hierarchical inference framework. The application of such an analysis to the Milky Way will require extremely high-quality data, which may be achievable with future LSST observations and the final Gaia data releases.

As highlighted in Chapter 5, the coherence of a stream is crucial for gap survival, and this must be modeled accurately to avoid overestimating gap counts. In order to obtain proper predictions, we must accurate model stream generation. While full N-body simulations would be the most physically accurate way to model internal cluster dynamics and their mapping into streams, they are computationally prohibitive for the parameter space we must explore. Capturing variations in the Galaxy's potential, cluster internal dynamics, orbital initial conditions, DM subhalo populations, and the properties of multiple streams could require computing tens of thousands of stream realizations. N-body simulations have long been at the avant-garde of computational astrophysics, often driving innovations in both hardware and software. A notable example is the GRAPE (GRAvity PipE) series of special-purpose computers developed for gravitational N-body problems (Fukushige et al., 1991; Makino et al., 1997). For over a decade, GRAPE systems enabled simulations that would have been prohibitively slow on general-purpose hardware, pushing the limits of the field. Eventually, advances in general-purpose graphics processing units (GPUs) offered comparable performance with greater flexibility, leading to the widespread adoption of GPU-accelerated N-body codes (Nitadori & S. J. Aarseth, 2012; L. Wang, Spurzem, S. Aarseth, Nitadori, et al., 2015). Despite these hardware revolutions, the computational cost of the large ensembles of simulations required for our purposes remains high.

Several methods have been developed to avoid the need for full N-body modeling. The "streak-line" method (Küpper, R. R. Lane, et al., 2012) approximates streams as having the same orbital parameters as their progenitor. The action-angle formalism of Eyre & Binney (2011) describes each stream star as having a small offset from the progenitor's Hamiltonian, expressible via a second-order Taylor expansion. Bovy (2014) used this to develop the "particle-spray" method, which improves upon the streak-line model by introducing velocity dispersion into the streams. As noted by Fardal et al. (2015), this is one of the most elegant stream modeling approaches to date.

Fardal et al. (2015) also developed a prescriptive stream-generative model, fitting analytic functions to escape rates measured from N-body simulations. This method operates on the dynamical timescale of the Galaxy rather than the cluster's internal timescale, greatly speeding up computations.

The internal dynamics of globular clusters involve a rich range of processes (Meylan

& D. C. Heggie, 1997). While particle-spray and semi-analytic methods can be extremely efficient, extrapolating beyond the regime covered by their N-body calibrations can be risky. However, machine learning techniques (Tenachi et al., 2023) offer a promising way to emulate N-body simulations without assuming a specific parametric form, providing both flexibility and speed.

In summary, with upcoming improvements in both data quality and modeling techniques, there is strong potential to make significant progress in this field.

2.2 The bulk gravitational field of the MW

At the onset of this thesis, our aim was to investigate large-scale features of the Milky Way such as spiral arms, the Galactic bar, giant molecular clouds, and satellite galaxies and their effect of globular cluster streams. Each of these components represents a potential avenue for further study.

In particular, we are interested in the role of the Galactic bar. Previous works have shown that the bar can induce chaotic orbits, causing stellar streams to “fan out” more than they otherwise would (Price-Whelan, Sesar, et al., 2016; Bonaca, Pearson, et al., 2020). Our preliminary investigation, based on the simulations of S. Ferrone, Di Matteo, et al. (2023), revealed several intriguing effects. As noted by other authors (see Fig. 9 of Bonaca & Price-Whelan, 2025), the bar can generate large underdensities along streams. Our own simulations suggest additional signatures beyond this.

The total mass, orientation, and length of the bar have been constrained in previous studies, though significant uncertainties remain. Most notably, the bar pattern speed (its angular velocity) still has two plausible regimes: slow or fast rotation (Wegg, Gerhard & Portail, 2015; Bland-Hawthorn & Gerhard, 2016; Lucey et al., 2023; Vislosky et al., 2024), not to mention the effect of the the bar deceleration (Haywood, Khoperskov, et al., 2024) on the streams.

We are conducting new experiments to explore whether stellar streams can help break some of these degeneracies. As an example, Fig. 6.2 shows simulations of the Palomar 5 stream for a range of bar pattern speeds. In some cases, the bar splits the stream and creates prominent gaps; in others, it shifts part of the stream off its typical track; in yet others, it suppresses the stream’s growth entirely, keeping debris bound near the progenitor cluster.

The results in Fig. 6.2 raise several questions. There is room to understand the underlying mechanisms theoretically, and to identify whether any Milky Way globular clusters or streams occupy one of these “special” resonances. Such signatures could occur only for a restricted range of bar pattern speeds (or other bar parameters), making them valuable dynamical probes. This is especially important because most existing models of the Milky Way potential, such as that of R. Ibata, Malhan, Tenachi, et al. (2024), are

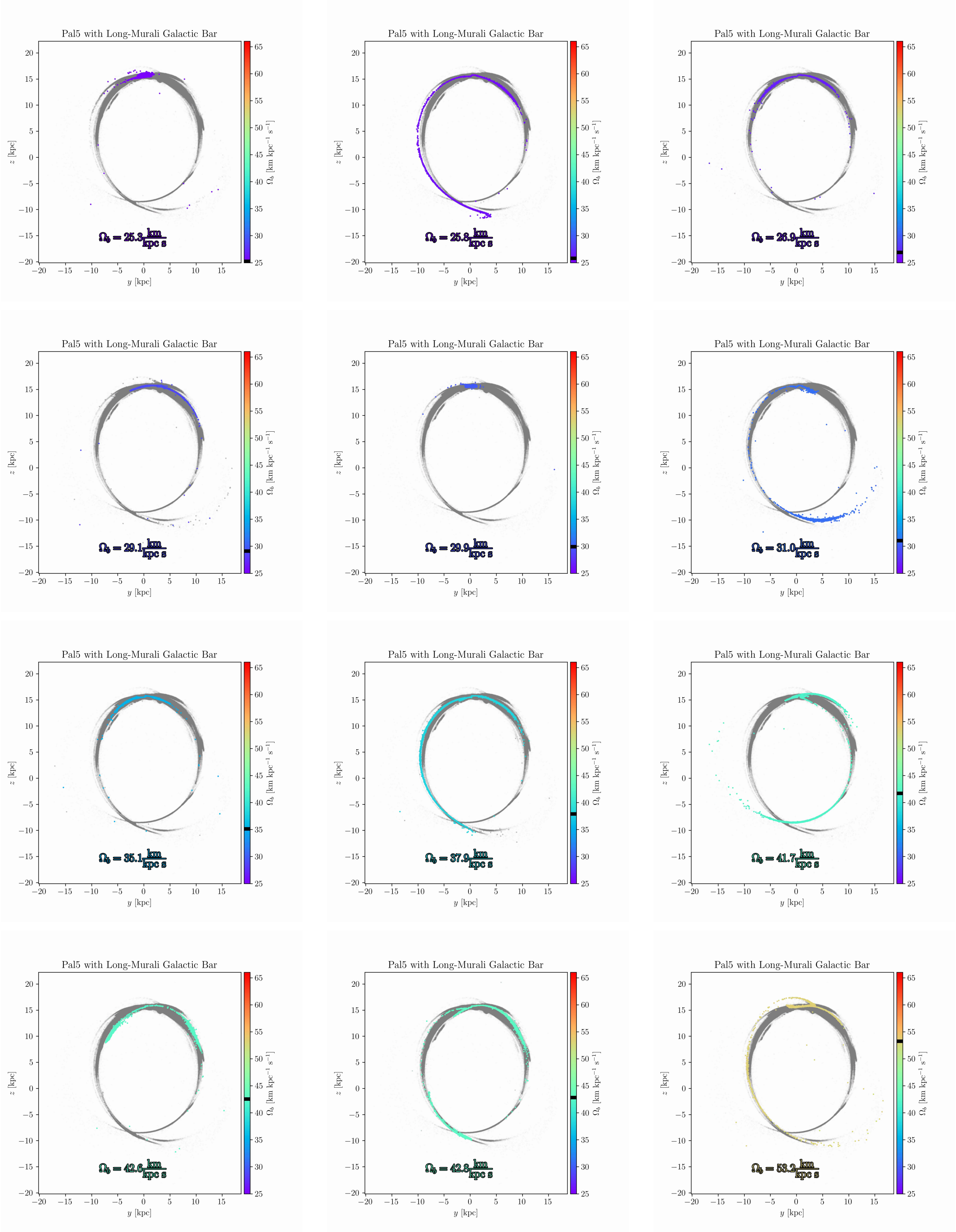

Figure 6.2 – Simulations of the Palomar 5 stream using `tstrippy` with 5000 particles. The Galactic potential follows Pouliasis et al. (2017) with a bar model from Murali & Weinberg (1997a), as described in Chapter 4. Palomar 5's initial conditions are identical in all runs, but the bar pattern speed is varied between 25 and 61 km s^{-1} kpc^{-1} over 150 samples. The animated version of this figure is available in the online thesis (Many thanks to Raif Moibi who helped launch and analyze these simulations)

static and axisymmetric, omitting the bar due to its complexity. If these resonances can be robustly identified in observed streams, they may offer a new route to constraining the Galactic bar and its evolution with time.

2.3 Multiple stellar populations, stellar evolution, and globular cluster formation and internal dynamics

Globular clusters are peculiar objects. In addition to being massive star clusters, they exhibit distinctive chemical abundance patterns compared to typical Galactic field stars (R. G. Gratton et al., 2012; Bastian & Lardo, 2018; R. Gratton et al., 2019). Many globular clusters host multiple stellar populations, often interpreted as different generations of star formation. However, no single formation and evolution scenario fully reproduces the observed abundance patterns.

Some studies have explored dynamical pathways for producing a second generation. For example, Lacchin et al. (2024) investigated a scenario in which a gaseous disk within a globular cluster forms a second generation of stars. As the disk relaxes into a spherical configuration, the cluster loses roughly 95% of its mass, resulting in roughly equal numbers of first- and second-generation stars. In this model, material lost to tidal streams is predominantly first-generation.

While theoretical models link stellar evolution to cluster dynamics, observational studies are beginning to provide kinematic evidence for multiple populations. For instance, Cordoni et al. (2025) measured kinematic differences between two stellar generations in 47 Tuc.

Stars with the peculiar chemistry of globular clusters start to be found in all Galactic components, from the halo and bulge (Martell et al., 2016; Schiavon et al., 2017) to the disk, where - for example - Fernández-Trincado, Zamora, et al. (2017) stars with the characteristic signatures of second-generation cluster members, and Fernández-Trincado, Beers, et al. (2021) identified relatively metal-rich cluster debris (still below solar metallicity). This is further evidence that globular cluster mass loss contributed to the Galactic field populations, in an amount which is still difficult to estimate (see, for example Martell et al., 2016).

Many halo stars share similar chemical patterns with clusters, suggesting that globular clusters may have contributed to the stellar halo (Martell et al., 2016; Schiavon et al., 2017). There are, however, notable exceptions: Fernández-Trincado, Zamora, et al. (2017) reported 11 stars with the characteristic signatures of second-generation cluster members within the Galactic disk, and Fernández-Trincado, Beers, et al. (2021) identified relatively metal-rich cluster debris in the disk (still below solar metallicity).

With improving data quality, it is becoming possible to trace multiple stellar populations beyond the clusters themselves, into their tidal debris (Phillips et al., 2022). For example, Usman et al. (2024) found evidence for multiple populations within a stellar stream not linked to any known cluster. Detailed chemical abundances allowed them to identify the stream as globular cluster debris, even uncovering a star with the distinct chemical fingerprint of a second-generation population.

In the coming years, as chemical abundance measurements become available for more stars in tidal tails, it may be possible to map the spatial distribution of first- and second-generation stars within streams. Their relative kinematics could provide a direct probe of the progenitor cluster's internal dynamical evolution.

The models I have presented in this thesis can be enriched by these observations to provide initial constraints on the mass loss history of these clusters.

Appendices

1 Additional Publications

Galactic Astronomy

reference

(Casamiquela et al., 2022) Casamiquela, L., J. Olivares, Y. Tarricq, S. Ferrone, C. Soubiran, P. Jofre, et al. (2022). “Unravelling UBC 274: A morphological, kinematical, and chemical analysis of a disrupting open cluster.” A&A 664, A31, A31. doi: 10.1051/0004-6361/202243658.

(R. Ibata, Malhan, Tenachi, et al., 2024) Ibata, R., K. Malhan, W. Tenachi, A. Ardern-Arentsen, M. Bellazzini, P. Bianchini, et al. (2024). “Charting the Galactic Acceleration Field. II. A Global Mass Model of the Milky Way from the STREAMFINDER Atlas of Stellar Streams Detected in Gaia DR3.” ApJ 967.2, 89, p. 89. doi: 10.3847/1538-4357/ad382d

The development of `tstrippy`, along with my work on the disruption of globular cluster systems, enabled me to readily apply both the tool and the associated expertise to modeling the disruption of Milky Way open clusters (Casamiquela et al., 2022). Modeling the globular cluster system naturally led to my interest in using stellar streams in the Galactic halo to constrain the Milky Way potential (R. Ibata, Malhan, Tenachi, et al., 2024). In the following, I describe these two projects.

Regarding Casamiquela et al. (2022), Casamiquela reported the discovery of an open cluster in the Galactic disk and analyzed its spatial and chemical properties. They noted that the cluster was not spherically symmetric but instead showed a distorted shape. Using `tstrippy`'s predecessor, GCsTTs, we modeled this cluster and demonstrated that its observed deviation from spherical symmetry can be explained by tidal features. See their Figure 1.

We have already discussed R. Ibata, Malhan, Tenachi, et al. (2024) several times throughout this thesis, as this work reported the detection of many new stellar streams using Gaia DR3, increasing the known total from roughly 60 to about 100. In addition, the paper developed a framework to correct for the known misalignment between a stream and its progenitor orbit (Montuori et al., 2007; Sanders & Binney, 2013). The recovered progenitor orbits were then used in a Markov Chain Monte Carlo (MCMC) analysis to obtain best-fit parameters for the Milky Way's gravitational potential. This work is particularly exciting and opens many avenues for future investigation. For instance, the stream catalog itself is immensely valuable and can serve as a foundation for follow-up observations and analyses. Furthermore, as argued in G. F. Thomas, Famaey, Monari, et al. (2023), these streams could also be used to constrain the Galactic bar through MCMC modeling.

Asteroid science

reference

(S. Ferrone, Delbo, et al., 2023) Ferrone, S., M. Delbo, C. Avdellidou, R. Melikyan, A. Morbidelli, K. Walsh, et al. (2023). "Identification of a 4.3 billion year old asteroid family and planetesimal population in the Inner Main Belt." A&A 676, A5, A5. doi: 10.1051/0004-6361/202245594.

(Bourdelle de Micas et al., 2024) Bourdelle de Micas, J., S. Fornasier, M. Delbo, S. Ferrone, G. van Belle, P. Ochner, et al. (2024). "Compositional characterization of a primordial S-type asteroid family of the inner main belt." A&A 682, A64, A64. doi: 10.1051/0004-6361/202347391

During my Bachelor's thesis, I contributed to NASA's asteroid sample-return mission OSIRIS-REx (Lauretta et al., 2017). From 2018 to 2020, I continued working on the mission as a research assistant, producing two first-author publications (S. M. Ferrone, Clark, Hawley, et al., 2021; S. M. Ferrone, Clark, Kaplan, et al., 2021) and contributing to several others (Barucci et al., 2020; Kaplan et al., 2020; Zou et al., 2021; Deshapriya et al., 2021; J.-Y. Li et al., 2021; Sen et al., 2021; Golish et al., 2022; Clark et al., 2023). This experience, and the opportunity to collaborate with European colleagues, motivated me to pursue further studies abroad at the Paris Observatory. I continued asteroid research as a *stagiaire* between the first and second years of my master's program at the Observatoire de la Côte d'Azur with Professor Marco Delbo, and later for my master's thesis. This work culminated in a publication (S. Ferrone, Delbo, et al., 2023).

In S. Ferrone, Delbo, et al. (2023), we reported the discovery of an ancient asteroid family in the main belt using the "V-shape" technique. Asteroid families are groups of bodies that share similar Keplerian orbital parameters—semi-major axis, eccentricity, and inclination. These bodies once belonged to the same parent body, but a catastrophic collision can produce a violent breakup, ejecting smaller fragments. The ejection velocities cause the fragments to acquire slightly different orbital elements. Over time, however, the Yarkovsky effect, a non-gravitational force, can cause an asteroid's semi-major axis to drift. The drift rate is inversely proportional to the asteroid's diameter, meaning smaller bodies drift more efficiently. Moreover, prograde rotators drift outward, while retrograde rotators drift inward. As a result, when plotting inverse diameter against semi-major axis, the distribution of family members takes the shape of a "V". The opening angle of the V correlates with the family's age, with wider shapes corresponding to older families. This technique has been successfully applied to identify other families (Delbo et al., 2019; Delbo' et al., 2017).

An additional outcome of our study was that, once known asteroid families are removed from the main belt, the remaining bodies are likely primordial—objects that formed in the proto-planetary disk and were not significantly altered by subsequent collisional evolution. In S. Ferrone, Delbo, et al. (2023), we provided a list of such candidate primordial asteroids. In Bourdelle de Micas et al. (2024), we carried out spectroscopic follow-up observations to characterize the taxonomic classes of the objects within the newly identified family.

List of Publications

Peer-reviewed papers

Pagnini, G., Di Matteo, P., Haywood, M., Bianchini, P., **Ferrone, S.**, & Mastrobuono-Battisti, A.. "*Chemically tagging stars to globular clusters streams: an application to ω Centauri and the Nephele accretion*". Astronomy & Astrophysics. In prep.

Ferrone, S., Montuori, M., Di Matteo, P., Mastrobuono-Battisti, A., Ibata, R., Bianchini, P., Khoperskov, S., Leclerc, N., Hottier, C., Stein, E., Valls-Gabaud, D., Snaith, O. N., & Haywood M.. "*Gaps in stellar streams as a result of globular cluster flybys: The case of Palomar 5*". Astronomy & Astrophysics. Volume 699, July 2025. DOI: 10.1051/0004-6361/202553923

Ibata, R., Malhan, K., Tenachi, W., . . . , **Ferrone, S.**, . . . , & Yuan, Z.. "*Charting the Galactic Acceleration Field. II. A Global Mass Model of the Milky Way from the STREAMFINDER Atlas of Stellar Streams Detected in Gaia DR3*". The Astrophysical Journal, 2024, 967.2: 89. DOI: 10.3847/1538-4357/ad382d

Bourdelle de Micas, J. Fornasier, S., Delbo, M., . . . , **Ferrone, S.**, . . . , & Avdellidou, C.. "*Compositional characterization of a primordial S-type asteroid family of the inner main belt*". Astronomy & Astrophysics, 2024, 682: A64. DOI: 10.1051/0004-6361/202347391

Ferrone, S., Delbo, M., Avdellidou, C., Melikyan, R., Morbidelli, A., Walsh, K., & Deienno, R.. "*Identification of a 4.3 billion year old asteroid family and planetesimal population in the Inner Main Belt*". Astronomy & Astrophysics, 2023, 676: A5.. DOI: 10.1051/0004-6361/202245594

Ferrone, S., Di Matteo, P., Mastrobuono-Battisti, A., Haywood, M., Snaith, O. N., Montuori, M., Khoperskov, S., & Valls-Gabaud, D.. "*The e-TidalGCs project. Modeling the extra-tidal features generated by Galactic globular clusters*". Astronomy & Astrophysics, 2023, 673: A44. DOI: 10.1051/0004-6361/202244141

International conferences

Salvatore Ferrone. "*Modeling Milky Way Stellar Streams*". Istituto di sistemi complessi, Consiglio Nazionale delle Ricerche Workshop 2025. The Science of Complex Systems. 20 years of collaboration with other Institutions. February 6-7, 2025. Sala Marconi, CNR

Sede Centrale - Piazzale A. Moro 7, 00185 Roma.

Salvatore Ferrone. "*Milky Way Stellar Streams for Galactic Archaeology*". Journées Scientifiques Galaxies. Oct 7-9 2024. Lyon, France.

Salvatore Ferrone. "*Gaps in stellar streams as a result of globular cluster flybys*". Phases of Galactic Evolution: Accretion in the Local Group. 26 - 30 August 2024. Strasbourg, France.

Salvatore Ferrone. "*The e-TidalGCs project. Modeling the extra-tidal features generated by Galactic globular clusters*". European Astronomical Society Annual Meeting. 10 - 14 July, 2023. ICE Kraków, Poland.

Salvatore Ferrone. "*Poster: The impact of the Galactic bar on Milky Way Stellar Streams*". Galactic bars: driving and decoding galaxy evolution. 3 - 7 July 2023. Grenada, Spain.

Salvatore Ferrone. "*The e-TidalGCs project. Modeling the extra-tidal features generated by Galactic globular clusters*". Phases of Galactic Evolution as traced by stellar populations and star clusters. 26 - 30 June 2023. Sesto, Italy.

Salvatore Ferrone. "*poster: the e-TidalGCs project. Modeling the extra-tidal features generated by Galactic globular clusters*". European Astronomical Society Annual Meeting. 27 June - 1 July 2022, Valencia Conference Centre, Valencia, Spain.

Bibliography

Aarseth, S. J., D. N. C. Lin & J. C. B. Papaloizou (1988). « On the Collapse and Violent Relaxation of Protoglobular Clusters ». *ApJ* 324, p. 288. DOI: `10.1086/165895` (cit. on p. 4).

Abel, T., G. L. Bryan & M. L. Norman (2002). « The Formation of the First Star in the Universe ». *Science* 295.5552, pp. 93–98. DOI: `10.1126/science.1063991`. arXiv: `astro-ph/0112088 [astro-ph]` (cit. on p. 4).

Adamo, A., P. Zeidler, J. M. D. Kruijssen, M. Chevance, M. Gieles, D. Calzetti, et al. (2020). « Star Clusters Near and Far; Tracing Star Formation Across Cosmic Time ». *Space Sci. Rev.* 216.4, 69, p. 69. DOI: `10.1007/s11214-020-00690-x`. arXiv: `2005.06188 [astro-ph.GA]` (cit. on p. 4).

Adams, D. K., A. Parikh, O. Slone, R. Essig, M. Kaplinghat & A. M. Price-Whelan (2024). « Semi-Analytic Modeling of Dark Matter Subhalo Encounters with Thin Stellar Streams: Statistical Predictions for GD-1-like Streams in CDM ». *arXiv e-prints*, arXiv:2412.13144, arXiv:2412.13144. DOI: `10.48550/arXiv.2412.13144`. arXiv: `2412.13144 [astro-ph.GA]` (cit. on pp. 213, 214).

Allen, C. & M. A. Martos (1986). « A simple, realistic model of the galactic mass distribution for orbitcomputations. » *Rev. Mexicana Astron. Astrofis.* 13, pp. 137–147 (cit. on pp. 23, 46).

Allen, C. & A. Santillan (1991). « An improved model of the galactic mass distribution for orbit computations. » *Rev. Mexicana Astron. Astrofis.* 22, p. 255 (cit. on pp. 21–23, 46, 111, 112).

Amorisco, N. C. (2021). « Cold dark matter subhaloes at arbitrarily low masses ». *arXiv e-prints*, arXiv:2111.01148, arXiv:2111.01148. DOI: `10.48550/arXiv.2111.01148`. arXiv: `2111.01148 [astro-ph.CO]` (cit. on p. 177).

Amorisco, N. C., F. A. Gómez, S. Vegetti & S. D. M. White (2016). « Gaps in globular cluster streams: giant molecular clouds can cause them too ». *MNRAS* 463.1, pp. L17–L21. DOI: `10.1093/mnrasl/slw148`. arXiv: `1606.02715 [astro-ph.GA]` (cit. on pp. 104, 178).

Arca Sedda, M., A. W. H. Kamlah, R. Spurzem, M. Giersz, P. Berczik, S. Rastello, et al. (2024). « The DRAGON-II simulations - I. Evolution of single and binary compact objects in star clusters with up to 1 million stars ». *MNRAS* 528.3, pp. 5119–5139. DOI: `10.1093/mnras/stad3952`. arXiv: `2307.04805 [astro-ph.GA]` (cit. on p. 5).

Arora, A., R. E. Sanderson, N. Panithanpaisal, E. C. Cunningham, A. Wetzel & N. Garavito-Camargo (2022). « On the Stability of Tidal Streams in Action Space ». *ApJ* 939.1, 2, p. 2. DOI: `10.3847/1538-4357/ac93fb`. arXiv: `2207.13481 [astro-ph.GA]` (cit. on p. 19).

Astropy Collaboration, A. M. Price-Whelan, B. M. Sipőcz, H. M. Günther, P. L. Lim, S. M. Crawford, et al. (2018). « The Astropy Project: Building an Open-science Project and Status of the v2.0 Core Package ». *AJ* 156.3, 123, p. 123. DOI: `10.3847/1538-3881/aabc4f`. arXiv: `1801.02634 [astro-ph.IM]` (cit. on p. 108).

Astropy Collaboration, T. P. Robitaille, E. J. Tollerud, P. Greenfield, M. Droettboom, E. Bray, et al. (2013). « Astropy: A community Python package for astronomy ». *A&A* 558, A33, A33. DOI: `10.1051/0004-6361/201322068`. arXiv: `1307.6212 [astro-ph.IM]` (cit. on pp. 74, 108, 180).

Atchley, S., C. Zimmer, J. Lange, D. Bernholdt, V. Melesse Vergara, T. Beck, et al. (2023). « Frontier: exploring exascale ». *Proceedings of the International Conference for High Performance Computing, Networking, Storage and Analysis*, pp. 1–16 (cit. on p. 12).

Baade, W. (1944). « The Resolution of Messier 32, NGC 205, and the Central Region of the Andromeda Nebula. » *ApJ* 100, p. 137. DOI: `10.1086/144650` (cit. on p. 4).

Balbinot, E. & M. Gieles (2018). « The devil is in the tails: the role of globular cluster mass evolution on stream properties ». *MNRAS* 474.2, pp. 2479–2492. DOI: `10.1093/mnras/stx2708`. arXiv: `1702.02543 [astro-ph.GA]` (cit. on pp. 68, 70).

Banik, N. & J. Bovy (2019). « Effects of baryonic and dark matter substructure on the Pal 5 stream ». *MNRAS* 484.2, pp. 2009–2020. DOI: `10.1093/mnras/stz142`. arXiv: `1809.09640 [astro-ph.GA]` (cit. on pp. 105, 178, 184, 199, 200).

Banik, N., J. Bovy, G. Bertone, D. Erkal & T. J. L. de Boer (2021). « Novel constraints on the particle nature of dark matter from stellar streams ». *J. Cosmology Astropart. Phys.* 2021.10, 043, p. 043. DOI: `10.1088/1475-7516/2021/10/043`. arXiv: `1911.02663 [astro-ph.GA]` (cit. on pp. 105, 177).

Barucci, M. A., P. H. Hasselmann, A. Praet, M. Fulchignoni, J. D. P. Deshapriya, S. Fornasier, et al. (2020). « OSIRIS-REx spectral analysis of (101955) Bennu by multivariate statistics ». *A&A* 637, L4, p. L4. DOI: `10.1051/0004-6361/202038144` (cit. on p. 222).

Bastian, N. & C. Lardo (2018). « Multiple Stellar Populations in Globular Clusters ». *ARA&A* 56, pp. 83–136. DOI: `10.1146/annurev-astro-081817-051839`. arXiv: `1712.01286 [astro-ph.SR]` (cit. on pp. 5, 218).

Baumgardt, H. (1998). « The initial distribution and evolution of globular cluster systems ». *A&A* 330, pp. 480–491 (cit. on p. 67).

— (2017). « N -body modelling of globular clusters: masses, mass-to-light ratios and intermediate-mass black holes ». *MNRAS* 464.2, pp. 2174–2202. DOI: `10.1093/mnras/stw2488`. arXiv: `1609.08794 [astro-ph.GA]` (cit. on pp. 26, 117).

Baumgardt, H. & M. Hilker (2018). « A catalogue of masses, structural parameters, and velocity dispersion profiles of 112 Milky Way globular clusters ». *MNRAS* 478.2, pp. 1520–1557. DOI: `10.1093/mnras/sty1057`. arXiv: `1804.08359 [astro-ph.GA]` (cit. on pp. 13, 17, 26, 74, 79, 97, 105, 109, 180).

Baumgardt, H., M. Hilker, A. Sollima & A. Bellini (2019). « Mean proper motions, space orbits, and velocity dispersion profiles of Galactic globular clusters derived from Gaia DR2 data ». *MNRAS* 482.4, pp. 5138–5155. DOI: `10.1093/mnras/sty2997`. arXiv: `1811.01507 [astro-ph.GA]` (cit. on pp. 26, 175, 180).

Baumgardt, H., A. Sollima & M. Hilker (2020). « Absolute V-band magnitudes and mass-to-light ratios of Galactic globular clusters ». *PASA* 37, e046, e046. DOI: `10.1017/pasa.2020.38`. arXiv: `2009.09611 [astro-ph.GA]` (cit. on pp. 26, 180).

Baumgardt, H. & E. Vasiliev (2021). « Accurate distances to Galactic globular clusters through a combination of Gaia EDR3, HST, and literature data ». *MNRAS* 505.4, pp. 5957–5977. DOI: `10.1093/mnras/stab1474`. arXiv: `2105.09526 [astro-ph.GA]` (cit. on pp. 7, 26, 79, 105, 109, 179–181).

Belokurov, V., D. Erkal, N. W. Evans, S. E. Koposov & A. J. Deason (2018). « Co-formation of the disc and the stellar halo ». *MNRAS* 478.1, pp. 611–619. DOI: `10.1093/mnras/sty982`. arXiv: `1802.03414 [astro-ph.GA]` (cit. on p. 108).

Belokurov, V., N. W. Evans, M. J. Irwin, P. C. Hewett & M. I. Wilkinson (2006). « The Discovery of Tidal Tails around the Globular Cluster NGC 5466 ». *ApJ* 637.1, pp. L29–L32. DOI: `10.1086/500362`. arXiv: `astro-ph/0511767 [astro-ph]` (cit. on pp. 104, 140, 176).

Belokurov, V. & A. Kravtsov (2024). « In-situ versus accreted Milky Way globular clusters: a new classification method and implications for cluster formation ». *MNRAS* 528.2, pp. 3198–3216. DOI: `10.1093/mnras/stad3920`. arXiv: `2309.15902 [astro-ph.GA]` (cit. on p. 5).

Bernard, E. J., A. M. N. Ferguson, E. F. Schlafly, M. Abbas, E. F. Bell, N. R. Deacon, et al. (2014). « Serendipitous discovery of a thin stellar stream near the Galactic bulge in the Pan-STARRS1 3π Survey. » *MNRAS* 443, pp. L84–L88. DOI: `10.1093/mnrasl/slu089`. arXiv: `1405.6645 [astro-ph.GA]` (cit. on pp. 176, 178).

Bernard, E. J., A. M. N. Ferguson, E. F. Schlafly, N. F. Martin, H.-W. Rix, E. F. Bell, et al. (2016). ≪ A Synoptic Map of Halo Substructures from the Pan-STARRS1 3π Survey ≫. *MNRAS* 463.2, pp. 1759–1768. DOI: `10.1093/mnras/stw2134`. arXiv: `1607.06088 [astro-ph.GA]` (cit. on p. 176).

Bianchini, P., R. Ibata & B. Famaey (2019). ≪ Exploring the Outskirts of Globular Clusters: The Peculiar Kinematics of NGC 3201 ≫. *ApJ* 887.1, L12, p. L12. DOI: `10.3847/2041-8213/ab58d1`. arXiv: `1912.02195 [astro-ph.GA]` (cit. on pp. 104, 105).

Bianchini, P., G. van de Ven, M. A. Norris, E. Schinnerer & A. L. Varri (2016). ≪ A novel look at energy equipartition in globular clusters ≫. *MNRAS* 458.4, pp. 3644–3654. DOI: `10.1093/mnras/stw552`. arXiv: `1603.00878 [astro-ph.GA]` (cit. on p. 68).

Bienayme, O., A. C. Robin & M. Creze (1987). ≪ The mass density in our galaxy. I. A dynamical model constrained by general star counts ≫. *A&A* 180, pp. 94–110 (cit. on p. 20).

Binney, J. & S. Tremaine (2008). *Galactic Dynamics: Second Edition* (cit. on pp. 12, 30, 67, 191).

Binney, J. & E. Vasiliev (2023). ≪ Self-consistent models of our Galaxy ≫. *MNRAS* 520.2, pp. 1832–1847. DOI: `10.1093/mnras/stad094`. arXiv: `2206.03523 [astro-ph.GA]` (cit. on p. 21).

— (2024). ≪ Chemodynamical models of our Galaxy ≫. *MNRAS* 527.2, pp. 1915–1934. DOI: `10.1093/mnras/stad3312`. arXiv: `2306.11602 [astro-ph.GA]` (cit. on p. 21).

Blaauw, A. (1965). ≪ The Concept of Stellar Populations ≫. *Galactic structure. Edited by Adriaan Blaauw and Maarten Schmidt. Published by the University of Chicago Press.* Ed. by A. Blaauw & M. Schmidt, p. 435 (cit. on p. 4).

Bland-Hawthorn, J. & O. Gerhard (2016). ≪ The Galaxy in Context: Structural, Kinematic, and Integrated Properties ≫. *ARA&A* 54, pp. 529–596. DOI: `10.1146/annurev-astro-081915-023441`. arXiv: `1602.07702 [astro-ph.GA]` (cit. on pp. 19, 112, 113, 116, 216).

Boldrini, P. & E. Vitral (2021). ≪ Absence of obvious tidal tails around the globular cluster NGC 6397 ≫. *MNRAS* 507.2, pp. 1814–1826. DOI: `10.1093/mnras/stab2035`. arXiv: `2104.03635 [astro-ph.GA]` (cit. on p. 104).

Bonaca, A. (2021). ≪ Reconstruction of the dark matter distribution in the Milky Way ≫. *AAS/Division of Dynamical Astronomy Meeting #52*. Vol. 53. AAS/Division of Dynamical Astronomy Meeting, 401.06, p. 401.06 (cit. on p. 105).

Bonaca, A., C. Conroy, D. W. Hogg, P. A. Cargile, N. Caldwell, R. P. Naidu, et al. (2020). ≪ High-resolution Spectroscopy of the GD-1 Stellar Stream Localizes the Perturber near the Orbital Plane of Sagittarius ≫. *ApJ* 892.2, L37, p. L37. DOI: `10.3847/2041-8213/ab800c`. arXiv: `2001.07215 [astro-ph.GA]` (cit. on pp. 9, 104, 177).

Bonaca, A., M. Geha & N. Kallivayalil (2012). ≪ A Cold Milky Way Stellar Stream in the Direction of Triangulum ≫. *ApJ* 760.1, L6, p. L6. DOI: `10.1088/2041-8205/760/1/L6`. arXiv: `1209.5391 [astro-ph.GA]` (cit. on p. 176).

Bonaca, A. & D. W. Hogg (2018). ≪ The Information Content in Cold Stellar Streams ≫. *ApJ* 867.2, 101, p. 101. DOI: `10.3847/1538-4357/aae4da`. arXiv: `1804.06854 [astro-ph.GA]` (cit. on pp. 10, 176).

Bonaca, A., D. W. Hogg, A. M. Price-Whelan & C. Conroy (2019). ≪ The Spur and the Gap in GD-1: Dynamical Evidence for a Dark Substructure in the Milky Way Halo ≫. *ApJ* 880.1, 38, p. 38. DOI: `10.3847/1538-4357/ab2873`. arXiv: `1811.03631 [astro-ph.GA]` (cit. on pp. 9, 105, 177, 200).

Bonaca, A., R. P. Naidu, C. Conroy, N. Caldwell, P. A. Cargile, J. J. Han, et al. (2021). ≪ Orbital Clustering Identifies the Origins of Galactic Stellar Streams ≫. *ApJ* 909.2, L26, p. L26. DOI: `10.3847/2041-8213/abeaa9`. arXiv: `2012.09171 [astro-ph.GA]` (cit. on p. 9).

Bonaca, A., S. Pearson, A. M. Price-Whelan, A. Dey, M. Geha, N. Kallivayalil, et al. (2020). ≪ Variations in the Width, Density, and Direction of the Palomar 5 Tidal Tails ≫. *ApJ* 889.1, 70, p. 70. DOI: `10.3847/1538-4357/ab5afe`. arXiv: `1910.00592 [astro-ph.GA]` (cit. on pp. 142, 177, 198, 216).

Bonaca, A. & A. M. Price-Whelan (2025). ≪ Stellar streams in the Gaia era ≫. *New A Rev.* 100, 101713, p. 101713. DOI: `10.1016/j.newar.2024.101713`. arXiv: `2405.19410 [astro-ph.GA]` (cit. on pp. 9, 176, 216).

Bond, H. E. (1981). « Where is population III ? » *ApJ* 248, pp. 606–611. DOI: 10.1086/159186 (cit. on p. 4).

Bourdelle de Micas, J., S. Fornasier, M. Delbo, S. Ferrone, G. van Belle, P. Ochner, et al. (2024). « Compositional characterization of a primordial S-type asteroid family of the inner main belt ». *A&A* 682, A64, A64. DOI: 10.1051/0004-6361/202347391 (cit. on pp. 221, 222).

Bovy, J. (2014). « Dynamical Modeling of Tidal Streams ». *ApJ* 795.1, 95, p. 95. DOI: 10.1088/0004-637X/795/1/95. arXiv: 1401.2985 [astro-ph.GA] (cit. on pp. 104, 184, 215).

— (2015). « galpy: A python Library for Galactic Dynamics ». *ApJS* 216.2, 29, p. 29. DOI: 10.1088/0067-0049/216/2/29. arXiv: 1412.3451 [astro-ph.GA] (cit. on pp. 21–24, 27, 71, 73, 180).

Bovy, J. (2016). « Detecting the Disruption of Dark-Matter Halos with Stellar Streams ». *Phys. Rev. Lett.* 116.12, 121301, p. 121301. DOI: 10.1103/PhysRevLett.116.121301. arXiv: 1512.00452 [astro-ph.GA] (cit. on p. 34).

— (2025a). *Dynamics and Astrophysics of Galaxies.* Princeton, NJ: Princeton University Press (cit. on pp. 13, 14, 30, 34, 75).

— (2025b). *Python Packaging User Guide.* https://pythonpackaging.info/ (cit. on p. 96).

Bovy, J., A. Bahmanyar, T. K. Fritz & N. Kallivayalil (2016). « The Shape of the Inner Milky Way Halo from Observations of the Pal 5 and GD–1 Stellar Streams ». *ApJ* 833.1, 31, p. 31. DOI: 10.3847/1538-4357/833/1/31. arXiv: 1609.01298 [astro-ph.GA] (cit. on pp. 6, 22, 176).

Brandt, T. D. (2018). « The Hipparcos-Gaia Catalog of Accelerations ». *ApJS* 239.2, 31, p. 31. DOI: 10.3847/1538-4365/aaec06. arXiv: 1811.07283 [astro-ph.SR] (cit. on p. 22).

— (2021). « The Hipparcos-Gaia Catalog of Accelerations: Gaia EDR3 Edition ». *ApJS* 254.2, 42, p. 42. DOI: 10.3847/1538-4365/abf93c. arXiv: 2105.11662 [astro-ph.GA] (cit. on p. 22).

Breen, P. G. & D. C. Heggie (2013). « Dynamical evolution of black hole subsystems in idealized star clusters ». *MNRAS* 432.4, pp. 2779–2797. DOI: 10.1093/mnras/stt628. arXiv: 1304.3401 [astro-ph.GA] (cit. on p. 5).

Brodie, J. P. & J. Strader (2006). « Extragalactic Globular Clusters and Galaxy Formation ». *ARA&A* 44.1, pp. 193–267. DOI: 10.1146/annurev.astro.44.051905.092441. arXiv: astro-ph/0602601 [astro-ph] (cit. on pp. 4, 5, 9).

Bromm, V. (2013). « Formation of the first stars ». *Reports on Progress in Physics* 76.11, 112901, p. 112901. DOI: 10.1088/0034-4885/76/11/112901. arXiv: 1305.5178 [astro-ph.CO] (cit. on p. 4).

Bromm, V. & R. B. Larson (2004). « The First Stars ». *ARA&A* 42.1, pp. 79–118. DOI: 10.1146/annurev.astro.42.053102.134034. arXiv: astro-ph/0311019 [astro-ph] (cit. on p. 4).

Buckingham, E. (1914). « On Physically Similar Systems; Illustrations of the Use of Dimensional Equations ». *Physical Review* 4.4, pp. 345–376. DOI: 10.1103/PhysRev.4.345 (cit. on p. 72).

Caldwell, N., A. Bonaca, A. M. Price-Whelan, B. Sesar & M. G. Walker (2020). « A Larger Extent for the Ophiuchus Stream ». *AJ* 159.6, 287, p. 287. DOI: 10.3847/1538-3881/ab8cbf. arXiv: 2004.14350 [astro-ph.GA] (cit. on p. 104).

Capuzzo Dolcetta, R., P. Di Matteo & P. Miocchi (2005). « Formation and Evolution of Clumpy Tidal Tails around Globular Clusters ». *AJ* 129.4, pp. 1906–1921. DOI: 10.1086/426006. arXiv: astro-ph/0406313 [astro-ph] (cit. on p. 104).

Carlberg, R. G. (2012). « Dark Matter Sub-halo Counts via Star Stream Crossings ». *ApJ* 748.1, 20, p. 20. DOI: 10.1088/0004-637X/748/1/20. arXiv: 1109.6022 [astro-ph.CO] (cit. on pp. 34, 177, 189).

— (2013). « The Dynamics of Star Stream Gaps ». *ApJ* 775.2, 90, p. 90. DOI: 10.1088/0004-637X/775/2/90. arXiv: 1307.1929 [astro-ph.GA] (cit. on pp. 34, 214).

Carlberg, R. G. & C. J. Grillmair (2013). « Gaps in the GD-1 Star Stream ». *ApJ* 768.2, 171, p. 171. DOI: 10.1088/0004-637X/768/2/171. arXiv: 1303.4342 [astro-ph.CO] (cit. on p. 177).

Carlberg, R. G., C. J. Grillmair & N. Hetherington (2012). « The Pal 5 Star Stream Gaps ». *ApJ* 760.1, 75, p. 75. DOI: `10.1088/0004-637X/760/1/75`. arXiv: `1209.1741 [astro-ph.CO]` (cit. on p. 197).

Carlberg, R. G. (2018). « Globular Clusters in a Cosmological N-body Simulation ». *ApJ* 861.1, 69, p. 69. DOI: `10.3847/1538-4357/aac88a`. arXiv: `1706.01938 [astro-ph.GA]` (cit. on p. 105).

— (2020). « The Density Structure of Simulated Stellar Streams ». *ApJ* 889.2, 107, p. 107. DOI: `10.3847/1538-4357/ab61f0`. arXiv: `1811.10084 [astro-ph.GA]` (cit. on p. 105).

Carlip, S. (2000). « Aberration and the speed of gravity ». *Physics Letters A* 267.2-3, pp. 81–87. DOI: `10.1016/S0375-9601(00)00101-8`. arXiv: `gr-qc/9909087 [gr-qc]` (cit. on p. 15).

Carroll, S. M. (2001). « The Cosmological Constant ». *Living Reviews in Relativity* 4.1, 1, p. 1. DOI: `10.12942/lrr-2001-1`. arXiv: `astro-ph/0004075 [astro-ph]` (cit. on p. 3).

Casamiquela, L., J. Olivares, Y. Tarricq, S. Ferrone, C. Soubiran, P. Jofré, et al. (2022). « Unravelling UBC 274: A morphological, kinematical, and chemical analysis of a disrupting open cluster ». *A&A* 664, A31, A31. DOI: `10.1051/0004-6361/202243658`. arXiv: `2206.03777 [astro-ph.GA]` (cit. on pp. 220, 221).

Chandrasekhar, S. (1943a). « Dynamical Friction. I. General Considerations: the Coefficient of Dynamical Friction. » *ApJ* 97, p. 255. DOI: `10.1086/144517` (cit. on p. 68).

— (1943b). « Dynamical Friction. II. The Rate of Escape of Stars from Clusters and the Evidence for the Operation of Dynamical Friction. » *ApJ* 97, p. 263. DOI: `10.1086/144518` (cit. on p. 68).

— (1943c). « Dynamical Friction. III. a More Exact Theory of the Rate of Escape of Stars from Clusters. » *ApJ* 98, p. 54. DOI: `10.1086/144544` (cit. on p. 68).

Chemin, L., F. Renaud & C. Soubiran (2015). « Incorrect rotation curve of the Milky Way ». *A&A* 578, A14, A14. DOI: `10.1051/0004-6361/201526040`. arXiv: `1504.01507 [astro-ph.GA]` (cit. on p. 111).

Chen, B., C. Stoughton, J. A. Smith, A. Uomoto, J. R. Pier, B. Yanny, et al. (2001). « Stellar Population Studies with the SDSS. I. The Vertical Distribution of Stars in the Milky Way ». *ApJ* 553.1, pp. 184–197. DOI: `10.1086/320647` (cit. on pp. 106, 180).

Chen, Y. & O. Y. Gnedin (2022). « Modeling the kinematics of globular cluster systems ». *MNRAS* 514.4, pp. 4736–4755. DOI: `10.1093/mnras/stac1651`. arXiv: `2203.00599 [astro-ph.GA]` (cit. on p. 56).

— (2023). « Formation of globular clusters in dwarf galaxies of the Local Group ». *MNRAS* 522.4, pp. 5638–5653. DOI: `10.1093/mnras/stad1328`. arXiv: `2301.08218 [astro-ph.GA]` (cit. on p. 56).

Chernoff, D. F. & M. D. Weinberg (1990). « Evolution of Globular Clusters in the Galaxy ». *ApJ* 351, p. 121. DOI: `10.1086/168451` (cit. on p. 67).

Chon, S., K. Omukai & R. Schneider (2021). « Transition of the initial mass function in the metal-poor environments ». *MNRAS* 508.3, pp. 4175–4192. DOI: `10.1093/mnras/stab2497`. arXiv: `2103.04997 [astro-ph.GA]` (cit. on p. 4).

Clark, B. E., A. Sen, X. .-. Zou, D. N. DellaGiustina, S. Sugita, N. Sakatani, et al. (2023). « Overview of the search for signs of space weathering on the low-albedo asteroid (101955) Bennu ». *Icarus* 400, 115563, p. 115563. DOI: `10.1016/j.icarus.2023.115563` (cit. on p. 222).

Combes, F., S. Leon & G. Meylan (1999). « N-body simulations of globular cluster tides ». *A&A* 352, pp. 149–162. DOI: `10.48550/arXiv.astro-ph/9910148`. arXiv: `astro-ph/9910148 [astro-ph]` (cit. on p. 104).

Conroy, C. & D. N. Spergel (2011). « On the Formation of Multiple Stellar Populations in Globular Clusters ». *ApJ* 726.1, 36, p. 36. DOI: `10.1088/0004-637X/726/1/36`. arXiv: `1005.4934 [astro-ph.GA]` (cit. on p. 5).

Corazza, L. C., O. D. Miranda & C. A. Wuensche (2022). « Potential contributions of Pop III and intermediate-mass Pop II stars to cosmic chemical enrichment ». *A&A* 668, A191, A191. DOI: `10.1051/0004-6361/202244334`. arXiv: `2211.15828 [astro-ph.CO]` (cit. on p. 4).

Cordoni, G., L. Casagrande, A. P. Milone, E. Dondoglio, A. Mastrobuono-Battisti, S. Jang, et al. (2025). « Internal dynamics of multiple populations in 28 Galactic globular clusters: a wide-field study with Gaia and the Hubble Space Telescope ». *MNRAS* 537.3, pp. 2342–2361. DOI: `10.1093/mnras/staf102`. arXiv: `2409.02330 [astro-ph.GA]` (cit. on p. 218).

Cyburt, R. H., B. D. Fields, K. A. Olive & T.-H. Yeh (2016). « Big bang nucleosynthesis: Present status ». *Reviews of Modern Physics* 88.1, 015004, p. 015004. DOI: `10.1103/RevModPhys.88.015004`. arXiv: `1505.01076 [astro-ph.CO]` (cit. on p. 3).

D'Ercole, A., E. Vesperini, F. D'Antona, S. L. W. McMillan & S. Recchi (2008). « Formation and dynamical evolution of multiple stellar generations in globular clusters ». *MNRAS* 391.2, pp. 825–843. DOI: `10.1111/j.1365-2966.2008.13915.x`. arXiv: `0809.1438 [astro-ph]` (cit. on p. 5).

Dalton, G., S. Trager, D. C. Abrams, P. Bonifacio, J. A. López Aguerri, K. Middleton, et al. (2014). « Project overview and update on WEAVE: the next generation wide-field spectroscopy facility for the William Herschel Telescope ». *Ground-based and Airborne Instrumentation for Astronomy V*. Ed. by S. K. Ramsay, I. S. McLean & H. Takami. Vol. 9147. Society of Photo-Optical Instrumentation Engineers (SPIE) Conference Series, 91470L, p. 91470L. DOI: `10.1117/12.2055132`. arXiv: `1412.0843 [astro-ph.IM]` (cit. on p. 7).

Davidon, W. C. (1991). « Variable metric method for minimization ». *SIAM Journal on optimization* 1.1, pp. 1–17 (cit. on p. 209).

Davies, M. B., G. Piotto & F. de Angeli (2004). « Blue straggler production in globular clusters ». *MNRAS* 349.1, pp. 129–134. DOI: `10.1111/j.1365-2966.2004.07474.x`. arXiv: `astro-ph/0401502 [astro-ph]` (cit. on p. 5).

de Boer, T., M. Gieles & D. Erkal (2020). « A new view of the GD-1 stream using Gaia DR2 ». *American Astronomical Society Meeting Abstracts #235*. Vol. 235. American Astronomical Society Meeting Abstracts, 336.07, p. 336.07 (cit. on p. 200).

de Boer, T. J. L., V. Belokurov, S. E. Koposov, L. Ferrarese, D. Erkal, P. Côté, et al. (2018). « A deeper look at the GD1 stream: density variations and wiggles ». *MNRAS* 477.2, pp. 1893–1902. DOI: `10.1093/mnras/sty677`. arXiv: `1801.08948 [astro-ph.GA]` (cit. on p. 200).

de Jong, R. S., O. Agertz, A. A. Berbel, J. Aird, D. A. Alexander, A. Amarsi, et al. (2019). « 4MOST: Project overview and information for the First Call for Proposals ». *The Messenger* 175, pp. 3–11. DOI: `10.18727/0722-6691/5117`. arXiv: `1903.02464 [astro-ph.IM]` (cit. on p. 7).

Dehnen, W., M. Odenkirchen, E. K. Grebel & H.-W. Rix (2004). « Modeling the Disruption of the Globular Cluster Palomar 5 by Galactic Tides ». *AJ* 127.5, pp. 2753–2770. DOI: `10.1086/383214`. arXiv: `astro-ph/0401422 [astro-ph]` (cit. on pp. 34, 105, 142, 185, 211).

Delbo, M., C. Avdellidou & A. Morbidelli (2019). « Ancient and primordial collisional families as the main sources of X-type asteroids of the inner main belt ». *A&A* 624, A69, A69. DOI: `10.1051/0004-6361/201834745`. arXiv: `1902.01633 [astro-ph.EP]` (cit. on p. 222).

Delbo', M., K. Walsh, B. Bolin, C. Avdellidou & A. Morbidelli (2017). « Identification of a primordial asteroid family constrains the original planetesimal population ». *Science* 357.6355, pp. 1026–1029. DOI: `10.1126/science.aam6036` (cit. on p. 222).

Deshapriya, J. D. P., M. A. Barucci, E. B. Bierhaus, S. Fornasier, P. H. Hasselmann, F. Merlin, et al. (2021). « Spectral analysis of craters on (101955) Bennu ». *Icarus* 357, 114252, p. 114252. DOI: `10.1016/j.icarus.2020.114252` (cit. on p. 222).

Di Matteo, P., R. Capuzzo Dolcetta & P. Miocchi (2005). « Clumpy Substructures in Globular Cluster Tidal Tails ». *Celestial Mechanics and Dynamical Astronomy* 91.1-2, pp. 59–73. DOI: `10.1007/s10569-005-3221-y` (cit. on p. 104).

Di Matteo, P., A. Gómez, M. Haywood, F. Combes, M. D. Lehnert, M. Ness, et al. (2015). « Why the Milky Way's bulge is not only a bar formed from a cold thin disk ». *A&A* 577, A1, A1. DOI: `10.1051/0004-6361/201424457`. arXiv: `1411.1416 [astro-ph.GA]` (cit. on p. 111).

Di Matteo, P., M. Haywood, M. D. Lehnert, D. Katz, S. Khoperskov, O. N. Snaith, et al. (2019). « The Milky Way has no in-situ halo other than the heated thick disc. Composition of the stellar halo and age-dating the last significant merger with Gaia DR2 and APOGEE ». *A&A* 632, A4, A4. DOI: `10.1051/0004-6361/201834929`. arXiv: `1812.08232 [astro-ph.GA]` (cit. on p. 108).

Doke, Y. & K. Hattori (2022). « Probability of Forming Gaps in the GD-1 Stream by Close Encounters of Globular Clusters ». *ApJ* 941.2, 129, p. 129. DOI: `10.3847/1538-4357/aca090`. arXiv: `2203.15481 [astro-ph.GA]` (cit. on pp. 178, 200).

Erkal, D. & V. Belokurov (2015). « Forensics of subhalo-stream encounters: the three phases of gap growth ». *MNRAS* 450.1, pp. 1136–1149. DOI: `10.1093/mnras/stv655`. arXiv: `1412.6035 [astro-ph.GA]` (cit. on pp. 34, 59–62, 191, 205, 214).

Erkal, D., V. Belokurov, J. Bovy & J. L. Sanders (2016). « The number and size of subhalo-induced gaps in stellar streams ». *MNRAS* 463.1, pp. 102–119. DOI: `10.1093/mnras/stw1957`. arXiv: `1606.04946 [astro-ph.GA]` (cit. on pp. 104, 214).

Erkal, D., S. E. Koposov & V. Belokurov (2017). « A sharper view of Pal 5's tails: discovery of stream perturbations with a novel non-parametric technique ». *MNRAS* 470.1, pp. 60–84. DOI: `10.1093/mnras/stx1208`. arXiv: `1609.01282 [astro-ph.GA]` (cit. on pp. 177, 178, 184, 198, 199).

European Central Bank (2025). *Euro foreign exchange reference rate US dollar: 1 EUR = 1.1726 USD.* Retrieved from ECB website (cit. on p. 12).

Eyre, A. & J. Binney (2011). « The mechanics of tidal streams ». *MNRAS* 413.3, pp. 1852–1874. DOI: `10.1111/j.1365-2966.2011.18270.x`. arXiv: `1011.3672 [astro-ph.GA]` (cit. on p. 215).

Fall, S. M. & Q. Zhang (2001). « Dynamical Evolution of the Mass Function of Globular Star Clusters ». *ApJ* 561.2, pp. 751–765. DOI: `10.1086/323358`. arXiv: `astro-ph/0107298 [astro-ph]` (cit. on p. 103).

Fardal, M. A., S. Huang & M. D. Weinberg (2015). « Generation of mock tidal streams ». *MNRAS* 452.1, pp. 301–319. DOI: `10.1093/mnras/stv1198`. arXiv: `1410.1861 [astro-ph.GA]` (cit. on p. 215).

Fellhauer, M., M. I. Wilkinson & P. Kroupa (2009). « Merging time-scales of stellar subclumps in young star-forming regions ». *MNRAS* 397.2, pp. 954–962. DOI: `10.1111/j.1365-2966.2009.15009.x`. arXiv: `0905.0399 [astro-ph.GA]` (cit. on p. 4).

Fernández-Trincado, J. G., O. Zamora, D. A. García-Hernández, D. Souto, F. Dell'Agli, R. P. Schiavon, et al. (2017). « Atypical Mg-poor Milky Way Field Stars with Globular Cluster Second-generation-like Chemical Patterns ». *ApJ* 846.1, L2, p. L2. DOI: `10.3847/2041-8213/aa8032`. arXiv: `1707.03108 [astro-ph.GA]` (cit. on p. 218).

Fernández-Trincado, J. G., T. C. Beers, A. B. A. Queiroz, C. Chiappini, D. Minniti, B. Barbuy, et al. (2021). « APOGEE-2 Discovery of a Large Population of Relatively High-metallicity Globular Cluster Debris ». *ApJ* 918.2, L37, p. L37. DOI: `10.3847/2041-8213/ac225b`. arXiv: `2109.02669 [astro-ph.GA]` (cit. on p. 218).

Ferrone, S., M. Delbo, C. Avdellidou, R. Melikyan, A. Morbidelli, K. Walsh, et al. (2023). « Identification of a 4.3 billion year old asteroid family and planetesimal population in the Inner Main Belt ». *A&A* 676, A5, A5. DOI: `10.1051/0004-6361/202245594`. arXiv: `2306.07725 [astro-ph.EP]` (cit. on pp. 1, 221, 222).

Ferrone, S. M., B. E. Clark, H. H. Kaplan, J. .-. Rizos, X. .-. Zou, J. .-. Li, et al. (2021). « Visible-near-infrared observations of organics and carbonates on (101955) Bennu: Classification method and search for surface context ». *Icarus* 368, 114579, p. 114579. DOI: `10.1016/j.icarus.2021.114579` (cit. on p. 222).

Ferrone, S., P. Di Matteo, A. Mastrobuono-Battisti, M. Haywood, O. N. Snaith, M. Montuori, et al. (2023). « The e-TidalGCs project. Modeling the extra-tidal features generated by Galactic globular clusters ». *A&A* 673, A44, A44. DOI: `10.1051/0004-6361/202244141`. arXiv: `2301.05166 [astro-ph.GA]` (cit. on pp. 93, 103, 180, 181, 183, 201, 212, 216).

Ferrone, S., M. Montuori, P. Di Matteo, A. Mastrobuono-Battisti, R. Ibata, P. Bianchini, et al. (2025). « Gaps in stellar streams as a result of globular cluster flybys: The case of Palomar 5 ». *A&A* 699, A289, A289. DOI: `10.1051/0004-6361/202553923`. arXiv: `2502.03941 [astro-ph.GA]` (cit. on pp. 1, 93, 213).

Ferrone, S. M., B. E. Clark, C. L. Hawley, J. Joseph, M. C. Nolan, C. Bennett, et al. (2021). « Analysis of Projection Effects in OSIRIS REx Spectral Mapping Methods: Recommended Protocols for Facet Based Mapping ». *Earth and Space Science* 8.3, e00613, e00613. DOI: `10.1029/2019EA000613` (cit. on p. 222).

Folkner, W. M., J. G. Williams, D. H. Boggs, R. S. Park & P. Kuchynka (2014). « The Planetary and Lunar Ephemerides DE430 and DE431 ». *Interplanetary Network Progress Report* 42-196, pp. 1–81 (cit. on p. 40).

Forbes, D. A., J. I. Read, M. Gieles & M. L. M. Collins (2018). « Extending the globular cluster system-halo mass relation to the lowest galaxy masses ». *MNRAS* 481.4, pp. 5592–5605. DOI: `10.1093/mnras/sty2584`. arXiv: `1809.07831 [astro-ph.GA]` (cit. on p. 4).

Forbes, D. A. & R.-S. Remus (2018). « Metallicity gradients in the globular cluster systems of early-type galaxies: in situ and accreted components? » *MNRAS* 479.4, pp. 4760–4769. DOI: `10.1093/mnras/sty1767`. arXiv: `1807.02142 [astro-ph.GA]` (cit. on p. 5).

Forest, E. & R. D. Ruth (1990). « Fourth-order symplectic integration ». *Physica D Nonlinear Phenomena* 43.1, pp. 105–117. DOI: `10.1016/0167-2789(90)90019-L` (cit. on pp. 75, 77).

Freeman, K. C. (1970). « On the Disks of Spiral and S0 Galaxies ». *ApJ* 160, p. 811. DOI: `10.1086/150474` (cit. on p. 23).

Fritz, T. K. & N. Kallivayalil (2015). « The Proper Motion of Palomar 5 ». *ApJ* 811.2, 123, p. 123. DOI: `10.1088/0004-637X/811/2/123`. arXiv: `1508.06647 [astro-ph.GA]` (cit. on p. 142).

Fukushige, T., T. Ito, J. Makino, T. Ebisuzaki, D. Sugimoto & M. Umemura (1991). « GRAPE-1A: Special-Purpose Computer for N-body Simulation with a Tree Code ». *PASJ* 43, pp. 841–858 (cit. on p. 215).

Gaia Collaboration, A. G. A. Brown, A. Vallenari, T. Prusti, J. H. J. de Bruijne, C. Babusiaux, C. A. L. Bailer-Jones, et al. (2018). « Gaia Data Release 2. Summary of the contents and survey properties ». *A&A* 616, A1, A1. DOI: `10.1051/0004-6361/201833051`. arXiv: `1804.09365 [astro-ph.GA]` (cit. on pp. 6, 22, 104).

Gaia Collaboration, A. G. A. Brown, A. Vallenari, T. Prusti, J. H. J. de Bruijne, C. Babusiaux, M. Biermann, et al. (2021a). « Gaia Early Data Release 3. Summary of the contents and survey properties ». *A&A* 649, A1, A1. DOI: `10.1051/0004-6361/202039657`. arXiv: `2012.01533 [astro-ph.GA]` (cit. on pp. 79, 104).

— (2021b). « Gaia Early Data Release 3. Summary of the contents and survey properties (Corrigendum) ». *A&A* 650, C3, p. C3. DOI: `10.1051/0004-6361/202039657e` (cit. on pp. 6, 104).

Gaia Collaboration, A. G. A. Brown, A. Vallenari, T. Prusti, J. H. J. de Bruijne, F. Mignard, et al. (2016). « Gaia Data Release 1. Summary of the astrometric, photometric, and survey properties ». *A&A* 595, A2, A2. DOI: `10.1051/0004-6361/201629512`. arXiv: `1609.04172 [astro-ph.IM]` (cit. on p. 6).

Gaia Collaboration, D. Katz, T. Antoja, M. Romero-Gómez, R. Drimmel, C. Reylé, et al. (2018). « Gaia Data Release 2. Mapping the Milky Way disc kinematics ». *A&A* 616, A11, A11. DOI: `10.1051/0004-6361/201832865`. arXiv: `1804.09380 [astro-ph.GA]` (cit. on p. 19).

Gaia Collaboration, T. Prusti, J. H. J. de Bruijne, A. G. A. Brown, A. Vallenari, C. Babusiaux, et al. (2016). « The Gaia mission ». *A&A* 595, A1, A1. DOI: `10.1051/0004-6361/201629272`. arXiv: `1609.04153 [astro-ph.IM]` (cit. on pp. 6, 104, 176).

Gaia Collaboration, A. Recio-Blanco, G. Kordopatis, P. de Laverny, P. A. Palicio, A. Spagna, et al. (2023). « Gaia Data Release 3. Chemical cartography of the Milky Way ». *A&A* 674, A38, A38. DOI: `10.1051/0004-6361/202243511`. arXiv: `2206.05534 [astro-ph.GA]` (cit. on p. 20).

Gaia Collaboration, A. Vallenari, A. G. A. Brown, T. Prusti, J. H. J. de Bruijne, F. Arenou, et al. (2023). « Gaia Data Release 3. Summary of the content and survey properties ». *A&A* 674, A1, A1. DOI: 10.1051/0004-6361/202243940. arXiv: 2208.00211 [astro-ph.GA] (cit. on pp. 6, 19, 21, 79).

Gallart, C., E. J. Bernard, C. B. Brook, T. Ruiz-Lara, S. Cassisi, V. Hill, et al. (2019). « Uncovering the birth of the Milky Way through accurate stellar ages with Gaia ». *Nature Astronomy* 3, pp. 932–939. DOI: 10.1038/s41550-019-0829-5. arXiv: 1901.02900 [astro-ph.GA] (cit. on p. 108).

Garro, E. R., D. Minniti, B. Alessi, D. Patchick, M. Kronberger, J. Alonso-García, et al. (2022). « Unveiling the nature of 12 new low-luminosity Galactic globular cluster candidates ». *A&A* 659, A155, A155. DOI: 10.1051/0004-6361/202142248. arXiv: 2112.13591 [astro-ph.GA] (cit. on p. 103).

Garro, E. R., D. Minniti, M. Gómez, J. Alonso-García, R. H. Barbá, B. Barbuy, et al. (2020). « VVVX-Gaia discovery of a low luminosity globular cluster in the Milky Way disk ». *A&A* 642, L19, p. L19. DOI: 10.1051/0004-6361/202039233. arXiv: 2010.02113 [astro-ph.GA] (cit. on p. 103).

Garro, E. R., D. Minniti, M. Gómez, J. Alonso-García, T. Palma, L. C. Smith, et al. (2021). « Confirmation and physical characterization of the new bulge globular cluster Patchick 99 from the VVV and Gaia surveys ». *A&A* 649, A86, A86. DOI: 10.1051/0004-6361/202039255. arXiv: 2103.03592 [astro-ph.GA] (cit. on p. 103).

Garro, E. R., D. Minniti, M. Gómez, J. Alonso-García, V. Ripepi, J. G. Fernández-Trincado, et al. (2022). « Inspection of 19 globular cluster candidates in the Galactic bulge with the VVV survey ». *A&A* 658, A120, A120. DOI: 10.1051/0004-6361/202141819. arXiv: 2111.08317 [astro-ph.GA] (cit. on p. 103).

Gieles, M., D. Erkal, F. Antonini, E. Balbinot & J. Peñarrubia (2021). « A supra-massive population of stellar-mass black holes in the globular cluster Palomar 5 ». *Nature Astronomy* 5, pp. 957–966. DOI: 10.1038/s41550-021-01392-2. arXiv: 2102.11348 [astro-ph.GA] (cit. on p. 180).

Giersz, M., N. Leigh, A. Hypki, N. Lützgendorf & A. Askar (2015). « MOCCA code for star cluster simulations - IV. A new scenario for intermediate mass black hole formation in globular clusters ». *MNRAS* 454.3, pp. 3150–3165. DOI: 10.1093/mnras/stv2162. arXiv: 1506.05234 [astro-ph.GA] (cit. on p. 5).

Gilmore, G., S. Randich, C. C. Worley, A. Hourihane, A. Gonneau, G. G. Sacco, et al. (2022). « The Gaia-ESO Public Spectroscopic Survey: Motivation, implementation, GIRAFFE data processing, analysis, and final data products ». *A&A* 666, A120, A120. DOI: 10.1051/0004-6361/202243134. arXiv: 2208.05432 [astro-ph.SR] (cit. on p. 7).

Gilmore, G. & N. Reid (1983). « New light on faint stars - III. Galactic structure towards the South Pole and the Galactic thick disc. » *MNRAS* 202, pp. 1025–1047. DOI: 10.1093/mnras/202.4.1025 (cit. on p. 22).

Giovinazzi, M. R., C. H. Blake, P. Robertson, A. S. J. Lin, A. F. Gupta, S. Mahadevan, et al. (2025). « The NEID Earth Twin Survey. II. Dynamical Masses in Seven High-acceleration Star Systems ». *AJ* 170.1, 52, p. 52. DOI: 10.3847/1538-3881/add922. arXiv: 2505.12563 [astro-ph.EP] (cit. on p. 22).

Girardi, L., M. A. T. Groenewegen, E. Hatziminaoglou & L. da Costa (2005). « Star counts in the Galaxy. Simulating from very deep to very shallow photometric surveys with the TRILEGAL code ». *A&A* 436.3, pp. 895–915. DOI: 10.1051/0004-6361:20042352. arXiv: astro-ph/0504047 [astro-ph] (cit. on p. 20).

Glover, S. (2005). « The Formation Of The First Stars In The Universe ». *Space Sci. Rev.* 117.3-4, pp. 445–508. DOI: 10.1007/s11214-005-5821-y. arXiv: astro-ph/0409737 [astro-ph] (cit. on p. 4).

Gnedin, O. Y. & J. P. Ostriker (1997). « Destruction of the Galactic Globular Cluster System ». *ApJ* 474.1, pp. 223–255. DOI: 10.1086/303441. arXiv: astro-ph/9603042 [astro-ph] (cit. on p. 103).

Golish, D. R., A. A. Simon, D. C. Reuter, S. Ferrone, B. E. Clark, J. .-. Li, et al. (2022). « Cross-Instrument Comparison of MapCam and OVIRS on OSIRIS-REx ». *Space Sci. Rev.* 218.2, 5, p. 5. DOI: 10.1007/s11214-022-00873-8 (cit. on p. 222).

Gómez, A., P. Di Matteo, M. Schultheis, F. Fragkoudi, M. Haywood & F. Combes (2018). « Searching for a kinematic signature of the moderately metal-poor stars in the Milky Way bulge using N-body simulations ». *A&A* 615, A100, A100. DOI: 10.1051/0004-6361/201732568. arXiv: 1803.09626 [astro-ph.GA] (cit. on p. 111).

Gran, F., M. Zoccali, R. Contreras Ramos, E. Valenti, A. Rojas-Arriagada, J. A. Carballo-Bello, et al. (2019). « Globular cluster candidates in the Galactic bulge: Gaia and VVV view of the latest discoveries ». *A&A* 628, A45, A45. DOI: 10.1051/0004-6361/201834986. arXiv: 1904.10872 [astro-ph.GA] (cit. on p. 103).

Gran, F., M. Zoccali, I. Saviane, E. Valenti, A. Rojas-Arriagada, R. Contreras Ramos, et al. (2022). « Hidden in the haystack: low-luminosity globular clusters towards the Milky Way bulge ». *MNRAS* 509.4, pp. 4962–4981. DOI: 10.1093/mnras/stab2463. arXiv: 2108.11922 [astro-ph.GA] (cit. on p. 103).

Gratton, R. G. (1985). « Deep photometry of globular clusters. V. Age derivations and their implications for galactic evolution. » *A&A* 147, pp. 169–177 (cit. on p. 4).

Gratton, R., A. Bragaglia, E. Carretta, V. D'Orazi, S. Lucatello & A. Sollima (2019). « What is a globular cluster? An observational perspective ». *A&A Rev.* 27.1, 8, p. 8. DOI: 10.1007/s00159-019-0119-3. arXiv: 1911.02835 [astro-ph.SR] (cit. on p. 218).

Gratton, R. G., E. Carretta & A. Bragaglia (2012). « Multiple populations in globular clusters. Lessons learned from the Milky Way globular clusters ». *A&A Rev.* 20, 50, p. 50. DOI: 10.1007/s00159-012-0050-3. arXiv: 1201.6526 [astro-ph.SR] (cit. on pp. 5, 218).

GRAVITY Collaboration, R. Abuter, A. Amorim, N. Anugu, M. Bauböck, M. Benisty, et al. (2018). « Detection of the gravitational redshift in the orbit of the star S2 near the Galactic centre massive black hole ». *A&A* 615, L15, p. L15. DOI: 10.1051/0004-6361/201833718. arXiv: 1807.09409 [astro-ph.GA] (cit. on p. 107).

Green, A. M., S. Hofmann & D. J. Schwarz (2005). « The first WIMPy halos ». *J. Cosmology Astropart. Phys.* 2005.8, 003, p. 003. DOI: 10.1088/1475-7516/2005/08/003. arXiv: astro-ph/0503387 [astro-ph] (cit. on p. 177).

Greene, J. E., J. Strader & L. C. Ho (2020). « Intermediate-Mass Black Holes ». *ARA&A* 58, pp. 257–312. DOI: 10.1146/annurev-astro-032620-021835. arXiv: 1911.09678 [astro-ph.GA] (cit. on p. 5).

Grillmair, C. J. (1998). « Probing the Galactic Halo with Globular Cluster Tidal Tails ». *Galactic Halos.* Ed. by D. Zaritsky. Vol. 136. Astronomical Society of the Pacific Conference Series, p. 45. DOI: 10.48550/arXiv.astro-ph/9711223. arXiv: astro-ph/9711223 [astro-ph] (cit. on p. 104).

— (2009). « Four New Stellar Debris Streams in the Galactic Halo ». *ApJ* 693.2, pp. 1118–1127. DOI: 10.1088/0004-637X/693/2/1118. arXiv: 0811.3965 [astro-ph] (cit. on p. 176).

— (2014). « Two New Halo Debris Streams in the Sloan Digital Sky Survey ». *ApJ* 790.1, L10, p. L10. DOI: 10.1088/2041-8205/790/1/L10. arXiv: 1407.0397 [astro-ph.GA] (cit. on p. 176).

Grillmair, C. J. & O. Dionatos (2006a). « A 22° Tidal Tail for Palomar 5 ». *ApJ* 641.1, pp. L37–L39. DOI: 10.1086/503744. arXiv: astro-ph/0603062 [astro-ph] (cit. on pp. 103, 142, 175).

— (2006b). « Detection of a 63° Cold Stellar Stream in the Sloan Digital Sky Survey ». *ApJ* 643.1, pp. L17–L20. DOI: 10.1086/505111. arXiv: astro-ph/0604332 [astro-ph] (cit. on pp. 104, 176).

Grillmair, C. J. & R. Johnson (2006). « The Detection of a 45° Tidal Stream Associated with the Globular Cluster NGC 5466 ». *ApJ* 639.1, pp. L17–L20. DOI: 10.1086/501439. arXiv: astro-ph/0602602 [astro-ph] (cit. on pp. 140, 141).

Grillmair, C. J. (2017). « At a Crossroads: Stellar Streams in the South Galactic Cap ». *ApJ* 847.2, 119, p. 119. DOI: 10.3847/1538-4357/aa8872. arXiv: 1708.09029 [astro-ph.GA] (cit. on p. 176).

— (2022). « The Extended Tidal Tails of NGC 7089 (M2) ». *ApJ* 929.1, 89, p. 89. DOI: 10.3847/1538-4357/ac5bd7. arXiv: 2203.04425 [astro-ph.GA] (cit. on p. 106).

Grillmair, C. J., R. Cutri, F. J. Masci, T. Conrow, B. Sesar, P. R. M. Eisenhardt, et al. (2013). « Detection of a Nearby Halo Debris Stream in the WISE and 2MASS Surveys ». *ApJ* 769.2, L23, p. L23. DOI: `10.1088/2041-8205/769/2/L23`. arXiv: `1304.1170 [astro-ph.GA]` (cit. on p. 176).

Grillmair, C. J., K. C. Freeman, M. Irwin & P. J. Quinn (1995). « Globular Clusters with Tidal Tails: Deep Two-Color Star Counts ». *AJ* 109, p. 2553. DOI: `10.1086/117470`. arXiv: `astro-ph/9502039 [astro-ph]` (cit. on pp. 103, 175).

Grillmair, C. J., L. Hetherington, R. G. Carlberg & B. Willman (2015). « An Orphan No Longer? Detection of the Southern Orphan Stream and a Candidate Progenitor ». *ApJ* 812.2, L26, p. L26. DOI: `10.1088/2041-8205/812/2/L26`. arXiv: `1509.07503 [astro-ph.GA]` (cit. on p. 176).

Grondin, S. M., J. J. Webb, J. M. M. Lane, J. S. Speagle & N. W. C. Leigh (2024). « A catalogue of Galactic GEMS: Globular cluster Extra-tidal Mock Stars ». *MNRAS* 528.3, pp. 5189–5211. DOI: `10.1093/mnras/stae203`. arXiv: `2310.09331 [astro-ph.GA]` (cit. on pp. 68, 69, 181).

Grondin, S. M., J. J. Webb, N. W. C. Leigh, J. S. Speagle & R. J. Khalifeh (2023). « Searching for the extra-tidal stars of globular clusters using high-dimensional analysis and a core particle spray code ». *MNRAS* 518.3, pp. 4249–4264. DOI: `10.1093/mnras/stac3367`. arXiv: `2207.11263 [astro-ph.SR]` (cit. on p. 68).

Hansen, T. T., A. H. Riley, L. E. Strigari, J. L. Marshall, P. S. Ferguson, J. Zepeda, et al. (2020). « A Chemo-dynamical Link between the Gjöll Stream and NGC 3201 ». *ApJ* 901.1, 23, p. 23. DOI: `10.3847/1538-4357/ababa5`. arXiv: `2007.12165 [astro-ph.SR]` (cit. on p. 135).

Harris, C. R., K. J. Millman, S. J. van der Walt, R. Gommers, P. Virtanen, D. Cournapeau, et al. (2020). « Array programming with NumPy ». *Nature* 585.7825, pp. 357–362. DOI: `10.1038/s41586-020-2649-2`. arXiv: `2006.10256 [cs.MS]` (cit. on p. 95).

Harris, W. E., G. L. Harris & M. J. Hudson (2015). « Dark Matter Halos in Galaxies and Globular Cluster Populations. II. Metallicity and Morphology ». *ApJ* 806.1, 36, p. 36. DOI: `10.1088/0004-637X/806/1/36`. arXiv: `1504.03199 [astro-ph.GA]` (cit. on p. 5).

Harris, W. E., G. L. H. Harris & M. Alessi (2013). « A Catalog of Globular Cluster Systems: What Determines the Size of a Galaxy's Globular Cluster Population? » *ApJ* 772.2, 82, p. 82. DOI: `10.1088/0004-637X/772/2/82`. arXiv: `1306.2247 [astro-ph.GA]` (cit. on p. 4).

Hattori, K., D. Erkal & J. L. Sanders (2016). « Shepherding tidal debris with the Galactic bar: the Ophiuchus stream ». *MNRAS* 460.1, pp. 497–512. DOI: `10.1093/mnras/stw1006`. arXiv: `1512.04536 [astro-ph.GA]` (cit. on pp. 178, 214).

Haywood, M., P. Di Matteo, M. D. Lehnert, O. Snaith, S. Khoperskov & A. Gómez (2018). « In Disguise or Out of Reach: First Clues about In Situ and Accreted Stars in the Stellar Halo of the Milky Way from Gaia DR2 ». *ApJ* 863.2, 113, p. 113. DOI: `10.3847/1538-4357/aad235`. arXiv: `1805.02617 [astro-ph.GA]` (cit. on p. 171).

Haywood, M., P. Di Matteo, M. D. Lehnert, D. Katz & A. Gómez (2013). « The age structure of stellar populations in the solar vicinity. Clues of a two-phase formation history of the Milky Way disk ». *A&A* 560, A109, A109. DOI: `10.1051/0004-6361/201321397`. arXiv: `1305.4663 [astro-ph.GA]` (cit. on p. 22).

Haywood, M., S. Khoperskov, V. Cerqui, P. Di Matteo, D. Katz & O. Snaith (2024). « Timing the Milky Way bar formation and the accompanying radial migration episode ». *A&A* 690, A147, A147. DOI: `10.1051/0004-6361/202348767`. arXiv: `2403.08963 [astro-ph.GA]` (cit. on p. 216).

Heggie, D. & P. Hut (2003). *The Gravitational Million-Body Problem: A Multidisciplinary Approach to Star Cluster Dynamics* (cit. on pp. 67, 109).

Helmi, A. (2004). « Is the dark halo of our Galaxy spherical? » *MNRAS* 351.2, pp. 643–648. DOI: `10.1111/j.1365-2966.2004.07812.x`. arXiv: `astro-ph/0309579 [astro-ph]` (cit. on p. 176).

Helmi, A., C. Babusiaux, H. H. Koppelman, D. Massari, J. Veljanoski & A. G. A. Brown (2018). « The merger that led to the formation of the Milky Way's inner stellar halo and thick disk ». *Nature* 563.7729, pp. 85–88. DOI: `10.1038/s41586-018-0625-x`. arXiv: `1806.06038 [astro-ph.GA]` (cit. on p. 108).

Helmi, A. & H. H. Koppelman (2016). « The Time Evolution of Gaps in Tidal Streams ». *ApJ* 828.1, L10, p. L10. DOI: `10.3847/2041-8205/828/1/L10`. arXiv: `1606.08782 [astro-ph.GA]` (cit. on p. 177).

Hermans, J., N. Banik, C. Weniger, G. Bertone & G. Louppe (2021). « Towards constraining warm dark matter with stellar streams through neural simulation-based inference ». *MNRAS* 507.2, pp. 1999–2011. DOI: `10.1093/mnras/stab2181`. arXiv: `2011.14923 [astro-ph.GA]` (cit. on p. 177).

Hilmi, T., D. Erkal, S. E. Koposov, T. S. Li, S. Lilleengen, A. P. Ji, et al. (2024). « Inferring dark matter subhalo properties from simulated subhalo-stream encounters ». *arXiv e-prints*, arXiv:2404.02953, arXiv:2404.02953. DOI: `10.48550/arXiv.2404.02953`. arXiv: `2404.02953 [astro-ph.GA]` (cit. on p. 177).

Hoyle, F. (1959). « The ages of Type I and Type II subgiants ». *MNRAS* 119, p. 124. DOI: `10.1093/mnras/119.2.124` (cit. on p. 4).

Hubble, E. P. (1926). « Extragalactic nebulae. » *ApJ* 64, pp. 321–369. DOI: `10.1086/143018` (cit. on p. 18).

Hübner, P., A. Hu, I. Peng & S. Markidis (2025). « Apple vs. Oranges: Evaluating the Apple Silicon M-Series SoCs for HPC Performance and Efficiency ». *arXiv preprint arXiv:2502.05317* (cit. on p. 12).

Hunt, J. A. S. & E. Vasiliev (2025). « Milky Way dynamics in light of Gaia ». *New A Rev.* 100, 101721, p. 101721. DOI: `10.1016/j.newar.2024.101721`. arXiv: `2501.04075 [astro-ph.GA]` (cit. on p. 16).

Ibata, R. A., G. Gilmore & M. J. Irwin (1994). « A dwarf satellite galaxy in Sagittarius ». *Nature* 370.6486, pp. 194–196. DOI: `10.1038/370194a0` (cit. on p. 175).

Ibata, R. A., G. F. Lewis, M. J. Irwin & T. Quinn (2002). « Uncovering cold dark matter halo substructure with tidal streams ». *MNRAS* 332.4, pp. 915–920. DOI: `10.1046/j.1365-8711.2002.05358.x`. arXiv: `astro-ph/0110690 [astro-ph]` (cit. on pp. 6, 104, 177).

Ibata, R., K. Malhan, N. Martin, D. Aubert, B. Famaey, P. Bianchini, et al. (2021). « Charting the Galactic Acceleration Field. I. A Search for Stellar Streams with Gaia DR2 and EDR3 with Follow-up from ESPaDOnS and UVES ». *ApJ* 914.2, 123, p. 123. DOI: `10.3847/1538-4357/abfcc2`. arXiv: `2012.05245 [astro-ph.GA]` (cit. on pp. 7, 8, 56, 104, 135, 137–143, 196, 197).

Ibata, R., K. Malhan, W. Tenachi, A. Ardern-Arentsen, M. Bellazzini, P. Bianchini, et al. (2024). « Charting the Galactic Acceleration Field. II. A Global Mass Model of the Milky Way from the STREAMFINDER Atlas of Stellar Streams Detected in Gaia DR3 ». *ApJ* 967.2, 89, p. 89. DOI: `10.3847/1538-4357/ad382d`. arXiv: `2311.17202 [astro-ph.GA]` (cit. on pp. 10, 21–23, 26, 56, 177, 184, 216, 220, 221).

Ibata, R., G. Thomas, B. Famaey, K. Malhan, N. Martin & G. Monari (2020). « Detection of Strong Epicyclic Density Spikes in the GD-1 Stellar Stream: An Absence of Evidence for the Influence of Dark Matter Subhalos? » *ApJ* 891.2, 161, p. 161. DOI: `10.3847/1538-4357/ab7303`. arXiv: `2002.01488 [astro-ph.GA]` (cit. on pp. 7, 104, 214).

Ibata, R. A., M. Bellazzini, K. Malhan, N. Martin & P. Bianchini (2019). « Identification of the long stellar stream of the prototypical massive globular cluster ω Centauri ». *Nature Astronomy* 3, pp. 667–672. DOI: `10.1038/s41550-019-0751-x`. arXiv: `1902.09544 [astro-ph.GA]` (cit. on pp. 7, 104).

Ibata, R. A., G. F. Lewis & N. F. Martin (2016). « Feeling the Pull: a Study of Natural Galactic Accelerometers. I. Photometry of the Delicate Stellar Stream of the Palomar 5 Globular Cluster ». *ApJ* 819.1, 1, p. 1. DOI: `10.3847/0004-637X/819/1/1`. arXiv: `1512.03054 [astro-ph.GA]` (cit. on pp. 142, 198).

Ibata, R. A., G. F. Lewis, G. Thomas, N. F. Martin & S. Chapman (2017). « Feeling the Pull: A Study of Natural Galactic Accelerometers. II. Kinematics and Mass of the Delicate Stellar Stream of the Palomar 5 Globular Cluster ». *ApJ* 842.2, 120, p. 120. DOI: `10.3847/1538-4357/aa7514`. arXiv: `1708.06360 [astro-ph.GA]` (cit. on pp. 142, 185).

Ibata, R. A., K. Malhan & N. F. Martin (2019). « The Streams of the Gaping Abyss: A Population of Entangled Stellar Streams Surrounding the Inner Galaxy ». *ApJ* 872.2, 152, p. 152. DOI: `10.3847/1538-4357/ab0080`. arXiv: `1901.07566 [astro-ph.GA]` (cit. on pp. 104, 135, 176).

Ibata, R. A., K. Malhan, N. F. Martin & E. Starkenburg (2018). ≪ Phlegethon, a Nearby 75°-long Retrograde Stellar Stream ≫. *ApJ* 865.2, 85, p. 85. DOI: `10.3847/1538-4357/aadba3`. arXiv: `1806.01195 [astro-ph.GA]` (cit. on pp. 104, 176).

Irrgang, A., B. Wilcox, E. Tucker & L. Schiefelbein (2013). ≪ Milky Way mass models for orbit calculations ≫. *A&A* 549, A137, A137. DOI: `10.1051/0004-6361/201220540`. arXiv: `1211.4353 [astro-ph.GA]` (cit. on p. 111).

Ishchenko, M., M. Sobolenko, P. Berczik, S. Khoperskov, C. Omarov, O. Sobodar, et al. (2023). ≪ Milky Way globular clusters on cosmological timescales. I. Evolution of the orbital parameters in time-varying potentials ≫. *A&A* 673, A152, A152. DOI: `10.1051/0004-6361/202245117`. arXiv: `2304.03547 [astro-ph.GA]` (cit. on p. 181).

Ishchenko, M., M. Sobolenko, P. Berczik, C. Omarov, O. Sobodar, M. Kalambay, et al. (2023). ≪ Milky Way globular clusters on cosmological timescales. III. Interaction rates ≫. *A&A* 678, A69, A69. DOI: `10.1051/0004-6361/202346553`. arXiv: `2308.12699 [astro-ph.GA]` (cit. on p. 178).

Ishigaki, M. N., N. Hwang, M. Chiba & W. Aoki (2016). ≪ Line-of-sight Velocity and Metallicity Measurements of the Palomar 5 Tidal Stream ≫. *ApJ* 823.2, 157, p. 157. DOI: `10.3847/0004-637X/823/2/157`. arXiv: `1604.03188 [astro-ph.GA]` (cit. on p. 142).

Ivezić, Ž., A. J. Connolly, J. T. VanderPlas & A. Gray (2020). *Statistics, Data Mining, and Machine Learning in Astronomy. A Practical Python Guide for the Analysis of Survey Data, Updated Edition.* DOI: `10.1515/9780691197050` (cit. on p. 214).

Jensen, J., G. Thomas, A. W. McConnachie, E. Starkenburg, K. Malhan, J. Navarro, et al. (2021). ≪ Uncovering fossils of the distant Milky Way with UNIONS: NGC 5466 and its stellar stream ≫. *MNRAS* 507.2, pp. 1923–1936. DOI: `10.1093/mnras/stab2325`. arXiv: `2108.04340 [astro-ph.GA]` (cit. on pp. 104, 140).

Ji, A. P., T. S. Li, T. T. Hansen, A. R. Casey, S. E. Koposov, A. B. Pace, et al. (2020). ≪ The Southern Stellar Stream Spectroscopic Survey (S^5): Chemical Abundances of Seven Stellar Streams ≫. *AJ* 160.4, 181, p. 181. DOI: `10.3847/1538-3881/abacb6`. arXiv: `2008.07568 [astro-ph.SR]` (cit. on p. 176).

Johnson, C. I. & C. A. Pilachowski (2010). ≪ Chemical Abundances for 855 Giants in the Globular Cluster Omega Centauri (NGC 5139) ≫. *ApJ* 722.2, pp. 1373–1410. DOI: `10.1088/0004-637X/722/2/1373`. arXiv: `1008.2232 [astro-ph.SR]` (cit. on p. 56).

Johnston, K. V., D. R. Law & S. R. Majewski (2005). ≪ A Two Micron All Sky Survey View of the Sagittarius Dwarf Galaxy. III. Constraints on the Flattening of the Galactic Halo ≫. *ApJ* 619.2, pp. 800–806. DOI: `10.1086/426777`. arXiv: `astro-ph/0407565 [astro-ph]` (cit. on p. 176).

Johnston, K. V., D. N. Spergel & C. Haydn (2002). ≪ How Lumpy Is the Milky Way's Dark Matter Halo? ≫ *ApJ* 570.2, pp. 656–664. DOI: `10.1086/339791`. arXiv: `astro-ph/0111196 [astro-ph]` (cit. on p. 104).

Kaderali, S., J. A. S. Hunt, J. J. Webb, N. Price-Jones & R. Carlberg (2019). ≪ Rediscovering the tidal tails of NGC 288 with Gaia DR2 ≫. *MNRAS* 484.1, pp. L114–L118. DOI: `10.1093/mnrasl/slz015`. arXiv: `1809.04108 [astro-ph.GA]` (cit. on p. 104).

Kant, I. & S. L. Jaki (1981). *Universal natural history and theory of the heavens* (cit. on p. 22).

Kaplan, H. H., D. S. Lauretta, A. A. Simon, V. E. Hamilton, D. N. DellaGiustina, D. R. Golish, et al. (2020). ≪ Bright carbonate veins on asteroid (101955) Bennu: Implications for aqueous alteration history ≫. *Science* 370.6517, eabc3557, eabc3557. DOI: `10.1126/science.abc3557` (cit. on p. 222).

Katz, D., P. Sartoretti, A. Guerrier, P. Panuzzo, G. M. Seabroke, F. Thévenin, et al. (2023). ≪ Gaia Data Release 3. Properties and validation of the radial velocities ≫. *A&A* 674, A5, A5. DOI: `10.1051/0004-6361/202244220`. arXiv: `2206.05902 [astro-ph.GA]` (cit. on p. 123).

Keenan, D. W. & K. A. Innanen (1975). ≪ Numerical investigation of galactic tidal effects on spherical stellar systems. ≫ *AJ* 80, pp. 290–302. DOI: `10.1086/111744` (cit. on pp. 104, 175).

Khoperskov, S., A. Mastrobuono-Battisti, P. Di Matteo & M. Haywood (2018). « Mergers, tidal interactions, and mass exchange in a population of disc globular clusters ». *A&A* 620, A154, A154. DOI: `10.1051/0004-6361/201833534`. arXiv: `1809.04350 [astro-ph.GA]` (cit. on p. 178).

Khoperskov, S., G. van de Ven, M. Steinmetz, B. Ratcliffe, I. Minchev, D. Krajnović, et al. (2025). « Rediscovering the Milky Way with an orbit superposition approach and APOGEE data: I. Method validation ». *A&A* 695, A220, A220. DOI: `10.1051/0004-6361/202453304`. arXiv: `2411.15062 [astro-ph.GA]` (cit. on p. 20).

Kimm, T., R. Cen, J. Rosdahl & S. K. Yi (2016). « Formation of Globular Clusters in Atomic-cooling Halos Via Rapid Gas Condensation and Fragmentation during the Epoch of Reionization ». *ApJ* 823.1, 52, p. 52. DOI: `10.3847/0004-637X/823/1/52`. arXiv: `1510.05671 [astro-ph.GA]` (cit. on pp. 5, 9).

Kippenhahn, R., A. Weigert & A. Weiss (2013). *Stellar Structure and Evolution*. DOI: `10.1007/978-3-642-30304-3` (cit. on p. 4).

Klüter, J., M. J. Huston, A. Aronica, S. A. Johnson, M. T. Penny, M. Newman, et al. (2025). « SYNTHPOP: A New Framework for Synthetic Milky Way Population Generation ». *AJ* 169.6, 317, p. 317. DOI: `10.3847/1538-3881/adcd7a`. arXiv: `2411.18821 [astro-ph.IM]` (cit. on p. 21).

Koch, A. & P. Côté (2017). « Galactic Pal-eontology: abundance analysis of the disrupting globular cluster Palomar 5 ». *A&A* 601, A41, A41. DOI: `10.1051/0004-6361/201629872`. arXiv: `1703.02972 [astro-ph.GA]` (cit. on p. 142).

Koch, A., E. K. Grebel, M. Odenkirchen, D. Martínez-Delgado & J. A. R. Caldwell (2004). « Mass Segregation in the Globular Cluster Palomar 5 and its Tidal Tails ». *AJ* 128.5, pp. 2274–2287. DOI: `10.1086/425046`. arXiv: `astro-ph/0408208 [astro-ph]` (cit. on p. 142).

Koon, W. S., M. W. Lo, J. E. Marsden & S. D. Ross (2000). « Dynamical systems, the three-body problem and space mission design ». *Equadiff 99: (In 2 Volumes)*. World Scientific, pp. 1167–1181 (cit. on pp. 34, 37).

Koposov, S. E., M. Irwin, V. Belokurov, E. Gonzalez-Solares, A. K. Yoldas, J. Lewis, et al. (2014). « Discovery of a cold stellar stream in the ATLAS DR1 data. » *MNRAS* 442, pp. L85–L89. DOI: `10.1093/mnrasl/slu060`. arXiv: `1403.3409 [astro-ph.GA]` (cit. on p. 176).

Koposov, S. E., H.-W. Rix & D. W. Hogg (2010). « Constraining the Milky Way Potential with a Six-Dimensional Phase-Space Map of the GD-1 Stellar Stream ». *ApJ* 712.1, pp. 260–273. DOI: `10.1088/0004-637X/712/1/260`. arXiv: `0907.1085 [astro-ph.GA]` (cit. on p. 6).

Kroupa, P. (2001). « On the variation of the initial mass function ». *MNRAS* 322.2, pp. 231–246. DOI: `10.1046/j.1365-8711.2001.04022.x`. arXiv: `astro-ph/0009005 [astro-ph]` (cit. on p. 68).

Kruijssen, J. M. D. & H. J. G. L. M. Lamers (2008). « The photometric evolution of star clusters and the preferential loss of low-mass bodies - with an application to globular clusters ». *A&A* 490.1, pp. 151–171. DOI: `10.1051/0004-6361:200810167`. arXiv: `0809.0307 [astro-ph]` (cit. on p. 68).

Kruijssen, J. M. D. (2025). « The Formation of Globular Clusters ». *arXiv e-prints*, arXiv:2501.16438, arXiv:2501.16438. DOI: `10.48550/arXiv.2501.16438`. arXiv: `2501.16438 [astro-ph.GA]` (cit. on pp. 5, 9).

Kruijssen, J. M. D., J. L. Pfeffer, M. Chevance, A. Bonaca, S. Trujillo-Gomez, N. Bastian, et al. (2020). « Kraken reveals itself - the merger history of the Milky Way reconstructed with the E-MOSAICS simulations ». *MNRAS* 498.2, pp. 2472–2491. DOI: `10.1093/mnras/staa2452`. arXiv: `2003.01119 [astro-ph.GA]` (cit. on pp. 5, 108).

Krumholz, M. R. (2014). « The big problems in star formation: The star formation rate, stellar clustering, and the initial mass function ». *Phys. Rep.* 539, pp. 49–134. DOI: `10.1016/j.physrep.2014.02.001`. arXiv: `1402.0867 [astro-ph.GA]` (cit. on p. 4).

Krumholz, M. R., C. F. McKee & J. Bland-Hawthorn (2019). « Star Clusters Across Cosmic Time ». *ARA&A* 57, pp. 227–303. DOI: `10.1146/annurev-astro-091918-104430`. arXiv: `1812.01615 [astro-ph.GA]` (cit. on p. 4).

Kunder, A., A. Koch, R. M. Rich, R. de Propris, C. D. Howard, S. A. Stubbs, et al. (2012). « The Bulge Radial Velocity Assay (BRAVA). II. Complete Sample and Data Release ». *AJ* 143.3, 57, p. 57. DOI: `10.1088/0004-6256/143/3/57`. arXiv: `1112.1955 [astro-ph.SR]` (cit. on p. 111).

Kundu, R., D. Minniti & H. P. Singh (2019). « Search for extra-tidal RR Lyrae stars in Milky Way globular clusters from Gaia DR2 ». *MNRAS* 483.2, pp. 1737–1743. DOI: `10.1093/mnras/sty3239`. arXiv: `1811.11130 [astro-ph.GA]` (cit. on p. 129).

Küpper, A. H. W., E. Balbinot, A. Bonaca, K. V. Johnston, D. W. Hogg, P. Kroupa, et al. (2015). « Globular Cluster Streams as Galactic High-Precision Scales—the Poster Child Palomar 5 ». *ApJ* 803.2, 80, p. 80. DOI: `10.1088/0004-637X/803/2/80`. arXiv: `1502.02658 [astro-ph.GA]` (cit. on p. 142).

Küpper, A. H. W., P. Kroupa, H. Baumgardt & D. C. Heggie (2010). « Tidal tails of star clusters ». *MNRAS* 401.1, pp. 105–120. DOI: `10.1111/j.1365-2966.2009.15690.x`. arXiv: `0909.2619 [astro-ph.SR]` (cit. on p. 104).

Küpper, A. H. W., R. R. Lane & D. C. Heggie (2012). « More on the structure of tidal tails ». *MNRAS* 420.3, pp. 2700–2714. DOI: `10.1111/j.1365-2966.2011.20242.x`. arXiv: `1111.5013 [astro-ph.GA]` (cit. on pp. 104, 215).

Kuzma, P. B., G. S. Da Costa, S. C. Keller & E. Maunder (2015). « Palomar 5 and its tidal tails: a search for new members in the tidal stream ». *MNRAS* 446.4, pp. 3297–3309. DOI: `10.1093/mnras/stu2343`. arXiv: `1411.0776 [astro-ph.GA]` (cit. on pp. 142, 175).

Kuzma, P. B., M. N. Ishigaki, T. Kirihara & I. Ogami (2025). « Constructing a Pristine View of Extended Globular Cluster Structure ». *arXiv e-prints*, arXiv:2507.05590, arXiv:2507.05590. DOI: `10.48550/arXiv.2507.05590`. arXiv: `2507.05590 [astro-ph.GA]` (cit. on p. 213).

Lacchin, E., A. Mastrobuono-Battisti, F. Calura, C. Nipoti, A. P. Milone, M. Meneghetti, et al. (2024). « Multiple stellar population mass loss in massive Galactic globular clusters ». *A&A* 681, A45, A45. DOI: `10.1051/0004-6361/202347268`. arXiv: `2309.15161 [astro-ph.GA]` (cit. on p. 218).

Lamers, H. J. G. L. M., H. Baumgardt & M. Gieles (2010). « Mass-loss rates and the mass evolution of star clusters ». *MNRAS* 409.1, pp. 305–328. DOI: `10.1111/j.1365-2966.2010.17309.x`. arXiv: `1007.1078 [astro-ph.GA]` (cit. on p. 70).

Lane, R. R., L. L. Kiss, G. F. Lewis, R. A. Ibata, A. Siebert, T. R. Bedding, et al. (2010). « Halo globular clusters observed with AAOmega: dark matter content, metallicity and tidal heating ». *MNRAS* 406.4, pp. 2732–2742. DOI: `10.1111/j.1365-2966.2010.16874.x`. arXiv: `1004.4696 [astro-ph.GA]` (cit. on p. 104).

Lane, R. R., A. H. W. Küpper & D. C. Heggie (2012). « The tidal tails of 47 Tucanae ». *MNRAS* 423.3, pp. 2845–2853. DOI: `10.1111/j.1365-2966.2012.21093.x`. arXiv: `1204.2549 [astro-ph.GA]` (cit. on pp. 106, 134).

Lauretta, D. S., S. S. Balram-Knutson, E. Beshore, W. V. Boynton, C. Drouet d'Aubigny, D. N. DellaGiustina, et al. (2017). « OSIRIS-REx: Sample Return from Asteroid (101955) Bennu ». *Space Sci. Rev.* 212.1-2, pp. 925–984. DOI: `10.1007/s11214-017-0405-1`. arXiv: `1702.06981 [astro-ph.EP]` (cit. on p. 222).

Law, D. R., K. V. Johnston & S. R. Majewski (2005). « A Two Micron All-Sky Survey View of the Sagittarius Dwarf Galaxy. IV. Modeling the Sagittarius Tidal Tails ». *ApJ* 619.2, pp. 807–823. DOI: `10.1086/426779`. arXiv: `astro-ph/0407566 [astro-ph]` (cit. on p. 176).

Law, D. R., S. R. Majewski & K. V. Johnston (2010). « Evidence for a Triaxial Milky Way Dark Matter Halo from the Sagittarius Stellar Tidal Stream ». *American Astronomical Society Meeting Abstracts #215*. Vol. 215. American Astronomical Society Meeting Abstracts, 321.03, p. 321.03 (cit. on p. 22).

Law, D. R. & S. R. Majewski (2010). « Assessing the Milky Way Satellites Associated with the Sagittarius Dwarf Spheroidal Galaxy ». *ApJ* 718.2, pp. 1128–1150. DOI: `10.1088/0004-637X/718/2/1128`. arXiv: `1005.5390 [astro-ph.GA]` (cit. on pp. 6, 176).

Lee, K. H., H. M. Lee, G. G. Fahlman & M. G. Lee (2003). « Wide-Field CCD Photometry of the Globular Cluster M92 ». *AJ* 126.2, pp. 815–825. DOI: `10.1086/376738`. arXiv: `astro-ph/0212252 [astro-ph]` (cit. on p. 175).

Lehmann, I. & R. .-. Scholz (1997). « Tidal radii of the globular clusters M 5, M 12, M 13, M 15, M 53, NGC 5053 and NGC 5466 from automated star counts. » *A&A* 320, pp. 776–782 (cit. on p. 175).

Leon, S., G. Meylan & F. Combes (2000). « Tidal tails around 20 Galactic globular clusters. Observational evidence for gravitational disk/bulge shocking ». *A&A* 359, pp. 907–931. DOI: `10.48550/arXiv.astro-ph/0006100`. arXiv: `astro-ph/0006100 [astro-ph]` (cit. on pp. 103, 175).

Li, J.-Y., X.-D. Zou, D. R. Golish, B. E. Clark, S. Ferrone, S. Fornasier, et al. (2021). « Spectrophotometric Modeling and Mapping of (101955) Bennu ». *Planetary Science Journal* 2.3, 117, p. 117. DOI: `10.3847/PSJ/abfd2d` (cit. on p. 222).

Li, T. S., S. E. Koposov, D. B. Zucker, G. F. Lewis, K. Kuehn, J. D. Simpson, et al. (2019). « The southern stellar stream spectroscopic survey (S^5): Overview, target selection, data reduction, validation, and early science ». *MNRAS* 490.3, pp. 3508–3531. DOI: `10.1093/mnras/stz2731`. arXiv: `1907.09481 [astro-ph.GA]` (cit. on pp. 2, 176).

Li, T. S., A. P. Ji, A. B. Pace, D. Erkal, S. E. Koposov, N. Shipp, et al. (2022). « S^5: The Orbital and Chemical Properties of One Dozen Stellar Streams ». *ApJ* 928.1, 30, p. 30. DOI: `10.3847/1538-4357/ac46d3`. arXiv: `2110.06950 [astro-ph.GA]` (cit. on p. 176).

Li, T. S., S. E. Koposov, D. Erkal, A. P. Ji, N. Shipp, A. B. Pace, et al. (2021). « Broken into Pieces: ATLAS and Aliqa Uma as One Single Stream ». *ApJ* 911.2, 149, p. 149. DOI: `10.3847/1538-4357/abeb18`. arXiv: `2006.10763 [astro-ph.GA]` (cit. on p. 176).

Li, Y.-B., A. .-. Luo, Y.-J. Lu, X.-S. Zhang, J. Li, R. Wang, et al. (2021). « 591 High-velocity Stars in the Galactic Halo Selected from LAMOST DR7 and Gaia DR2 ». *ApJS* 252.1, 3, p. 3. DOI: `10.3847/1538-4365/abc16e`. arXiv: `2011.10206 [astro-ph.GA]` (cit. on p. 68).

Licquia, T. C. & J. A. Newman (2015). « Improved Estimates of the Milky Way's Stellar Mass and Star Formation Rate from Hierarchical Bayesian Meta-Analysis ». *ApJ* 806.1, 96, p. 96. DOI: `10.1088/0004-637X/806/1/96`. arXiv: `1407.1078 [astro-ph.GA]` (cit. on p. 19).

Lightman, A. P. & S. L. Shapiro (1978). « The dynamical evolution of globular clusters ». *Reviews of Modern Physics* 50.2, pp. 437–481. DOI: `10.1103/RevModPhys.50.437` (cit. on p. 67).

Lintott, C. J., K. Schawinski, A. Slosar, K. Land, S. Bamford, D. Thomas, et al. (2008). « Galaxy Zoo: morphologies derived from visual inspection of galaxies from the Sloan Digital Sky Survey ». *MNRAS* 389.3, pp. 1179–1189. DOI: `10.1111/j.1365-2966.2008.13689.x`. arXiv: `0804.4483 [astro-ph]` (cit. on p. 19).

Long, K. & C. Murali (1992). « Analytical Potentials for Barred Galaxies ». *ApJ* 397, p. 44. DOI: `10.1086/171764` (cit. on pp. 24, 95, 112, 113).

Lu, J., T. Lin, M. Sholapurkar & A. Bonaca (2025). « Detectability of dark matter subhalo impacts in Milky Way stellar streams ». *arXiv e-prints*, arXiv:2502.07781, arXiv:2502.07781. DOI: `10.48550/arXiv.2502.07781`. arXiv: `2502.07781 [astro-ph.GA]` (cit. on pp. 213, 214).

Lucey, M., S. Pearson, J. A. S. Hunt, K. Hawkins, M. Ness, M. S. Petersen, et al. (2023). « Dynamically constraining the length of the Milky way bar ». *MNRAS* 520.3, pp. 4779–4792. DOI: `10.1093/mnras/stad406`. arXiv: `2206.01798 [astro-ph.GA]` (cit. on p. 216).

Maiolino, R. & F. Mannucci (2019). « De re metallica: the cosmic chemical evolution of galaxies ». *A&A Rev.* 27.1, 3, p. 3. DOI: `10.1007/s00159-018-0112-2`. arXiv: `1811.09642 [astro-ph.GA]` (cit. on p. 3).

Majewski, S. R., R. J. Patterson, D. I. Dinescu, W. Y. Johnson, J. C. Ostheimer, W. E. Kunkel, et al. (2000). « ω Centauri : Nucleus of a milky way dwarf spheroidal ? » *Liege International Astrophysical Colloquia*. Ed. by A. Noels, P. Magain, D. Caro, E. Jehin, G. Parmentier & A. A. Thoul. Vol. 35. Liege International Astrophysical Colloquia, p. 619. DOI: `10.48550/arXiv.astro-ph/9910278`. arXiv: `astro-ph/9910278 [astro-ph]` (cit. on p. 56).

Majewski, S. R., R. P. Schiavon, P. M. Frinchaboy, C. Allende Prieto, R. Barkhouser, D. Bizyaev, et al. (2017). « The Apache Point Observatory Galactic Evolution Experiment (APOGEE) ». *AJ* 154.3, 94, p. 94. DOI: 10.3847/1538-3881/aa784d. arXiv: 1509.05420 [astro-ph.IM] (cit. on pp. 7, 21).

Makino, J., M. Taiji, T. Ebisuzaki & D. Sugimoto (1997). « GRAPE-4: A Massively Parallel Special-Purpose Computer for Collisional N-Body Simulations ». *ApJ* 480.1, pp. 432–446. DOI: 10.1086/303972 (cit. on p. 215).

Malhan, K. (2022). « A New Member of the Milky Way's Family Tree: Characterizing the Pontus Merger of Our Galaxy ». *ApJ* 930.1, L9, p. L9. DOI: 10.3847/2041-8213/ac67da. arXiv: 2204.09058 [astro-ph.GA] (cit. on p. 5).

Malhan, K. & R. A. Ibata (2018). « STREAMFINDER - I. A new algorithm for detecting stellar streams ». *MNRAS* 477.3, pp. 4063–4076. DOI: 10.1093/mnras/sty912. arXiv: 1804.11338 [astro-ph.GA] (cit. on pp. 7, 56, 176).

— (2019). « Constraining the Milky Way halo potential with the GD-1 stellar stream ». *MNRAS* 486.3, pp. 2995–3005. DOI: 10.1093/mnras/stz1035. arXiv: 1807.05994 [astro-ph.GA] (cit. on p. 200).

Malhan, K., R. A. Ibata, R. G. Carlberg, M. Bellazzini, B. Famaey & N. F. Martin (2019). « Phase-space Correlation in Stellar Streams of the Milky Way Halo: The Clash of Kshir and GD-1 ». *ApJ* 886.1, L7, p. L7. DOI: 10.3847/2041-8213/ab530e. arXiv: 1911.00009 [astro-ph.GA] (cit. on p. 104).

Malhan, K., R. A. Ibata, R. G. Carlberg, M. Valluri & K. Freese (2019). « Butterfly in a Cocoon, Understanding the Origin and Morphology of Globular Cluster Streams: The Case of GD-1 ». *ApJ* 881.2, 106, p. 106. DOI: 10.3847/1538-4357/ab2e07. arXiv: 1903.08141 [astro-ph.GA] (cit. on p. 104).

Malhan, K., R. A. Ibata, B. Goldman, N. F. Martin, E. Magnier & K. Chambers (2018). « STREAMFINDER II: A possible fanning structure parallel to the GD-1 stream in Pan-STARRS1 ». *MNRAS* 478.3, pp. 3862–3870. DOI: 10.1093/mnras/sty1338. arXiv: 1805.08205 [astro-ph.GA] (cit. on pp. 7, 56, 104).

Malhan, K., R. A. Ibata & N. F. Martin (2018). « Ghostly tributaries to the Milky Way: charting the halo's stellar streams with the Gaia DR2 catalogue ». *MNRAS* 481.3, pp. 3442–3455. DOI: 10.1093/mnras/sty2474. arXiv: 1804.11339 [astro-ph.GA] (cit. on pp. 104, 176).

Malhan, K., R. A. Ibata, S. Sharma, B. Famaey, M. Bellazzini, R. G. Carlberg, et al. (2022). « The Global Dynamical Atlas of the Milky Way Mergers: Constraints from Gaia EDR3-based Orbits of Globular Clusters, Stellar Streams, and Satellite Galaxies ». *ApJ* 926.2, 107, p. 107. DOI: 10.3847/1538-4357/ac4d2a. arXiv: 2202.07660 [astro-ph.GA] (cit. on p. 56).

Malhan, K., M. Valluri & K. Freese (2021). « Probing the nature of dark matter with accreted globular cluster streams ». *MNRAS* 501.1, pp. 179–200. DOI: 10.1093/mnras/staa3597. arXiv: 2005.12919 [astro-ph.GA] (cit. on p. 104).

Malhan, K., M. Valluri, K. Freese & R. A. Ibata (2022). « New Constraints on the Dark Matter Density Profiles of Dwarf Galaxies from Proper Motions of Globular Cluster Streams ». *ApJ* 941.2, L38, p. L38. DOI: 10.3847/2041-8213/aca6e5. arXiv: 2201.03571 [astro-ph.GA] (cit. on p. 9).

Malhan, K., Z. Yuan, R. A. Ibata, A. Arentsen, M. Bellazzini & N. F. Martin (2021). « Evidence of a Dwarf Galaxy Stream Populating the Inner Milky Way Halo ». *ApJ* 920.1, 51, p. 51. DOI: 10.3847/1538-4357/ac1675. arXiv: 2104.09523 [astro-ph.GA] (cit. on pp. 5, 9).

Mancillas, B., P.-A. Duc, F. Combes, F. Bournaud, E. Emsellem, M. Martig, et al. (2019). « Probing the merger history of red early-type galaxies with their faint stellar substructures ». *A&A* 632, A122, A122. DOI: 10.1051/0004-6361/201936320. arXiv: 1909.07500 [astro-ph.GA] (cit. on p. 115).

Martell, S. L., M. D. Shetrone, S. Lucatello, R. P. Schiavon, S. Mészáros, C. Allende Prieto, et al. (2016). « Chemical Tagging in the SDSS-III/APOGEE Survey: New Identifications of Halo Stars with Globular Cluster Origins ». *ApJ* 825.2, 146, p. 146. DOI: 10.3847/0004-637X/825/2/146. arXiv: 1605.05792 [astro-ph.GA] (cit. on p. 218).

Martin, N. F., R. A. Ibata, E. Starkenburg, Z. Yuan, K. Malhan, M. Bellazzini, et al. (2022). ≪ The Pristine survey - XVI. The metallicity of 26 stellar streams around the Milky Way detected with the STREAMFINDER in Gaia EDR3 ≫. *MNRAS* 516.4, pp. 5331–5354. DOI: `10.1093/mnras/stac2426`. arXiv: `2201.01310 [astro-ph.GA]` (cit. on p. 9).

Massari, D., H. H. Koppelman & A. Helmi (2019). ≪ Origin of the system of globular clusters in the Milky Way ≫. *A&A* 630, L4, p. L4. DOI: `10.1051/0004-6361/201936135`. arXiv: `1906.08271 [astro-ph.GA]` (cit. on pp. 127, 171).

Mastrobuono-Battisti, A., P. Di Matteo, M. Montuori & M. Haywood (2012). ≪ Clumpy streams in a smooth dark halo: the case of Palomar 5 ≫. *A&A* 546, L7, p. L7. DOI: `10.1051/0004-6361/201219563`. arXiv: `1209.0466 [astro-ph.GA]` (cit. on pp. 14, 104–106, 142, 180, 197, 211).

Mastrobuono-Battisti, A., S. Khoperskov, P. Di Matteo & M. Haywood (2019). ≪ Mergers, tidal interactions, and mass exchange in a population of disc globular clusters. II. Long-term evolution ≫. *A&A* 622, A86, A86. DOI: `10.1051/0004-6361/201834087`. arXiv: `1811.07907 [astro-ph.GA]` (cit. on p. 178).

Mateu, C. (2023). ≪ galstreams: A library of Milky Way stellar stream footprints and tracks ≫. *MNRAS* 520.4, pp. 5225–5258. DOI: `10.1093/mnras/stad321`. arXiv: `2204.10326 [astro-ph.GA]` (cit. on pp. 104, 115, 135, 138, 176, 196).

McMillan, P. J. (2011). ≪ Mass models of the Milky Way ≫. *MNRAS* 414.3, pp. 2446–2457. DOI: `10.1111/j.1365-2966.2011.18564.x`. arXiv: `1102.4340 [astro-ph.GA]` (cit. on p. 21).

— (2017). ≪ The mass distribution and gravitational potential of the Milky Way ≫. *MNRAS* 465.1, pp. 76–94. DOI: `10.1093/mnras/stw2759`. arXiv: `1608.00971 [astro-ph.GA]` (cit. on pp. 19, 21–24, 27, 180).

Meson Developers (2025). *The Meson Build System: Manual and Reference Documentation.* `https://mesonbuild.com/index.html` (cit. on p. 96).

Messier, C. (1781). *Catalogue des Nébuleuses et des Amas d'Étoiles (Catalog of Nebulae and Star Clusters).* Connoissance des Temps ou des Mouvements Célestes, for 1784, p. 227-267 (cit. on p. 1).

Meylan, G. & D. C. Heggie (1997). ≪ Internal dynamics of globular clusters ≫. *A&A Rev.* 8, pp. 1–143. DOI: `10.1007/s001590050008`. arXiv: `astro-ph/9610076 [astro-ph]` (cit. on pp. 67, 103, 215).

Ministere de l'Enseignement superieur et de la Recherche (2025). *Le financement doctoral* (cit. on p. 12).

Minniti, D., M. Hempel, I. Toledo, V. D. Ivanov, J. Alonso-García, R. K. Saito, et al. (2011). ≪ Discovery of VVV CL001. A low-mass globular cluster next to UKS 1 in the direction of the Galactic bulge ≫. *A&A* 527, A81, A81. DOI: `10.1051/0004-6361/201015795`. arXiv: `1012.2450 [astro-ph.GA]` (cit. on p. 103).

Minniti, D., T. Palma, D. Camargo, M. Chijani-Saballa, J. Alonso-García, J. J. Clariá, et al. (2021). ≪ An intriguing globular cluster in the Galactic bulge from the VVV survey ≫. *A&A* 652, A129, A129. DOI: `10.1051/0004-6361/202140347`. arXiv: `2106.13904 [astro-ph.GA]` (cit. on p. 103).

Minniti, D., J. G. Fernández-Trincado, M. Gómez, L. C. Smith, P. W. Lucas & R. Contreras Ramos (2021). ≪ Discovery of a new nearby globular cluster with extreme kinematics located in the extension of a halo stream ≫. *A&A* 650, L11, p. L11. DOI: `10.1051/0004-6361/202141129`. arXiv: `2106.01383 [astro-ph.GA]` (cit. on p. 103).

Minniti, D., D. Geisler, J. Alonso-García, T. Palma, J. C. Beamín, J. Borissova, et al. (2017). ≪ New VVV Survey Globular Cluster Candidates in the Milky Way Bulge ≫. *ApJ* 849.2, L24, p. L24. DOI: `10.3847/2041-8213/aa95b8` (cit. on p. 103).

Minniti, D., T. Palma, I. Dékány, M. Hempel, M. Rejkuba, J. Pullen, et al. (2017). ≪ FSR 1716: A New Milky Way Globular Cluster Confirmed Using VVV RR Lyrae Stars ≫. *ApJ* 838.1, L14, p. L14. DOI: `10.3847/2041-8213/838/1/L14`. arXiv: `1703.02033 [astro-ph.GA]` (cit. on p. 103).

Minniti, D., E. F. Schlafly, T. Palma, J. J. Clariá, M. Hempel, J. Alonso-García, et al. (2018). ≪ Confirmation of a New Metal-poor Globular Cluster in the Galactic Bulge ≫. *ApJ* 866.1, 12, p. 12. DOI: `10.3847/1538-4357/aadd06` (cit. on p. 103).

Miyamoto, M. & R. Nagai (1975). ≪ Three-dimensional models for the distribution of mass in galaxies. ≫ *PASJ* 27, pp. 533–543 (cit. on p. 23).

Mo, H., F. C. van den Bosch & S. White (2010). *Galaxy Formation and Evolution*. DOI: 10.1017/CBO9780511807244 (cit. on p. 3).

Moliné, Á., M. A. Sánchez-Conde, S. Palomares-Ruiz & F. Prada (2017). ≪ Characterization of subhalo structural properties and implications for dark matter annihilation signals ≫. *MNRAS* 466.4, pp. 4974–4990. DOI: 10.1093/mnras/stx026. arXiv: 1603.04057 [astro-ph.CO] (cit. on p. 177).

Moni Bidin, C., F. Mauro, D. Geisler, D. Minniti, M. Catelan, M. Hempel, et al. (2011). ≪ Three Galactic globular cluster candidates ≫. *A&A* 535, A33, A33. DOI: 10.1051/0004-6361/201117488. arXiv: 1109.1854 [astro-ph.GA] (cit. on p. 103).

Montuori, M., R. Capuzzo-Dolcetta, P. Di Matteo, A. Lepinette & P. Miocchi (2007). ≪ Tidal Tails around Globular Clusters: Are They a Good Tracer of Cluster Orbits? ≫ *ApJ* 659.2, pp. 1212–1221. DOI: 10.1086/512114. arXiv: astro-ph/0611204 [astro-ph] (cit. on pp. 104, 175, 221).

Murali, C. & M. D. Weinberg (1997a). ≪ Evolution of the Galactic globular cluster system ≫. *MNRAS* 291.4, pp. 717–731. DOI: 10.1093/mnras/291.4.717 (cit. on pp. 103, 217).

— (1997b). ≪ The effect of the Galactic spheroid on globular cluster evolution ≫. *MNRAS* 288.3, pp. 749–766. DOI: 10.1093/mnras/288.3.749. arXiv: astro-ph/9604049 [astro-ph] (cit. on p. 103).

Murray, S. D. & D. N. C. Lin (1992). ≪ Globular Cluster Formation: The Fossil Record ≫. *ApJ* 400, p. 265. DOI: 10.1086/171993 (cit. on p. 4).

Naik, A. P., N. W. Evans, E. Puchwein, H. Zhao & A. .-. Davis (2020). ≪ Stellar streams in chameleon gravity ≫. *Phys. Rev. D* 102.8, 084066, p. 084066. DOI: 10.1103/PhysRevD.102.084066. arXiv: 2002.05738 [astro-ph.GA] (cit. on p. 105).

Navarrete, C., V. Belokurov & S. E. Koposov (2017). ≪ The Discovery of Tidal Tails around the Globular Cluster NGC 7492 with Pan-STARRS1 ≫. *ApJ* 841.2, L23, p. L23. DOI: 10.3847/2041-8213/aa72e1. arXiv: 1705.04324 [astro-ph.GA] (cit. on p. 104).

Nelson, D., V. Springel, A. Pillepich, V. Rodriguez-Gomez, P. Torrey, S. Genel, et al. (2019). ≪ The IllustrisTNG simulations: public data release ≫. *Computational Astrophysics and Cosmology* 6.1, 2, p. 2. DOI: 10.1186/s40668-019-0028-x. arXiv: 1812.05609 [astro-ph.GA] (cit. on p. 56).

Nibauer, J., A. Bonaca, D. N. Spergel, A. M. Price-Whelan, J. E. Greene, N. Starkman, et al. (2025). ≪ StreamSculptor: Hamiltonian Perturbation Theory for Stellar Streams in Flexible Potentials with Differentiable Simulations ≫. *ApJ* 983.1, 68, p. 68. DOI: 10.3847/1538-4357/adb8e8. arXiv: 2410.21174 [astro-ph.GA] (cit. on p. 177).

Nie, J., H. Tian, J. Li, C. Liu, M. C. Smith, B. Tang, et al. (2022). ≪ Searching Extra-tidal Features around the Globular Cluster Whiting 1 ≫. *ApJ* 930.1, 23, p. 23. DOI: 10.3847/1538-4357/ac6264. arXiv: 2204.11064 [astro-ph.GA] (cit. on p. 104).

Nitadori, K. & S. J. Aarseth (2012). ≪ Accelerating NBODY6 with graphics processing units ≫. *MNRAS* 424.1, pp. 545–552. DOI: 10.1111/j.1365-2966.2012.21227.x. arXiv: 1205.1222 [astro-ph.IM] (cit. on p. 215).

NumPy Developers (2025). *F2PY User Guide and Reference Manual*. https://numpy.org/doc/stable/f2py/ (cit. on p. 95).

Odenkirchen, M., E. K. Grebel, W. Dehnen, H. W. Rix, C. M. Rockosi, H. Newberg, et al. (2002). ≪ The Extended Tails of Palomar 5: A Ten Degree Arc of Globular Cluster Tidal Debris ≫. *American Astronomical Society Meeting Abstracts #200*. Vol. 200. American Astronomical Society Meeting Abstracts, 10.01, p. 10.01 (cit. on p. 175).

Odenkirchen, M., E. K. Grebel, W. Dehnen, H.-W. Rix, B. Yanny, H. J. Newberg, et al. (2003). ≪ The Extended Tails of Palomar 5: A 10° Arc of Globular Cluster Tidal Debris ≫. *AJ* 126.5, pp. 2385–2407. DOI: 10.1086/378601. arXiv: astro-ph/0307446 [astro-ph] (cit. on pp. 103, 142, 175).

Odenkirchen, M., E. K. Grebel, A. Kayser, H.-W. Rix & W. Dehnen (2009). ≪ Kinematics of the Tidal Debris of the Globular Cluster Palomar 5 ≫. *AJ* 137.2, pp. 3378–3387. DOI: 10.1088/0004-6256/137/2/3378 (cit. on pp. 103, 142).

Odenkirchen, M., E. K. Grebel, C. M. Rockosi, W. Dehnen, R. Ibata, H.-W. Rix, et al. (2001). « Detection of Massive Tidal Tails around the Globular Cluster Palomar 5 with Sloan Digital Sky Survey Commissioning Data ». *ApJ* 548.2, pp. L165–L169. DOI: `10.1086/319095`. arXiv: `astro-ph/0012311 [astro-ph]` (cit. on pp. 103, 135, 142, 175).

Oh, K. S. & D. N. C. Lin (1992). « Tidal Evolution of Globular Clusters. II. The Effects of Galactic Tidal Field and Diffusion ». *ApJ* 386, p. 519. DOI: `10.1086/171037` (cit. on p. 104).

Oh, K. S., D. N. C. Lin & S. J. Aarseth (1992). « Tidal Evolution of Globular Clusters. I. Method ». *ApJ* 386, p. 506. DOI: `10.1086/171036` (cit. on p. 104).

Oort, J. H. (1927). « Additional notes concerning the rotation of the galactic system ». *Bull. Astron. Inst. Netherlands* 4, p. 91 (cit. on p. 18).

Pagnini, G., P. Di Matteo, M. Haywood, A. Mastrobuono-Battisti, F. Renaud, M. Mondelin, et al. (2025). « Abundance ties: Nephele and the globular cluster population accreted with ω Cen: Based on APOGEE DR17 and Gaia EDR3 ». *A&A* 693, A155, A155. DOI: `10.1051/0004-6361/202450264`. arXiv: `2410.22479 [astro-ph.GA]` (cit. on p. 5).

Pagnini, G., P. Di Matteo, S. Khoperskov, A. Mastrobuono-Battisti, M. Haywood, F. Renaud, et al. (2023). « The distribution of globular clusters in kinematic spaces does not trace the accretion history of the host galaxy ». *A&A* 673, A86, A86. DOI: `10.1051/0004-6361/202245128`. arXiv: `2210.04245 [astro-ph.GA]` (cit. on p. 5).

Palau, C. G. & J. Miralda-Escudé (2019). « Statistical detection of a tidal stream associated with the globular cluster M68 using Gaia data ». *MNRAS* 488.2, pp. 1535–1557. DOI: `10.1093/mnras/stz1790`. arXiv: `1905.01193 [astro-ph.GA]` (cit. on pp. 104, 106, 110, 138, 139).

— (2021). « The tidal stream generated by the globular cluster NGC 3201 ». *MNRAS* 504.2, pp. 2727–2741. DOI: `10.1093/mnras/stab1024`. arXiv: `2010.14381 [astro-ph.GA]` (cit. on pp. 104, 135, 137).

Pancino, E., M. Bellazzini, G. Giuffrida & S. Marinoni (2017). « Globular clusters with Gaia ». *MNRAS* 467.1, pp. 412–427. DOI: `10.1093/mnras/stx079`. arXiv: `1701.03003 [astro-ph.GA]` (cit. on p. 7).

Pearson, S., A. Bonaca, Y. Chen & O. Y. Gnedin (2024). « Forecasting the Population of Globular Cluster Streams in Milky Way–type Galaxies ». *ApJ* 976.1, 54, p. 54. DOI: `10.3847/1538-4357/ad8348`. arXiv: `2405.15851 [astro-ph.GA]` (cit. on pp. 53, 56, 57, 199).

Pearson, S., A. M. Price-Whelan & K. V. Johnston (2017). « Gaps and length asymmetry in the stellar stream Palomar 5 as effects of Galactic bar rotation ». *Nature Astronomy* 1, pp. 633–639. DOI: `10.1038/s41550-017-0220-3`. arXiv: `1703.04627 [astro-ph.GA]` (cit. on pp. 104, 142, 178, 184, 200, 214).

Peebles, P. J. E. (1966). « Primordial Helium Abundance and the Primordial Fireball. II ». *ApJ* 146, p. 542. DOI: `10.1086/148918` (cit. on p. 3).

Pelupessy, F. I., A. van Elteren, N. de Vries, S. L. W. McMillan, N. Drost & S. F. Portegies Zwart (2013). « The Astrophysical Multipurpose Software Environment ». *A&A* 557, A84, A84. DOI: `10.1051/0004-6361/201321252`. arXiv: `1307.3016 [astro-ph.IM]` (cit. on p. 71).

Peñarrubia, J., R. Errani, M. G. Walker, M. Gieles & T. C. N. Boekholt (2024). « Capture of field stars by dark substructures ». *MNRAS* 533.3, pp. 3263–3282. DOI: `10.1093/mnras/stae1961`. arXiv: `2404.19069 [astro-ph.GA]` (cit. on p. 36).

Perivolaropoulos, L. & F. Skara (2022). « Challenges for ΛCDM: An update ». *New A Rev.* 95, 101659, p. 101659. DOI: `10.1016/j.newar.2022.101659`. arXiv: `2105.05208 [astro-ph.CO]` (cit. on p. 3).

Perryman, M. A. C., K. S. de Boer, G. Gilmore, E. Høg, M. G. Lattanzi, L. Lindegren, et al. (2001). « GAIA: Composition, formation and evolution of the Galaxy ». *A&A* 369, pp. 339–363. DOI: `10.1051/0004-6361:20010085`. arXiv: `astro-ph/0101235 [astro-ph]` (cit. on p. 6).

Perryman, M. A. C., L. Lindegren, J. Kovalevsky, E. Hoeg, U. Bastian, P. L. Bernacca, et al. (1997). « The HIPPARCOS Catalogue ». *A&A* 323, pp. L49–L52 (cit. on p. 20).

Peterson, P. (2009). « F2PY: a tool for connecting Fortran and Python programs ». *International Journal of Computational Science and Engineering* 4.4, pp. 296–305. DOI: `10.1504/IJCSE.2009.029165` (cit. on p. 95).

Phillips, S. G., R. P. Schiavon, J. T. Mackereth, C. Allende Prieto, B. Anguiano, R. L. Beaton, et al. (2022). ≪ APOGEE detection of N-rich stars in the tidal tails of Palomar 5 ≫. *MNRAS* 510.3, pp. 3727–3733. DOI: `10.1093/mnras/stab3532`. arXiv: `2112.02117 [astro-ph.GA]` (cit. on pp. 142, 218).

Piatti, A. E. (2017). ≪ Detection of a Diffuse Extended Halo-like Structure around 47 Tuc ≫. *ApJ* 846.1, L10, p. L10. DOI: `10.3847/2041-8213/aa8773`. arXiv: `1708.06194 [astro-ph.GA]` (cit. on p. 134).

— (2021). ≪ The surroundings of the Milky Way globular cluster NGC 6809 ≫. *MNRAS* 505.2, pp. 3033–3040. DOI: `10.1093/mnras/stab1532`. arXiv: `2105.11289 [astro-ph.GA]` (cit. on pp. 104, 106).

— (2022). ≪ Dark Energy Camera photometry reveals extra-tidal stars around the Milky Way globular cluster NGC 6864 (M75) ≫. *MNRAS* 509.3, pp. 3709–3716. DOI: `10.1093/mnras/stab3238`. arXiv: `2111.02496 [astro-ph.GA]` (cit. on p. 104).

Piatti, A. E. & J. A. Carballo-Bello (2019). ≪ Extra-tidal structures around the Gaia Sausage candidate globular cluster NGC 6779 (M56) ≫. *MNRAS* 485.1, pp. 1029–1035. DOI: `10.1093/mnras/stz500`. arXiv: `1902.05824 [astro-ph.GA]` (cit. on p. 104).

— (2020). ≪ The tidal tails of Milky Way globular clusters ≫. *A&A* 637, L2, p. L2. DOI: `10.1051/0004-6361/202037994`. arXiv: `2004.11747 [astro-ph.GA]` (cit. on pp. 7, 104).

Piatti, A. E., J. A. Carballo-Bello, M. D. Mora, C. Cenzano, C. Navarrete & M. Catelan (2020). ≪ The elusive tidal tails of the Milky Way globular cluster NGC 7099 ≫. *A&A* 643, A15, A15. DOI: `10.1051/0004-6361/202039012`. arXiv: `2009.04290 [astro-ph.GA]` (cit. on p. 104).

Piatti, A. E., M. F. Mestre, J. A. Carballo-Bello, D. D. Carpintero, C. Navarrete, M. D. Mora, et al. (2021). ≪ Signatures of tidal disruption in the Milky Way globular cluster NGC 6981 (M72) ≫. *A&A* 646, A176, A176. DOI: `10.1051/0004-6361/202040038`. arXiv: `2101.01818 [astro-ph.GA]` (cit. on p. 104).

Pillepich, A., V. Springel, D. Nelson, S. Genel, J. Naiman, R. Pakmor, et al. (2018). ≪ Simulating galaxy formation with the IllustrisTNG model ≫. *MNRAS* 473.3, pp. 4077–4106. DOI: `10.1093/mnras/stx2656`. arXiv: `1703.02970 [astro-ph.GA]` (cit. on p. 181).

Planck Collaboration, N. Aghanim, Y. Akrami, M. Ashdown, J. Aumont, C. Baccigalupi, et al. (2020). ≪ Planck 2018 results. VI. Cosmological parameters ≫. *A&A* 641, A6, A6. DOI: `10.1051/0004-6361/201833910`. arXiv: `1807.06209 [astro-ph.CO]` (cit. on p. 3).

Plionis, M., O. López-Cruz & D. Hughes (2008). *A Pan-Chromatic View of Clusters of Galaxies and the Large-Scale Structure*. Vol. 740. DOI: `10.1007/978-1-4020-6941-3` (cit. on p. 3).

Plummer, H. C. (1911). ≪ On the problem of distribution in globular star clusters ≫. *MNRAS* 71, pp. 460–470. DOI: `10.1093/mnras/71.5.460` (cit. on p. 24).

Pohlen, M. & I. Trujillo (2006). ≪ The structure of galactic disks. Studying late-type spiral galaxies using SDSS ≫. *A&A* 454.3, pp. 759–772. DOI: `10.1051/0004-6361:20064883`. arXiv: `astro-ph/0603682 [astro-ph]` (cit. on p. 23).

Portegies Zwart, S. F., S. L. W. McMillan & M. Gieles (2010). ≪ Young Massive Star Clusters ≫. *ARA&A* 48, pp. 431–493. DOI: `10.1146/annurev-astro-081309-130834`. arXiv: `1002.1961 [astro-ph.GA]` (cit. on p. 4).

Pouliasis, E., P. Di Matteo & M. Haywood (2017). ≪ A Milky Way with a massive, centrally concentrated thick disc: new Galactic mass models for orbit computations ≫. *A&A* 598, A66, A66. DOI: `10.1051/0004-6361/201527346`. arXiv: `1611.07979 [astro-ph.GA]` (cit. on pp. vii, ix, 21–25, 52, 74, 95, 97, 110–112, 180, 182, 217).

Press, W. H. & P. Schechter (1974). ≪ Formation of Galaxies and Clusters of Galaxies by Self-Similar Gravitational Condensation ≫. *ApJ* 187, pp. 425–438. DOI: `10.1086/152650` (cit. on p. 3).

Press, W. H., S. A. Teukolsky, W. T. Vetterling & B. P. Flannery (1992). *Numerical recipes in C. The art of scientific computing* (cit. on p. 75).

Price-Whelan, A. M. (2017). ≪ Gala: A Python package for galactic dynamics ≫. *The Journal of Open Source Software* 2, 388, p. 388. DOI: `10.21105/joss.00388` (cit. on p. 71).

Price-Whelan, A. M., C. Mateu, G. Iorio, S. Pearson, A. Bonaca & V. Belokurov (2019). « Kinematics of the Palomar 5 Stellar Stream from RR Lyrae Stars ». *AJ* 158.6, 223, p. 223. DOI: 10.3847/1538-3881/ab4cef. arXiv: 1910.00595 [astro-ph.GA] (cit. on pp. 142, 143, 196, 197).

Price-Whelan, A. M., B. Sesar, K. V. Johnston & H.-W. Rix (2016). « Spending Too Much Time at the Galactic Bar: Chaotic Fanning of the Ophiuchus Stream ». *ApJ* 824.2, 104, p. 104. DOI: 10.3847/0004-637X/824/2/104. arXiv: 1601.06790 [astro-ph.GA] (cit. on pp. 178, 214, 216).

Reid, M. J., K. M. Menten, A. Brunthaler, X. W. Zheng, T. M. Dame, Y. Xu, et al. (2014). « Trigonometric Parallaxes of High Mass Star Forming Regions: The Structure and Kinematics of the Milky Way ». *ApJ* 783.2, 130, p. 130. DOI: 10.1088/0004-637X/783/2/130. arXiv: 1401.5377 [astro-ph.GA] (cit. on pp. 106, 111, 112, 180).

Riley, A. H. & L. E. Strigari (2020). « The Milky Way's stellar streams and globular clusters do not align in a Vast Polar Structure ». *MNRAS* 494.1, pp. 983–1001. DOI: 10.1093/mnras/staa710. arXiv: 2001.11564 [astro-ph.GA] (cit. on p. 135).

Robin, A. & M. Creze (1986). « Stellar populations in the milky way: a synthetic model. » *A&A* 157, pp. 71–90 (cit. on p. 20).

Robin, A. C., O. Bienaymé, J. B. Salomon, C. Reylé, N. Lagarde, F. Figueras, et al. (2022). « A self-consistent dynamical model of the Milky Way disc adjusted to Gaia data ». *A&A* 667, A98, A98. DOI: 10.1051/0004-6361/202243686. arXiv: 2208.13827 [astro-ph.GA] (cit. on pp. 21, 23).

Robin, A. C., C. Reylé, S. Derrière & S. Picaud (2003). « A synthetic view on structure and evolution of the Milky Way ». *A&A* 409, pp. 523–540. DOI: 10.1051/0004-6361:20031117 (cit. on p. 21).

Rockosi, C. M., M. Odenkirchen, E. K. Grebel, W. Dehnen, K. M. Cudworth, J. E. Gunn, et al. (2002). « A Matched-Filter Analysis of the Tidal Tails of the Globular Cluster Palomar 5 ». *AJ* 124.1, pp. 349–363. DOI: 10.1086/340957 (cit. on p. 142).

Salpeter, E. E. (1955). « The Luminosity Function and Stellar Evolution. » *ApJ* 121, p. 161. DOI: 10.1086/145971 (cit. on p. 68).

Sandage, A. (1970). « Main-sequence photometry, color-magnitude diagrams, and ages for the globular clusters M3, M13, M15 and M92. » *ApJ* 162, p. 841. DOI: 10.1086/150715 (cit. on p. 4).

Sanders, J. L. & J. Binney (2013). « Stream-orbit misalignment - I. The dangers of orbit-fitting ». *MNRAS* 433.3, pp. 1813–1825. DOI: 10.1093/mnras/stt806. arXiv: 1305.1935 [astro-ph.GA] (cit. on pp. 104, 221).

Sanders, J. L., J. Bovy & D. Erkal (2016). « Dynamics of stream-subhalo interactions ». *MNRAS* 457.4, pp. 3817–3835. DOI: 10.1093/mnras/stw232. arXiv: 1510.03426 [astro-ph.GA] (cit. on pp. 34, 61, 62, 104, 187, 196, 200, 205, 214).

Schiavon, R. P., O. Zamora, R. Carrera, S. Lucatello, A. C. Robin, M. Ness, et al. (2017). « Chemical tagging with APOGEE: discovery of a large population of N-rich stars in the inner Galaxy ». *MNRAS* 465.1, pp. 501–524. DOI: 10.1093/mnras/stw2162. arXiv: 1606.05651 [astro-ph.GA] (cit. on p. 218).

Schneider, R., A. Ferrara, P. Natarajan & K. Omukai (2002). « First Stars, Very Massive Black Holes, and Metals ». *ApJ* 571.1, pp. 30–39. DOI: 10.1086/339917. arXiv: astro-ph/0111341 [astro-ph] (cit. on p. 4).

Schneider, R., R. Salvaterra, A. Ferrara & B. Ciardi (2006). « Constraints on the initial mass function of the first stars ». *MNRAS* 369.2, pp. 825–834. DOI: 10.1111/j.1365-2966.2006.10331.x. arXiv: astro-ph/0510685 [astro-ph] (cit. on p. 4).

Schönrich, R. (2012). « Galactic rotation and solar motion from stellar kinematics ». *MNRAS* 427.1, pp. 274–287. DOI: 10.1111/j.1365-2966.2012.21631.x. arXiv: 1207.3079 [astro-ph.GA] (cit. on p. 180).

Schönrich, R., J. Binney & W. Dehnen (2010). « Local kinematics and the local standard of rest ». *MNRAS* 403.4, pp. 1829–1833. DOI: 10.1111/j.1365-2966.2010.16253.x. arXiv: 0912.3693 [astro-ph.GA] (cit. on p. 106).

Sen, A., B. E. Clark, E. A. Cloutis, D. N. DellaGiustina, A. R. Hendrix, A. A. Simon, et al. (2021). ≪ Spectral effects of varying texture and composition in two-component “mudpie” simulations: Insights for asteroid (101955) Bennu ≫. *Meteoritics & Planetary Science* 56.6, pp. 1173–1190. DOI: `10.1111/maps.13699` (cit. on p. 222).

Shen, J., R. M. Rich, J. Kormendy, C. D. Howard, R. De Propris & A. Kunder (2010). ≪ Our Milky Way as a Pure-disk Galaxy—A Challenge for Galaxy Formation ≫. *ApJ* 720.1, pp. L72–L76. DOI: `10.1088/2041-8205/720/1/L72`. arXiv: `1005.0385 [astro-ph.CO]` (cit. on p. 111).

Shipp, N., A. Drlica-Wagner, E. Balbinot, P. Ferguson, D. Erkal, T. S. Li, et al. (2018). ≪ Stellar Streams Discovered in the Dark Energy Survey ≫. *ApJ* 862.2, 114, p. 114. DOI: `10.3847/1538-4357/aacdab`. arXiv: `1801.03097 [astro-ph.GA]` (cit. on p. 104).

Shipp, N., A. M. Price-Whelan, K. Tavangar, C. Mateu & A. Drlica-Wagner (2020). ≪ Discovery of Extended Tidal Tails around the Globular Cluster Palomar 13 ≫. *AJ* 160.5, 244, p. 244. DOI: `10.3847/1538-3881/abbd3a`. arXiv: `2006.12501 [astro-ph.GA]` (cit. on p. 104).

Siegal-Gaskins, J. M. & M. Valluri (2008). ≪ Signatures of ΛCDM Substructure in Tidal Debris ≫. *ApJ* 681.1, pp. 40–52. DOI: `10.1086/587450`. arXiv: `0710.0385 [astro-ph]` (cit. on p. 104).

Siegel, M. H. (2001). ≪ Starcounts, Outer Halo Clusters and the Formation of the Milky Way ≫. *American Astronomical Society Meeting Abstracts*. Vol. 199. American Astronomical Society Meeting Abstracts, 109.06, p. 109.06 (cit. on p. 175).

Skrutskie, M. F., R. M. Cutri, R. Stiening, M. D. Weinberg, S. Schneider, J. M. Carpenter, et al. (2006). ≪ The Two Micron All Sky Survey (2MASS) ≫. *AJ* 131.2, pp. 1163–1183. DOI: `10.1086/498708` (cit. on p. 20).

Snaith, O., M. Haywood, P. Di Matteo, M. D. Lehnert, F. Combes, D. Katz, et al. (2015). ≪ Reconstructing the star formation history of the Milky Way disc(s) from chemical abundances ≫. *A&A* 578, A87, A87. DOI: `10.1051/0004-6361/201424281`. arXiv: `1410.3829 [astro-ph.GA]` (cit. on p. 22).

Sofue, Y. (2012). ≪ Grand Rotation Curve and Dark Matter Halo in the Milky Way Galaxy ≫. *PASJ* 64, 75, p. 75. DOI: `10.1093/pasj/64.4.75`. arXiv: `1110.4431 [astro-ph.GA]` (cit. on p. 111).

Sollima, A. (2020). ≪ The eye of Gaia on globular clusters structure: tidal tails ≫. *MNRAS* 495.2, pp. 2222–2233. DOI: `10.1093/mnras/staa1209`. arXiv: `2004.13754 [astro-ph.GA]` (cit. on pp. 175, 196, 197).

Sollima, A., D. Martínez Delgado, R. R. Muñoz, J. A. Carballo-Bello, D. Valls-Gabaud, E. K. Grebel, et al. (2018). ≪ A survey for dwarf galaxy remnants around 14 globular clusters in the outer halo ≫. *MNRAS* 476.4, pp. 4814–4829. DOI: `10.1093/mnras/sty539`. arXiv: `1802.09255 [astro-ph.GA]` (cit. on p. 175).

Sollima, A., D. Martínez-Delgado, D. Valls-Gabaud & J. Peñarrubia (2011). ≪ Discovery of Tidal Tails Around the Distant Globular Cluster Palomar 14 ≫. *ApJ* 726.1, 47, p. 47. DOI: `10.1088/0004-637X/726/1/47`. arXiv: `1010.6303 [astro-ph.GA]` (cit. on pp. 104, 175).

Somerville, R. S. & R. Davé (2015). ≪ Physical Models of Galaxy Formation in a Cosmological Framework ≫. *ARA&A* 53, pp. 51–113. DOI: `10.1146/annurev-astro-082812-140951`. arXiv: `1412.2712 [astro-ph.GA]` (cit. on p. 5).

Springel, V., J. Wang, M. Vogelsberger, A. Ludlow, A. Jenkins, A. Helmi, et al. (2008). ≪ The Aquarius Project: the subhaloes of galactic haloes ≫. *MNRAS* 391.4, pp. 1685–1711. DOI: `10.1111/j.1365-2966.2008.14066.x`. arXiv: `0809.0898 [astro-ph]` (cit. on p. 177).

Starkenburg, E., N. Martin, K. Youakim, D. S. Aguado, C. Allende Prieto, A. Arentsen, et al. (2017). ≪ The Pristine survey - I. Mining the Galaxy for the most metal-poor stars ≫. *MNRAS* 471.3, pp. 2587–2604. DOI: `10.1093/mnras/stx1068`. arXiv: `1705.01113 [astro-ph.GA]` (cit. on p. 9).

Starkman, N., J. Bovy & J. J. Webb (2020). ≪ An extended Pal 5 stream in Gaia DR2 ≫. *MNRAS* 493.4, pp. 4978–4986. DOI: `10.1093/mnras/staa534`. arXiv: `1909.03048 [astro-ph.GA]` (cit. on pp. 103, 142, 143).

Steigman, G. (2007). ≪ Primordial Nucleosynthesis in the Precision Cosmology Era ≫. *Annual Review of Nuclear and Particle Science* 57.1, pp. 463–491. DOI: `10.1146/annurev.nucl.56.080805.140437`. arXiv: `0712.1100 [astro-ph]` (cit. on p. 3).

Table, E. (2024). « 5.6. A. Average Price of Electricity to Ultimate Customers by End-Use Sector ». *US Energy Information Administration* (cit. on p. 12).

Tenachi, W., R. Ibata & F. I. Diakogiannis (2023). « Deep Symbolic Regression for Physics Guided by Units Constraints: Toward the Automated Discovery of Physical Laws ». *ApJ* 959.2, 99, p. 99. DOI: `10.3847/1538-4357/ad014c`. arXiv: `2303.03192 [astro-ph.IM]` (cit. on p. 216).

Testa, V., S. R. Zaggia, S. Andreon, G. Longo, R. Scaramella, S. G. Djorgovski, et al. (2000). « Use of DPOSS data to study globular cluster halos: an application to ¡ASTROBJ¿M 92¡/ASTROBJ¿ ». *A&A* 356, pp. 127–133. DOI: `10.48550/arXiv.astro-ph/0002280`. arXiv: `astro-ph/0002280 [astro-ph]` (cit. on p. 175).

Thomas, G. F., B. Famaey, R. Ibata, F. Renaud, N. F. Martin & P. Kroupa (2018). « Stellar streams as gravitational experiments. II. Asymmetric tails of globular cluster streams ». *A&A* 609, A44, A44. DOI: `10.1051/0004-6361/201731609`. arXiv: `1709.01934 [astro-ph.GA]` (cit. on p. 105).

Thomas, G. F., B. Famaey, G. Monari, C. F. P. Laporte, R. Ibata, P. de Laverny, et al. (2023). « Impact of the Galactic bar on tidal streams within the Galactic disc. The case of the tidal stream of the Hyades ». *A&A* 678, A180, A180. DOI: `10.1051/0004-6361/202346650`. arXiv: `2309.05733 [astro-ph.GA]` (cit. on pp. 214, 221).

Thomas, G. F., R. Ibata, B. Famaey, N. F. Martin & G. F. Lewis (2016). « Exploring the reality of density substructures in the Palomar 5 stellar stream ». *MNRAS* 460.3, pp. 2711–2719. DOI: `10.1093/mnras/stw1189`. arXiv: `1605.05520 [astro-ph.GA]` (cit. on pp. 103, 104, 142, 177).

Usman, S. A., A. P. Ji, T. S. Li, A. B. Pace, L. R. Cullinane, G. S. Da Costa, et al. (2024). « Multiple populations and a CH star found in the 300S globular cluster stellar stream ». *MNRAS* 529.3, pp. 2413–2427. DOI: `10.1093/mnras/stae185`. arXiv: `2401.02476 [astro-ph.GA]` (cit. on pp. 176, 219).

VandenBerg, D. A., K. Brogaard, R. Leaman & L. Casagrande (2013). « The Ages of 55 Globular Clusters as Determined Using an Improved Method along with Color-Magnitude Diagram Constraints, and Their Implications for Broader Issues ». *ApJ* 775.2, 134, p. 134. DOI: `10.1088/0004-637X/775/2/134`. arXiv: `1308.2257 [astro-ph.GA]` (cit. on p. 13).

Varghese, A., R. Ibata & G. F. Lewis (2011). « Stellar streams as probes of dark halo mass and morphology: a Bayesian reconstruction ». *MNRAS* 417.1, pp. 198–215. DOI: `10.1111/j.1365-2966.2011.19097.x`. arXiv: `1106.1765 [astro-ph.GA]` (cit. on pp. 6, 176).

Vasiliev, E. (2018). « Agama reference documentation ». *arXiv e-prints*, arXiv:1802.08255, arXiv:1802.08255. DOI: `10.48550/arXiv.1802.08255`. arXiv: `1802.08255 [astro-ph.IM]` (cit. on pp. 71, 74).

Vasiliev, E. & H. Baumgardt (2021). « Gaia EDR3 view on galactic globular clusters ». *MNRAS* 505.4, pp. 5978–6002. DOI: `10.1093/mnras/stab1475`. arXiv: `2102.09568 [astro-ph.GA]` (cit. on pp. 27, 53, 79, 103, 106, 109, 180).

Vasiliev, E., V. Belokurov & D. Erkal (2021). « Tango for three: Sagittarius, LMC, and the Milky Way ». *MNRAS* 501.2, pp. 2279–2304. DOI: `10.1093/mnras/staa3673`. arXiv: `2009.10726 [astro-ph.GA]` (cit. on pp. 19, 105, 108).

Vegetti, S., D. J. Lagattuta, J. P. McKean, M. W. Auger, C. D. Fassnacht & L. V. E. Koopmans (2012). « Gravitational detection of a low-mass dark satellite galaxy at cosmological distance ». *Nature* 481.7381, pp. 341–343. DOI: `10.1038/nature10669`. arXiv: `1201.3643 [astro-ph.CO]` (cit. on p. 177).

Vesperini, E. & D. C. Heggie (1997). « On the effects of dynamical evolution on the initial mass function of globular clusters ». *MNRAS* 289.4, pp. 898–920. DOI: `10.1093/mnras/289.4.898`. arXiv: `astro-ph/9705073 [astro-ph]` (cit. on p. 103).

Virtanen, P., R. Gommers, T. E. Oliphant, M. Haberland, T. Reddy, D. Cournapeau, et al. (2020). « SciPy 1.0: fundamental algorithms for scientific computing in Python ». *Nature Methods* 17, pp. 261–272. DOI: `10.1038/s41592-019-0686-2`. arXiv: `1907.10121 [cs.MS]` (cit. on p. 205).

Vislosky, E., I. Minchev, S. Khoperskov, M. Martig, T. Buck, T. Hilmi, et al. (2024). « Gaia DR3 data consistent with a short bar connected to a spiral arm ». *MNRAS* 528.2, pp. 3576–3591. DOI: 10.1093/mnras/stae083. arXiv: 2312.03854 [astro-ph.GA] (cit. on p. 216).

Vitral, E. & P. Boldrini (2022). « Properties of globular clusters formed in dark matter mini-halos ». *A&A* 667, A112, A112. DOI: 10.1051/0004-6361/202244530. arXiv: 2112.01265 [astro-ph.GA] (cit. on pp. 9, 105).

Waisberg, I., Y. Klein & B. Katz (2023). « Binarity and beyond in A stars - I. Survey description and first results of VLTI/GRAVITY observations of VAST targets with high Gaia-Hipparcos accelerations ». *MNRAS* 521.4, pp. 5232–5254. DOI: 10.1093/mnras/stad872. arXiv: 2206.05251 [astro-ph.SR] (cit. on p. 22).

Wan, Z., G. F. Lewis, T. S. Li, J. D. Simpson, S. L. Martell, D. B. Zucker, et al. (2020). « The tidal remnant of an unusually metal-poor globular cluster ». *Nature* 583.7818, pp. 768–770. DOI: 10.1038/s41586-020-2483-6. arXiv: 2007.14577 [astro-ph.GA] (cit. on p. 9).

Wang, L., R. Spurzem, S. Aarseth, M. Giersz, A. Askar, P. Berczik, et al. (2016). « The DRAGON simulations: globular cluster evolution with a million stars ». *MNRAS* 458.2, pp. 1450–1465. DOI: 10.1093/mnras/stw274. arXiv: 1602.00759 [astro-ph.SR] (cit. on pp. 5, 180).

Wang, L., R. Spurzem, S. Aarseth, K. Nitadori, P. Berczik, M. B. N. Kouwenhoven, et al. (2015). « NBODY6++GPU: ready for the gravitational million-body problem ». *MNRAS* 450.4, pp. 4070–4080. DOI: 10.1093/mnras/stv817. arXiv: 1504.03687 [astro-ph.IM] (cit. on pp. 71, 215).

Wang, S., J. Nie, B. Jiang, H. Tian, C. Liu & Y.-H. Zhang (2025). « The Structural and Kinematical Properties of NGC 5634, a Globular Cluster Associated with the Sagittarius Dwarf Galaxy? » *ApJ* 988.1, 39, p. 39. DOI: 10.3847/1538-4357/ade0b6. arXiv: 2506.04806 [astro-ph.GA] (cit. on p. 213).

Webb, J. J. & J. Bovy (2019). « Searching for the GD-1 stream progenitor in Gaia DR2 with direct N-body simulations ». *MNRAS* 485.4, pp. 5929–5938. DOI: 10.1093/mnras/stz867. arXiv: 1811.07022 [astro-ph.GA] (cit. on p. 104).

Wegg, C. & O. Gerhard (2013). « Mapping the three-dimensional density of the Galactic bulge with VVV red clump stars ». *MNRAS* 435.3, pp. 1874–1887. DOI: 10.1093/mnras/stt1376. arXiv: 1308.0593 [astro-ph.GA] (cit. on p. 113).

Wegg, C., O. Gerhard & M. Portail (2015). « The structure of the Milky Way's bar outside the bulge ». *MNRAS* 450.4, pp. 4050–4069. DOI: 10.1093/mnras/stv745. arXiv: 1504.01401 [astro-ph.GA] (cit. on pp. 113, 216).

Weyl, H. (1946). *The classical groups: their invariants and representations.* Vol. 1. Princeton university press (cit. on p. 75).

Yim, K.-J. & H. M. Lee (2002). « Tidal Tails of Globular Clusters ». *Journal of Korean Astronomical Society* 35.2, pp. 75–85. DOI: 10.5303/JKAS.2002.35.2.075 (cit. on p. 104).

York, D. G., J. Adelman, J. E. Anderson Jr., S. F. Anderson, J. Annis, N. A. Bahcall, et al. (2000). « The Sloan Digital Sky Survey: Technical Summary ». *AJ* 120.3, pp. 1579–1587. DOI: 10.1086/301513. arXiv: astro-ph/0006396 [astro-ph] (cit. on p. 20).

Yuan, Z., J. Chang, T. C. Beers & Y. Huang (2020). « A Low-mass Stellar-debris Stream Associated with a Globular Cluster Pair in the Halo ». *ApJ* 898.2, L37, p. L37. DOI: 10.3847/2041-8213/aba49f. arXiv: 2007.05132 [astro-ph.GA] (cit. on p. 9).

Yuan, Z., K. Malhan, F. Sestito, R. A. Ibata, N. F. Martin, J. Chang, et al. (2022). « The Complexity of the Cetus Stream Unveiled from the Fusion of STREAMFINDER and StarGO ». *ApJ* 930.2, 103, p. 103. DOI: 10.3847/1538-4357/ac616f. arXiv: 2112.05775 [astro-ph.GA] (cit. on p. 104).

Yuan, Z., T. Matsuno, T. M. Sitnova, N. F. Martin, R. A. Ibata, A. Ardern-Arentsen, et al. (2025). « The Pristine survey: XXVII. The extremely metal-poor stream C-19 stretches over more than 100 degrees ». *A&A* 698, A82, A82. DOI: 10.1051/0004-6361/202554119. arXiv: 2502.09710 [astro-ph.GA] (cit. on p. 9).

Zhang, S., D. Mackey & G. S. Da Costa (2022). ≪ A search for stellar structures around nine outer halo globular clusters in the Milky Way ≫. *MNRAS* 513.3, pp. 3136–3164. DOI: `10.1093/mnras/stac751`. arXiv: `2111.09072 [astro-ph.GA]` (cit. on p. 104).

Ziliotto, T., A. P. Milone, G. Cordoni, F. I. Aros, E. Vesperini, J. .-. Lee, et al. (2025). ≪ A JWST project on 47 Tucanae: Kinematics, energy equipartition, and anisotropy of multiple populations ≫. *A&A* 698, A209, A209. DOI: `10.1051/0004-6361/202554038`. arXiv: `2502.03140 [astro-ph.SR]` (cit. on p. 68).

Zou, X.-D., J.-Y. Li, B. E. Clark, D. R. Golish, S. Ferrone, A. A. Simon, et al. (2021). ≪ Photometry of asteroid (101955) Bennu with OVIRS on OSIRIS-REx ≫. *Icarus* 358, 114183, p. 114183. DOI: `10.1016/j.icarus.2020.114183` (cit. on p. 222).

Zucker, D. B., G. de Silva, K. Freeman, J. Bland-Hawthorn & Hermes Team (2012). ≪ The Galactic Archaeology with HERMES Survey ≫. *Galactic Archaeology: Near-Field Cosmology and the Formation of the Milky Way*. Ed. by W. Aoki, M. Ishigaki, T. Suda, T. Tsujimoto & N. Arimoto. Vol. 458. Astronomical Society of the Pacific Conference Series, p. 421 (cit. on p. 7).

RÉSUMÉ

La mission astrométrique *Gaia* a permis l'étude à grande échelle des étoiles et des sous-structures galactiques. Environ 160 amas globulaires (AG) de la Voie lactée, chacun contenant de centaines de milliers à plusieurs millions d'étoiles, peuvent désormais être caractérisés par des distances, des mouvements propres, des vitesses radiales, des masses et des tailles précises. Parallèlement, le nombre de courants stellaires connus est passé d'environ 60 au début de cette thèse à plus de 120 aujourd'hui. Comme les courants tracent les orbites de leurs progéniteurs, ils constituent d'excellents sondages du potentiel gravitationnel de la Voie lactée et des perturbations induites par la matière noire. Grâce à ces données, nous avons étudié le système des courants stellaires et des amas globulaires galactiques. J'ai développé le code open-source tstrippy, qui modélise la perte d'étoiles d'amas par effet de marée via le problème restreint à trois corps. Dans ce cadre, nous prédisons la distribution des débris de marée de tous les AG galactiques et réalisons des simulations du courant de Palomar 5, en montrant la formation de ≪ gaps ≫ dus aux passages proches d'autres amas globulaires. Nous présentons les premières prédictions globales des débris de marée de tous les AG de la Voie lactée. Ces simulations sont accessibles publiquement et utilisées par la communauté. Dans l'étude suivante, nous quantifions la fréquence et l'ampleur des rencontres d'amas globulaires perturbant Palomar 5, montrant que ces interactions doivent être prises en compte pour éviter les faux positifs dans les recherches de sous-halos de matière noire. Nous démontrons également que la présence, dans la même région d'un courant, de populations d'étoiles perdues à différents moments, peut réduire la persistance des gaps, diminuant la sensibilité des courants aux perturbations externes. Ce travail établit la distribution attendue des courants stellaires des AG galactiques et quantifie l'importance des perturbations induites par les AG sur Palomar 5. C'est une première étape pour distinguer l'origine des perturbations des courants, étudier la dynamique interne et l'évolution des amas globulaires, et contraindre le potentiel gravitationnel de la Voie lactée dans sa partie visible et noire.

MOTS CLÉS

Voie Lactée ; Amas globulaires ; courants stellaires ; Matière noire ; Dynamique galactique ; Forces de marée

ABSTRACT

The *Gaia* astrometric mission has enabled large-scale studies of stars and Galactic substructures. About 160 Milky Way globular clusters (GCs), each with hundreds of thousands to millions of stars, can now be characterized via accurate distances, proper motions, radial velocities, masses, and sizes. Meanwhile, known stellar streams have grown from about 60 at the start of this thesis to over 120 today. Because streams trace progenitor orbits, they provide excellent probes of the Milky Way's gravitational potential and dark matter perturbations. Enabled by this data, we studied the Galactic stellar stream and globular cluster system. I developed the open-source code `tstrippy`, which models tidal stripping of cluster stars via the restricted three-body problem. Using this framework, we predicted the distribution of tidal debris from all Galactic GCs and ran targeted simulations of Palomar 5's stream, finding that "gaps" can be generated by GC flybys. We present the first global predictions of tidal debris from all Milky Way GCs. These simulations are publicly available and used by the community. In a follow-up study, we quantified the frequency and range of GC encounters perturbing Palomar 5, showing such interactions must be considered to avoid false positives in dark matter subhalo searches. We also showed that the presence, in a given region of the stellar stream, of populations of stars lost at different times can reduce gap persistence, lowering stream sensitivity to external perturbations. This work establishes the expected distribution of tidal streams from Galactic GCs and quantifies the rate at which GCs perturb Palomar 5. It provides a foundation for disentangling the origins of stream perturbations, studying the internal dynamics and evolution of globular clusters, and constraining the Milky Way's gravitational potential in both visible and dark matter.

KEYWORDS

Milky Way; Globular Clusters; Stellar Streams; Dark Matter; Galactic Dynamics; Tidal Forces